

Personalized Functional Near Infra-Red Optical Tomography to
Investigate the Hemodynamic Correlates of Fluctuations in
Neuronal Excitability

Zhengchen Cai

A Thesis
In the Department of
Physics

Presented in Partial Fulfillment of the Requirements
For the Degree of
Doctor of Philosophy (Physics) at
Concordia University
Montreal, Quebec, Canada

August 2021

© Zhengchen Cai, 2021

CONCORDIA UNIVERSITY
SCHOOL OF GRADUATE STUDIES

This is to certify that the thesis prepared

By: Zhengchen Cai

Entitled: Personalized Functional Near Infra-Red Optical Tomography to Investigate the
Hemodynamic Correlates of Fluctuations in Neuronal Excitability

and submitted in partial fulfillment of the requirements for the degree of

DOCTOR OF PHILOSOPHY (Physics)

complies with the regulations of the University and meets the accepted standards with respect to originality and quality.

Signed by the final Examining Committee:

_____	Chair
Dr. Karen Li	
_____	External Examiner
Dr. Theodore Huppert	
_____	External to Program
Dr. Marta Kersten-Oertel	
_____	Examiner
Dr. Pablo Bianucci	
_____	Examiner
Dr. Claudine Gauthier	
_____	Thesis Supervisor
Dr. Christophe Grova	

Approved by _____

Dr. Alexandre Champagne Graduate Program Director

August 23, 2021
Date of Defence

Dr. Pascale Sicotte Dean, Faculty of Arts and Science

Abstract

Personalized Functional Near Infra-Red Optical Tomography to Investigate the Hemodynamic Correlates of Fluctuations in Neuronal Excitability

Zhengchen Cai, Ph.D.

Concordia University, 2021

The relationship between cortical excitability and hemodynamic activity has been demonstrated in animal studies. However, it is poorly reproduced and understood in humans, limited by the requirement of simultaneous measurements of excitability and hemodynamic activity. Transcranial Magnetic Stimulation (TMS) is a non-invasive technique that induces human cortical plasticity and allows the assessment of modulated cortical excitability. Functional Near Infra-Red Spectroscopy (fNIRS) is a non-invasive neuroimaging modality, which allows monitoring changes in oxy- and deoxy-hemoglobin (i.e., HbO/HbR) in the cerebral cortex. Taking advantage of the fNIRS technique being insensitive to electromagnetic artifacts and wearable, the combination with TMS provides a unique and promising way to assess the relationship between cortical excitability and hemodynamic responses in humans.

This Ph.D. thesis consists of four original studies combining personalized Near Infra-Red Optical Tomography (NIROT) and TMS to investigate the hemodynamic correlates of fluctuations in neuronal excitability, each including key methodological developments. In the first manuscript, we proposed and evaluated a new NIROT reconstruction method – the Maximum Entropy on the Mean (MEM), by adapting and improving its original version proposed for Electro-/Magneto-encephalography source imaging. After detailed evaluations of MEM NIROT on realistic simulated data, we introduced in the second manuscript the original concept of personalized NIROT workflow combining MEM reconstruction and personalized optimal montage. Using functional magnetic resonance imaging as the reference, the evaluation of finger tapping data demonstrated that our proposed workflow allowed better spatial accuracy and reliability than other widely used NIROT methods. The third manuscript applied this workflow on a simultaneous TMS and fNIRS study and demonstrated a positive relationship between motor task-related hemodynamic activity and cortical excitability. The last manuscript applied advanced Bayesian data analysis and hierarchical models to the same data set, which improved the accuracy and

reliability of the results when dealing with relatively high variability and small sample size data. Our results showed a significant positive correlation between the effects of TMS modulated cortical excitability and its effects on task-related hemodynamic activity. Therefore, our studies contribute to further expand the application of brain stimulation to the treatment of neuronal disorders that may require modulations of the hemodynamic response.

Résumé

Tomographie Optique Proche Infra-Rouge fonctionnelle et Personnalisée dans l'étude des corrélations entre les fluctuations hémodynamiques et l'excitabilité neuronale.

Zhengchen Cai, Ph.D.

Université Concordia, 2021

La relation entre l'excitabilité corticale et l'activité hémodynamique a été démontrée dans des études animales. Cependant, cette relation est mal reproduite et comprise chez l'humain en raison de la nécessité de mesurer de façon simultanée l'excitabilité neuronale et l'activité hémodynamique. La Stimulation Magnétique Transcrânienne (SMT) est une technique non invasive qui permet d'induire une plasticité corticale chez l'humain et de moduler l'excitabilité corticale. La Spectroscopie Proche Infra-Rouge fonctionnelle (SPIRf) est une modalité de neuro-imagerie non invasive qui permet de mesurer les modifications d'oxy- et de désoxy-hémoglobines (c'est-à-dire HbO/HbR) au sein du cortex cérébral. L'utilisation de la SPIRf, qui a comme principaux avantages d'être portable et insensible aux artefacts électromagnétiques, en combinaison avec la SMT, offre ainsi un moyen unique et prometteur d'évaluer la relation entre l'excitabilité corticale et la réponse hémodynamique chez l'humain.

Cette thèse de doctorat s'articule autour de quatre études originales combinant la Tomographie Optique Proche Infra-Rouge Personnalisée (TOPIR) et la SMT pour étudier les corrélations entre les fluctuations hémodynamiques et l'excitabilité neuronale, chacune incluant des développements méthodologiques clés. Dans le premier manuscrit, nous avons proposé et évalué une nouvelle méthode de reconstruction TOPIR - l'entropie maximale sur la moyenne (EMM), en adaptant et améliorant sa version originale proposée pour l'imagerie de source électrique/électromagnétique. Après des évaluations détaillées de l'EMM-TOPIR sur des données de simulations réelles, nous avons introduit dans le deuxième manuscrit le concept original d'analyse TOPIR personnalisée à l'aide du montage optimal personnalisé combinée à l'EMM. En utilisant l'imagerie par résonance magnétique fonctionnelle (IRMf) comme référence, l'analyse des données de tapotement des doigts a démontré que notre méthode permettait une meilleure précision spatiale et une meilleure fiabilité que les autres méthodes NIROT largement utilisées. Dans le troisième manuscrit, nous avons appliqué cette méthode à une étude simultanée SMT et SPIRf. Nous avons démontré qu'il

existait une relation positive entre l'activité hémodynamique liée à la tâche réalisée et l'excitabilité corticale. Dans le dernier manuscrit, nous avons appliqué une analyse bayésienne des données et des modèles hiérarchiques au même ensemble de données, ce qui a permis d'améliorer la précision et la fiabilité des résultats vue la grande variabilité de nos données et la petite taille de notre échantillon.

Nos résultats ont montré une corrélation positive et significative entre les effets de l'excitabilité corticale modulée par la SMT et l'effet de l'activité hémodynamique liée à la tâche. Nos études contribuent donc à mieux comprendre et probablement à élargir les indications de la stimulation cérébrale dans le traitement des maladies neurologiques pouvant nécessiter des modulations de la réponse hémodynamique.

Acknowledgments

My Ph.D. program was supported by a research bursary from my supervisor Dr. Christophe Grova, the Fonds de recherche du Québec – Santé (FRQS) Doctoral Training Scholarship and the PERFORM Graduate Scholarship in Preventive Health Research. The TMS/fNIRS project was supported by a FRQS-Quebec Bio-Imaging Network (QBIN) Pilot Project grant.

I would like to express my deepest gratitude to my supervisor Dr. Christophe Grova. All the work done in this thesis could not have been completed without his guidance and support. I thank for his kindness in recruiting me from the other hemisphere of the earth; for his professionalism in mentoring me to develop research skills; for his respect in providing me freedom to practice independent thinking; for his encouragement in motivating me to realize my ideas; for his patience in tolerating my mistakes; for his helpfulness in recommending my works to the research community; and for his personality in demonstrating me how colorful the life could be.

I would like to extend my great appreciation to my Ph.D. committee: Dr. Claudine Gauthier and Dr. Pablo Bianucci for their assistance, tolerance and valuable comments at each stage of this program.

My sincere thanks to Dr. Giovanni Pellegrino who initiated me to the TMS/fNIRS project with my supervisor, trained me on brain stimulation techniques, illustrated to me how to deliver the message of a study, and demonstrated to me how to manage time by working hard. My special thanks to Dr. Jean-Marc Lina for his valuable suggestions and validations from the methodological aspects of the MEM framework and all other techniques applied in this thesis. My sincere thanks to Édouard Delaire, Giovanni Pellegrino, Jawata Afnan, Makoto Uji and Yimeng Wang for commenting on my thesis.

No word can express how lucky I feel to work in this fantastic Multifunkim laboratory. For every former and current colleague, I love you all so much. It is your kindness and friendship that made these six years being the happiest period in my life so far. I wish you the best of luck in all of your future endeavors and wonderful life.

Finally, my deepest gratitude to my family for their unfailing support and unconditional love. My parents always encourage me to pursue what I prefer, my wife makes me feel so lucky, and my dog is so generous for her sweetest smile.

Dedications

“Let us have, the serenity to embrace the variation that we cannot reduce, the courage to reduce the variation we cannot embrace, and the wisdom to distinguish one from the other.”

– Dr. Andrew Gelman

“Ask your questions, they are never dumb. Follow them, and try to understand in your own way”

– Dr. Judea Pearl

“Data and analysis are the product of science, not paper which is the advertisement.”

– Dr. Richard McElreath

“Effective communication for rational minds is about maximizing the signal to noise ratio of the message.”

– Dr. Jean-luc Doumont

“Remember that using Bayes' Theorem doesn't make you a Bayesian. Quantifying uncertainty with probability makes you a Bayesian.”

– Dr. Michael Betancourt

This thesis is dedicated to all the wise people who inspired, encouraged and mentored me during my Ph.D. program.

Contributions of Authors

This thesis was authored by myself, under the supervision of my supervisor Dr. Christophe Grova. Together we designed the studies, developed the methodologies, conducted the analyses, interpreted the results, and wrote the manuscripts. All data acquisitions were carried out by myself with substantial assistance from the co-authors. This thesis consists of four studies, in which the contributions of each co-author other than myself and my supervisor are summarized below.

Manuscript 1: Diffuse Optical Reconstructions of Functional Near Infra-Red Spectroscopy Data using Maximum Entropy on the Mean

In revision in Scientific Reports

Authors: Zhengchen Cai, Alexis Machado, Rasheda Arman Chowdhury, Amanda Spilkin, Thomas Vincent, Ümit Aydın, Giovanni Pellegrino, Jean-Marc Lina, Christophe Grova

- **Dr. Alexis Machado** trained me on fNIRS data acquisition, assisted with the fNIRS data analysis, and provided useful guidance on applying optimal montage. He also contributed significantly on reviewing and editing the manuscript.
- **Dr. Rasheda Arman Chowdhury** provided useful advice in understanding the details of the original MEM framework. She also reviewed the manuscript.
- **Amanda Spilkin** assisted with data acquisitions and reviewed the manuscript.
- **Dr. Thomas Vincent** assisted with the experiment protocol design.
- **Dr. Ümit Aydın** helped with the anatomical and fMRI data processing and reviewed the manuscript.
- **Dr. Giovanni Pellegrino** helped with the definition of the anatomical region of interest and reviewed the manuscript.
- **Dr. Jean-Marc Lina** was involved with the methodology development, the interpretation of the results, writing and reviewing the manuscript.

Manuscript 2: Evaluation of a Personalized Functional Near Infra-Red Optical Tomography Workflow using Maximum Entropy on the Mean

Published in Human Brain Mapping, DOI: 10.1002/hbm.25566

Authors: Zhengchen Cai, Makoto Uji, Ümit Aydın, Giovanni Pellegrino, Amanda Spilkin, Edouard Delaire, Chifaou Abdallah, Jean-Marc Lina, Christophe Grova

- **Dr. Makoto Uji** trained me on fMRI data analysis, assisted with data acquisitions, and contributed significantly on reviewing and editing the manuscript.
- **Dr. Ümit Aydin** provided useful advice in results validation and reviewed the manuscript.
- **Dr. Giovanni Pellegrino** was involved with experiment protocol design and reviewed the manuscript.
- **Amanda Spilkin** assisted with data acquisitions and reviewed the manuscript.
- **MSc. Edouard Delaire** assisted with data acquisitions and reviewed the manuscript.
- **Dr. Chifaou Abdallah** assisted with data acquisitions and reviewed the manuscript.
- **Dr. Jean-Marc Lina** was involved with the methodology development, the interpretation of the results, writing and reviewing the manuscript.

Manuscript 3: Hemodynamic Correlates of Fluctuations in Neuronal Excitability: A Simultaneous Paired Associative Stimulation (PAS) and functional Near Infra-Red Spectroscopy (fNIRS) Study

In preparation

Authors: Zhengchen Cai, Giovanni Pellegrino, Amanda Spilkin, Edouard Delaire, Makoto Uji, Chifaou Abdallah, Jean-Marc Lina, Shirley Fecteau, Christophe Grova

- **Dr. Giovanni Pellegrino** contributed equally to this work and trained me on applying TMS. He was involved with conceptualization, investigation, original draft preparation, and reviewing and editing the manuscript. He is sharing with me the first authorship of this article.
- **Amanda Spilkin** assisted with pilot investigation and data acquisitions.
- **MSc. Edouard Delaire** assisted with data acquisitions and reviewed the manuscript.
- **Dr. Makoto Uji** assisted with data acquisitions and reviewed the manuscript.
- **Dr. Chifaou Abdallah** assisted with data acquisitions and reviewed the manuscript.
- **Dr. Jean-Marc Lina** was involved with the methodology development, writing, and reviewing of the manuscript.
- **Dr. Shirley Fecteau** was involved with the conceptualization of the project, and significantly helped in reviewing the manuscript.

Manuscript 4: Hierarchical Bayesian Modeling of Task Related Hemodynamic Correlates of Neuronal Excitability Changes using Simultaneous Transcranial Magnetic Stimulation (TMS) and functional Near Infra-Red Spectroscopy (fNIRS)

In preparation

Authors: Zhengchen Cai, Giovanni Pellegrino, Jean-Marc Lina, Habib Benali, Christophe Grova

- **Dr. Giovanni Pellegrino** was involved with conceptualization, investigation, and the original draft preparation.
- **Dr. Jean-Marc Lina** was involved with the methodology development.
- **Dr. Habib Benali** provided useful advice in the validation of the proposed methodology.

Originality of Thesis

This Ph.D. thesis is based on four studies, each consisting of an original research manuscript. Statements of originality corresponding with each of the projects are summarized below.

Manuscript 1: Diffuse Optical Reconstructions of Functional Near Infra-Red Spectroscopy Data using Maximum Entropy on the Mean

- We introduced a new fNIRS reconstruction method - the Maximum Entropy on the Mean (MEM), which was adapted and improved based on its original version designed for Electroencephalogram (EEG) and Magnetoencephalography (MEG) source imaging.
- For the first time, we implemented a depth weighting strategy within the MEM framework allowing more accurate spatial localizations along different generator depths and sizes.
- We improved the temporal accuracy of the original MEM reconstruction, providing similar temporal performance compared to the standard linear reconstruction method Minimum Norm Estimate (MNE) which is usually considered to provide a good temporal accuracy. This feature is crucial for reconstructing hemodynamic responses.
- Performances of MEM and MNE were evaluated using 4,000 realistic simulations containing different generator depths and sizes. We showed that MEM provided more robust reconstructions than MNE, when reconstructing low SNR data.

Manuscript 2: Evaluation of a Personalized Functional Near Infra-Red Optical Tomography Workflow using Maximum Entropy on the Mean

- We introduced an original workflow denoted personalized Near Infra-Red Optical Tomography (NIROT), integrating several methodological developments of our lab, i.e., MEM reconstruction and fNIRS personalized optimal montage.
- We introduced a new procedure to extract the region of interests from fMRI Z-map as the evaluation reference of NIROT images, considering the known spatial variability of fMRI main cluster due to within-subject variability of fMRI data.
- We demonstrated that MEM method performed better than the MNE method in terms of spatial accuracy and achieved similar temporal accuracy when applied to a real motor task. We also proved aforementioned advantages of our proposed workflow was robust among all time points in the whole reconstructed time course (not only on the peak). Excellent performance of MEM in terms of spatial accuracy remained valid even when further thresholding the reconstructed maps. We also

demonstrated that our proposed optimal montage of the NIRS layout, aiming at maximizing light sensitivity to a target region, did not introduce bias on the reconstruction results.

- We conducted reliability analysis and showed that MEM was a more reliable method than MNE when considering within-/between-subject variability.
- To practice open science, all methodologies of the workflow have been implemented in NIRSTORM - a plugin of fNIRS data analysis in the Brainstorm software, and openly available for those who are interested in this approach.

Manuscript 3: Hemodynamic Correlates of Fluctuations in Neuronal Excitability: A Simultaneous Paired Associative Stimulation (PAS) and functional Near Infra-Red Spectroscopy (fNIRS) Study

- This study is the first one to investigate the relationship between excitability and hemodynamic activity with simultaneous PAS-fNIRS in humans. It contributes to the field from both scientific and methodology perspectives.
- We demonstrated a positive linear relationship between primary motor cortex (M1) excitability and task-related hemodynamic response regardless of the intervention type. We also showed that PAS could modulate both M1 excitability and elicited hemodynamic responses, suggesting that PAS effects on M1 excitability and hemodynamic activity are positively and linearly correlated.
- We proposed a resampling technique designed to extract reliable, robust, and data-driven HbO/HbR measures from fNIRS reconstructions, being blind to PAS intervention types. This strategy was applied considering the variability of each hemodynamic response to the motor task, instead of using only one averaged hemodynamic response. This approach can be further applied in general applications for reliable fNIRS analysis.

Manuscript 4: Hierarchical Bayesian Modelling of Task Related Hemodynamic Correlates of Neuronal Excitability Changes using Simultaneous Transcranial Magnetic Stimulation (TMS) and functional Near Infra-Red Spectroscopy (fNIRS)

- We developed original hierarchical Bayesian models for PAS effects on M1 excitability and hemodynamic activity. The variability of Motor Evoked Potential (MEP), HbO, and HbR amplitudes were directly involved in the estimation of PAS effects rather than only using the averaged amplitude of each session.
- For the first time, we modeled and demonstrated PAS effects on the whole time-course of task-related hemodynamic responses. This approach can bring more insights into PAS effects on

hemodynamic responses – not only peak amplitudes before and after the interventions can be compared, but also intervention effects on the overall shape of HbO/HbR time courses.

- We demonstrated an improvement in data analysis procedure when compared to our previous study, this time involving data variability in an advanced data analysis method using probabilistic modeling. We illustrated the added value of the Bayesian framework along with informative inferences when dealing with relatively high variabilities in the data.

Table of Contents

List of Tables	xiii
List of Figures	xiv
Introduction	1
Chapter 1 Personalized Functional Near Infra-Red Optical Tomography	7
1.1 Continuous Wave fNIRS.....	7
1.1.1 Cerebral neuronal activity related hemodynamics	7
1.1.2 The principle of CW-fNIRS	10
1.1.3 Other components of CW-fNIRS signal.....	13
1.1.4 Channel space analysis for CW-fNIRS	14
1.2 Personalized NIROT	16
1.2.1 Personalized fNIRS montage.....	17
1.2.2 Model of NIROT	19
1.3 NIROT forward problem.....	20
1.4 Solving NIROT inverse problem	25
1.4.1 Back projection (BP)	25
1.4.2 Truncated singular value decomposition (tSVD)	26
1.4.3 Minimum norm estimation (MNE).....	26
1.4.4 Low-resolution electromagnetic tomography (LORETA)	27
1.4.5 Sparse reconstructions based on ℓ_1 – and ℓ_0 – norm	27
1.4.6 Bayesian model averaging (BMA)	28
1.4.7 Bayesian approach using Automatic Relevance Determination (ARD) hierarchical prior	29
1.4.8 Maximum Entropy on the Mean (MEM) framework.....	30
1.5 Depth weighting	33
1.5.1 Depth weighted MNE.....	34
1.5.2 Depth weighted MEM	35
1.5.3 Other depth weighting approaches	35
1.6 Summary	36
Chapter 2 Combination of TMS and fNIRS	37
2.1 Spike timing dependent plasticity	37
2.2 Inducing neuronal plasticity noninvasively.....	39

2.2.1 Single pulse TMS	40
2.2.2 Repetitive TMS.....	42
2.2.3 Pair associative stimulation	44
2.3 Combination of TMS and fNIRS	46
2.3.1 Combination of TMS and human brain mapping.....	46
2.3.2 Advantages and challenges of TMS/fNIRS.....	48
2.3.3 Hemodynamic responses evoked by spTMS.....	53
2.3.4 Effects of excitability modulations on hemodynamic responses.....	54
2.3.5 TMS effects on task evoked hemodynamics	56
2.4 Summary	56
Chapter 3 Introduction of Bayesian Data Analysis	58
3.1 Probabilistic modeling.....	58
3.1.1 Bayes' rule.....	59
3.1.2 Modeling the association between data and parameters.....	61
3.1.3 Weakly informative prior	63
3.2 Estimation of the posterior distributions	65
3.2.1 Analytical solution.....	65
3.2.2 Grid approximation.....	66
3.2.3 Markov Chain Monte Carlo.....	68
3.2.4 Hamiltonian Monte Carlo.....	72
3.3 Markov Chain Diagnostic statistics.....	75
3.3.1 General MCMC diagnostics	75
3.3.2 HMC diagnostic statistics.....	77
3.4 Bayesian Inferences vs. frequentist inferences	77
3.4.1 Bayesian inferences	78
3.4.3 Comparison with frequentist inferences	79
3.5 Conclusions	81
Chapter 4 Manuscript 1	83
Context	83
Abstract	84
4.1 Introduction	84
4.2 Material and methods	87
4.2.1 fNIRS reconstruction	87

4.2.2 Minimum Norm Estimation (MNE).....	88
4.2.3 Depth weighted MNE.....	88
4.2.4 Maximum Entropy on the Mean (MEM) for fNIRS 3D reconstruction.....	89
4.2.5 Validation of fNIRS reconstruction methods.....	93
4.2.6 Statistics.....	100
4.3 Results.....	101
4.3.1 Evaluation of MEM v.s. MNE using realistic simulations.....	101
4.3.2 Effects of depth weighting on the reconstructed generator as a function of the depth and size of the simulated generators.....	105
4.3.3 Robustness of 3D reconstructions to the noise level.....	107
4.3.4 Evaluation of MEM and MNE on real fNIRS data.....	108
4.4 Discussion.....	111
4.4.1 Spatial accuracy of 3D fNIRS reconstruction using MEM.....	111
4.4.2 Implementation of depth weighting strategy within the MEM framework.....	112
4.4.3 Temporal accuracy of 3D fNIRS reconstruction using MEM.....	113
4.4.4 Robustness of fNIRS reconstructions to the noise level.....	113
4.4.5 Comprehensive evaluation and comparison of the reconstruction performance using MEM and MNE.....	114
4.4.6 Availability of the proposed MEM framework.....	114
4.4.7 Limitations and Perspectives.....	115
4.5 Conclusion.....	116
4.6 Supplementary material.....	116
Chapter 5 Manuscript 2	122
Context.....	122
Abstract.....	123
5.1 Introduction.....	123
5.2 Materials and methods.....	126
5.2.1 Subject cohort and experiment protocol.....	126
5.2.2 Structural and functional MRI acquisitions.....	126
5.2.3 Anatomical data processing.....	127
5.2.4 fMRI data processing.....	127
5.2.5 Personalized fNIRS data acquisition and pre-processing.....	128
5.2.6 Forward model estimation for NIROT.....	129

5.2.7 NIROT reconstruction	131
5.2.8 Quantitative evaluation by comparing NIROT to fMRI	131
5.2.9 Reliability of the performance differences between MEM and MNE.....	136
5.2.10 Data availability.....	137
5.3 Results.....	137
5.3.1 Reconstruction performance comparisons at the individual-level	138
5.3.2 Reconstruction performance comparisons at the group-level	144
5.3.3 NIROT performance along time.....	145
5.3.4 NIROT performance when applying spatial thresholding on reconstruction maps ...	146
5.3.5 AUC of the sensitivity profile of the optimal montage	146
5.3.6 Reliability of performance differences between MEM and MNE	147
5.4 Discussion	148
5.4.1 Evaluation of the performance of personalized NIROT using MEM	148
5.4.2 Comparison of MEM and MNE reconstruction performance along time	149
5.4.3 Comparison of MEM and MNE reconstruction performance with spatial thresholding	149
5.4.4 Assessment whether the local forward model of personalized optimal montage was biasing NIROT reconstructions	150
5.4.5 Using fMRI as the reference for NIROT evaluation	151
5.4.6 Difference between NIROT and fMRI maps	153
5.4.7 Comparison with other NIROT workflows	154
5.4.8 Implementation of the workflow in an open-source toolbox	155
5.4.9 Limitations and future directions.....	156
5.5 Conclusion.....	157
5.6 Appendices	157
5.7 Supplementary Materials.....	162
Chapter 6 Manuscript 3	165
Context	165
Abstract	166
6.1 Introduction.....	166
6.2 Material and methods	168
6.2.1 Subjects and study design.....	168
6.2.2 Personalized fNIRS using the optimal montage.....	172

6.2.3 Excitability data analysis	174
6.2.4 fNIRS data processing	174
6.2.5 Statistical analysis	175
6.3 Results	175
6.3.1 Correlation between cortical excitability and task-related hemodynamic responses .	176
6.3.2 PAS effects on cortical excitability and task-related hemodynamic activity	177
6.3.3 Relationship between PAS-related excitability and hemodynamic changes	182
6.4 Discussion	183
6.4.1 Correlation between cortical excitability and hemodynamic activity	184
6.4.2 PAS effects on hemodynamic activity	184
6.4.3 Correlation between PAS effects on excitability and PAS effects on hemodynamic activity	185
6.4.4 Reliability and robustness	186
6.4.5 Limitations	187
6.5 Conclusion	187
6.6 Appendices	187
Chapter 7 Manuscript 4	195
Context	195
Abstract	196
7.1 Introduction	197
7.2 Material and methods	201
7.2.1 Study design and subjects	201
7.2.2 Data acquisitions	203
7.2.3 Data preprocessing	205
7.2.4 Hierarchical Bayesian Modeling	208
7.2.5 Prior predictive simulation	217
7.2.6 Hierarchical Bayesian model fitting	218
7.2.7 Statistical inferences	220
7.3 Results	222
7.3.1 Prior predictive simulation	222
7.3.2 Diagnosis of HMC	223
7.3.3 PAS effects on cortical excitability	224
7.3.4 PAS effects on task-related HbO/HbR responses	227

7.3.5 Relationship between PAS effects on task-related cortical hemodynamic activity and PAS effects on M1 excitability.....	229
7.4 Discussion	231
7.4.1 PAS effects on cortical excitability	231
7.4.2 PAS effects on the whole HbO/HbR time course of finger tapping responses	232
7.4.3 Relationship between PAS effects on task-related hemodynamic and PAS effects on M1 excitability	235
7.4.4 HMC sampling and diagnostic	235
7.4.5 Limitations and perspectives	236
7.5 Conclusion.....	238
7.6 Supplementary material.....	238
Chapter 8 General Discussion.....	240
8.1 Summary of main contributions and limitations	240
8.1.1 Development and evaluation of MEM framework for NIROT	240
8.1.2 Evaluation and application of the personalized NIROT workflow using MEM.....	241
8.1.3 Application of personalized NIROT workflow on a simultaneous PAS/fNIRS study.....	243
8.1.4 Application of probabilistic modeling (Bayesian data analysis) to investigate the correlation between task-related hemodynamic responses and neuronal excitability.....	245
8.2 Future directions.....	247
8.2.1 Upgrading NIROT workflow using a hybrid montage containing both locally optimized montage and global fNIRS measurements	247
8.2.2 Assessment of the integrity of neurovascular coupling at the time of transient discharges evoked by TMS under the stable cortical excitability changes modulated by PAS	249
8.3 Conclusion.....	252
Bibliography	254

List of Tables

Table.4.1 Wilcoxon signed rank test results of reconstruction performance comparison of MEM and MNE in superficial seeds case.	103
Table.4.2 Reconstruction performance comparison of MEM and MNE with different SNR levels.	108
Table.4.S1 Wilcoxon signed rank test results of reconstruction performance comparison of MEM and MNE in middle seeds case..	120
Table.4.S2 Wilcoxon signed rank test results of reconstruction performance comparison of MEM and MNE in deep seeds case.....	121
Table.5.1 Statistical comparison of reconstructed HbO/HbR peak times.	143
Table.6.1 Group-level PAS effects on cortical excitability and hemodynamic activity.....	178

List of Figures

Fig.1.1 Structure of hemoglobin and the oxygen equilibrium curve..	9
Fig.1.2 Mechanism of HbO/HbR concentration changes and the signal component of interest for functional brain activity measurement..	10
Fig.1.3 Demonstration of the principle of CW-fNIRS.	12
Fig.1.4 CW-fNIRS signal components.	16
Fig.1.5 Demonstration of personalized optimal montage probing the ‘hand knob’ area using different configurations.....	19
Fig.1.6 Solving NIROT forward problem by Monte Carlo Simulation.....	24
Fig.1.7. Illustration of Maximum entropy on the mean (MEM) framework.	32
Fig.1.8 Illustration of the relationship between sensitivity and depth for the cortical area..	34
Fig.2.1 Principle of spike timing-dependent plasticity (STDP).....	39
Fig.2.2 Demonstration of spTMS consisting of the physics principle of TMS, TMS evoked activities and pulse configurations.....	41
Fig.2.3 Three typically used TMS protocols for modulation of cortical excitability..	43
Fig.2.4 Demonstration of Paired Associative Stimulation (PAS).....	45
Fig.2.5 Demonstration of two approaches for combination TMS and neuroimaging.	48
Fig.2.6 NIRS optodes from different commercial products.	50
Fig.2.7 Relationship between TMS coil to scalp distance and stimulation strength.	51
Fig.2.8 Concurrent TMS and fNIRS acquisition set-up and optodes design.....	52
Fig.3.1 Demonstration of grid approximation for a 2D Gaussian distribution.	67
Fig.3.2 Demonstration of Metropolis-Hastings algorithm when sampling a bivariate normal distribution.	70
Fig.3.3 Demonstration of Gibbs sampling when sampling the same 2D Gaussian distribution in Fig.3.2.	71
Fig.3.4 Demonstration of the concept called concentration of measure.....	72
Fig.3.5 Demonstration of Hamiltonian Monte Carlo (HMC) algorithm.	73
Fig.3.6 Demonstration of No-U-Turn Sampler (NUTS).	74
Fig.3.7 Visualization of MCMC chain traces to diagnose convergence.....	76
Fig.4.1 fNIRS measurement montage 1 and the anatomical model considered for DOT forward model estimation.	95
Fig.4.2 Workflow describing our proposed realistic fNIRS simulation framework.....	99
Fig.4.3 Evaluation of the performances of MEM and MNE using realistic simulations involving superficial seeds for different spatial extent ($Se = 3, 5, 7, 9$)..	102

Fig.4.4 Comparisons of the reconstruction maps using MEM and MNE in realistic simulations.	105
Fig.4.5 Effects of depth weighting on the depth and size of the simulated generators.	106
Fig.4.6 Evaluation of the performances of MEM and MNE at four different SNR levels. colors.	108
Fig.4.7 Application of MEM versus MNE reconstruction of HbR during a finger tapping task on one healthy subject.....	109
Fig.4.8 Personalized fNIRS montage and comparisons between MEM and MNE reconstructions with respect to fMRI Z-map at individual level.....	110
Fig.4.S1 Evaluation of the performances of depth weighted MNE for different depth weighting factors $\omega = 0, 0.1, 0.3, 0.5, 0.7, 0.9$	119
Fig.4.S2 Evaluation of the performances of MEM and MNE using realistic simulations involving middle seeds for different spatial extent ($Se = 3, 5, 7, 9$)..	119
Fig.4.S3 Evaluation of the performances of MEM and MNE using realistic simulations involving deep seeds for different spatial extent ($Se = 3, 5, 7, 9$).....	120
Fig.5.1 Personalized fNIRS investigation using an optimal montage targeting the right motor cortex.....	130
Fig.5.2 Determination of the cortical regions used for quantitative evaluations.	133
Fig.5.3 Quantitative evaluation of the performances of MEM and MNE reconstructions.	138
Fig.5.4 Visual and quantitative evaluation for NIROT images at the individual level (subjects 1 to 5).	141
Fig.5.5 Visual and quantitative evaluation for NIROT images at the individual level (subjects 6 to 10).	143
Fig.5.6 Comparisons of MEM and MNE group averaged reconstructions with fMRI Z-maps at the group-level, 10 subjects included.....	144
Fig.5.7 AUC comparisons of MEM and MNE reconstructions with respect to time and amplitude threshold value.	145
Fig.5.8 Distribution of AUC values estimated for MEM and MNE local reconstructions with the personalized optimal montage, in comparison to the AUC values obtained when considering only the montage light sensitivity profile (SP) for each subject.	147
Fig.5.A1 Histograms of paired evaluation metric differences between MEM and MNE estimated over 100 sessions (10 within subject resampled sessions \times 10 subjects)..	160
Fig.5.A2 Evaluations of reliability of performance differences between MEM and MNE using discriminability.	161
Fig.5.S1 FSL group-level fMRI activation maps of each slice thresholded by $Z>3.1$ (cluster-wise inference, $p<0.01$, corrected).	162
Fig.5.S2 Group-level NIROT Z-maps and standard deviation maps.....	163

Fig.6.1 Study design. Each acquisition session described above contains sections following the order of a, b, c and b, a.....	171
Fig.6.2 Personalized optimal montage and simultaneous PAS-fNIRS acquisition setup.....	173
Fig.6.3 Correlation between MEP peak-peak amplitude and task-related HbO/HbR amplitudes.	176
Fig.6.4 Group-level PAS effects on cortical excitability and hemodynamic activity.	178
Fig.6.5 PAS effects on task-related hemodynamic responses using personalized fNIRS tomography for Sub02.	179
Fig.6.6 Group-level PAS effects on task-related hemodynamic responses.	181
Fig.6.7 Correlates of task-related hemodynamic changes and PAS modulated excitability changes.....	183
Fig.6.C1 PAS effects on cortical excitability and hemodynamic activity.	191
Fig.6.C2 Simulated Pearson correlation distribution of the concordant MEP and HbO and HbR ratios.....	193
Fig.7.1 Experimental paradigm and set-up (adapted from Chapter 6).	205
Fig.7.2 The hierarchical model of PAS effects on either cortical excitability (MEP) or hemodynamic responses (Hb).....	212
Fig.7.3 The hierarchical Bayesian spline model for PAS effects on the whole HbO/HbR time course.	216
Fig.7.4 Modeling the relationship of task-related M1 hemodynamic activity and M1 excitability..	217
Fig.7.5 Prior predictive simulations for the hierarchical model of PAS effects on cortical excitability.....	223
Fig.7.6 Diagnostic statistics of key features of the models considered in this study.....	224
Fig.7.7 PAS effects on cortical excitability.	226
Fig.7.8 Effects of spTMS intensity on PAS assessment.	227
Fig.7.9 PAS effects on the whole time course of HbO/HbR.	228
Fig.7.10 The relationship between task-related cortical hemodynamic activity and M1 excitability.....	230
Fig.7.11 Posterior distributions of the correlations between slope[s]MEP and several selected slope[s]Hb(wn).	231
Fig.7.S1 PAS effects on M1 excitability at the individual level.....	239
Fig.8.1 Demonstration of a possible hybrid montage.	249
Fig.8.2 Preliminary results of the proposed method for deconvolution of HRF and estimation of stimuli amplitudes.	252

Introduction

Both voluntary and spontaneous neural activity are inducing two physiological reactions known as neurometabolic coupling which is directly related to O_2 consumptions of the brain for oxidative glucose metabolism (Clarke and Sokoloff, 1999), measured as the cerebral metabolic rate of oxygen ($CMRO_2$); and the neurovascular coupling (NVC) which regulates the local cerebral blood flow (CBF) for O_2 and glucose delivery (Phillips *et al.*, 2015). The uncoupling of CBF and $CMRO_2$ is called ‘functional hyperemia’ (Fox and Raichle, 1986; Fox, 2012), which results in increases in oxygenated hemoglobin (HbO) concentration and decreases in deoxygenated hemoglobin (HbR) concentration. Functional Near Infra-Red spectroscopy (fNIRS) measures fluctuations of both HbO and HbR non-invasively in the human head with high temporal resolution (Jöbsis, 1977; Scholkmann, Klein, *et al.*, 2014). When only measuring the attenuation of infra-red light emitted at a constant intensity through the head, the hemodynamic activity represented by the relative concentration changes of HbO and HbR within the light pathway can be estimated. This technique is referred to as continuous wave (CW) fNIRS (Ferrari, Mottola and Quaresima, 2004; Ferrari and Quaresima, 2012).

The associative synaptic plasticity (James, 1890; Feldman, 2012), explaining the mechanisms of neuroplasticity, is related to synapse's ability to adapt to continuous changes in the external and internal environment. The strengthening of synapses is known as Long-Term Potentiation (LTP, Bliss and Lomo, 1970; Bliss and Lømo, 1973) and the weakening of synapses is known as Long-Term Depression (LTD, Sejnowski, 1977; Bienenstock, Cooper and Munro, 1982). Several noninvasive brain stimulation approaches have been proposed to induce transit and stable changes in neuronal excitability, such as transcranial Electrical Stimulation (tES) (Merton and Morton, 1980; Reed and Cohen Kadosh, 2018), Transcranial Magnetic Stimulation (TMS) (Barker, Jalinous and Freeston, 1985; Klomjai, Katz and Lackmy-Vallée, 2015) and transcranial focused ultrasound (tFUS) (Legon *et al.*, 2014; Blackmore *et al.*, 2019).

TMS is the most widely used technique, that can not only modulate neuronal excitability but also assess the modulation effect per se. For instance, excitability modulation can be obtained using repetitive TMS (rTMS). This procedure delivers repetitions of TMS pulses following a specific frequency, normally between 5 to 20Hz can increase cortical excitability, whereas stimulating with a lower frequency between 1 to 4Hz can decrease excitability (Fitzgerald, Fountain and Daskalakis,

2006). Another procedure, known as Paired Associative Stimulation (PAS), inspired by the concept of Spike-Timing Dependent Plasticity (STDP) from animal studies (Levy and Steward, 1983) was established about two decades ago (Stefan, 2000). PAS consists in combining TMS with a peripheral electrical stimulation such as Median Nerve Stimulation (MNS). It relies on the principle that repetitive stimulation pairs (TMS and MNS) delivered with appropriate timing and pace can induce LTP and LTD-like plasticity. For example, when the interstimulus intervals (ISI) between MNS and TMS is around 25ms (PAS25), it would increase cortical excitability, whereas an ISI of 10ms (PAS10) would induce excitability decrease. Cortical excitability assessment has been conventionally obtained via the measurement of the Motor Evoked Potentials (MEPs) amplitude on the targeted muscles while delivering single pulse TMS (spTMS) on the motor cortex before and after PAS interventions.

The relationship between hemodynamic activity and cortical excitability has been illustrated in several animal studies. For instance, a study on the visual cortex of anesthetized cats using low frequency rTMS (e.g., 1Hz) and invasive optical imaging reported immediately increased tissue oxygenations peaking from 10s to 15s after applying rTMS, followed by a reduction of oxygenation lasting around 2 minutes (Allen *et al.*, 2007). Excitatory low-intensity rTMS was also shown to increase healthy rat's resting-state connectivity and GABA, glutamine, and glutamate levels, whereas inhibitory stimulation resulted in reduced connectivity and glutamine levels (Seewoo *et al.*, 2019). ***However, the relationship between cortical excitability and elicited hemodynamic activity is poorly understood in humans.*** Such investigation requires simultaneous measurements of excitability and hemodynamic activity (Siebner *et al.*, 2009). Functional magnetic resonance imaging (fMRI) is a typical tool that measures hemodynamic activity considering its reliability, ease of use, high spatial resolution, and sensitivity to deep brain regions (Bandettini *et al.*, 1992; Kwong *et al.*, 1992; Glover, 2011). Unfortunately, conducting concurrent TMS and fMRI is technically challenging (Hallett *et al.*, 2017), considering the fact that both techniques involve high magnetic fields, raising safety issues, and introducing substantial artifacts. MRI-compatible TMS coils have been developed (Navarro De Lara *et al.*, 2015; Wang, Xu and Butman, 2017) and applied to investigate TMS induced hemodynamic responses, showing similar time courses of fMRI signal when compared to the one evoked by a motor task (Navarro de Lara *et al.*, 2017). However, a recent fMRI study did not reproduce these findings of the TMS induced hemodynamic responses (Rafiei *et al.*, 2021). On the other hand, fNIRS relies on optical signals,

hence signals that are insensitive to electromagnetic artifacts (Curtin, Tong, *et al.*, 2019). Besides, fNIRS acquisition does not limit the space for TMS coil placement when stimulating different cortical areas. In general, these advantages allow the implementation of concurrent TMS and fNIRS in a much more straightforward manner than simultaneous TMS/fMRI. More importantly, fNIRS brings more insights into hemodynamic responses by measuring both HbO and HbR concentration changes, with excellent temporal resolution. Therefore, simultaneous TMS/fNIRS appears as a unique tool to investigate the TMS stimulation effects on cortical hemodynamic fluctuations.

However, the combination of TMS and fNIRS remains challenging especially when considering the following aspects. **Firstly**, conventional fNIRS channel space analysis relies on the usage of modified Beer-Lambert Law (MBLL), which makes a strong assumption on homogeneous concentration changes of hemoglobin within the underlying region(s) of interest. Indeed, the cortical hemodynamic is rather focal and not homogeneous within the brain, hence the analysis under this assumption induces systemic errors (O’Leary *et al.*, 1995; Pogue *et al.*, 1995). Fortunately, such errors could be substantially reduced when considering Near Infra-Red Optical Tomography (NIROT) suggested by Boas, Gaudette, *et al.*, 2001; Strangman, Franceschini and Boas, 2003. NIROT avoids this assumption of underlying homogeneity, by reconstructing the light intensity changes measured in the channel space along the underneath cortical areas. It actually consists in solving an ill-posed inverse problem that requires specific regularizations to obtain a unique solution. Besides, standard fNIRS caps may also provide less reliable estimations of hemodynamic responses due to the lack of personalization and spatial information of fNIRS sensors (Novi *et al.*, 2020). **Secondly**, similar to other non-invasive brain stimulation techniques, PAS response might be variable, exhibiting sometimes even unpredictable effects. For instance, López-Alonso *et al.*, (2014) showed that only 39% of subjects provided an expected response to PAS25, and Suppa *et al.*, (2017) suggested that PAS efficiency can be as low as 50% or even less. Such variability of the brain response to neurostimulation depends upon multiple factors, including the genetic susceptibility, position of the coil, and other aspects (Ziemann and Siebner, 2015). Similarly, variability has also been reported in task-evoked hemodynamic responses when measured using fNIRS (Novi *et al.*, 2020). **Lastly**, a general problem for neuroimaging studies is the small sample size, especially when dealing with technical acquisition challenges, ethical

considerations, and costs. This brings up the issue of the robustness and reliability of research findings (M. Yu *et al.*, 2018; Zuo, Xu and Milham, 2019).

Overall, the investigation on the relationship between hemodynamic activity and cortical excitability not only requires the technical combination of TMS and fNIRS but also requires methodological developments aiming to reduce/solve the above-mentioned limitations. Such methodology improvements could include: the development of more accurate inverse problem estimation for NIROT; the integration of NIROT within a workflow designed to improve the reliability of estimated hemodynamic responses; the establishment of an analysis strategy considering the variability of the data; and finally, the application of sophisticated statistical framework carefully handling small sample size while allowing more informative and reliable inferences.

The overall objective of this Ph.D. thesis was to develop and comprehensively evaluate personalized NIROT workflow using the MEM reconstruction framework combined with personalized fNIRS montage, and to apply it to the investigation on hemodynamic correlates of fluctuations in neuronal excitability using the concurrent TMS and fNIRS acquisition.

This thesis is organized as follows:

Chapter 1 to Chapter 3 are state of the art chapters reviewing essential background information.

- Chapter 1 introduces the fundamentals of CW-fNIRS, focusing on explaining fNIRS signal components; how conventional data analysis processes the data in the channel space; and what could be the corresponding disadvantages. Then we present the concept of personalized NIROT workflow, from probe design using optimal montage to NIROT reconstruction using the MEM framework, designed to estimate more accurately and reliably hemodynamic responses using fNIRS. This chapter is also including a short review of the existing methodologies proposed to solve the NIROT inverse problem.
- Chapter 2 reviews the concept of the combination of TMS and fNIRS. Biological mechanisms of brain plasticity are first briefly presented, followed by the introduction of several commonly used TMS sequences to elicit excitability changes, especially focusing on the PAS paradigm considered in this thesis. We then review the concept of combining

brain stimulations and neuroimaging modalities, including the advantages and challenges of commonly used neuroimaging modalities when conducting experiments with TMS, such as EEG, fMRI, and PET. The same perspectives are then discussed in detail for TMS/fNIRS followed by literature reviews covering most of the TMS/fNIRS-related studies on healthy subjects.

- Chapter 3 introduces the fundamental aspects of Bayesian data analysis, which explicitly deals with the problems of small sample size and large variability when considering most non-invasive human brain studies combining neuroimaging and neurostimulation. This introduction includes the presentation of Bayes' theorem and probability modeling; posterior distribution sampling techniques following the history of technical evolutions; the strategies to diagnose Bayesian models through sampling techniques and evaluation of the accuracy and reliability of the estimated posterior distribution; and finally, statistical inferences using the concept of posterior predictive simulations.

Four manuscripts, presented in Chapters 4 to 7, are then composing the main contribution of this thesis.

- Chapter 4 presents our work developing and evaluating the MEM framework for NIROT (Cai et al., under review). We adapted the MEM method, previously developed and validated by our team in the context of EEG/MEG source imaging, to solve the inverse problem of NIROT reconstruction. We originally introduced a depth weighting strategy within the MEM framework for NIROT reconstruction, to avoid biasing the reconstruction results of NIROT towards superficial regions. We also proposed a new initialization of the MEM framework to improve the temporal accuracy of the reconstructions when compared to the original framework. To evaluate MEM performance and compare it with the widely used depth-weighted Minimum Norm Estimate (MNE) inverse solution, we applied a realistic simulation scheme that contained 4,000 generators with different locations, spatial extents, and depths along the cortical surface.
- Chapter 5 presents the study in which we proposed and evaluated an original workflow entitled the personalized NIROT (Cai et al., 2021, in press HBM). Personalized NIROT integrates methodological developments proposed in our lab to deliver accurate and reliable hemodynamic response estimations. This workflow carefully considered each step

of a fNIRS study from the experiment design, data acquisition, to the final data analysis, and was optimized to improve the accuracy and reliability of reconstructed hemodynamic responses. This workflow was evaluated on finger-tapping fNIRS data acquired from ten healthy subjects for whom we estimated the reconstructed NIROT spatiotemporal images and compared them with fMRI results of the same individuals. We also compared the performance of MEM reconstructions with MNE solutions and assessed the reliability of the performance differences between them, using a non-parametric measure called discriminability.

- Chapter 6 includes our application study using the previously developed personalized NIROT workflow when investigating the relationship between task-related hemodynamic activity and brain excitability (Cai et al., under review). To do so, we conducted the first PAS-fNIRS investigation using simultaneous TMS and fNIRS. Sixteen healthy subjects participated in a sham-controlled, pseudorandomized, counterbalanced study with PAS on the right primary motor cortex. The relationship between primary motor cortex excitability and hemodynamic responses to finger tapping reconstructed via personalized NIROT was assessed. We also introduced an original resampling technique to ensure reliable, robust and data-driven (intervention type blind) estimation of HbO/HbR measures extracted from NIROT results, that was independent of PAS intervention types.
- Chapter 7 presents the last study included in this thesis (Cai et al., in preparation), in which we revisited data analysis from our previous TMS/fNIRS study, considering this time an advanced Bayesian data analysis workflow in order to take into account inter-/intra-subject variability from both brain stimulation induced cortical excitability measures and task-related hemodynamic responses. To do so, we proposed hierarchical Bayesian models investigating PAS effects on M1 excitability; PAS effects on the whole time course of task-related hemodynamic responses; and the correlation between them. Diagnostics of the models were conducted to assess the robustness of the estimated posterior distributions. Finally, statistical inferences were conducted via posterior predictive simulations.

In the end, Chapter 8 concludes this thesis with a general discussion of the main results, contributions, limitations, and perspectives of our proposed studies.

Chapter 1

Personalized Functional Near Infra-Red Optical Tomography

This chapter will present the personalized functional Near Infra-Red Optical Tomography proposed in this thesis for estimating spatiotemporal maps of hemodynamic responses along the human cortex. We will start by introducing the continuous wave fNIRS (CW-fNIRS), focusing on the explanation of 1) what CW-fNIRS measures and 2) conventional data analysis in the channel space and corresponding limitations. We then summarize our proposed personalized functional Near Infra-Red Optical Tomography (personalized NIROT) workflow from probe design using optimal montage to NIROT reconstruction methodologies, including how to solve fNIRS reconstruction forward and inverse problems.

1.1 Continuous Wave fNIRS

fNIRS measures non-invasively fluctuations of both oxygenated (HbO) and deoxygenated (HbR) hemoglobin in the head with high temporal resolution (Jöbsis, 1977; Scholkmann, Kleiser, *et al.*, 2014; Yücel *et al.*, 2021). When only measuring the attenuation of infra-red light through the head emitted at a constant intensity, the relative concentration changes of HbO and HbR within the light pathway can be estimated. This technique is referred to the continuous wave (CW) fNIRS (Ferrari, Mottola and Quaresima, 2004; Martin Wolf, Marco Ferrari and Quaresima, 2007; Ferrari and Quaresima, 2012). This section will explain what CW-fNIRS measures and how to conduct conventional data analysis to infer the cortical hemodynamic responses.

1.1.1 Cerebral neuronal activity related hemodynamics

Hemodynamics is defined as the dynamics of blood flow and of all the structures through which it passes (Secomb, 2016). Cerebral neuronal activity related hemodynamics is defined as the process of glucose and oxygen (O_2) delivery by the blood within local vessels along the cortex, which is required by various metabolisms of cerebral neuronal activity. Cellular processes of neurons consume energy in the form of adenosine triphosphate (ATP), and almost 90% of ATP is synthesized by oxidative glucose metabolism which requires O_2 (Dienel and Hertz, 2001; Phillips *et al.*, 2015). It is of interest to note that the human brain consumes more than 20% of oxygen and glucose at rest while only taking 2% of whole body weight.

Hemoglobin (Hb), which is present in the red blood cells, is known as a two-way O_2 carrier protein, delivering O_2 from the lung to tissues (Marengo-Rowe, 2006). The binding of O_2 and Hb was first reported by a French physiologist Paul Bert (Bert, 1878). Almost a century after this first report, in 1962, an Austrian-British molecular biologist Max Perutz won the Nobel Prize in chemistry by studying the structure of Hb using X-ray crystallography. Each hemoglobin actually consists of four subunits (see Fig.1a), and each subunit is constructed by two components: 1) the heme group (green in Fig.1a), which contains the ferrous ion atom that reversibly binds to a O_2 molecule; and 2) the polypeptide chain, which is either α -like (red in Fig.1a) or β -like chain (blue in Fig.1a) (Marengo-Rowe, 2006; Mairbäurl and Weber, 2012).

The dynamic of O_2 and Hb binding is known as cooperative binding (Ahmed, Ghatge and Safo, 2020), meaning once Hb is bound with one O_2 , the other heme groups become more likely to bind with O_2 . In contrast, Hb is also allosterically inhibited by carbon dioxide (CO_2). Therefore, when CO_2 concentration is increasing in blood plasma of local tissue, Hb will dump the bundled O_2 to support O_2 consumptions. These two states of Hb are referred to as the tense state (T) when less O_2 molecules are bound to Hb; and the relaxed state (R) when more O_2 molecules are bound to Hb. Such sophisticated mechanism allows efficient delivery of O_2 to where it is needed. The cooperative binding can be summarized by the equilibrium between T and R states (Perutz *et al.*, 1998; Safo and Bruno, 2011; Safo *et al.*, 2011) following the oxygen equilibrium curve (OEC) shown in Fig.1b, which represents the O_2 saturation of Hb (i.e. SO_2) as a function of partial pressures of O_2 (i.e. PO_2). When Hb is in T state (red curve), OEC shifts to the left side, therefore it is more likely to bind with O_2 , shown by increased slope and higher SO_2 than the one on the black curve with the same PO_2 . Additionally in the R state (blue curve), OEC shifts to the right side thus tends to release O_2 , indicated by decreased slope and lower SO_2 than the one at the equilibrium state.

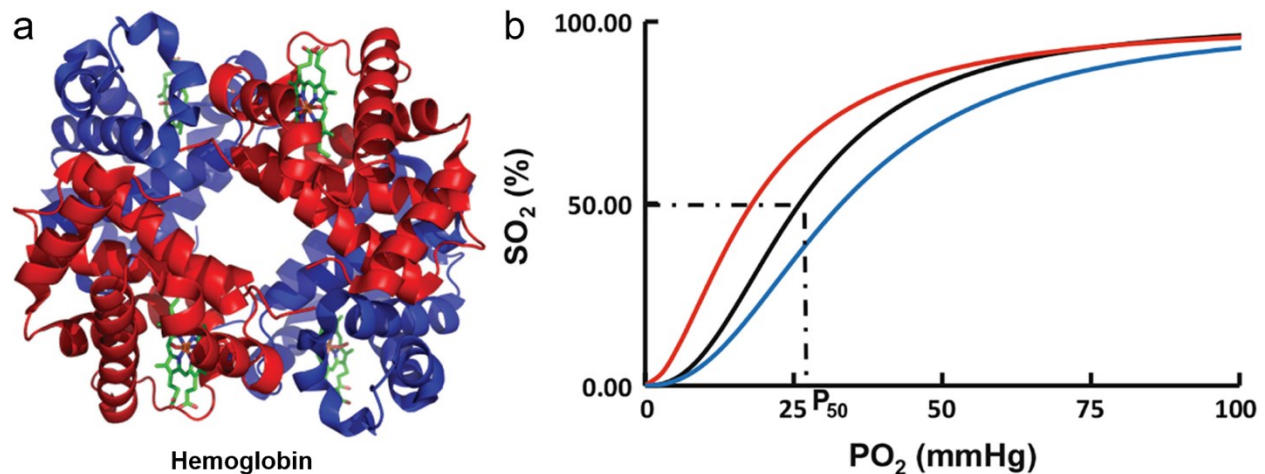


Fig.1.1 Structure of hemoglobin and the oxygen equilibrium curve. a) molecule structure of human hemoglobin. The green color represents the heme group contains ferrous ion atoms where O_2 binds with; red and blue color represent the two α -chains and two β -chains, respectively. Figure taken from *Mairbäurl and Weber, 2012*. b) oxygen equilibrium curve, dashed lines indicate PO_2 at 50% SO_2 value under the equilibrium state represented by black curve, red and blue curves represent the left shift (T state) and right shift (R state), respectively. Figure taken from *Ahmed, Ghatge and Safo, 2020*.

Voluntary or spontaneous neural activity will induce two physiological reactions, as shown in Fig1.2a, that is, **neurometabolic coupling** and **neurovascular coupling**. Neurometabolic coupling is directly related to the O_2 consumption of the brain for oxidative glucose metabolism synthesizing ATP mentioned above, which is quantified by the cerebral metabolic rate of oxygen ($CMRO_2$). It will increase the local concentration of HbR and decrease the local concentration of HbO. The second process is the neurovascular coupling (NVC) (*Roy and Sherrington, 1890; Phillips et al., 2015*), which regulate the local cerebral blood flow (CBF) for O_2 and glucose delivery. This regulation involves the neuron, the astrocyte glial cells and the vascular smooth muscles, in which the astrocyte mediates the coupling of neuronal activity and the vascular smooth muscle to dilate cerebral arteries (*Zonta et al., 2003; Metea and Newman, 2006; Huneau, Benali and Chabriat, 2015*). However, CBF will not just deliver the right amount of O_2 required by $CMRO_2$, it rather increase with a larger fraction (2-4 times) of $CMRO_2$ (*Buxton, 2012; Fox, 2012*). This fraction is called oxygen extraction fraction (OEF) (*Hoge et al., 1999; Buxton et al., 2004; Gauthier and Hoge, 2012*). The uncoupling of CBF and $CMRO_2$ is historically referred as ‘functional hyperemia’ (*Fox and Raichle, 1986; Fox, 2012*) or ‘wash out’ effect. This effect will result in local concentration increases of HbO and decreases of HbR. The combination of the above

two reactions will eventually induce the HbO increase and HbR decrease. Ideally, when investigating task evoked hemodynamic, CW-fNIRS is intended to measure (i.e. the measurement of interest) HbO/HbR concentration changes evoked by the voluntary neuronal activity within cerebral region, illustrated in the red cube of Fig.1.2b.

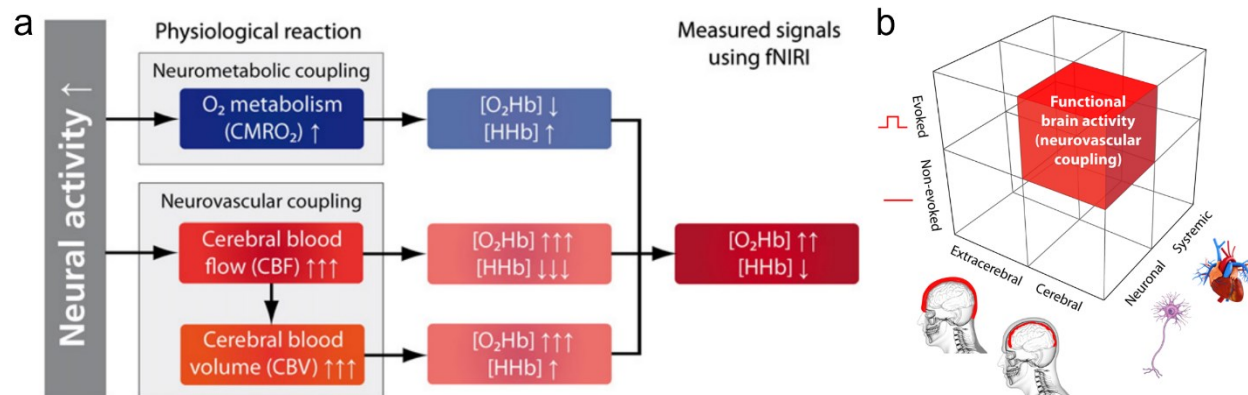


Fig.1.2 Mechanism of HbO/HbR concentration changes and the signal component of interest for functional brain activity measurement. a) neural activity induced cerebral metabolic rate of oxygen (CMRO₂) increase, and the functional hyperemia - neurovascular coupling (NVC). Eventually, these two physiological reactions result in the increase of HbO (O₂Hb) and decrease of HbR (HHb). Figure taken from *Scholkmann, Kleiser, et al., 2014*. b) assumed (ideal) measurement of interest for the hemodynamic response evoked by the voluntary functional brain activity. Figure adapted from *Tachtsidis and Scholkmann, 2016*.

1.1.2 The principle of CW-fNIRS

The work of Jöbsis published in *Science* is often cited as the first in vivo measurement of hemodynamic responses induced by neuronal activity using fNIRS (Jöbsis, 1977). Indeed, that was the proposal of Jöbsis, but in detail, it was not intended to measure HbO and HbR, but rather the cytochrome-c-oxidase (CCO) at a cellular level, which is an enzyme in the mitochondria directly involved in O₂ metabolism (Bale, Elwell and Tachtsidis, 2016). More importantly, CCO related near infra-red light attenuation is a brain-specific signal since the concentration of it is much higher in the brain than in extracerebral tissues. Although the attenuation of CCO in the near infra-red band is higher than Hb (see Fig.2.3a, the green curve in shade area), the signal amplitude fluctuation induced by CCO concentration changes is just 5% to 10% of that from Hb, especially because of the overall low quantity of CCO when compared to Hb (Bale, Elwell and Tachtsidis, 2016). This brings technical challenges to improve the sensitivity of optical instrumentation even

nowadays. Fortunately, HbO and HbR, which are related to O_2 delivery required by O_2 metabolism can also absorb light within the near infra-red band called ‘optical window’ shown in Fig.1.3a (from 650nm to 950 nm). The selection of this optical window considers the facts that 1) light attenuation of water is much lower than for other wavelength bands, therefore, ensuring sufficient light intensity remain detectable after being absorbed by human tissues (around 73% is composed by water); 2) HbO and HbR have distinctive absorption coefficients μ_a , therefore, allowing to differentiate them by using IR light sources operating by at least two wavelengths. For details of the history and development of fNIRS, please refer to this review (Ferrari and Quaresima, 2012).

Wavelength selection for differentiating HbO and HbR was initially based on the idea to have one lower and one higher wavelength in the absorption spectrum shown in Fig.1.3a, rather than the isosbestic point where the absorption coefficient is the same for HbO and HbR (around 800nm) (Zijlstra, Buursma and van Assendelft, 2000). Different studies have investigated the optimal combination to increase the signal to noise ratio (SNR) and decrease the cross-talk between HbO and HbR. In general, 830nm was determined to pair with the other wavelengths that are lower than the isosbestic point. Studies have located the typical values of the other wavelength based on different criteria such as 1) the lower uncertainty of light absorbance change (Yamashita, Maki and Koizumi, 2001); 2) higher SNR of estimated HbO/HbR (H. Sato *et al.*, 2004) and 3) lower HbO/HbR cross-talk estimated either theoretically or simulated by Monte Carlo simulations (Strangman, Franceschini and Boas, 2003; Okui and Okada, 2005; Kawaguchi *et al.*, 2008). So far 690nm and 750nm have been used by most of the commercial CW-fNIRS devices to pair with 830nm. More details of the fNIRS instrument review can be found in Martin Wolf, Marco Ferrari and Quaresima, 2007.

In practice, a light source (S), emitted by either a laser diode or a light-emitting diode (LED), is placed on the scalp surface and illuminates near infra-red light into the head tissue. Light diffuses in the head, and is detected by a detector (D) placed at a specific distance away from the light source. Due to the scattering, the path of the detected light follows a banana shape shown in Fig.1.3b, and the bottom of it can reach the superficial area of the cortex (e.g., grey matter). Depending on the distance of the SD pair, one can probe cortical regions that are less than 2cm in depth to the scalp using an SD separation of around 3cm. On the other hand, it is possible to only

monitor scalp Hb concentration fluctuations, using the short-separation (SD or SS) channel around 0.8cm (see Fig.1.3b).

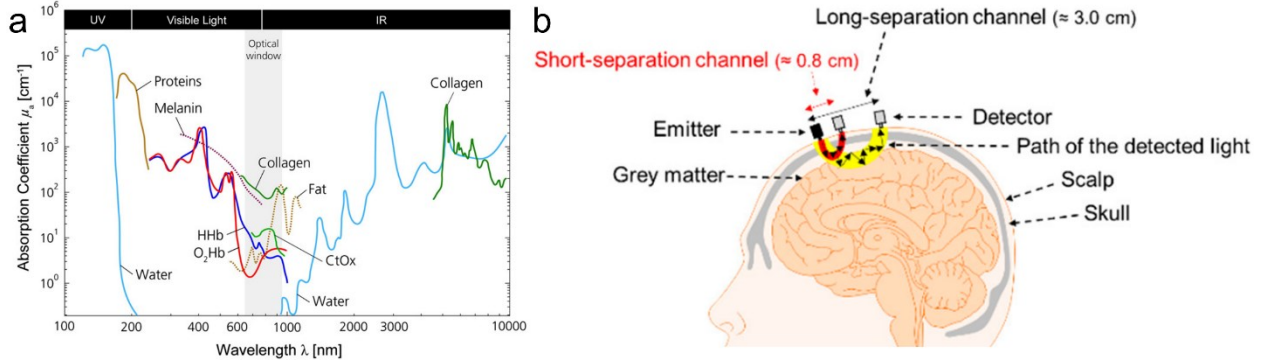


Fig.1.3 Demonstration of the principle of CW-fNIRS. a) the absorption spectrum for different chromophores in the human head, the optical window is defined from 650nm to 950 nm, in which water has a low absorption coefficient, and HbO(O₂Hb)/HbR(HHb) have distinctive absorption coefficients. Figure taken from *Scholkmann, Kleiser, et al., 2014*. b) demonstration of the CW-fNIRS channel consists of a light source and detector. The path of the detected light follows a so-called ‘banana shape’ (yellow path) due to the scattering of the light. The penetration depth depends on the separation of the SD pair. A typical channel with a 3cm SD distance would probe as deep as 2cm from the scalp, whereas a short-separation channel (around 0.8cm) only detects Hb concentration fluctuations within the scalp. Figure taken from *Herold et al., 2020*.

Solving the concentration changes of HbO and HbR from the light absorption changes measured for two (or more) wavelengths requires two (or more) equations, obtained by the modified Beer-Lambert Law (mBLL) first proposed by *Delpy et al., 1988; Delpy and Cope, 1997*, and based on the original work of Beer-Lambert Law (*Bouguer, 1729; Lambert, 1760; Beer, 1852*). In mBLL, relative changes of optical density $\Delta OD^\lambda(\Delta t)$ within a specific time span Δt at a certain wavelength λ , is expressed as a function of Hb concentration changes,

$$\begin{aligned}
 \Delta OD^\lambda(\Delta t) &= (\Delta OD^\lambda(t_1) + G^\lambda(t_1)) - (\Delta OD^\lambda(t_0) + G^\lambda(t_0)) \\
 &= -\log_{10} \left(\frac{I^\lambda(t_1)}{I^\lambda(t_0)} \right) \\
 &= \sum_{i=1}^N \varepsilon_i^\lambda \cdot \Delta c_i \cdot DPF^\lambda \cdot d
 \end{aligned} \tag{1.1}$$

where $I^\lambda(t_1)$ is the light intensity (in W) of wavelength λ (in nm) transmitted through the medium at time instant t_1 . $I^\lambda(t_0)$ represents the baseline light intensity used to normalize the previous one so that relative changes could be estimated. ε_i^λ (in $L \cdot mol^{-1} \cdot mm^{-1}$) is the molar extinction coefficient of chromophore i specific to wavelength λ (index i referring to either HbO or HbR). Δc_i (in $mol \cdot L^{-1}$) is the concentration changes of chromophore i (e.g., HbO or HbR). $DPF^\lambda \cdot d$ estimates the path length of the ‘banana shape’ and consists of two parts, where DPF^λ is the differential path length factor used to correct the source-detector distance d (in mm) to the actual path length, which is affected by scattering of the light denoted as G^λ . This reflects the ‘modification’ in the mBLL. In the end, G^λ is considered as stationary by assuming the changes of OD resulted from scattering are much less than the ones resulted from absorptions. Therefore, $G^\lambda(t_1)$ and $G^\lambda(t_0)$ are canceled out. When HbO and HbR are the chromophores of interest, two above equations can be used to solve the relative concentration changes of them as follows,

$$\begin{bmatrix} \Delta HbR \\ \Delta HbO \end{bmatrix} = \begin{bmatrix} \varepsilon_{HbR}^{\lambda_1} & \varepsilon_{HbO}^{\lambda_1} \\ \varepsilon_{HbR}^{\lambda_2} & \varepsilon_{HbO}^{\lambda_2} \end{bmatrix}^{-1} \begin{bmatrix} \Delta OD^{\lambda_1}(\Delta t) / DPF^{\lambda_1} d \\ \Delta OD^{\lambda_2}(\Delta t) / DPF^{\lambda_2} d \end{bmatrix} \quad (1.2)$$

The estimation of molar extinction coefficients of HbO and HbR used in CW-fNIRS are reviewed in [Matcher *et al.*, 1995](#); [Jacques, 2013](#). Although DPF^λ was shown to vary from age, gender and even brain region ([Duncan *et al.*, 1995](#); [Zhao *et al.*, 2002](#); [Strangman, Li and Zhang, 2013](#)), most of the fNIRS studies nowadays still use the fixed empirical values reported in the literature ([Hiraoka *et al.*, 1993](#); [Fukui, Ajichi and Okada, 2003](#); [Li, Gong and Luo, 2011](#)). Please also note that the effective pathlength $DPF^\lambda \cdot d$ can also be estimated individually by conducting Monte Carlo simulation on subject-specific anatomy ([Nakamura *et al.*, 2016](#); [Whiteman *et al.*, 2017](#)).

1.1.3 Other components of CW-fNIRS signal

Knowing the principle of CW-fNIRS mentioned above, we can conclude that it is actually not ideal only measuring the evoked hemodynamic responses within the cerebral region shown in Fig.1.2b. As lights pass through multiple head tissues, the attention of it can not strictly reflect only the cortical hemodynamic. The components of the CW-fNIRS signal are well-reviewed by [Scholkmann, Kleiser, *et al.*, 2014](#); [Tachtsidis and Scholkmann, 2016](#). We will briefly summarize them to emphasize what is really measured by CW-fNIRS, more importantly, how to reduce the

confounding. There are six components of the fNIRS signal proposed by Tachtsidis and Scholkmann, 2016 shown in Fig1.4a, including the voluntary task-evoked cerebral HbO/HbR concentration changes, which is the signal of interest in most CW-fNIRS applications. The second component may be the other signal of interest, which represents the spontaneous neuronal activity induced hemodynamic changes. It is often considered as the baseline activity that may not confound too much the voluntary task-evoked hemodynamics in CW-fNIRS applications since the latter one measures the relative changes to the baseline. This component is also the input of resting-state functional connectivity analysis using fNIRS (Sasai *et al.*, 2011; Sakakibara *et al.*, 2016; Santosa *et al.*, 2017), aiming to estimate the functional network of the brain, inspired by the same research topic in the field of functional magnetic resonance imaging (fMRI) (Bandettini *et al.*, 1992; Kwong *et al.*, 1992; Smitha *et al.*, 2017). The other four components consist of the systemic physiological noise (i.e., pairwise combinations between rest/task and extracerebral/cerebral) related to circulatory changes (Mesquita *et al.*, 2013; Cabrerizo *et al.*, 2014). These noises (see Fig.1.4b) are often contributed by cardiac (Bauernfeind *et al.*, 2014; N and SK, 2018), blood pressure (Tachtsidis *et al.*, 2009; Minati *et al.*, 2011), respiration (Scholkmann *et al.*, 2013; Scholkmann, Klein, *et al.*, 2014), Mayer waves (Kirlilna *et al.*, 2013; Yücel *et al.*, 2016), and low-frequency oscillations (Tong, Lindsey and Frederick, 2011; Tong *et al.*, 2012). In the end, non-physiological noise can be induced by motions (Brigadoi *et al.*, 2014; Jahani *et al.*, 2018).

1.1.4 Channel space analysis for CW-fNIRS

The conventional data analysis for estimating HbO/HbR concentration changes (see Fig1.4a) in CW-fNIRS applications consists of data processing to remove the above noises and to apply mBLL for each SD pair (channel). At the study design stage, one can introduce long jitters between task events or even totally randomize them, and then combine with simple trial averaging or deconvolution (Aarabi, Osharina and Wallois, 2017) to minimize systemic circulatory changes that are not phase-locked with stimulus. The most straightforward way to denoise is to directly reject the noisy channels or trials prior to further inferences. The noisy signal can be marked empirically by visualization or quantified by thresholding on SNR (Yücel *et al.*, 2021); coefficient of variation (CV) (Schmitz *et al.*, 2005; Schneider *et al.*, 2011; Eggebrecht *et al.*, 2012; Piper *et al.*, 2014); and contrast to background ratio (CBR) (Selb *et al.*, 2005). Cardiac, respiration, and Mayer waves related noises can be removed at some level by simple bandpass filtering (e.g. 0.01 to 0.1 Hz) depends on the frequency of interest (Yücel *et al.*, 2016). Although systemic

physiological noise that typically overlaps with this frequency band is difficult to remove, the general approach is to regress them out from the signals using general linear models (GLM) (von Lühmann, Li, *et al.*, 2020; von Lühmann, Ortega-Martinez, *et al.*, 2020). The estimation approaches do not require extra measurements approximating the noise. Such as the studies using global averaged fNIRS signal (Haeussinger *et al.*, 2014) or applying a principal component spatial filter algorithm (Zhang, Noah and Hirsch, 2016; Zhang *et al.*, 2017). The most popular approach to measure the extracerebral noise is applying the short distance (see Fig.1.3b and Fig.1.4b) channels that detect superficial physiological noise (Zeff *et al.*, 2007; Gregg *et al.*, 2010). A specially designed peripheral device measuring the low-frequency blood flow oscillation placed on ear lobe(s) or finger(s) can be utilized to estimate more accurate systemic physiological noise (Tong *et al.*, 2012, 2013; Sutoko *et al.*, 2019). In the end, motion artifacts can be removed by spline interpolation (Scholkmann *et al.*, 2010; Cooper *et al.*, 2012), principal component analysis (PCA) (Zhang *et al.*, 2005; Brigadoi *et al.*, 2014), correlation based signal improvement (CBSI) (Cui, Bray and Reiss, 2010), discrete Kalman filtering (Izzetoglu *et al.*, 2010) and Wavelet filtering (Molavi and Dumont, 2010). Motion artifact components can also be detected directly by the accelerometer (see Fig.1.4b).

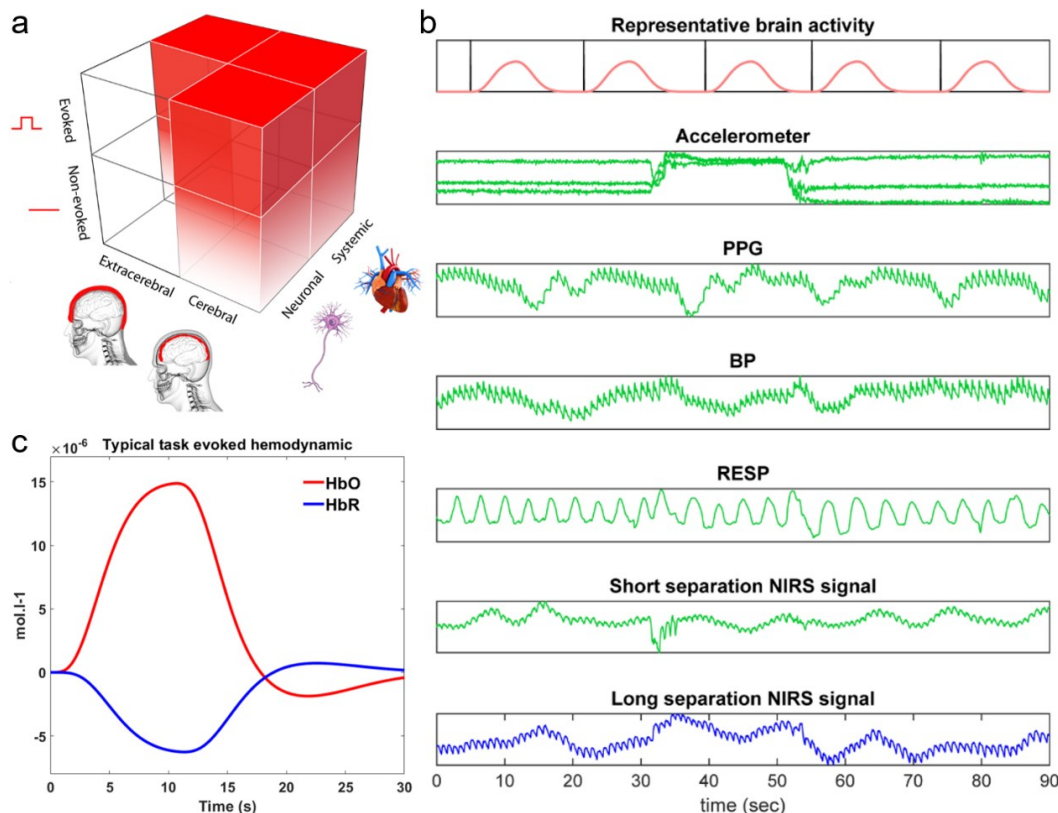


Fig.1.4 CW-fNIRS signal components. a) six components of CW-fNIRS signal, the first two components are voluntary (evoked) and spontaneous (non-evoked) neuronal activity induced hemodynamic, which are the signal of interest, other four components are often considered as systemic physiological noise induced by circulatory changes, related to voluntary and spontaneous activity, exist in both cerebral and extracerebral (scalp) regions. Figure taken from *Scholkmann, Kleiser, et al., 2014*. b) demonstration of the typical CW-fNIRS noise. Motion artifact (detected by accelerometer), cardiac noise (detected by Photoplethysmographic (PPG)), blood pressure and respiration (detected by respiration band) are shown by each green curve. They both exhibit in short separation and long separation channels. Figure taken from *von Lüthmann, Ortega-Martinez, et al., 2020*. c) a typical HbO/HbR response evoked by 10s task, simulated using convolution model and canonical hemodynamic response function (HRF).

1.2 Personalized NIROT

While the channel space analysis relies on the usage of mBLL, it actually makes three strong assumptions 1) the effects of scattering on the relative Hb concentration changes is negligible; 2) the medium (i.e. human head) under the fNIRS channels is homogeneous and 3) homogeneous concentration changes of Hb within the underlying region(s) of interest. Although assumption 1) is valid in CW-fNIRS and 2) is physically not true but would not influence the estimation of relative changes, the invalidity of assumption 3) can actually introduce systematic errors. Indeed, the cortical hemodynamic response is focal (especially for task-evoked ones) rather homogeneous within the brain. Inspired by studies (*O'Leary et al., 1995; Pogue et al., 1995*) showing that such errors could be substantially reduced by the diffusion optical tomography (DOT), *Boas, Gaudette, et al., 2001; Strangman, Franceschini and Boas, 2003* have demonstrated the misestimation of HbO/HbR concentration changes using mBLL-based channel space analysis. *Boas et al.* clearly showed that focal hemodynamic perturbation could be inaccurately estimated due to the partial volume effect (i.e., heterogeneous of Hb concentration changes induced for instance by a task) and the differential wavelength sensitivity (i.e., different optical pathlength depends on wavelength). It is also interesting to notice that the reason why mBLL was initially used in fNIRS is that the early human related applications were mainly on measuring the global (rather local) hemodynamic: 1) in tissues such as muscle, which is more valid as a homogeneous medium and the changes of Hb are also relatively homogenous; or 2) in the human head but focusing on general oxygenation level not specific to the task-evoked activity.

To solve the above problem, Near Infra-Red Optical Tomography (NIROT), also called DOT, has been proposed (Arridge, 1999; Boas, Brooks, *et al.*, 2001). NIROT avoids assuming homogeneity by reconstructing the light intensity changes measured in the channel space onto the underneath cortical area before converting them into local hemodynamic HbO/HbR changes. It also provides a more flexible way for inferencing the results. One can visualize the reconstructed spatiotemporal map, extract the reconstructed HbO/HbR time course and even conduct statistical parametric mapping similar to fMRI studies. In this section, we will go through our workflow of NIROT proposed in this thesis – *the personalized NIROT*, based on the previous work of the lab (Machado *et al.*, 2014b, 2018) and Chapter 4 and 5.

1.2.1 Personalized fNIRS montage

A montage refers to the spatial layout of the fNIRS sources and detectors along the scalp. Traditional fNIRS montage uses a fixed distance (~3cm) between a source (S) and detector (D) to probe the cortex. However, for NIROT, different SD separations are often required not only because it is named tomography but also to improve the accuracy and resolution of resulting spatiotemporal maps. Constrained by optodes size and the installation using a cap, early applications of NIROT often used a montage called “double density”, which consists of two different SD separations, depending on devices but in general a short one around 1.5cm and a long one around 4cm. Many studies (Yamamoto *et al.*, 2002; Boas, Dale and Franceschini, 2004; Kawaguchi, Koyama and Okada, 2007; Yoshida *et al.*, 2011) have shown that simply using this setup could improve both accuracy and resolution of the NIROT results compared to standard all 3cm channel caps. A ‘multicentered geometries’, distributing sources and detectors symmetrically within a hexagon, was proposed by Zhao, Ji and Jiang, 2006. This montage contains more than two levels of SD separation and further improved the reconstruction image quality proved by simulations. One of the most used montages for NIROT was developed throughout the studies (Joseph *et al.*, 2006a; Zeff *et al.*, 2007; Koch, 2010; White and Culver, 2010), in which sources and detectors are arranged in different locations following a rectangular geometry with different SD separations. It could form up to 1,200 channels with four levels of separations 1.3, 3.0, 3.9, and 4.7cm to cover almost half of the scalp area (Eggebrecht *et al.*, 2012, 2014). These layouts indeed improved the reconstruction accuracy and resolution, but the location of the channels is manually designed based on a predefined geometry. In 2014, Machado *et al.*, 2014 proposed a personalized optimal fNIRS montage consists in estimating a subject-specific optimal fNIRS

layout, which maximizes the spatial sensitivity to the hemodynamic responses along a predefined targeted brain region. This optimal montage technique aimed to maximize the sum of the sensitivity of all possible channels along the scalp with constraints such as the optode number, SD separation range, and overlapping (i.e., adjacent describing how many detectors have to construct channels with each source) into a linear integer programming problem. Therefore, the resulting montage is quantified to be the optimized resolution with certain constraints (see Fig.1.5). Moreover, it is personalized since the sensitivity calculation and region of interest (ROI) definition are based on the individual anatomy (see details in Section 2.2.2). In this original work, all possible locations of the optodes were constrained in an electroencephalogram (EEG) /fNIRS cap due to the limitation of the device and optodes installation method. Finally, the optimal montage evolved in [Machado et al., 2018](#), where optodes can be freely installed anywhere along the scalp. This was inspired by the work ([Yücel et al., 2014](#)), in which fNIRS sensors were glued (rather than using a cap with fixed position) on the scalp using a clinical adhesive, called collodion, which would minimize the motion artifacts and improve the signal to noise ratios of fNIRS signals. Moreover, [Machado et al., 2018](#) showed that personalized optimal montage with a large number of locally overlapping channels allows accurate local reconstruction of NIROT images. Following these works on the optimal montage, [Brigadoi et al., 2018](#) even claimed to terminate the manual montage design. In this thesis, to improve the accuracy of the montage gluing and the further forward modeling, we introduced the digitalization of the optodes positions along with more than 150 head points using a neuronavigation system. This ensured accurate co-registration with the subject's head anatomy. Our pilot investigation showed that the average installation displacement to the theoretical optimal montage is 7mm among 120 optodes of 6 montages. This displacement is only the width of the optodes used in our studies.

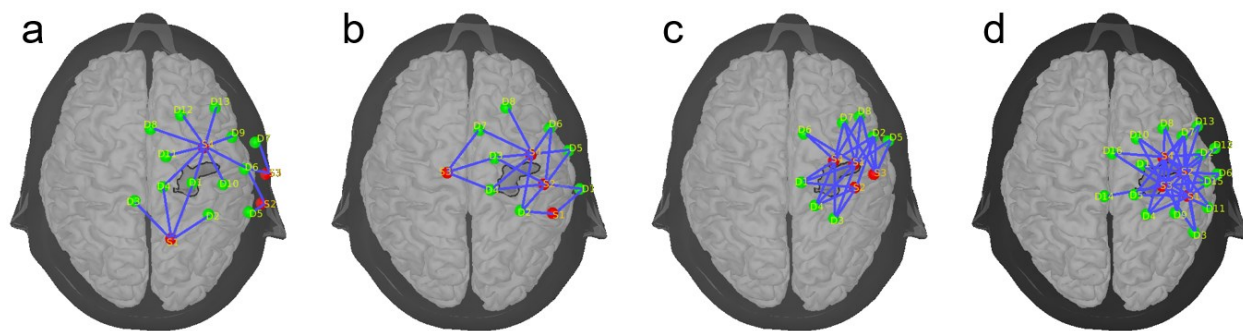


Fig.1.5 Demonstration of personalized optimal montage probing the ‘hand knob’ area using different configurations. a) 4 sources 16 detectors with 2 adjacent, SD separations ranging from 20mm to 40mm. Note that since the overlapping is set too low (adjacent =2), to place the optodes along the head, optimal montage has to spread them away from the region of interest. b) 4 sources 8 detectors with 2 adjacent, SD separation ranging from 20mm to 40mm, decreasing the detector number reduced the problem in a), but the montage is not dense enough due to fewer optodes. c) 4 sources 8 detectors with 2 adjacent, SD separation ranging from 15mm to 40mm, increase the range of SD separation increased the overlapping. d) 4 sources 16 detectors with 10 adjacent, SD separations ranging from 15mm to 40mm. High density (overlapping) montage is achieved by a higher number of optodes, SD separation rang, and adjacent, which is preferred for conducting NIROT.

1.2.2 Model of NIROT

In CW-fNIRS based diffusion optical tomography (Arridge, 1999), a linear model is used to describe the relationship between measured optical density changes on the scalp and wavelength-specific absorption changes within head tissue as follows,

$$\Delta OD^\lambda = A^\lambda \Delta \mu_a^\lambda \quad (1.3)$$

where ΔOD^λ is the optical density changes specific for wavelength λ . $\Delta \mu_a^\lambda$ (in mm^{-1}) represents the wavelength-specific absorption change within the medium. A^λ (in mm) is the sensitivity matrix (also called Jacobian matrix) relating absorption changes to optical density changes. Note that scattering is ignored from the full model of diffusion approximation since CW-fNIRS assumes only absorption related perturbations (Fantini and Franceschini, 2002). For convenience, a simplified notation is often used in NIROT literature,

$$Y = AX + e \quad (1.4)$$

where $Y(p \times t)$ is a matrix that represents the ΔOD^λ in fNIRS channel p at time samples t . $X(q \times t)$ is the $\Delta \mu_a^\lambda$ in location q along the cortex at time t . $A(p \times q)$ is the sensitivity matrix specific to the subject’s head anatomy. The additional term, $e(p \times t)$ models the additive measurement noise estimated from the baseline fluctuations. Solving the reconstruction problem for NIROT consists of solving two problems known as 1) the forward problem, which computes matrix A based on the modeling of light propagation within the heterogeneous medium – human head and 2) the inverse problem which estimates the matrix X (i.e. the amplitude for each location

q at time t). This inverse problem is ill-posed and admits an infinite number of possible solutions due to the fact that the number of possible generators q where a change of absorption could occur is much larger than the number of measurements p .

Note that the resulted X only estimates the relative absorption changes, i.e. $\Delta\mu_a^\lambda$, for one wavelength, it is not yet the relative HbO/HbR concentration changes. To complete the reconstruction process, the last step consists of ‘converting’ reconstructed $\Delta\mu_a$ of at least two wavelengths to HbO/HbR concentration changes as follows,

$$\begin{bmatrix} \Delta HbR \\ \Delta HbO \end{bmatrix} = M_s \begin{bmatrix} \Delta\mu_a^{\lambda_1} \\ \Delta\mu_a^{\lambda_2} \end{bmatrix} = \begin{bmatrix} \alpha_{HbR}^{\lambda_1} & \alpha_{HbO}^{\lambda_1} \\ \alpha_{HbR}^{\lambda_2} & \alpha_{HbO}^{\lambda_2} \end{bmatrix}^{-1} \begin{bmatrix} \Delta\mu_a^{\lambda_1} \\ \Delta\mu_a^{\lambda_2} \end{bmatrix} \quad (1.5)$$

where M_s is called the spectral composition matrix (Arridge, 1999; Zhan *et al.*, 2012b), which contains the wavelength-specific molar absorption coefficient α for HbO or HbR. This is similar as mBLL equation 1.2 but without the differential path length factor (DPF) corrected path length. $\Delta\mu_a$ is estimated along the cortex by solving the inverse problem. Therefore, the resulting HbO/HbR concentration changes avoid the partial volume effects existing in the mBLL approach. In the following two subsections, we will introduce how to solve the above two problems.

1.3 NIROT forward problem

The NIROT forward problem is to solve the forward photon migration within the complex turbid medium. An analytical solution like Radiative Transfer Equation (RTE) is often considered an accurate estimation but challenging to solve in real applications. Diffusion approximation (Ishimaru, 1978; Dehghani, Eames, *et al.*, 2009) was developed to approximate RTE solutions using the combination of few lower-order expansions of it. In general, the RTE for the photon fluence rate can be formulated by the diffusion approximation as follows (Wheelock, Culver and Eggebrecht, 2019),

$$\frac{\partial \Phi(\vec{r}, t)}{\partial t} - \nabla \cdot (D(\vec{r}) \nabla \Phi(\vec{r}, t)) + v\mu_a(\vec{r})\Phi(\vec{r}, t) = vQ(\vec{r}, t) \quad (1.6)$$

where $\Phi(\vec{r}, t)$ is the photon fluence rate (in W/cm^2) of a volume element at position \vec{r} and time t . $\nabla \cdot$ denotes the divergence and ∇ represents the gradient. $\mu_a(\vec{r})$ is the absorption coefficient (in

cm^{-1}) and v is the speed of light in biological tissue (in cm/ns). $Q(\vec{r}, t)$ is the total power of a unit volume radiating isotropically outward (in units of W/cm^3). $D(\vec{r})$ is the diffusion coefficient (in cm^2/ns) at position \vec{r} defined as

$$D(\vec{r}) = \frac{v(\vec{r})}{3(\mu_a(\vec{r}) + \mu'_s(\vec{r}))} \quad (1.7)$$

in which $\mu_s(\vec{r})$ is the scattering coefficient at position \vec{r} . When assuming the homogeneous medium, the above equation 1.6 is simplified as,

$$\frac{\partial \Phi(\vec{r}, t)}{\partial t} - D \nabla^2 \Phi(\vec{r}, t) + v \mu_a(\vec{r}) \Phi(\vec{r}, t) = v Q(\vec{r}, t) \quad (1.8)$$

According to [Svaasand, 1993](#); [Tromberg *et al.*, 1993](#); [Haskell *et al.*, 1994](#), the light source $Q(\vec{r}, t)$ modulated by intensity following a specific frequency can be expressed as the combination of direct current DC and alternating current (AC) parts with ω as the angular frequency of the intensity modulation as follows,

$$Q(\vec{r}, t) = Q_{DC}(\vec{r}, t) + Q_{AC}(\vec{r}, t) e^{-i\omega t} \quad (1.9)$$

In CW-fNIRS, where light intensity is constant, the above equation 1.9 then only consists of the DC part Q_0 , therefore the solution of equation 1.8 is ([Wheelock, Culver and Eggebrecht, 2019](#)),

$$\Phi(\vec{r}) = \frac{v Q_0}{4\pi D} \frac{e^{-r \left[\frac{v \mu_a}{D} \right]^{1/2}}}{r} \quad (1.10)$$

Note that this is only the static solution of the diffusion approximation under the assumption of the infinite and homogeneous medium. Although the fast finite element modeling (FEM) approach ([Arridge *et al.*, 1993](#); [Paulsen and Jiang, 1995](#); [Okada *et al.*, 1996](#)) is available when dealing with multiple tissue types of the medium such as the human brain, the accuracy of the above diffusion approximation is limited by the increase of the complexity of the medium. For more details of the diffusion approximation derivation specific NIRS, please refer to the recent review ([Wheelock, Culver and Eggebrecht, 2019](#)), which provides the clear equation derivation and the explanations of the underlying assumptions.

On the other hand, Monte Carlo (MC) algorithm (Harrison, 2009) is a general stochastic simulation approach to solve complex models numerically. It is also widely used to solve the RTE and is considered the gold standard solution (Prahl, 1989; Wang, Jacques and Zheng, 1995; Zhu and Liu, 2013). In this thesis, we applied the most used MC toolbox for light propagation modeling in biological tissues - the Monte Carlo eXtreme (MCX, <http://mcx.space/>) developed by Fang and Boas, 2009; Yao, Intes and Fang, 2018. It takes advantage of graphics processing unit (GPU) parallel computation to speed up the calculations, completing the simulation of photon migrations in few tens of seconds using a GeForce GTX 1080 Ti graphic card with the following set-up: 10^8 photons emitted by a point source migrating inside the human head model in $5ns$ with a step of $0.5ns$. MCX allows two approaches to estimate the sensitivity matrix (Jacobians), namely, the adjoint Monte Carlo (aMC) (Crane *et al.*, 2003; Fang *et al.*, 2004; Chen and Intes, 2011) and perturbation Monte Carlo (pMC) (Hayakawa *et al.*, 2001). The term ‘adjoint’ refers to the adjoint simulation of the light fluence from the detector position along with the one calculated for the source position per se. The Jacobian is then calculated by the normalized multiplication of these two fluences according to the reciprocity of light. The latter approach is a more efficient method that avoids calculating the adjoint fluences by a reply mode (Yao, Intes and Fang, 2017, 2018) but less accurate with the same computation cost. Considering the accuracy and acceptable computation costs, we utilized aMC approach for solving the Jacobian (A in equation 1.4).

To describe the changes in optical properties in X of equation 1.4, which reflects the neuronal activity evoked hemoglobin concentration changes, one needs to derive how Y is changed by perturbing $\Phi(\vec{r})$ with a slight change. This requires the Rytov approximation as follows (O’Leary *et al.*, 1995; Arridge, 1999),

$$\Phi(\vec{r}_j, \vec{r}_s) = \Phi_0(\vec{r}_j, \vec{r}_s) e^{\delta\Phi(\vec{r}_j, \vec{r}_s)} \quad (1.11)$$

the current fluence $\Phi(\vec{r}_j, \vec{r}_s)$ is expressed by the baseline fluence $\Phi_0(\vec{r}_j, \vec{r}_s)$ after a small perturbation $\delta\Phi(\vec{r}_j, \vec{r}_s) \ll \Phi(\vec{r}_j, \vec{r}_s)$. \vec{r}_s specifies the location of the light source and \vec{r}_j represents the location of the perturbation within the medium.

Under the Rytov approximation, the full expression of forward modeling of the equation 1.4 using the aMC approach for CW-fNIRS based NIROT is then expressed as (Yao, Intes and Fang, 2018; Wheelock, Culver and Eggebrecht, 2019),

$$\begin{aligned}
 Y &= -\ln\left(\frac{\Phi}{\Phi_0}\right) \\
 &= J^{\mu_a}(\Omega_j)\Delta\mu_a(\vec{r}_j) \\
 &= -\frac{v}{D} \int \frac{G(\vec{r}_j, \vec{r}_s)\Phi(\vec{r}_d, \vec{r}_j)}{\Phi(\vec{r}_d, \vec{r}_s)} \Delta\mu_a(\vec{r}_j) d\vec{r}
 \end{aligned} \tag{1.12}$$

where $\Delta\mu_a(\vec{r}_j)$ is the absorption changes at the location \vec{r}_j . $J^{\mu_a}(\Omega_j)$ is the Jacobin specific for absorption perturbations at \vec{r}_j within spatial regions Ω_j ; $G(\vec{r}_j, \vec{r}_s)$ is the Greens function of the diffusion equation defined at \vec{r}_j according to the isotropic point source location \vec{r}_s ; $\Phi(\vec{r}_d, \vec{r}_s)$ and $\Phi(\vec{r}_d, \vec{r}_j)$ represents the photon fluence (in mm^{-2}) measured at the point detector located at \vec{r}_d migrated from the location at \vec{r}_s (location of the point light source) and \vec{r}_j , respectively (see Fig1.6c). When measuring the fluence inside the diffusive medium (Furutsu and Yamada, 1994; Yao, Intes and Fang, 2018),

$$\Phi(\vec{r}_d, \vec{r}_j) = G(\vec{r}_d, \vec{r}_j) = G(\vec{r}_j, \vec{r}_d) \tag{1.13}$$

The photon fluence at any location \vec{r}_j within the medium can be solved by launching Monte Carlo simulations. The photon packet weight is initialized as 1 at a predefined location at the scalp surface and decreased according to 1) the scattering determines where the photon migrates to, the initial scattering direction is randomized according to the Henyey-Greenstein phase function (Furutsu and Yamada, 1994; Boas *et al.*, 2002a) and the scattering depends on the scattering coefficient (μ_s) and anisotropy facto (g); 2) absorption coefficient (μ_a) at each location within the medium determines the amount of weight loose. After launching sufficient number of photons, the wight of each photon packet at each location is accumulated and forms a fluence distribution of a specific source (see Fig1.6b) during a specified time gate (Fang and Boas, 2009).

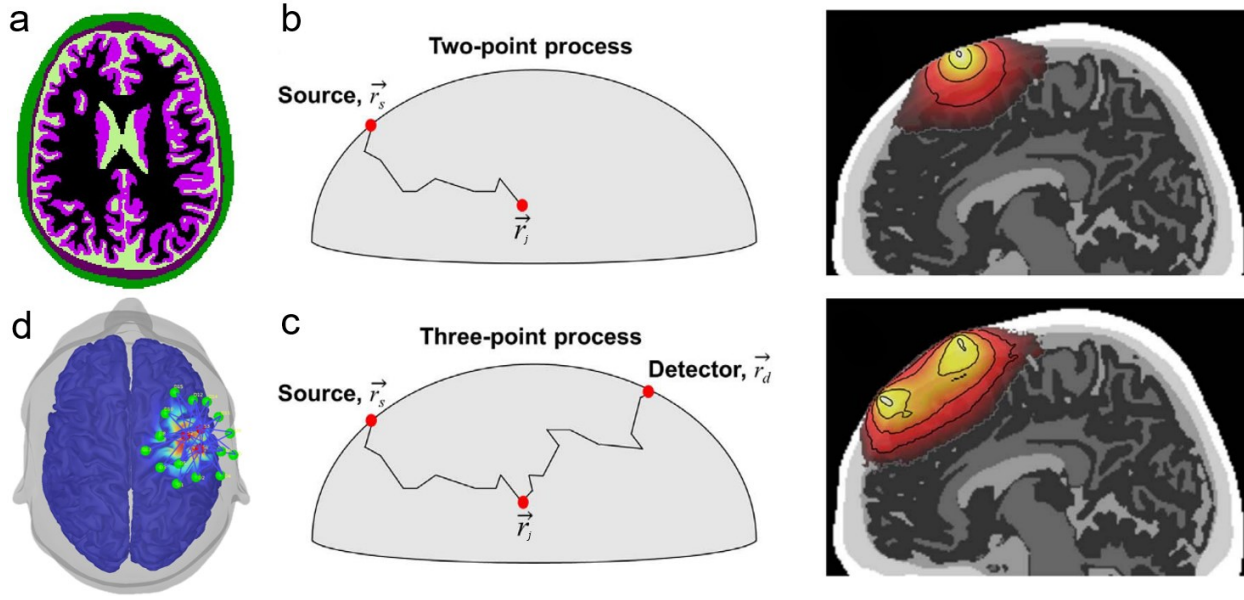


Fig.1.6 Solving NIROT forward problem by Monte Carlo Simulation. a) head tissue segmentation resulted in five tissues, scalp, skull, Cerebrospinal fluid (CSF), gray matter and white matter. Tissue-specific absorption coefficient (μ_a), scattering coefficient (μ_s) and anisotropy factor (g) (Yaroslavsky *et al.*, 2002) will be assigned to be the medium of MC simulation. b) launching photons at the source location \vec{r}_s to simulate the light migration inside the head and estimate the fluence at each location \vec{r}_j . c) adjoint MC to calculate the sensitivity for location \vec{r}_j by launching two MC simulations: one from b) and an adjoint one from the detector location \vec{r}_d d) projected sensitivity profile on cortical surface (i.e. mid-surface) using volume to surface projection process proposed by Grova, Makni, *et al.*, 2006. Figures b) and c) adapted from Strangman, Li and Zhang, 2013.

The above aMC approach is calculated specifically for a medium, which is the human head in NIROT. This requires the 3D anatomical image of the full head and its segmentations. The 3D anatomical image is acquired by high-resolution T1 and T2 weighted Magnetic resonance imaging (MRI) images (Bloch, 1946; Purcell, Torrey and Pound, 1946; Grover *et al.*, 2015). Due to the difference of μ_a , μ_s and g in different tissue types, it is often recommended to segment the head into five tissues (i.e. scalp, skull, Cerebrospinal fluid (CSF), gray matter and white matter) (Yaroslavsky *et al.*, 2002; Fang and Boas, 2009). In this thesis, the segmentation was processed using FreeSurfer6.0 (Fischl *et al.*, 2002) (<https://surfer.nmr.mgh.harvard.edu/>) and SPM12 [Penny *et al.*, 2011] (<https://www.fil.ion.ucl.ac.uk/spm/software/spm12/>). Gray matter and white matter masks were generated from the cortical/subcortical segmentation of FreeSurfer. Scalp and skull masks were segmented using SPM. All segmentation processes used both T1 and T2 weighted

images to achieve more accurate estimations of the tissue types by taking advantage of their complementary contrasts (see Fig1.6a).

In addition, considering the hemodynamic fluctuations are evoked in the cortical regions, anatomical constraints can be involved by defining the reconstruction solution space within the gray matter volume (Boas and Dale, 2005). Furthermore, in NIROT applications, the forward model in volume space was usually down-sampled considering the general spatial resolution of fNIRS. Such as $2 \times 2 \times 2\text{mm}^3$ used in (Eggebrecht et al., 2014), $3 \times 3 \times 3\text{mm}^3$ in (Eggebrecht et al., 2012) and $4 \times 4 \times 4\text{mm}^3$ applied in (Yamashita et al., 2016). Another NIROT approach (Pfeifer, Scholkmann and Labruyère, 2018) also projected the volumetric forward model to a cortical surface before conducting reconstruction. This is also seen in electroencephalogram (EEG) and magnetoencephalography (MEG) source localization studies (Dale and Sereno, 1993; Grova, Daunizeau, et al., 2006; Chowdhury et al., 2013). In this thesis, we assumed that there are many possible locations of absorption changes distributed over the reconstruction space defined on the cortical surface mesh (see Fig1.6d). Therefore we projected the sensitivity from volume to surface using a Voronoi based method proposed by Grova, Makni, et al., 2006. This cortical surface projection is also preferred by the fact that our inverse problem solution (Maximum Entropy on the Mean: MEM) was originally developed operating in the surface space.

1.4 Solving NIROT inverse problem

Several inverse problem solutions have been proposed for NIROT throughout the literature. This subsection reviews these methodologies from the most straightforward back projection to the one used in this thesis – MEM.

1.4.1 Back projection (BP)

Back project (BP) was first proposed in optical image reconstruction in Walker, Fantini and Gratton, 1997, firstly applied in NIROT for human cortical hemodynamic reconstruction in Boas et al., 2004 and still used in some studies (Zhai and Cummer, 2009; Das, Dileep and Dutta, 2018) nowadays. In the BP method, the sensitivity matrix A in equation 1.4 is assumed to be orthogonal, therefore, the pseudo-inverse of itself is A^T , and the solution of inverse problem \hat{X}_{BP} is defined as follows,

$$\hat{X}_{BP} = (AS)^T y \quad (1.14)$$

where S is a diagonal matrix that normalizes the column of A . BP is known to overestimate the reconstructed amplitude, therefore providing a larger spatial extend and more blurring image (Boas et al., 2004) compared to Tikhonov regularization-based reconstructions.

1.4.2 Truncated singular value decomposition (tSVD)

The tSVD method is based on the Moore–Penrose (MP) pseudo-inverse (Penrose, 1955) of the sensitivity matrix A used for instance in Piper *et al.*, 2014; Tremblay *et al.*, 2018, A^+ (pseudo-inverse of A) is estimated as,

$$A^+ = V\Sigma^{-1}U^T \quad (1.15)$$

where U (an orthogonal matrix) and V (consists of singular vectors in each column) are from the SVD decomposition of the matrix A , then the estimated solution of the inverse problem is,

$$\hat{X}_{tSVD} = (V_m \Sigma_m^{-1} U_m^T) y \quad (1.16)$$

in which m corresponds to the dimensionality of the truncated matrix (i.e., V_m , Σ_m^{-1} and U_m) in equation 1.16. The truncations discard the terms with singular values that are zero or very small. Moreover, m can be optimized by locating the point that exhibits the highest curvature in the L-curve (Hansen, 1999; Tremblay *et al.*, 2018). tSVD solution is also known for producing blurry reconstructed images (Habermehl *et al.*, 2014).

1.4.3 Minimum norm estimation (MNE)

Minimum norm estimation (MNE) is first proposed by Hämäläinen and Ilmoniemi, 1994 for EEG and MEG source localization. It is also one of the most widely used reconstruction algorithms in NIROT (Boas *et al.*, 2004a; Zeff *et al.*, 2007; Dehghani, Eames, *et al.*, 2009; White *et al.*, 2009; Eggebrecht *et al.*, 2012, 2014). MNE is based on the Tikhonov regularization, in which a penalty regularization term $\lambda \|X\|_{\Sigma_s}^2$ is added to the least squares of the data fit term $\|(Y - AX)\|_{\Sigma_d}^2$, and the MNE solution is to minimize the sum of them as follows,

$$\hat{X}_{MNE} = \operatorname{argmin}(\|(Y - AX)\|_{\Sigma_d}^2 + \lambda \|X\|_{\Sigma_s}^2) \quad (1.17)$$

$$= (A^T \Sigma_d A + \lambda \Sigma_s)^{-1} A^T \Sigma_d Y$$

where Σ_d and Σ_s are the inverse of noise covariance and the inverse of source covariance, respectively, λ is the hyperparameter to regularize the inversion. Σ_d is estimated from baseline recordings considered as the representation of the noise. Σ_s is assumed to be an identity matrix in conventional MNE. In the end, λ can be optimized by the L-Curve method suggested by Hansen, 2000. Like tSVD, MNE solution is also known for producing scattered and blurry reconstruction images (Haufe *et al.*, 2008).

1.4.4 Low-resolution electromagnetic tomography (LORETA)

LORETA was first proposed by Pascual-Marqui, Michel and Lehmann, 1994 for EEG source localization and applied in NIROT in Tremblay *et al.*, 2018, it introduces a spatial smoothness constrain for neighboring sources in matrix X using a Laplacian operator L , therefore the solution is expressed as,

$$\begin{aligned} \hat{X}_{LORETA} &= \operatorname{argmin}(\|(Y - AX)\|_{\Sigma_d}^2 + \lambda \|LX\|_{\Sigma_s}^2) \\ &= (A^T \Sigma_d A + \lambda L^T \Sigma_s L)^{-1} A^T \Sigma_d Y \end{aligned} \quad (1.18)$$

It can be understood as a weighted form of MNE solution seeking maximum spatial smoothness. However, it still produces large spatial extent results.

1.4.5 Sparse reconstructions based on ℓ_1 – and ℓ_0 – norm

To overcome the large spatial extent issues in the above approaches, several reconstruction methods have been developed to result in sparse maps. Therefore, the reconstructed maps tend to locate most of the amplitudes inside one or more focal regions. Such as the ℓ_1 – norm based sparsity regulation (Matsuura and Okabe, 1995; Lu, Lighter and Styles, 2018) and the ℓ_0 – norm based regulation combined with a parameter controls the smoothness (Mohimani, Babaie-Zadeh and Jutten, 2009; Prakash *et al.*, 2014). These methods can be generalized as follows,

$$\hat{X}_{\ell_p\text{-norm}} = \operatorname{argmin}(\|(Y - AX)\|_{\Sigma_d}^2 + \lambda \|X\|_{\Sigma_s}^p) \quad (1.19)$$

where p refers to the order of the norm, $0 \ll p \ll 1$, known as ℓ_p – norm based regulations. These methods might result in too focal results, therefore, having difficulty in the applications with extending generator along the cortex. There are also other methods proposed to combine MNE and

ℓ_p – norm to result in a trade-off between focality, extension, and smoothness, such as the Focal Vector Field Reconstruction (FVR) proposed by [Haufe *et al.*, 2008](#) combined ℓ_1 -norm and ℓ_2 -norm in the penalty function.

1.4.6 Bayesian model averaging (BMA)

Bayesian model averaging (BMA) relies on the Bayesian inferences, which estimate the probability distribution of X . It calculates the weighted average of the solutions estimated under different models ([MacKay, 1992](#); [Fragoso, Bertoli and Louzada, 2018](#)). The weight is defined by the posterior probability of each model. [Trujillo-Barreto, Aubert-Vázquez and Valdés-Sosa, 2004](#) introduced this framework in EEG source location and further applied it in NIROT by [Tremblay *et al.*, 2018](#). In general, it can be formulated as,

$$p(\hat{X}_{BMA}|Y) = \sum_{k=0}^K p(\hat{X}_{M_k}|Y, M_k)p(M_k|Y) \quad (1.20)$$

where $p(\hat{X}_{BMA}|Y)$ is the posterior probability distribution of BMA estimated X conditioned on data Y . It is calculated by the weighted average of the posterior probability distribution of a specific model M_k estimated X conditioned on data Y , namely, $p(\hat{X}_{M_k}|Y, M_k)$. The weight is represented by the posterior probability of each model M_k conditioned on data y , i.e. $p(M_k|Y)$, which is often referred to as the ‘evidence’ for the model. It is usually relying on the calculation of Baye’s factor, $B_{ij} = p(Y|M_i)/p(Y|M_j)$ between models, which quantifies the model uncertainty when conducting model comparisons. $p(M_k|y)$ can be derived for multiple models by the combination of Bayes factors between each model M_k to a reference model M_0 ([Trujillo-Barreto, Aubert-Vázquez and Valdés-Sosa, 2004a](#)). In practice, multiple models can be constructed by applying different inverse approaches mentioned above and using different prior of the underlying activation with different cortical parcellation. In both works on EEG ([Trujillo-Barreto, Aubert-Vázquez and Valdés-Sosa, 2004a](#)) and NIROT ([Tremblay *et al.*, 2018](#)), this approach improved the sensitivity and specificity of the reconstruction comparing to the others. However, it is well understood nowadays that the Bayes factor is not preferred as a model comparison approach in the modern Bayesian framework ([Gelman *et al.*, 2013a](#); [McElreath, 2020](#)) due to the facts that 1) it could be biased by prior selections and 2) difficult to calculate in practice since it requires to calculate the integral of a certain probability density function.

1.4.7 Bayesian approach using Automatic Relevance Determination (ARD) hierarchical prior

A hierarchical Bayesian (HB) approach has been proposed firstly to regularize the inverse problem resulting in sparse reconstructed maps in MEG source localization study (M. A. Sato *et al.*, 2004). The probability distribution of the generator along cortex (X in equation 1.4) conditioned on data y can be assumed as a Gaussian distribution as follows,

$$p(\hat{X}_{HB}|Y) = e^{-\frac{1}{2}X^T \Sigma_s X} \quad (1.21)$$

The prior of the inverse of source covariance Σ_s (also called precision, same as the one in equation 1.17) is modeled as a diagonal matrix in which the diagonal elements $\alpha_{n=1}^N$ (N for the number of voxel or vertex along the cortex) can be modeled by an Automatic Relevance Determination (ARD) hierarchical prior borrowed from the Bayesian machine learning field (Neal, 1996),

$$p(\alpha) = \prod_{n=1}^N \Gamma(\alpha_n | \bar{\alpha}_{0n}, \gamma_{0n\alpha}) \quad (1.22)$$

where α_n follows a Gamma distribution (Γ) with mean equals to $\bar{\alpha}_{0n}$ and degree of freedom equals to $\gamma_{0n\alpha}$. The use of Gamma distribution introduces a soft constraint for the source covariance Σ_s^{-1} , such that large mean of precision (large $\bar{\alpha}_{0n}$) would penalize small values of X and vice versa. In the original work of M. A. Sato *et al.*, 2004, $\bar{\alpha}_{0n}$ and $\gamma_{0n\alpha}$ were estimated from the fMRI activation map of the same subject. The approximated posterior distribution was calculated by using the Variational Bayesian (VB) method based on maximizing the free energy function equivalent to minimizing the Kullback-Leibler distance between the posterior distribution of X and a trial distribution (Attias, 1999; Sato, 2001).

This approach was adapted for solving the NIROT inverse problem firstly by Shimokawa *et al.*, 2012 using the MNE solution (in equation 1.17) to initialize the hierarchical prior (in equation 1.21). The authors also further introduced a spatial smoothing filter for X , using a 5-mm full width at half maximum (FWHM) Gaussian kernel. Considering the fact that fNIRS signal consists of physiological noise exhibits in scalp (see section 2.13), Shimokawa *et al.*, 2013 expanded the model in equation 1.4 into the summation of two parts, 1) cortical reconstruction using the above

method and 2) scalp reconstruction using a source covariance Σ_s^{-1} constructed by the combination of the Laplace operator (L) and a hyperparameter (η) controlling the smoothness, such that $\Sigma_s^{-1} = L^{-1}\eta^{-1}L^{-1T}$. Therefore, the physiological noise was assumed to be removed from the reconstruction directly. This method is finally validated on real data set of motor task by comparing to fMRI activation maps in Yamashita *et al.*, 2016.

The above method improved the accuracy of EEG/MEG and NIROT reconstructions and demonstrated the superiority of Bayesian approaches over conventional methods described previously. However, methodologically speaking, as also pointed out by Nummenmaa *et al.*, 2007; Yamashita *et al.*, 2016, it is hard to optimize the initialization value for the parameter $\gamma_{0n\alpha}$ which controls the balance between prior and data. Besides, the posterior is approximated by variational Bayesian (VB) rather than a full Bayesian approach using the posterior sampling technique (see section 3.2). VB solution can result in biased estimation of the posterior distribution.

1.4.8 Maximum Entropy on the Mean (MEM) framework

Maximum Entropy on the Mean (MEM) was first proposed by Amblard, Lapalme and Lina, 2004, before being adapted and carefully evaluated in our lab in the context of EEG/MEG source localization (Grova, Daunizeau, *et al.*, 2006; Chowdhury *et al.*, 2013). A key property of MEM source imaging is its ability to recover the spatial extent of the underlying generators accurately, as we demonstrated in the context of 1) localizing transient epileptic discharges (Chowdhury *et al.*, 2016; Grova *et al.*, 2016; Heers *et al.*, 2016; Pellegrino, Hedrich, *et al.*, 2016; Pellegrino *et al.*, 2020) and oscillations (Pellegrino, Hedrich, *et al.*, 2016; Avigdor *et al.*, 2021); 2) dealing with focal sources evoked by electrical median nerve stimulations (Hedrich *et al.*, 2017), 3) EEG/MEG fusion in the presurgical evaluation of epilepsy (Chowdhury *et al.*, 2018); and 4) MEG resting state connectivity (Aydin *et al.*, 2020). We will introduce MEM framework by two parts as follows,

1) MEM solution:

In the MEM framework, which is a probabilistic framework, the probability distribution of the amplitude of X , described as $dp(x) = p(x)dx$, can be estimated by Bayesian inference, starting from a predefined prior distribution of X denoted as $d\nu(x)$. The peak of the posterior of $dp(x)$ represented by $dp^*(x)$ is estimated by maximizing the Kullback-Leibler divergence or ν -entropy to the prior as following,

$$S_\nu(dp(x)) = - \int \log\left(\frac{dp(x)}{d\nu(x)}\right) dp(x) = - \int f(x) \log(f(x)) d\nu(x) \quad (1.23)$$

$$dp^*(x) = \operatorname{argmax}_{dp(x) \in \mathbb{C}_m} (S_\nu(dp(x)))$$

where $S_\nu(dp(x))$ is the ν -entropy of $dp(x)$ to prior $d\nu(x)$, \mathbb{C}_m is the set of probability distributions of x that explains the data Y on average,

$$Y - [A|I] \begin{bmatrix} E_{dp}[x] \\ e \end{bmatrix} = 0, \quad dp \in \mathbb{C}_m \quad (1.24)$$

where $E_{dp}[x]$ is the statistical expectation of x under the probability distribution dp , I is the identity matrix with the dimension of the number of vertices involved in the reconstruction. $E_{dp}[x] = \int x dp(x)$ represents the statical expectation of x under the probability distribution dp . Therefore, within the MEM framework, a unique solution of $dp(x)$ could be obtained as follows (see Fig.1.7),

$$dp^*(x) = \operatorname{argmax}_{dp(x) \in \mathbb{C}_m} (S_\nu(dp(x))) \quad (1.25)$$

As shown in above equation 1.25, the solution of $dp^*(x)$ can be solved by maximizing the ν -entropy which is a convex function. It is equivalent to minimizing an unconstrained concave Lagrangian function i.e. $L(dp(x), \kappa, \lambda)$, along with two Lagrangian constrain parameters, i.e. κ and λ . It is finally equivalent to maximizing a cost function $D(\lambda)$ which is described as,

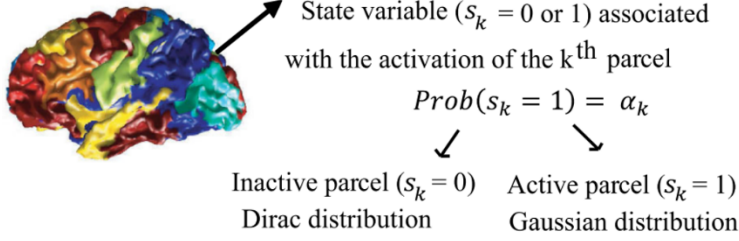
$$D(\lambda) = \lambda^T Y - F_\nu(A^T \lambda) - \frac{1}{2} \lambda^T \Sigma_d^{-1} (\Sigma_d^{-1})^T \lambda \quad (1.26)$$

where Σ_d^{-1} is the noise covariance matrix same as in equation 1.18. F_ν represents the free energy associated with reference $d\nu(x)$. Finally, if we denote $\lambda^* = \operatorname{argmax}_\lambda D(\lambda)$, the solution of MEM framework is,

$$\hat{X}_{MEM} = \nabla_\xi F_\nu^*(\xi) |_{\xi=A^T \lambda^*} \quad (1.27)$$

MEM Initialization of the reference distribution MEM Regularization

The spatial clustering leads to parcelling of the whole cortical surface into K cortical parcels.



$$d\mathbf{v}(\mathbf{j}) = \prod_{k=1}^K [(1 - \alpha_k)\delta(\mathbf{j}_k) + \alpha_k \mathcal{N}(\mu_k, \Sigma_k)(\mathbf{j}_k)] d\mathbf{j}$$

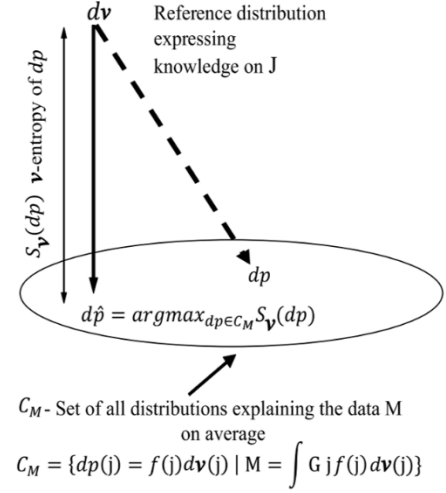


Fig.1.7 Illustration of Maximum entropy on the mean (MEM) framework. MEM assumes the brain activity could be described by K non-overlapping and independent cortical parcels along with α_k represents the probability of each parcel to be active. The joint distribution (initialized by MNE solution) of each parcel can form a reference distribution (i.e. prior). MEM solves the unique inverse problem solution by maximizing the Kullback-Leibler divergence to the prior. Figure taken from *Chowdhury et al., 2015*.

2) Prior distribution:

To construct the prior distribution $d\mathbf{v}(x)$, we assumed that brain activity could be described by K non-overlapping and independent cortical parcels (see Fig.1.7), therefore,

$$d\mathbf{v}(x) = \prod_{k=1}^K [(1 - \alpha_k)\delta(x_k) + \alpha_k N(\mu_k, \Sigma_k)] dx_k, \quad 0 < \alpha_k < 1 \quad (1.28)$$

where the hidden variable S_k defines the activation state (active or not) of each cortical parcel k . α_k is the probability of k^{th} parcel to be active, i.e. $Prob(S_k = 1)$. δ_k is a Dirac function that allows to ‘switch off’ the parcel when considered as inactive (i.e. $S_k = 0$). $N(\mu_k, \Sigma_k)$ is a Gaussian distribution, describing the distribution of absorptions changes within the k^{th} parcel, when the parcel is considered as active, $S_k = 1$. Note that the multiplication in the definition of $d\mathbf{v}(x)$ is referring to the assumption that all parcels are statistically independent.

A Data Driven Parcellization (DDP) technique (*Lapalme, Lina and Mattout, 2006*) was used to parcellate the cortical surface into K non-overlapping parcel. The probability of each parcel to be

active (α_k) was initialized as the median Multivariate Source Pre-localization (MSP) (Mattout *et al.*, 2005) score from all the sources within the parcels. To initialize the $N(\mu_k, \Sigma_k)$ in prior $d\nu(x)$, μ_k was set to zero. $\Sigma_k(t)$ at each time point t was defined according to Chowdhury *et al.*, 2013,

$$\begin{aligned}\Sigma_k(t) &= \eta(t)W_k(\sigma)^T W_k(\sigma) \\ \eta(t) &= 0.05 \frac{1}{\mathcal{P}_k} \sum_{i \in \mathcal{P}_k} \hat{X}_{MNE}^2(i, t)\end{aligned}\tag{1.29}$$

where $W_k(\sigma)$ is a spatial smoothness matrix, defined by Harrison *et al.*, 2007; Friston *et al.*, 2008, which controls the local spatial smoothness, similar to LORETA, within the parcel according to the geodesic surface neighborhood order. $\eta(t)$ was defined as 5% of the averaged energy of MNE solution within each parcel.

1.5 Depth weighting

As described in section 2.1 on mBLL, light intensity decreases exponentially along with the increase of the effective path length. In the meantime, the human cortex is highly folded with complex morphology exhibiting different depths relative to the scalp (see Fig.1.8a) where the optodes are installed. The deeper the region of interest is, the longer the SD separation is needed, therefore, the longer the effective path length is. The relationship between the sensitivity of fNIRS montage to the depth of the cortical area was comprehensively investigated by applying aMC method on the Colin27 human head template with different SD separations (Strangman, Li and Zhang, 2013). The above theoretical exponential relationship was exhibited in all channels and various regions of interest (see Fig.1.8b). The author fitted a formula from the simulation results as follows,

$$sensitivity = 0.075 \cdot 0.85^{depth}\tag{1.30}$$

Such reduction of sensitivity along depth not only limits the probing ability of fNIRS to about 2cm from the scalp in general (Culver *et al.*, 2003; Dehghani, White, *et al.*, 2009; Scholkmann, Kleiser, *et al.*, 2014; Scarapicchia *et al.*, 2017), but also introduces potential bias from the depth without further regulation when solving the inverse problem in the previous section. The reconstruction will tend to exhibit within the high sensitivity area (i.e. more superficial). This bias from the depth

has been investigated and compensated in EEG/MEG source localization studies (Fuchs *et al.*, 1999; Liu, Dale and Belliveau, 2002; Lin *et al.*, 2006) even though the forward model in EEG/MEG follows a more moderate reduction along with the depth. Depth-dependent regularization in reconstruction has also been proposed in NIROT by Culver *et al.*, 2003 and then widely applied in Zeff *et al.*, 2007; Dehghani, White, *et al.*, 2009; White *et al.*, 2009; Eggebrecht *et al.*, 2012, 2014. In general, the solution is to scale the source covariance matrix by a factor that plays a role in tuning the effective FOV for reconstructions. This means the higher the scaling factor, the more compensation for deeper regions. The tuning of the depth weighting then seeks a trade-off between under- and over-compensation, which is empirically defined by the researcher according to the specific applications.

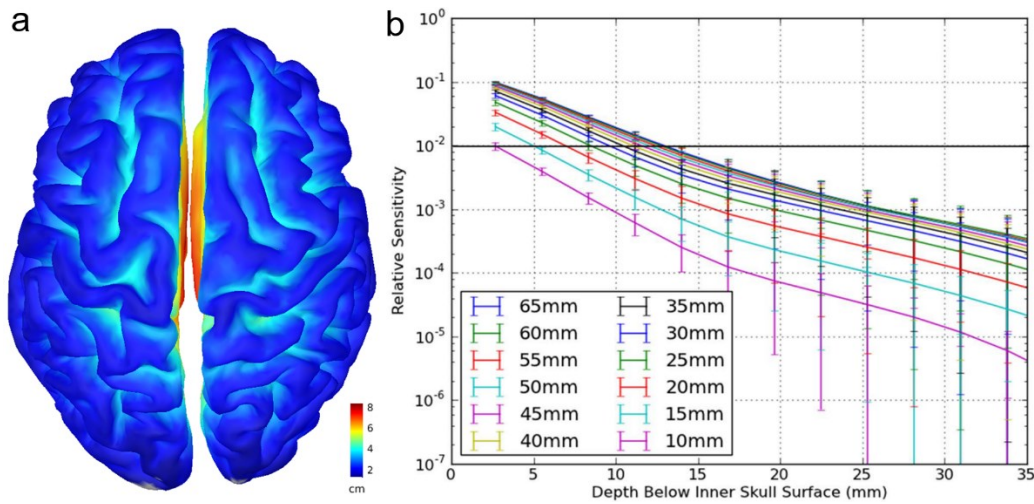


Fig.1.8 Illustration of the relationship between sensitivity and depth for the cortical area. a) depth map calculated for each vertex along the mid-surface of Colin27 template using the distance from a cortical vertex to its closest point along the head surface. b) relationship between the relative sensitivity and the depth from cortex to the inner skull surface for different SD separations. In general, sensitivity decrease along with the increase of depth, following an exponential relationship. Figures b) adapted from Strangman, Li and Zhang, 2013.

1.5.1 Depth weighted MNE

Depth-weighted MNE (Ioannides, Bolton and Clarke, 1990; Lin *et al.*, 2006) has been proposed as an approach to compensate for the above effect. It consists of using the following expression for the prior model of the source covariance Σ_s^{-1} in equation 1.17, which is no longer an identity matrix but scaled by a weighting matrix W as follows,

$$\text{diag}(W) = \frac{1}{\text{diag}((A^T \Sigma_d A)^\omega)} \quad (1.31)$$

where ω is a weighting parameter tuning the amount of depth compensation. The larger ω is, the more depth compensation is considered. $\omega = 0$ refers to no depth compensation and an identity source covariance model.

1.5.2 Depth weighted MEM

One of the contributions of this thesis is adapting MEM for fNIRS reconstruction, in which we implemented for the first time depth weighting within the MEM framework. Two depth weighting parameters, ω_1 and ω_2 were introduced. Therefore, the standard MNE solution \hat{X}_{MNE} in equation 1.17 is replaced by the depth weighted version of MNE solution \hat{X}_{dMNE} . And the depth weighted version of Σ_k for prior initialization is defined as,

$$\begin{aligned} \Sigma_{k_{dw}} &= \Lambda_{\mathcal{P}_k} \eta_{dw} W_k(\sigma)^T W_k(\sigma) \\ \eta_{dw} &= 0.05 \frac{1}{\mathcal{P}_k} \sum_{i \in \mathcal{P}_k} \hat{X}_{dMNE}^2 \end{aligned} \quad (1.32)$$

where $\Lambda_{\mathcal{P}_k}$ is the depth weighting matrix for each parcel k . ω_1 is used to weight the source covariance matrix of each parcel Σ_k in equation 1.28. ω_2 is applied to solve the depth weighted MNE in equation 1.29. This strategy is also seen in [Yamashita *et al.*, 2016](#), in which depth-weighted MNE solution is used to initialize the prior $p(\alpha)$ in equation 1.22.

1.5.3 Other depth weighting approaches

There are other depth weighting approaches based on the MNE method. The idea is to normalize the MNE solution in equation 1.17, using an empirical variance matrix denoted as S , such that the resulted reconstruction results $S^{-1/2} \hat{X}_{MNE}$ follow a t-distribution ([Hedrich, 2020](#)). For instance, the dynamic statistical parametric mapping (dSPM) proposed by [Dale *et al.*, 2000](#) used a variance matrix $S_{dSPM} = \text{diag}(W_{MNE} \Sigma_d W_{MNE}^T)$ and the standardized LORETA (sLORETA) proposed by [Pascual-Marqui, 2002](#) used the variance matrix to normalize the MNE solution, in which $S_{sLORETA} = \text{diag}(W_{MNE} (A^T \Sigma_d A + \lambda \Sigma_s) W_{MNE}^T)$. These two methods are considered as a depth

weighting approach since higher amplitude will be normalized by higher source variances (Hauk, Wakeman and Henson, 2011; Chowdhury, 2016).

1.6 Summary

This chapter introduced the personalized NIROT approach proposed in this thesis. We reviewed the principle of CW-fNIRS mainly focused on what it is actually measuring. The basic biological principle of O_2 consumption of the brain for oxidative glucose metabolism and the functionality of HbO/HbR was first explained, followed by the physics principle of detecting and differentiating HbO/HbR concentration changes using near infra-red light. Then we discussed that the components of CW-fNIRS signal are not only contributed by the cerebral hemodynamic but also consists of physiological noise from systemic circulations. The approaches of removing these noises were also reviewed along with the conventional channel space analysis. Acknowledging the disadvantage of mBLL based channel space analysis, we introduced the personalized NIROT approach consisting of 1) personalized optimal montage, 2) solution of the forward problem from diffusion approximation to the numerical solution using aMC, and 3) how to solve the inversion problem mainly using the MEM framework and the depth weighting compensation.

Chapter 2

Combination of TMS and fNIRS

This chapter will introduce the combination of Transcranial Magnetic Stimulation (TMS) and functional Near-Infrared Spectroscopy (fNIRS). We used this technique in Chapters 5 and 6 to investigate the hemodynamic correlates of cortical excitability. The hemodynamic activity was measured via fNIRS, while cortical excitability was assessed and modulated via TMS. Biological mechanisms of brain plasticity, such as long-term potentiation (LTP), long-term depression (LTD) and spike timing dependent plasticity (STDP) are briefly summarized before explaining the TMS techniques commonly used to induce plasticity: repetitive TMS (rTMS), intermittent Theta-Burst Stimulation (iTBS) and continuous Theta-Burst Stimulation (cTBS). Paired Associative Stimulation (PAS), another neuromodulatory technique that combines peripheral stimulation and TMS, will be reviewed with more details as it was applied in Chapters 5 and 6.

As the combination of non-invasive brain stimulation and brain mapping is challenging, we also shortly reviewed the pros and cons of commonly used neuroimaging modalities when applied in conjunction with TMS, such as Electroencephalogram (EEG), functional magnetic resonance imaging or functional MRI (fMRI), Positron emission tomography (PET) and, in more details, TMS/fNIRS.

In summary, this chapter aims to encapsulate the basic principle, technical details, and applications of TMS/fNIRS, which provide sufficient background for Chapters 5 and 6.

2.1 Spike timing dependent plasticity

Brain plasticity is the ability to adapt to continuous changes in the external and internal environment. This process relies on functional and anatomical modifications of the neuronal circuits. Associative synaptic plasticity (James, 1890; Feldman, 2012) is one of the most studied mechanisms of cortical plasticity (Feldman, 2009). Canadian neurophysiologist Donald O. Hebb proposed his famous theory called Hebbian or Hebbian learning (Hebb, 1949). As stated in Hebb, 1949: “When an axon of cell A is near enough to excite a cell B and repeatedly or persistently takes part in firing it, some growth process or metabolic change takes place in one or both cells such that A’s efficiency, as one of the cells firing B, is increased”. The work on Hebbian learning

focused on the effect of repetitive stimulation. [Bliss and Lomo, 1970](#); [Bliss and Lomo, 1973](#) discovered long lasting strengthening effects of repetitive stimulation on synapses, originally named 'frequency potentiation' and nowadays known as long-term potentiation (LTP). This type of plasticity was achieved with high frequency (10Hz to 20Hz) electric stimulations of the hippocampus of anesthetized rabbits. The effect of repetitive stimulation is not always an enhancement of effect: long lasting weakening was also found by [Sejnowski, 1977](#); [Bienenstock, Cooper and Munro, 1982](#) and termed long-term depression (LTD).

The first experiment to investigate the effects of timing between presynaptic and postsynaptic spike on synaptic plasticity, rather than the stimulated spike frequency, was proposed by [McNaughton, Douglas and Goddard, 1978](#). This work refined the understanding of LTP by clarifying that the timing of the postsynaptic spike is critical and found that LTP is possible only when the delay between postsynaptic and presynaptic spikes is lower than 25ms. Later on, [Levy and Steward, 1983](#) confirmed this finding comprehensively, showing that if the presynaptic spike leads postsynaptic spike, the synapse is strengthened and vice versa. This work established the concept of associative synaptic plasticity - known as spike timing-dependent plasticity (STDP) ([Markram, Gerstner and Sjöström, 2012](#)). For detailed reviews of STDP on technical evolution and biological mechanisms, please refer to [Müller-Dahlhaus, Ziemann and Classen, 2010](#); [Markram, Gerstner and Sjöström, 2011, 2012](#); [Feldman, 2012](#). Works on the implementation of STDP on the human cortex are further discussed in section 2.2.3.

As shown in Fig.2.1, when a presynaptic spike excites a neuron repeatedly while a postsynaptic spike is firing (see Fig.2.1a), the timing between these two spikes could induce either LTP or LTD. The effect of strengthening or weakening depends on which spike is leading the other. For instance, in the work of [Feldman, 2000](#) on rat barrel cortex (see Fig.2.1b), LTP indicated by the slope of excitatory postsynaptic potential (EPSP) is achieved by presynaptic leading postsynaptic spikes; and LTD is obtained by postsynaptic leading presynaptic spikes. Besides, only one of them could not modulate synaptic plasticity. In the end, this time delay is mostly within a few tens of milliseconds ([Fröhlich, 2016](#)) shown in Fig.2.1c.

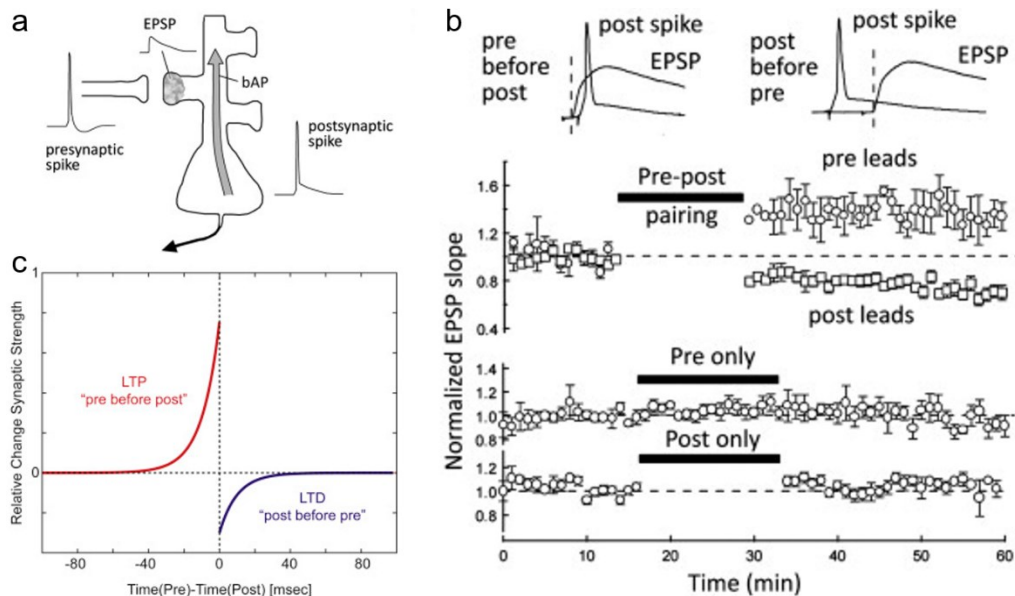


Fig2.1 Principle of spike timing-dependent plasticity (STDP). a) presynaptic spike is persistently exciting a neuro while a postsynaptic spike is firing, figure taken from Feldman, 2012, b) experimental results on rat barrel cortex showed that when presynaptic spikes were leading the postsynaptic ones, LTP was obtained; and LTD was obtained by postsynaptic leading presynaptic spikes. Synaptic plasticity is measured by the slope of excitatory postsynaptic potential (EPSP), figure taken from Feldman, 2012 which was originally published by Feldman, 2000, c) summary of STDP and the requirement of timing, the red curve, and the blue curve represents LTP and LTD, respectively. The delay between two spikes should be within few tens of milliseconds, figure taken from Fröhlich, 2016

2.2 Inducing neuronal plasticity noninvasively

The principle of neuronal plasticity can be exploited to modulate human cortical excitability noninvasively. Several noninvasive brain stimulation (NIBS) approaches have been proposed, such as the very first works using transcranial Electrical Stimulation (tES) (Merton and Morton, 1980; Reed and Cohen Kadosh, 2018), Transcranial Magnetic Stimulation (TMS) (Barker, Jalinous and Freeston, 1985; Klomjai, Katz and Lackmy-Vallée, 2015), and the more recent transcranial focused ultrasound (tFUS) (Legon *et al.*, 2014; Blackmore *et al.*, 2019). The common principle is to directly interact with neurons and synapses, following the basic principles of plasticity modulation learned from animal models. This section will only focus on TMS related approaches by first briefly review the commonly used protocols and then explain more details on Paired Associative Stimulation (PAS) used in Chapters 5 and 6.

2.2.1 Single pulse TMS

TMS was established at the beginning of the nineties as an evolution and improvement of tES. Indeed, tES induces plasticity by applying a current to the scalp, which flows through skin, skull, cerebrospinal fluid and reaches the cortical surface. tES directly interacts with the body of pyramidal neurons, but is a very uncomfortable and painful technique (Merton and Morton, 1980). To reduce the discomfort and improve the convenience of tES, Barker, Jalinous and Freeston, 1985 proposed TMS, for noninvasive brain stimulation on the human motor cortex. TMS generates a magnetic pulse ranging from 1 to 2.5 Tesla (Pawar *et al.*, 2008) through a coil (see Fig.2.2b). The magnetic field is generated by releasing charges stored in the capacitor (see Fig.2.2a) in less than 1 ms (Rossini *et al.*, 2015a). This type of magnetic pulse allows depolarizing neuronal pools, therefore triggering action potentials in axons instead of cell bodies of pyramidal neurons (Klomjai, Katz and Lackmy-Vallée, 2015). When TMS is delivered as a single pulse (without specific protocol on stimulation timing), it is called the single pulse TMS (spTMS) (Di Lazzaro, Rothwell and Capogna, 2018), it will temporarily excite (i.e., transit excitation) the corresponding cortical regions under the coil. Figure 2.2c demonstrated a typical pathway of the TMS stimulation of the motor cortex. Excited neurons induce descending corticospinal volleys through the pyramidal tract, which evoke motoneuron activations and eventually lead to a brief muscle contraction in the contralateral limb (Klomjai, Katz and Lackmy-Vallée, 2015). In terms of penetration depth and spatial resolution, a figure-8 coil usually stimulates around 1.5cm depth (from scalp) and an area as focal as 15cm² along the cortex (Gomez, Goetz and Peterchev, 2018).

The combination of simultaneous TMS and neuroimaging techniques such as EEG has allowed us to better understand the effects of spTMS. A typical waveform of the TMS evoked potentials (TEP) measured by the scalp EEG when conducting spTMS on the motor cortex is shown in Fig.2.2c. Similar to other event-related potentials (ERPs), it consists of several positive and negative peaks, such as P30, N45, N100 and P180 (Komssi and Kähkönen, 2006), which are related to neuronal activities induced by spTMS. When measuring the descending corticospinal volleys induced by spTMS at the level of cervical spine with invasive electrodes, there are two typical waveforms called direct wave (D-wave) and indirect waves (I-wave) as shown in Fig.2.2c. D-waves reflect the direct activation of axons and I-wave represents the synaptic (indirect) activation of corticospinal neurons (Day *et al.*, 1989; Di Lazzaro *et al.*, 1998, 2004). Electromyography (EMG) electrodes placed on the muscle belly allow measuring the last effects of TMS of the motor cortex

corresponding to the motor evoked potential (MEP) shown in Fig2.2c and Fig.2.4b. The peak-to-peak amplitude of MEP is often seen as an indicator of motor cortex excitability (see Fig.2.4). MEPs are also used to quantify the spTMS stimulation intensity while the muscle is relaxing (Rossini *et al.*, 1994) or contracting (Fitzgerald, Fountain and Daskalakis, 2006), called resting motor threshold (resting MT or RMT) and active motor threshold (active MT or AMT), respectively. Traditionally, RMT or AMT was defined such that 50 μ V peak-peak amplitude of MEP can be observed at least in half of 10 continuous spTMS (Rossini *et al.*, 1994). In Chapters 5 and 6, to improve the efficiency and accuracy of this process, we used the TMS Motor Threshold Assessment Tool (MTAT 2.0, <http://www.clinicalresearcher.org/software.html>) based on the maximum-likelihood parameter estimation by sequential testing approach (Awiszus *et al.*, 1999; Ah Sen *et al.*, 2017).

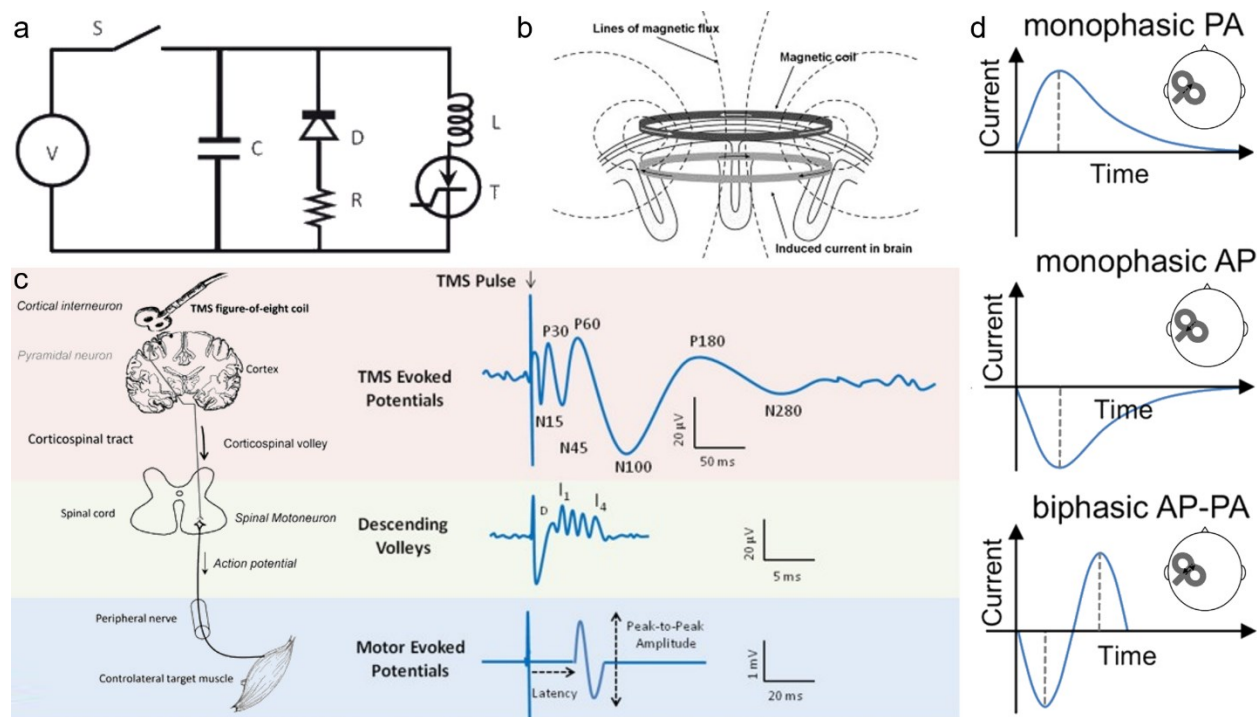


Fig2.2 Demonstration of spTMS consisting of the physics principle of TMS, TMS evoked activities and pulse configurations. a) TMS machine circuit which consists of a Voltage (V) source, Switch (S), Capacitor (C), Diode (D), Resistor (R), and Thyristor (T) taken from Farzan *et al.*, 2016. b) TMS coil's magnetic flux and induced current flows along the cortex, figure taken from Hallett, 2007 which was adapted from Hallett, 2000. c) Pathway and corresponding activation waveforms of TMS delivered on the motor cortex, figure adapted and merged from Klomjai, Katz and Lackmy-Vallée, 2015; Farzan *et al.*, 2016. d) three typical TMS pulse configurations depend on the current direction(s), the current direction(s) in the coil is from

posterior to anterior (PA) or/and from anterior to posterior (AP), figure adapted from Davila-Pérez *et al.*, 2018.

Last but not least, there are mainly three types of spTMS configurations that produce different pulse waveforms, as shown in Fig.2.2d. The monophasic pulse can be generated by a unidirectional current in the coil. In contrast, bidirectional currents can produce a biphasic pulse where an initial current is followed by a reversed one. Although it is shown biphasic pulse has higher efficiency when stimulating the motor cortex (Kammer *et al.*, 2001; Sommer *et al.*, 2006), monophasic activates a relatively uniform population of neurons when modulating long term plasticity using repetitive rTMS (Arai *et al.*, 2007; Taylor and Loo, 2007).

2.2.2 Repetitive TMS

Due to hardware limitation, earlier TMS applications could only deliver spTMS with an interstimulus interval (ISI) longer than 4s. The technology was soon improved to stimulate with an ISI of 10ms (Rossini and Caramia, 1992). This granted the ability to investigate the effects of repetitive or rhythmic TMS protocol on cortical function, especially on cortical excitability. Burst or prolonged trains of TMS could for instance be applied to induce speech arrest (which corresponds to a transient virtual lesion) (Pascual-Leone, Gates and Dhuna, 1991), and modulate cortical excitability (Chen and Seitz, 2001). Such repetition of spTMS pluses in a certain frequency is referred as repetitive TMS (rTMS). Throughout the years, it has been shown that (see Fig2.3a), when using stimulation frequency from 5-20Hz, one can increase the cortical excitability, whereas, 1-4Hz lower frequency can induce inhibition (Fitzgerald, Fountain and Daskalakis, 2006). The most successful clinical application of rTMS is probably on the treatment of depression (Eschweiler *et al.*, 2000; Voigt, Carpenter and Leuchter, 2019), which holds two US Food and Drug (FDA) clearances (Rossini *et al.*, 2015a).

A special type of rTMS protocol is the so-called Theta-Burst Stimulation (TBS). TBS is of more recent introduction and was established in Rothwell lab in London UK (Huang *et al.*, 2005; Talelli, Greenwood and Rothwell, 2007). The idea behind TBS is that theta and gamma rhythms are extremely important for brain function and plasticity. Therefore, it was hypothesized that TMS stimulation with these rhythms could be functionally relevant. TBS is typically performed below the motor threshold. There are two well-known types and several variants aiming at inducing LTP and LTD. Intermittent TBS (iTBS) can increase the cortical excitability (LTP). It consists of TMS

trains delivered at 5Hz, and each train contains 3 spTMS pluses burst delivered at 50Hz (see Fig2.3b). These trains are applied in the first 2s of every 10s and repeated often for about 3 minutes (Huang *et al.*, 2005; Suppa *et al.*, 2016). Inhibitory TBS, is a continuous TBS (cTBS) (Huang *et al.*, 2005) with TMS trains (i.e., 3 spTMS pluses burst delivered at 50Hz) at 5Hz for about 20 to 40s (see Fig2.3b). There is still debate on whether TBS induces the most effective and reliable plasticity modulation (Rossini *et al.*, 2015a; Suppa *et al.*, 2016), but the obvious advantage is the short application time. For instance, cTBS could induce LTD in about 20-40s, whereas it could take 20 minutes for low frequency rTMS.

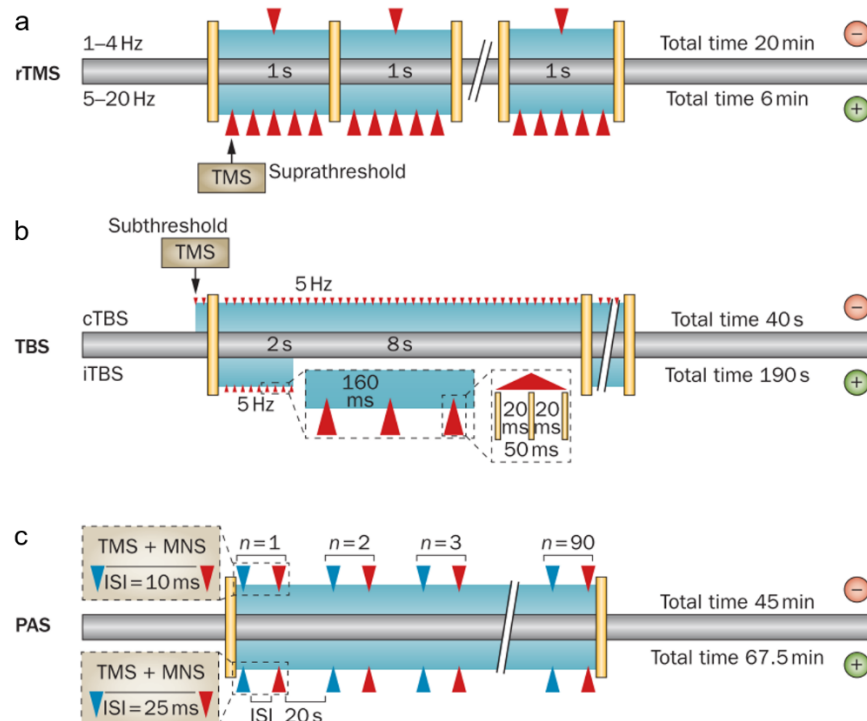


Fig2.3 Three typically used TMS protocols for modulation of cortical excitability. a) repetitive TMS (rTMS) delivered by high frequency (5-20Hz) and low frequency (1-4Hz) to induce long-term potentiation (LTP) and long-term depression (LTD), respectively. Stimulation intensity needs to be higher than the resting motor threshold (RMT). b) special protocols of rTMS, namely, intermittent Theta-Burst Stimulation (iTBS) and continuous TBS (cTBS). cTBS delivers a train of spTMS consisting of 3 TMS pulses at 50Hz and repeats this train at 5Hz for about 40s to induce LTP. iTBS utilizes the same spTMS train at 5Hz in the first 2s of every 10s and repeats for about 190s to induce LTD. c) Pair associative stimulation (PAS) combines pairs of TMS and Median Nerve Stimulation (MNS) delivered with proper timing – around 25ms or 10ms interstimulus intervals (ISI) to excite (PAS25) or inhibit (PAS10) cortical areas, respectively. Figure adapted from Di Pino *et al.*, 2014.

2.2.3 Pair associative stimulation

Paired Associative Stimulation (PAS) was first proposed by [Mariorenzi et al., 1991](#) and [Stefan, 2000](#), which consists of pairs of TMS and Median Nerve Stimulation (MNS) delivered with proper interstimulus intervals (ISI) (see Fig.2.3c). [Stefan, 2000](#) invented this protocol inspired by the concept of STDP from the animal study ([Levy and Steward, 1983](#)), which is also known as Hebbian learning ([Hebb, 1949](#)) mentioned in section 2.1. This means that TMS stimulation excites the pyramidal cells mimicking a postsynaptic spike, and somatosensory activations induced by MNS propagate to pyramidal cells along the motor cortex, acting as a presynaptic spike. Many studies have implemented this theory and reproduced the work of [Stefan, 2000](#) noninvasively on the human brain using PAS, for instance on the primary motor (M1) cortex ([Carson and Kennedy, 2013](#)), somatosensory (S1) cortex ([Müller-Dahlhaus, Ziemann and Classen, 2010](#)) and dorsal-lateral pre-frontal cortex (DLPFC) ([Casula et al., 2016](#)).

MEPs before and after PAS interventions are usually acquired by 10 to 20 spTMS, as shown in Fig.2.4a and c. The averaged pre- and post-PAS MEP peak-peak amplitudes are then compared by calculating the ratio between them (see Fig.2.4b). If this ratio is larger than 1 it indicates the excitability increase and vice versa. As shown in Fig.2.4b, ISI around 25ms (PAS25) usually induces LTP and ISI of 10ms (PAS10) usually induces LTD ([Stefan, 2000](#); [Wolters et al., 2003, 2005a](#)). It requires around 100 pairs of stimulations to have the desired modulation that could last for more than 30 minutes ([Stefan, 2000](#); [Stefan et al., 2002](#); [Lee et al., 2017](#)). The ISI could be refined individually using N20+5ms or N20-5ms for PAS25 and PAS10, respectively ([Carson and Kennedy, 2013](#)) to improve the efficiency (see Fig.2.4c). Where N20 latency ([Allison et al., 1991](#)) can be predefined by conducting electrical stimulation at the wrist (e.g., Median Nerve) and measuring response using two bipolar EEG electrodes located at CP3 and CP4 in 10-20 system. This latency estimates the propagation time of electric signal (induced by MNS) from the wrist (e.g., Median Nerve) to the somatosensory cortex.

PAS has been utilized in many applications. For instance, it could enhance the motor learning process ([Jung and Ziemann, 2009](#)); may provide a rehabilitative approach for stroke patients by promoting inter-hemispheric connectivity ([Michou et al., 2012, 2014a](#)); can help in understanding the mechanism of reduced plasticity on preventing seizures ([Strigaro et al., 2015](#)); and indicated

that motor cortex plasticity reduction might not progress during the development of the mild cognitive impairment (MCI) (Lahr *et al.*, 2016).

We selected PAS to modulate the cortical excitability in Chapters 6 and 7 due to the following advantages: 1) It triggers mechanisms of ‘heterosynaptic plasticity’, meaning that the activity of a particular neuron induces changes in synaptic connections strength between other neurons, which are highly involved in epilepsy (Chandler *et al.*, 2003). Therefore, we could reproduce in healthy subjects a ‘model of epilepsy’, where phasic changes of brain excitability (by spTMS) occur on top of stable enhanced excitability (by PAS); 2) The interval between stimulation pairs is relatively longer than rTMS (around 10s to 20s (Suppa *et al.*, 2017)) and the number of paired stimulation is sufficient (e.g., 100) to assess both the hemodynamic response to single paired pulses and the build-up of ongoing excitability changes and plasticity induction. 3) PAS might have higher efficiency when inducing LTP on the motor cortex than using TBS, as shown by Player *et al.*, 2012.

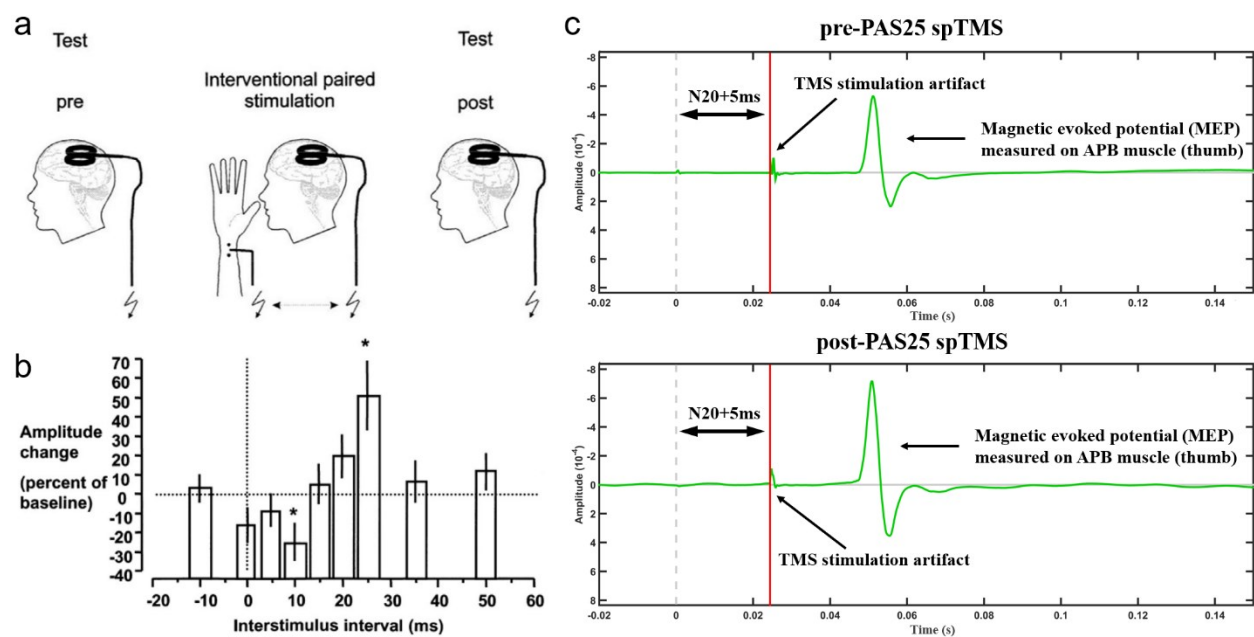


Fig2.4 Demonstration of Paired Associative Stimulation (PAS). a) a typical PAS experiment protocol which consists of PAS intervention in the middle of two spTMS sessions, used to measure the MEP peak-peak amplitude changes, therefore, indicating the effects of PAS on cortical excitability, figure adapted from Stefan, 2000. b) reflection of spike-timing dependent plasticity (STDP) when using different interstimulus intervals (ISI) in PAS. Typically, 25ms (PAS25) and 10ms (PAS10) ISI increase and decrease cortical excitability, respectively. Figure adapted from Suppa *et al.*, 2017. c) averaged MEPs measured

before and after PAS25, peak-peak amplitude of post-PAS25 MEP increased when comparing to pre-PAS25. The red vertical lines indicate the TMS stimulation artifact, which appears N20+5ms after the Median Nerve Stimulation (MNS). Figure from one subject of Chapter 6.

Finally, although the ability of PAS and rTMS to elicit significant cortical excitability changes have been replicated in many studies (Stefan, 2000; Chen and Seitz, 2001; Wolters *et al.*, 2005a; Fitzgerald, Fountain and Daskalakis, 2006; Tsang, Bailey and Nelson, 2015; Lee *et al.*, 2017; Suppa *et al.*, 2017), only 39% and 43% of 56 subjects showed expected MEP amplitude increase after conducting PAS25 and intermittent theta-burst stimulation (iTBS), respectively (López-Alonso *et al.*, 2014). The efficiency of PAS is estimated to be lower than 50% (Fratello *et al.*, 2006; Suppa *et al.*, 2017). This can be explained by the between- and within-subject variability of cortical plasticity modulated by non-invasive brain stimulations (Ziemann and Siebner, 2015). The variability might depend upon multiple factors, including state of the brain, genetic susceptibility, position of the coil and so on. However, a more recent study (Minkova *et al.*, 2019) did not conclude any of these known factors significantly influenced PAS efficiency with 41 subjects. Note that high variability in the induced effects of stimulation is not exclusive of PAS: all non-invasive brain stimulation techniques induce highly variable effects. This is also the motivation for conducting Bayesian data analysis in Chapter 7, so as to reduce the uncertainty of estimations of the effects from the methodological point of view.

2.3 Combination of TMS and fNIRS

2.3.1 Combination of TMS and human brain mapping

Combining TMS with neuroimaging brings benefits to both of them. For neuroimaging, TMS added a new dimension to human brain mapping (Siebner *et al.*, 2009). If we view TMS as an external intervention, it could bring insights into causal inferences when combined with neuroimaging modalities (O'Shea, Taylor and Rushworth, 2008). It has substantially expanded the application of TMS in neuroscience and clinical studies, and it helps us to understand brain functioning better. For instance, Braack, Koopman and Putten, 2016 applied single pulse TMS to the left/right motor cortex of healthy subjects and epilepsy patients and measured TMS evoked potentials (TEPs) using scalp electroencephalography (EEG). The topography of EEG showed different spatiotemporal patterns between healthy subjects and patients, indicating electrophysiology features of epilepsy. Using a similar protocol, Sarasso *et al.*, 2014 showed more

integrated TEPs time course patterns during consciousness and less integrated patterns during unconsciousness state, revealing the underlying mechanism of consciousness - engaging in complex activity patterns integrating more cortical areas. Concurrent TMS/fNIRS (Oliviero *et al.*, 1999; Noguchi, Watanabe and Sakai, 2003; Mochizuki *et al.*, 2006) and TMS/fMRI (Navarro de Lara *et al.*, 2017) studies investigated the hemodynamic response function to spTMS, demonstrated similar responses compared to voluntary stimulus. Resting-state functional connectivity study (Watanabe *et al.*, 2014) using non-concurrent fMRI and rTMS demonstrated decreased functional connectivity between bilateral primary motor cortices after excitatory rTMS interventions, and increased connectivity after inhibitory rTMS, bring insights into how brain networks associates to cortical plasticity. Finally, in Chapters 6 and 7, we also combined PAS and fNIRS to investigate the relationship between task-related cortical hemodynamic activity and cortical excitability changes.

On the other hand, brain mapping also provides a unique understanding of the mechanism of TMS per se while improving the efficiency of the intervention. Using resting state fMRI, Singh *et al.*, 2019 proposed a personalized rTMS stimulation target of interest selection of the left dorsolateral prefrontal cortex (DLPFC) for clinical application in treating depression; Another study using fNIRS (Thomson *et al.*, 2013) optimized the TMS coil orientation to maximizing the effects of signal pulse TMS and rTMS by showing the greatest relative changes in HbO amplitudes at a 45° angle to the midline of the head. The same group applied simultaneous inhibitory rTMS and fNIRS on the left prefrontal cortex and showed increased HbO over 20s to 40s after rTMS train (Thomson *et al.*, 2012, 2013) and then a long term reduction of HbO (Thomson *et al.*, 2012). These results reproduced the observations in an animal study on the visual cortex of the anesthetized cat using inhibitory rTMS and invasive optical imaging, which showed immediately increased tissue oxygen peaked at 10s to 15s after rTMS and followed by a 2 minutes long reduction (Allen *et al.*, 2007). Such combination helped us better understand the hemodynamics modulated by TMS interventions.

In practice, the combination of TMS and neuroimaging can be summarized in two categories proposed by Siebner *et al.*, 2009, which are ‘online’ and ‘offline’ approaches. The following Fig.2.5 summarizes these two approaches. The so-called ‘online’ approach (Fig.2.5a) conducts concurrent TMS and neuroimaging protocol. Therefore, neuroimaging measurement could reflect the TMS effects at the exact moment of the simulation. However, this approach brings more

technical challenges (briefly summarized in section 2.3.2). The first ‘offline’ approach (Fig.2.5b) applies TMS after the neuroimaging scans. It could take benefits from the observations of neuroimaging results to improve TMS efficiency as mentioned above. The other ‘offline’ approach (Fig.2.5c) performs the neuroimaging protocol after TMS, therefore, the long-term effects of TMS, such as modulated cortical excitability can be probed.

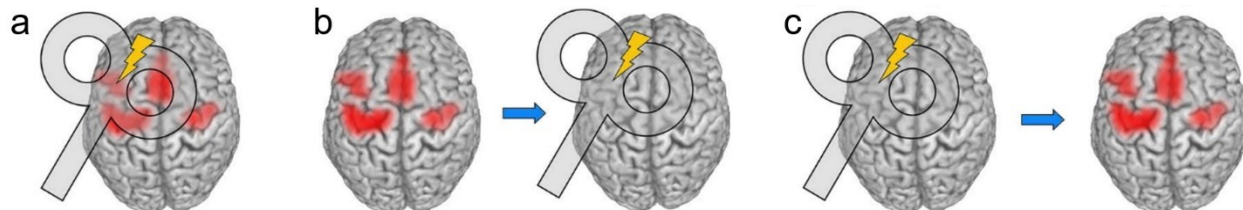


Fig.2.5 Demonstration of two approaches for combination TMS and neuroimaging. a) the ‘online’ approach in which TMS and neuroimaging are conducted simultaneously. b) one of ‘offline’ approaches in which TMS is performed after neuroimaging protocol and c) the other ‘offline’ approach in which TMS is applied before neuroimaging scans. Figure adapted from [Siebner et al., 2009](#).

2.3.2 Advantages and challenges of TMS/fNIRS

Reviewing the advantages of challenges of the combination of TMS and each neuroimaging modality in detail is beyond the scope of this thesis. However, it is essential to first briefly summarize these aspects on modalities except fNIRS to help to understand and emphasize the uniqueness of TMS/fNIRS.

When investigating hemodynamic responses evoked by TMS or the effects of TMS interventions on hemodynamic activity and brain connectivity, fMRI is usually considered as a possible option because of its reliability, ease of use, high spatial resolution and sensitivity to deep brain regions ([Bandettini et al., 1992](#); [Kwong et al., 1992](#); [Glover, 2011](#)). However, combining neurostimulation techniques within the MRI environment is challenging ([Hallett et al., 2017](#)). There is a safety issue as the MRI scanners used for human brain mapping produce a homogeneous magnetic field ranging from 1.5 to 7 Tesla. Any ferromagnetic material inside the scanner might cause a terrible accident ([Siebner et al., 2009](#)). MRI compatible TMS coils have been developed ([Navarro De Lara et al., 2015](#); [Wang, Xu and Butman, 2017](#)) and applied to investigate the TMS induced hemodynamic responses ([Navarro de Lara et al., 2017](#)). In addition, since the TMS pulse itself is a magnetic pulse, it could cause remarkable artifacts when scanning the brain simultaneously with fMRI. Therefore, special fMRI sequences ([Navarro De Lara et al., 2015](#); [Wang, Xu and Butman,](#)

2017) were developed to interleave the scanning sequence and TMS sequence to ensure artifacts could be blocked. Although concurrent TMS/fMRI is technically available nowadays, the resolution of the above limitations also reduced the signal quality of fMRI. Moreover, due to the physical space limitation of the scanner, it is also difficult to stimulate certain brain regions such as the visual cortex. This explains the reason why the majority of studies have had an “offline” approach (Siebner *et al.*, 2009), meaning that hemodynamic and excitability measures are not taken simultaneously.

Positron emission tomography (PET) and single-photon emission computed tomography (SPECT) are molecular imaging approaches that measure certain brain metabolism, such as blood flow, glucose and dopamine levels, using short-lived radioisotope agents (Zimmer and Luxen, 2012). PET and SPECT do not interface with TMS and have much less space limitation in the scanner (Paus *et al.*, 1997; Paus and Wolforth, 1998) when compared to fMRI. As such, most of earlier (back to 1990s) applications of concurrent neuroimaging and TMS were using PET and SPECT (Tremblay *et al.*, 2020). For example, the investigation on the blood flow fluctuation and its relationship to stimulation dose induced by 3Hz TMS trains (Fox *et al.*, 2006); blood flow changes during rTMS modulation of the cortical excitability and the temporal effects of it on baseline blood flows (Paus *et al.*, 1997, 1998; Siebner, Takano, *et al.*, 2001); and the corresponding glucose metabolism (Siebner, Peller, *et al.*, 2001; Kimbrell *et al.*, 2002); release of dopamine in the basal ganglia following frontal stimulation (Strafella *et al.*, 2003). However, the exposure to radiation in PET and SPECT limited the number of such applications (Siebner *et al.*, 2009). Another limitation is the poor temporal resolution of PET and SPECT mainly allowing one or very few "snapshots" in time of the underlying metabolism.

Using sources and detectors of infra-red light placed on the scalp, functional Near-Infrared Spectroscopy (fNIRS) is another noninvasive functional neuroimaging modality (Jöbsis, 1977; Scholkmann, Kleiser, *et al.*, 2014), which allows monitoring changes in oxy- and deoxy-hemoglobin (i.e., HbO/HbR) in the cerebral cortex, with higher temporal resolution than fMRI. Since it relies on the optical signal, TMS pulse does not introduce interferences. In general, this advantage allows the implantation of concurrent TMS and fNIRS much more straightforwardly than other modalities mentioned above. Similar to EEG, fNIRS acquisition is often performed with a cap, which does not limit the space for coil placement when stimulating different cortical areas. Finally, as introduced in Chapter 1, fNIRS bring more insights into the hemodynamic responses

by measuring both HbO and HbR concentration changes. This grants TMS/fNIRS the ability to provide more information when investigating stimulation effects on hemodynamics. However, there are still some challenges for combining TMS and fNIRS as summarized as follows.

Alike EEG electrodes which often have a low profile design (flat and thin), some fNIRS optodes are designed to be vertical to the scalp (as shown in Fig.2.6a and b) for the purpose of either 1) providing extra space for installing springs to push optodes towards the scalp, thus increasing signal quality; or 2) integrating light-emitting diode (LED) source directly inside the optodes. These optodes will increase the distance from TMS coil to the scalp when stimulating right on top of the region of interest probed by fNIRS.



Fig2.6 NIRS optodes from different commercial products. Vertical optodes design in a) NIRx (NIRx Medical Technologies, LLC, US) cap <https://nirx.net/nirscaps/> and b) Shimadzu (Shimadzu Corp., Japan) NIRS cap <https://shop.neurospec.com/shimadzul>; low profile NIRS optodes design in c) Brainsight (Rogue Research, Inc, Canada) NIRS cap <https://www.rogue-research.com/nirs/> and the same optodes used in Chapters 6 and 7 but installed with Collodion (Yücel et al., 2014; Pellegrino, Machado, et al., 2016; Machado et al., 2018) shown in d).

The relationship of coil-scalp distance and the stimulation electric field strength was investigated by Stokes et al., 2013, as shown in Fig.2.7a, the stimulation electric field strength decreased dramatically along with increased coil-scalp distance to the motor and visual cortical. In the meantime, the motor threshold (MT) (Rossini et al., 1994) and the phosphene threshold (PT)

(Abrahamyan *et al.*, 2011) used for motor cortex and visual cortex stimulations, respectively, increased with larger distances, shown in Fig.2.7.b.

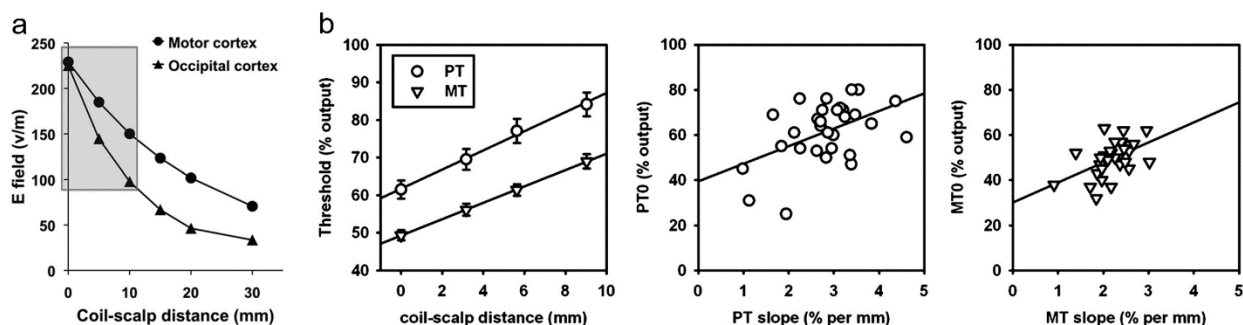


Fig2.7 Relationship between TMS coil to scalp distance and stimulation strength. a) TMS stimulation electric field strength as a function of coil-scalp distance measured when stimulating motor cortex and visual cortex. b) the motor threshold (MT) and the phosphene threshold (PT) used for motor cortex and visual cortex stimulations as a function of coil-scalp distance. Stimulation threshold at the scalp surface (denoted as MT0 and PT0) as a function of distance effect slope. Each circle (PT) and triangle (MT) represents a subject. Figure adapted from Stokes *et al.*, 2013.

Therefore, a higher stimulation dose is necessary when applying TMS/fNIRS with NIRS optodes that are not low profile. For instance, the coil-scalp distance was even up to 15mm in Kozel *et al.*, 2009, which requires high stimulation dose among 12 subjects - $95\% \pm 5\%$ (mean \pm sd) to the machine's maximum intensity, when compared to TMS only study (Stefan, 2000) in which the group level stimulation intensity was only $44\% \pm 6\%$ the maximum stimulator output (note that although this may vary from stimulator to stimulator, the general increase of the stimulation intensity is indeed considerable). To overcome this limitation, concurrent TMS/fNIRS approaches were categorized into two sets shown in Fig2.8 a and b, namely proximal and distal set-up proposed by Parks, 2013. Distal set-up (see in Fig.2.8b) means although the stimulation and fNIRS acquisition are conducted at the same time, the coil is placed away from the stimulation area seen in Nissilä *et al.*, 2002; Mochizuki *et al.*, 2007. Such an approach measures the hemodynamic response evoked in the cortical region that is functionally connected to the stimulation region. Whereas proximal set-up (see in Fig.2.8a) places the TMS coil directly on top of optodes. It could measure the TMS effects directly instead of indirectly informed by connectivity. Specially designed montage or optodes is then required. For instance, in Fig.2.8c optodes are placed in the empty space around the coil used by Noguchi, Watanabe and Sakai, 2003; Hada *et al.*, 2006; Mochizuki *et al.*, 2006; Furubayashi *et al.*, 2013; Groiss *et al.*, 2013; or as shown in Fig.2.8d,

optodes are right under the coil which requires low profile design used in the works of Näsi *et al.*, 2011; Thomson *et al.*, 2011, 2012, 2013. For this thesis, all fNIRS experiments were conducted with Brainsight NIRS machine (Rogue-Research Inc, Montréal, Canada), which uses low profile optodes by default (see Fig.2.5c). Moreover, we also applied clinical adhesive – collodion to glue the optodes on the scalp to ensure the tight contact of them, which resulted in only a small coil-scalp distance (~5mm) shown in Fig.2.5d.

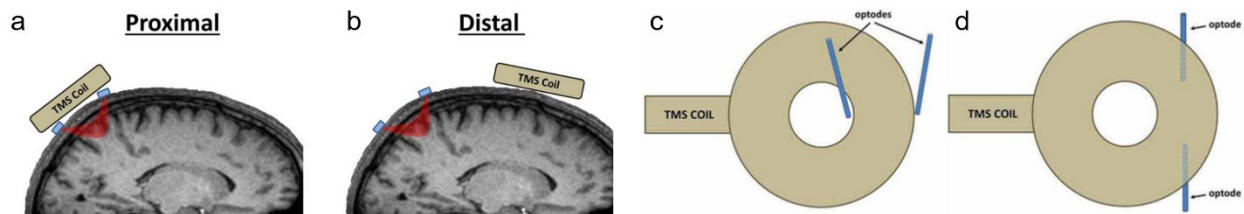


Fig2.8 Concurrent TMS and fNIRS acquisition set-up and optodes design. a) proximal set-up places the TMS coil directly on top of optodes b) distal set-up places the TMS coil away from the NIRS montage, the stimulation region is often functionally connected to the cortical region probed by NIRS, therefore, indirectly measure the stimulation effects. c) vertical optodes can be placed in the empty space around the TMS coil to allow small coil-scale distance. d) low profile designed optodes can be installed right under the TMS coil only lifting up it a small distance. Figure adapted from Parks, 2013

Although fNIRS signal is electromagnetic artifacts free, TMS indeed causes other artifacts that could be captured by fNIRS. These artifacts are often caused by 1) systemic physiological noise; 2) vascular contraction; 3) skeletal muscle contraction and 4) cortical sensory responses. Firstly, TMS could induce systemic circulatory changes (Mesquita *et al.*, 2013; Cabrerizo *et al.*, 2014) such as the amplitude of Photoplethysmographic (PPG) pulse waveforms, the pulse transit time and blood pressure. These circulatory changes could then influence the fNIRS signal measured at the same time (Kirilina *et al.*, 2012; Tong *et al.*, 2012, 2013; Erdoğan, Yücel and Akin, 2014). Then, smooth muscle walls of blood vessels could be contracted by TMS, such contraction may cause local blood volume changes lasting few seconds (Näsi *et al.*, 2011), therefore, introducing confounding to hemodynamic responses of the stimulation per se. Thirdly, magnetic pulses of TMS could also induce muscle contractions in the scalp (Mäki and Ilmoniemi, 2011). Such contraction would introduce two kinds of artifacts in fNIRS measurement, one is the local scalp blood volume changes that could be detected by fNIRS (Jaszewski *et al.*, 2003; Boden *et al.*, 2007), the other is the local motion that induces motion artifact in fNIRS signal. Finally, the ‘click’ sound of TMS and muscle contractions mentioned above could induce auditory and sensory

responses (Freche *et al.*, 2018; Salo *et al.*, 2020), respectively, along the cortex. These responses may directly introduce confounding by measuring the corresponding cortical area using fNIRS or indirectly bring confounding via underlying brain networks which involve the corresponding cortical area and the region of interest probed by fNIRS. Näsi *et al.*, 2011 demonstrated fNIRS signal confounded by these artifacts by comparing the TMS/fNIRS experiment conducted on the motor cortex and shoulder. High temporal correlation (Pearson's correlation ranging from 0.65 to 0.87) of hemodynamic response induced by TMS on the motor cortex and shoulder remind us to carefully denoise the TMS induced artifact in fNIRS.

Fortunately, several fNIRS denoising techniques have been proposed throughout the last decades. From the study design point of view, one can introduce long jitters between TMS events or even totally randomized stimulation pulses delivery, and then combine with simple trial averaging or deconvolution (Aarabi, Osharina and Wallois, 2017) to minimize non-phase locked artifacts such as systemic circulatory changes. Without introducing extra measurements for differentiating artifacts, one can apply simple regressions to denoise systemic physiological noise by using the global averaged fNIRS signal (Haeussinger *et al.*, 2014) as the regressor or applying a principal component spatial filter algorithm proposed by Zhang, Noah and Hirsch, 2016; Zhang *et al.*, 2017. In addition, so-called short distance (~5mm between source and detector of fNIRS montage) channels, allow better estimation of the local fluctuations within the scalp and regress it out from the normal distance channels, which are the mixture of cortical hemodynamic and superficial physiological noise (Zeff *et al.*, 2007; Gregg *et al.*, 2010). This approach helps in removing the TMS events phase-locked artifacts, and global physiological noise. A specially designed peripheral device measuring the low frequency blood flow oscillation placed on ear lobe(s) or finger(s) can be utilized to estimated more accurate systemic physiological noise (Tong *et al.*, 2012, 2013; Sutoko *et al.*, 2019) which can then be removed using recently developed general linear models (GLM) which involves artifacts regressions (von Lüthmann, Li, *et al.*, 2020; von Lüthmann, Ortega-Martinez, *et al.*, 2020). Finally, one can apply fNIRS reconstructions with a mixed forward model, which consists of superficial physiological in the scalp and cortical hemodynamics (Shimokawa *et al.*, 2012; Yamashita *et al.*, 2016a).

2.3.3 Hemodynamic responses evoked by spTMS

Taking advantage of the high temporal resolution of fNIRS, spTMS evoked hemodynamic responses can be measured when applying concurrent TMS/fNIRS acquisitions. spTMS on the left motor cortex significantly increases HbO with a stimulation intensity of 90% and 110% RMT (Noguchi, Watanabe and Sakai, 2003). Increases of HbO were found when contracting the right first dorsal interosseous muscle and delivering spTMS with 100% AMT by Mochizuki *et al.*, 2006. On the other hand, decreases of HbR were detected when the muscle was relaxed at rest and stimulating the left primary motor cortex at 120 and 140% AMT. Finally, significant increases of HbO after spTMS with intensities of 100%, 120 and 140% AMT at left M1 were reported by Furubayashi *et al.*, 2013.

Similar investigations were conducted on dorsal-lateral pre-frontal cortex (DLPFC), considering the application of TMS for the treatment of depression. Thomson *et al.*, 2011 studied the hemodynamic responses of spTMS delivered at the left DLPFC with intensities of 90%, 100% and 130% RMT; in contrast to the results on M1, a significant decrease of HbO was found with the highest dose. This observation was reproduced in Thomson, Daskalakis and Fitzgerald, 2011, showing significant decreases of HbO using 120% RMT intensity when comparing with a lower dose case (70% RMT). No differences were found when comparing spTMS and two sets of short (2ms or 15ms) inter stimulus interval (ISI) paired pulses. The same group reproduced this result again when rotating the TMS coil to be 135° to the middle headline (Thomson *et al.*, 2013) and did not find significant HbO changes with a 45° scenario. In the end, spTMS at 110% RMT did not induce considerable hemodynamic responses showed by Curtin *et al.*, 2017. All these studies seem to provide conflicting results when comparing M1 and DLPFC stimulations. These might indicate that spTMS elicited hemodynamics are region specific. However, none of these studies utilized the denoising approaches mentioned in the previous subsection, meaning that the conclusions might have been biased due to the systematic physiological noise or local muscle and vessel contractions.

2.3.4 Effects of excitability modulations on hemodynamic responses

Instead of spTMS, investigations on hemodynamic responses during or after cortical excitability modulations using TMS sequences may bring more insight into understanding the mechanism of neurovascular coupling and brain plasticity. Oliviero *et al.*, 1999 applied for the first time 2 minutes of 0.5Hz rTMS on the right M1 and found significant increases in HbO and decreases in

cytochrome oxidase. A more comprehensive investigation (Hada *et al.*, 2006) using pairwise combinations of two stimulation intensities (80% and 120% RMT) and frequencies (0.5Hz and 2Hz) on the left M1 showed decreased HbO lasting 60s and nonchanged HbR after all 4 interventions scenarios. A distal set-up study (Mochizuki *et al.*, 2007) found that excitatory theta burst stimulation (TBS) evoked HbO decreases in the contralateral side (right M1) of the stimulation, which was then reproduced by Kozel *et al.*, 2009 on both ipsilateral and contralateral side using inhibitory rTMS (1Hz). This result was further investigated on test-retest reliability by the same group (Tian *et al.*, 2012), reproducing similar observations from two rTMS sessions separated by 2 to 3 days. Total hemoglobin concentration changes (i.e., HbT = HbO+HbR) were observed decreasing in bilateral M1 when stimulating left M1 using 8s rTMS at three different frequencies (0.5, 1, and 2 Hz) at 75% RMT (Näsi *et al.*, 2011). The largest decrease was found at the highest stimulation frequency. Hirose *et al.*, 2011; Groiss *et al.*, 2013 applied both excitatory and inhibitory quadripulse rTMS (QPS), inducing bidirectional excitability modulations over the left M1. Decreases of HbO were found in the right M1 for both excitatory and inhibitory QPS (Hirose *et al.*, 2011); and in the left M1 for the excitatory case. In contrast to all these findings, both increased HbO and cerebral metabolic rate of oxygen consumption ($CMRO_2$) were observed ipsilaterally during inhibitory rTMS (1Hz) in Mesquita *et al.*, 2013. This is supported by another study (Park *et al.*, 2017) in which similar results were found in contralateral side of the inhibitory rTMS intervention.

Inconsistent results were also illustrated in studies modulating the excitability of DLPFC. For inhibitory rTMS at 1Hz, decreased HbO were found ipsilaterally with stimulation intensity using 120% (Thomson *et al.*, 2012) and 110% (Cao *et al.*, 2013) of RMT, respectively; contralateral in Hanaoka *et al.*, 2007 and Aoyama *et al.*, 2009 using 50% and 58% of resting MT, respectively; and bilaterally in Kozel *et al.*, 2009 using 120% of RMT. In contrast, Thomson *et al.*, 2013 reported bilaterally increased HbO when conducting 1Hz rTMS at 120% of RMT intensity and non-significant HbO changes using 120% of RMT (Thomson *et al.*, 2012). In excitatory rTMS studies using 110% of RMT, Cao *et al.*, 2013 and Curtin *et al.*, 2017 found bilaterally and ipsilaterally increased HbO, respectively. Similar results were obtained by Shinba *et al.*, 2018 when stimulating with 110% of RMT.

It is interesting to notice three points when summarizing these studies, 1) all of them involved a small sample size, the number of subjects ranges from 4 to 17 with a mean of 11 and a standard

deviation of 3. This may explain inconsistent findings since the combination of a small sample size and statistical significance test often leads to this issue, which will be further discussed in Chapter 3. It is also one of the main motivations of Chapter 7, in which Bayesian data analysis was applied to deal with this issue and attempted to make more reliable inferences; 2) only three studies reported HbR results. In Chapters 6 and 7, we indeed not only reported HbO and HbR results, but the observations on them were also consistent; and 3) stimulation intensity varies from study to study, and higher stimulation intensities might provide more observable effects. This was confirmed in Chapter 7 without conducting an experiment using different intensities but inferred from probabilistic modelling.

2.3.5 TMS effects on task evoked hemodynamics

As we investigated in Chapters 6 and 7, several studies aimed to reveal the effects of TMS interventions on task hemodynamic responses. The first work was conducted on motor task-related hemodynamic response and resting state. Increases of HbO lasting 40 minutes after inhibitory rTMS were found in the contralateral M1 of the stimulation site (Chiang *et al.*, 2007). Significantly increased HbO measured on the frontal lobe was observed when conducting a match-to-sample task under the condition that the right parietal cortex was excited by 5Hz rTMS (Yamanaka *et al.*, 2010). Tupak *et al.*, 2013 showed bilaterally reductions of emotional stroop task-evoked HbO after the inhibitory continuous theta burst stimulation (cTBS) applied on the left DLPFC. Another inhibitory cTBS applied on the right-DLPFC showed reduced HbO during dictator game in the right DLPFC comparing to sham (Maier *et al.*, 2018). In the end, decreased HbT was reported bilaterally in DLPFC when performing a cognitive task (i.e., speed of processing) after both excitatory rTMS and intermittent theta burst stimulation (iTBS), indicating increased efficiency of task performance. In Chapters 6 and 7, using PAS interventions and a finger tapping task, we found that enhanced excitability corresponds to higher hemodynamic activity and vice versa. It is of interest to notice that, for the first time, we demonstrated the results in this topic using NIROT (mentioned in Chapter 1), which provided spatiotemporal reconstruction maps of both HbO and HbR, rather than channel space analysis involved in these studies.

2.4 Summary

This chapter first introduced one of the principles of neuronal plasticity - STDP. We then reviewed the TMS related techniques on modulating human brain cortical plasticity noninvasively and

mainly focused on PAS which was used in Chapters 6 and 7. Our motivation for using PAS was explained in the meantime by briefly summarizing these commonly used TMS protocols. The followed reviews on the challenges and advantages of combining TMS and neuroimaging modalities introduced our rationale for applying TMS/fNIRS in this thesis. Finally, a literature review on TMS/fNIRS brought the general methodology development and findings on this topic, therefore, emphasizing the originalities and contributions of our works in Chapters 6 and 7.

Chapter 3

Introduction of Bayesian Data Analysis

This chapter will introduce fundamental aspects of Bayesian data analysis. It is a complete workflow, not only conducting appropriate statistical inferences of scientific research results, but also a true implementation of the “hypothesis-driven” philosophy into the whole research process from study design to data analysis and final inferences. Bayesian modeling explicitly addresses problems of small sample size and large variability of the data, which often exist in non-invasive human brain studies but are rarely carefully taken into account.

Bayesian is the principle of the MEM reconstruction introduced in Chapter 1 and was also the key approach in data analysis presented in Chapter 7. In this state of the art chapter, we introduce the workflow of Bayesian data analysis as follows: 1) the principle of Bayesian framework, which is Bayes’ theorem and probability modeling; 2) posterior sampling methodologies, describing several technical evolutions of corresponding implementation strategies; 3) diagnostics of the posterior distribution sampling to evaluate the accuracy and reliability of Markov chains; 4) statistical inferences using Bayesian framework and a brief comparison with the conventional frequentist approach, i.e., statistical significance hypothesis tests.

Last but not least, as Bayesian data analysis is not often seen in publications of our field, this chapter also attempts to clarify some misunderstandings and update our views on the latest Bayesian methodologies.

3.1 Probabilistic modeling

When statistically inferring a research finding, the Bayesian approach uses probability to quantify underlying uncertainty. According to the general Bayesian data analysis workflow (Gelman *et al.*, 2013a, 2020), there are mainly three steps involved,

- 1) **Probabilistic modeling**: constructing a full probability model which encapsulates the scientific problem, data collection process, and observable/unobservable variables using Bayes’ theorem.
- 2) **Estimating the joint posterior distribution**: conditioning the probabilistic model by the observed data and solving the posterior distribution of each parameter using analytical or numerical resolutions.

3) *Evaluating the model fitting and inferring results*: assessing how reliable the model fitting is and answering the research questions using Bayesian inferences.

This section will introduce the first step regarding probability modeling. Since this is a comprehensive topic, we will only focus on the techniques applied in this thesis, especially in Chapter 7.

3.1.1 Bayes' rule

In the 18th century, an English mathematician Thomas Bayes (1702-1761), proposed his famous conditional probability theory based on physical simulations of the probability theory, known as Bayes' rule (Thomas and Laplace, 1763). Here is a brief and simplified derivation of it, let us denote the joint probability of two events A and B as $Pr(A, B)$, which can be expressed as,

$$Pr(A, B) = Pr(A)Pr(B|A) \quad (3.1)$$

where $Pr(A)$ is the probability of occurrence of event A, and $Pr(B|A)$ is the probability of event B to happen, given that event A has occurred, also denoted as the conditional probability of observing B knowing A has occurred. Similarly, the joint probability $Pr(A, B)$ can also be expressed as,

$$Pr(A, B) = Pr(B)Pr(A|B) \quad (3.2)$$

where $Pr(B)$ is the probability of occurrence for event B, and $Pr(A|B)$ is the conditional probability of event A to happen, knowing that event B has occurred. Combining equation 3.1 and 3.2 yields,

$$\begin{aligned} Pr(A)Pr(B|A) &= Pr(B)Pr(A|B) \\ Pr(A|B) &= \frac{Pr(A)Pr(B|A)}{Pr(B)} \end{aligned} \quad (3.3)$$

Therefore, the conditional probability, i.e., $Pr(A|B)$, can then be estimated using Bayes' rule presented in equation (3.3), i.e., from the conditional probability of B knowing A as well as the marginal probabilities of A and B. Unfortunately, this highly relevant work was not published in Bayes' lifetime.

Nowadays, when Bayesian data analysis is mentioned, it is not only referring to Bayes' rule, which is only the theory about conditional probability. Instead, it is considering the framework called Bayes' theorem (Gelman et al., 2013), which was independently rediscovered based on Bayes' rule (Thomas and Laplace, 1763) and extensively developed for real applications (Laplace, 1810) by a French scholar Pierre-Simon Laplace (1749-1827). This work is considered as the first "inversion of the probability" (Thomas and Laplace, 1763), which means solving the posterior distribution of parameter θ conditioned on the observed data y . In Bayes' theorem, the prior distributions of the unknown parameters are denoted as $p(\theta)$. The data distribution or likelihood, also known as sampling distribution, is defined as $p(y|\theta)$. The posterior distribution of interest, i.e., $p(\theta|y)$ of parameters conditioned on the observed data is then expressed as,

$$p(\theta|y) = \frac{p(\theta)p(y|\theta)}{p(y)} \quad (3.4)$$

where $p(y)$ is the average likelihood of the data over all possible values of θ . This expression looks similar to the conditional probability in equation 3.3. However, the breakthrough Laplace contributed to, which is now the core of the Bayesian framework, was the development of analytic tools for computing the numerator of equation 3.4. In practice, calculating the probability of $p(\theta|y)$ in a certain range given by $\theta \in [\theta_1, \theta_2]$, denoted as $Pr(\theta \in [\theta_1, \theta_2]|y)$, is equivalent of calculating the area under the joint probability density function. Thus, one needs to solve the following integral,

$$\int_{\theta_1}^{\theta_2} p(\theta)p(y|\theta)d\theta \quad (3.5)$$

In the original work of Bayes and Laplace, data distribution function $p(y|\theta)$ is describing the probability of a randomly thrown ball lands on the right side of the previous randomly thrown ball. It was modeled as a binomial distribution,

$$\begin{aligned} p(y|\theta) &= Bin(y|n, \theta) \\ &= \binom{n}{y} \theta^y (1 - \theta)^{n-y} \end{aligned} \quad (3.6)$$

Laplace solved the integral presented in equation 3.5 with two assumptions. First, a non-informative prior for parameter θ using a uniform distribution was applied, therefore, $p(\theta)$ is constant along the range $\theta \in [\theta_1, \theta_2]$. Second, the shape of the posterior density function was approximated by a normal distribution. The mean of this normal distribution is equal to the mode (i.e., maximum of probability density function) of the joint posterior distribution. In binomial case, the mode is $\hat{\theta} = y/n$. The variance of it was estimated from the curvature of the posterior distribution at mode location $\hat{\theta}$. Such an approach is known as the normal approximation and inspired other posterior approximation techniques categorized as the variational Bayesian (Gelman *et al.*, 2013a). These approaches are usually computationally efficient since they rely on an analytical solution – the parametric form of the joint posterior distribution is approximated by an assumed known distribution. However, these approximations may provide inaccurate and biased estimations of the posterior distribution, when the approximated parametric form is far from the underlying real joint posterior distribution.

In modern Bayesian data analysis (Gelman *et al.*, 2013a), $p(\theta|y)$ is numerically sampled from the joint posterior distribution $p(\theta)p(y|\theta)$ using Markov Chain Monte Carlo (MCMC) (Neal, 1993; Gelman *et al.*, 2013a), while omitting the normalization factor $p(y)$, therefore,

$$p(\theta|y) \propto p(\theta)p(y|\theta) \tag{3.7}$$

This approach will be introduced later in section 3.2. To summarize this subsection, as well as to address some common misunderstandings of Bayesian: the Bayesian framework is not only about utilizing the Bayes' rule. In fact, the conventional significant test approach also makes use of Bayes' rule in a specific manner, which will be mentioned later in section 3.4.2. The uniqueness of Bayesian is to use Bayes' theorem more generally, which is a combination of 1) prior distribution of parameters that are not or cannot be observed but can be assumed based on prior knowledge; 2) hypothesized associations between parameters and data, expressed by a probabilistic model; 3) posterior sampling and diagnostics and 4) inferences using posterior predictive simulations. We will introduce these important concepts in the following sections.

3.1.2 Modeling the association between data and parameters

Modeling is the mathematical expression of the association between parameters and data. There are various ways of constructing models, but two principles may be of interest to consider when applied in scientific research.

The first one is to apply a hierarchical structure, also called multilevel modeling. This is useful for studies in neuroimaging field, which attempt to infer both individual and group level effects. The underlying motivation of hierarchical modeling is all about how we can handle the variances of the data at the different levels of the analysis. Suppose we conducted an experiment on a group of subjects, and each subject went through several trials of the same experiment. The conventional statistics would analyze the trials of each individual first and then infer group-level effects by summarizing statistics among subjects. This approach has “amnesia” by assuming all subjects are unrelated (infinite between-subject variance), therefore, nothing can be shared between each subject, meaning no pooling of information. The other opposite way would be to put all trials together and summarize statistics directly, this time ignoring the heterogeneity of the subjects (zero between-subject variance), by completely pooling all the information from all subjects and all trials.

On the other hand, hierarchical modeling assumes that subjects share some common features, and heterogeneity also exists between them. This means between-subject variance is a finite number (neither infinite nor zero mentioned above), which is more realistic and is called partial pooling. Partial pooling allows the variance to propagate from lower levels to higher levels. The estimated group-level effects of the experiment are then more accurate and reliable since it respects the natural structure of the data. Moreover, since everything is encoded in one model and solved simultaneously, group-level information also helps to regularize individual-level inferences and vice versa. These features are critical for the neuroimaging field, in which between- and within-subject variability are often discussed but not always carefully modeled.

The second principle is to try to construct scientific models rather than general models. Every research question is unique and requires a bespoke (customized) model to encounter data that are collected differently and hypotheses that are assumed based on specific knowledge. This approach will also push us to think generatively, hence, the resulted inferences may be closer to the truth. One probable bad example in the neuroimaging field is the abuse of the General Linear Model (GLM) in some literature. A common and simple procedure is to consider all possible confounding factors as additional regressors (e.g., age, gender, cognitive test scores) into a GLM model and

claim that confounding effects are therefore regressed out. However, it will not disentangle the effect of confounding factors as expected but may rather result in biased inferences, since the underlying interactions are not considered. For instance, age value per se may not quantify the effect of age on the variable of interest. Therefore, simply adding age values as a regressor into the linear model assumes the age effects are linear and homogeneous along the age range, which is often not the case. Fortunately, the Bayesian framework suggests several modeling techniques addressing these issues. For instance, when looking for the effect of age, it can be modeled as an ordered categorical predictor when assuming the effect is consistent within several subranges of age. Bayesian inferences could then estimate the cut-off age points as hyperparameters. When assuming a nonlinear continuous effect of age, it can be modeled as an autoregressive (AR) model or using a specific kernel for a Gaussian process model.

Good examples of bespoke modeling are for instance studies in computational neuroscience (Sotero and Trujillo-Barreto, 2007; Jirsa *et al.*, 2017; Hashemi *et al.*, 2020) or calibrated fMRI (Hoge *et al.*, 1999; Gauthier and Hoge, 2012, 2013), modeling neuroimaging data or metabolism processes generatively, while involving scientific knowledge in the design, from animal or human published studies. They reflect the hypothesis of a specific research question. In most studies, we do not know the exact underlying relationship between quantities of interest, especially when using non-invasive measures of brain activity. However, multiple models can be constructed based on different hypotheses. Then we can compare the proposed models to find the one(s) offering the best trade-off between data fitting and predicting abilities. Actually, model comparisons can bring us much more insights into the research question than inferring any single model. Bayesian model comparisons could be of great interest when studying neuroimaging data, for instance, studies from our group assessing the correspondence between several modalities like EEG source imaging and fMRI responses (Daunizeau *et al.*, 2007; Grova *et al.*, 2008).

3.1.3 Weakly informative prior

Once a model is defined and data are collected, one needs to determine the prior distribution for each parameter to complete the probabilistic modeling. This aspect is actually the most misunderstood part of Bayesian, often criticized as being a “subjective” approach because of the use of priors. Debating whether any scientific approach is “subjective” or not will always bring circular because the definition of so-called “objective” is vague and inconsistent. This section will

introduce best practices in choosing priors while trying to clarify some of those misunderstandings from technical views.

Early Bayesian approaches were using the so-called “non-informative” priors. For instance, in Laplace’s work ([Thomas and Laplace, 1763](#)) mentioned in section 3.1.1, a uniform distribution was used as the prior. Since all possible values of a parameter will have the same probability in a uniform distribution, it is then considered as “non-informative”. In that sense, no new information is introduced and the approach is as “objective” as conventional approaches. If one only checks the mode (peak(s) in probability density function) of the posterior distribution, maximum likelihood-based optimization approaches will end up with the same results. However, Bayesian still contains the advantage of estimating the whole “posterior” distribution of the parameter rather than only its mode.

We often have some basic knowledge of the parameters included in a typical model. For instance, if the parameter is human height, at least we know it should be positive; it should have a mean and a finite variance. Such weak information could help us in selecting priors from known probability distributions, and then these priors can be referred to as “weakly informative” priors. How to choose the priors depends on the specific parameter of interest, but a general rule is to follow the concept of maximum entropy introduced in Chapter 1, when solving an ill-posed inverse problem. We just need to choose the distribution which has the maximum entropy, with respect to the knowledge constraints we could have. Then the prior would contain the highest uncertainty and would be as “objective” as possible. For instance, when assuming a parameter should contain real value and with finite variance, Gaussian distribution is the one that corresponding to maximum entropy. When assigning prior for a variance parameter (i.e., a scale), which should be a non-negative real number and has a unique mean, then exponential distribution is the one providing maximum entropy. When a parameter of interest is a binary event with a fixed probability (e.g., tossing a coin), Binomial distribution provides maximum entropy. Furthermore, one can introduce field-specific knowledge from the literature review to set reasonable values for parameters in prior distributions and to help the model regulating outliers. Such regulation is always more conservative than conventional arbitrary thresholding since the thresholding value itself will have a distribution to allow more or fewer outliers, and the further away from the value to the threshold, the lower plausible it will be.

If one is skeptical that the chosen prior is still too “subjective” or even tends to hack the expected results, one can perform the prior predictive simulation to assess the impact of the choice of a prior. The prior predictive simulation consists in simulating data using only the model and prior distributions, i.e., when considering no observed data. This is a purely generative process aimed at exploring the parameter values spanned by the model before introducing any observed data. Therefore, by comparing the distribution of such simulated data to some known knowledge, one can evaluate whether or not the priors are too informative and could eventually bias the results. In Chapter 7, we performed prior predictive simulation for linear regressions. We demonstrated that our choice of priors allowed us to span a large proportion of possible linear regressions (i.e., post-versus pre-PAS MEP to assess the effect of PAS), spanning actually more possibilities of regression lines than when considering arbitrary thresholding for outlier rejections. More importantly, when conducting such an approach, it forces us to do a comprehensive literature review of the research topic, and consider the variance of each parameter into the probabilistic model, rather than just discussing the variability of results as a limitation at the end of the study.

3.2 Estimation of the posterior distributions

Once probability modeling is complete, the next step will be the estimation of the joint posterior distributions by conditioning the model with observed data, which is a probabilistic model fitting procedure. This step is the most critical part of the Bayesian framework and requires significant efforts, especially on computation algorithms and power (not available decades ago). This is the main reason why the Bayesian approach was rarely considered in research applications during the 20th century. This section will briefly summarize the efforts that have been made throughout the history of the development of Bayesian and mainly focus on Hamiltonian Monte Carlo, which was used in Chapter 7.

3.2.1 Analytical solution

As mentioned previously in section 3.1.1, the original Bayesian approach proposed by **Thomas and Laplace, 1763** was an analytical resolution using the normal approximation. Instead of using the uniform distribution as prior (i.e., $p(\theta)$) in equation 3.4 proposed by Laplace, one can use a Beta distribution as the prior. It is proven that the resulted posterior density function $p(\theta|y)$ will have the same parametric form (i.e., Beta distribution) as the prior itself. This brings algebraic convenience and accuracy for the analytical solution, since $p(\theta|y)$ can be calculated in closed

form by knowing the exact parametric of the posterior distribution. Such an approach often relies on the property called conjugacy (Gelman *et al.*, 2013a), which means if the likelihood distribution $p(y|\theta)$ belongs to a certain distribution family \mathcal{F} , and the prior distribution $p(\theta)$ belongs to a certain distribution family \mathcal{P} , then the family \mathcal{P} is conjugate for \mathcal{F} when the resulted posterior distribution $p(\theta|y)$ satisfying the following expression,

$$p(\theta|y) \in \mathcal{P} \text{ for all } p(y|\theta) \in \mathcal{F} \text{ and } p(\theta) \in \mathcal{P} \quad (3.8)$$

There are several but not many known conjugate priors, mainly from the exponential family. For instance, Bata distribution is a conjugate prior for binomial likelihood; Gamma distribution is a conjugate prior for Poisson and exponential likelihood; normal distribution is a conjugate prior for normal likelihood. Therefore Beta, Gamma, and normal distributions are often used as priors traditionally in Bayesian models. The disadvantages of such analytical approaches are less flexibility regarding the choice of the prior especially introducing difficulties when dealing with multiparameter models.

3.2.2 Grid approximation

Without constraining the prior by a specific form for a particular likelihood distribution, it is impossible to solve the posterior distribution analytically. Therefore, numerical techniques are then required to approximate the analytical solutions. The most straightforward numerical approach, which is pedagogical to understand other more advanced approaches, is the grid approximation, also called grid sampling. The idea behind grid approximation is simple: although we cannot solve the continuous probability density function of each parameter, a finite grid of parameter values can be used to approximate its distribution. The algorithm for grid approximation can be summarized as follows (McElreath, 2020): 1) define the grid on probability value range $[0, 1]$ according to the preference of the resolution; 2) calculate the corresponding prior and likelihood values on each grid location; 3) calculate the posterior value by multiplying the prior and likelihood values; 4) normalize the resulted posterior by dividing the sum of all posterior values. The accuracy of this approach is highly influenced by the resolution of the grid. The more grid points we define, the more accurate the resulting posterior distributions will be. However, this approach may only work for models with very few parameters. For instance, if one proposes to sample the posterior with 100 grids, the required number of multiplications to compute for a model with N parameters will

then be N^{100} . It will more likely take “forever” to finish calculations for most real applications. Moreover, it is also tricky to set grid locations and resolution because the probability density function varies from parameter to parameter and the joint distribution is even more complicated. It is not easy to know which region in the probability range should be explored with more samples and sufficient density of the grid. This difficult issue can be explained by the following example: imagine one needs to sample a 1D Gaussian using 9 homogeneously distributed grid points shown on the top marginal distribution of Fig.3.1. The typical set, which contains the most probability density, of this 1D Gaussian would only be sampled by 3 grid points. Therefore the efficiency (i.e., the portion of points used for sampling the typical set over the total number of grid points) would only be $3/9 = 1/3$. This will become even worse when increasing the dimensionality of the model, for instance, in Fig.3.1, to sample a 2D Gaussian with the same resolution, one needs $9 \times 9 = 81$ grid points, whereas the typical set of this 2D Gaussian is only sampled from $3 \times 3 = 9$ grid points, resulting in an even lower efficiency $1/9$.

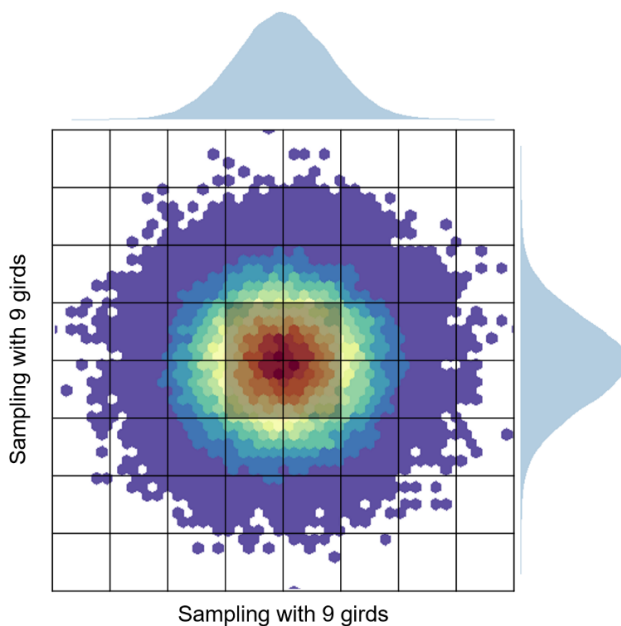


Fig.3.1 Demonstration of grid approximation for a 2D Gaussian distribution. Joint distribution density is shown in the middle as a heat map. Marginal density (blue) is illustrated on the side of each axis. A 9×9 grid is used to sample the joint distribution. The typical set of marginal density was sampled by only 3 grid points. The efficiency is even worse when sampling joint distribution, only 9 grid points (points in the black shade) were used, resulting in lower efficiency of $1/9$

The numerical approach and its limitation illustrated above are at the origin of the development of more advanced methods – sampling the joint distribution numerically along with high efficiency and accuracy.

3.2.3 Markov Chain Monte Carlo

Nowadays, the general approach used to sample the posterior probability distribution is called Markov Chain Monte Carlo (MCMC) (Robert and Casella, 1999; Brooks *et al.*, 2011). It is a stochastic process that explores the target probability distribution by so-called “random walk”. It randomly initiates a starting point of a Markov chain and then “random walk” through the target joint distribution by accepting/rejecting a proposal to move to the next randomly assigned new location. After a sufficient amount of iterations, the stationary distribution of the Markov chain is close enough to the target distribution. The proof of the convergence can be found in Chapter 11 of Gelman *et al.*, 2013.

Note that MCMC is a general approach. The actual algorithm used in Bayesian is called the Metropolis-Hastings algorithm. Before we briefly summarize the process in Table3.1, let us recall some essential notations: $p(\theta|y)$ is the posterior distribution, which is our target to sample by MCMC; θ is the parameter of the model, y is the observational data.

Table3.1 Process of Metropolis-Hastings algorithm.

Step 1. Initiate a starting point for parameter θ , denoted as θ^0 , the corresponding location of it on the posterior distribution $p(\theta|y)$ will be the starting point of a Marko chain. Note that this initialization needs to satisfy $p(\theta^0|y) > 0$.

Step 2. Define a so-called jumping distribution, $J_t(\theta^*|\theta^{t-1})$, that propose a randomly assigned new location for the chain to proceed at time $t - 1$, $t = 1, 2, 3, \dots, T$. * represents a proposal but not yet the actual next move of the chain.

Step 3. Randomly sample a θ^* according to $J_t(\theta^*|\theta^{t-1})$, therefore, the chain has a proposed location to move.

Step 4. Calculate the acceptance ratio of the proposal defined as $r = \frac{p(\theta^*|y)/J_t(\theta^*|\theta^{t-1})}{p(\theta^{t-1}|y)/J_t(\theta^{t-1}|\theta^*)}$

Step 5. Random sample a value $\alpha \in [0, 1]$ from a uniform distribution.

Step 6. Accept or reject the proposal by, $\theta^t = \begin{cases} \theta^*, & r \geq \alpha \\ \theta^{t-1}, & r < \alpha \end{cases}$, where θ^t is the next location for the chain to proceed.

Step 7. Repeat the above process with T iterations. Since the acceptance ratio r is related to $p(\theta^*|y)$, the higher the density of $p(\theta^*|y)$ the higher probability θ tends to stay at θ^* , the target posterior distribution $p(\theta|y)$ is then estimated by the probability density of θ among all locations θ^t .

Step 8. Launch several Markov chains with different initiations and mix them to get a stable estimation of $p(\theta|y)$

According to Step 4-6, the current state of a Markov chain is dependent on the previous one. Therefore, the samples are not always independent from each other. It is rather a lag-1 autocorrelation sequence (green trajectory in Fig.3.2). In fact, the accuracy and efficiency of a Markov chain are related to so-called effective samples that are independent from each other.

The other problem of the Metropolis-Hastings algorithm is the low acceptance ratio since the jumping proposal is randomly defined, and it is not guaranteed to jump to a higher density location on the target distribution. Computations times for rejected proposals will be wasted. Fig3.2 demonstrates the Metropolis-Hastings algorithm to sample a bivariate normal distribution. After 200 draws, it has not yet fully explored the target distribution. Actually, the first 500 samples are considered as a warm-up phase in which the Markov chain is still wandering outside the typical set of the target distribution. These samples are often discarded for final inferences. In the end, even with 1000 samples in Fig3.2 right column, the contrast (between the high-density region and low-density tails) of the 2D Gaussian is not well shown. This can be explained by the low proportion of independent samples.

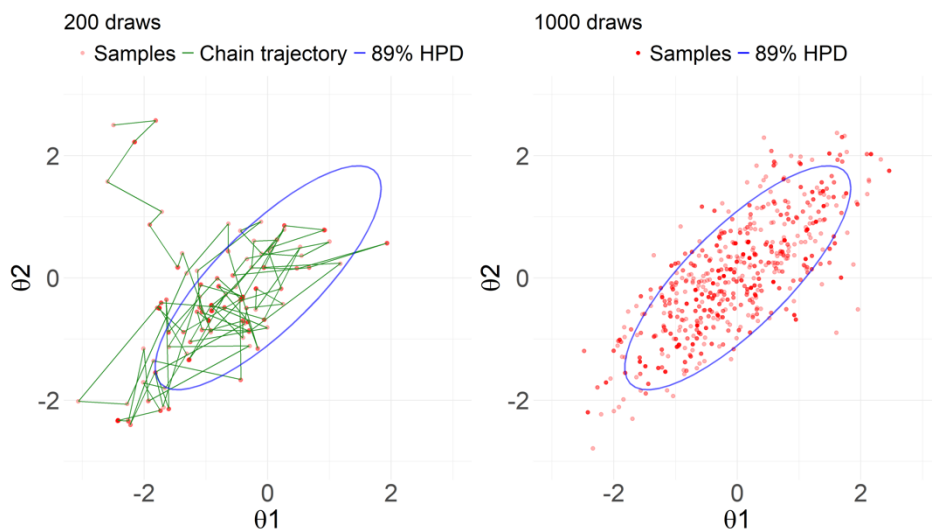


Fig.3.2 Demonstration of Metropolis-Hastings algorithm when sampling a bivariate normal distribution. The ground truth distribution is $(\theta_1, \theta_2) \sim \text{Normal}(0, 0.8, 1)$, meaning two 1D Gaussian distributions (mean=0, standard deviation =1) that have a correlation of 0.8. The blue ellipse covers the 89% Highest Posterior Density (HPD). One chain is conducted and the trajectory is shown with green bars. Each sample is represented by a red dot. The first column showed the first 200 draws from the initial point. The second column showed 1000 draws after removing the first 500 draws as the warm-up samples. Figures are produced from the adaption of the code in https://github.com/avehtari/BDA_course_Aalto

To solve the low acceptance ratio problem, one of the most famous MCMC algorithms called Gibbs sampling was proposed by [Geman and Geman, 1984](#); [Gelfand and Smith, 1990](#). It is actually a special case of Metropolis-Hastings algorithm which was implemented in the software package called Bayesian inference using Gibbs sampling (BUGS) ([Gilks, Thomas and Spiegelhalter, 1994](#); [Lunn et al., 2009](#)) that is not maintained anymore. Gibbs sampling allows high-efficiency jumps by replacing the jumping distribution, $J_t(\theta^*|\theta^{t-1})$ with the conjugate prior distribution introduced previously in section 3.2.1. It could be proved that doing so the resulted acceptance ratio will always equal to 1, therefore, accepting all jumps. However, using conjugate priors limits the number of parameters in the model, meaning the priors together may not be conjugate for the joint distribution condising all parameters rather than one of them. The solution is then to divide the parameters into few subsets in which conjugate priors are available. Then each subset of parameters will be sampled one by one from the conditional distribution of the other parameters. This is why Gibbs sampling is also called alternating conditional sampling. Fig3.3 illustrate the Gibbs sampling version of Fig.3.2, the alternating property is reflected by the fact that resulting

Markov chain trajectory is either horizontal or vertical, so sampling θ_1 (horizontal) and θ_2 (vertical) in an alternating way. The chain jumped to the typical set of the target distribution rapidly even if it was initialized around the boarder. This observation demonstrates the high acceptance ratio (almost every jumping proposal is accepted by Metropolis-Hastings algorithm in Table.3.1) of Gibbs sampling. It actually took only 50 samples to complete the warm-up phase. The 1000 sample draws in the right panel of Fig.3.3 also demonstrated better contrast of the estimated 2D Gaussian distribution.

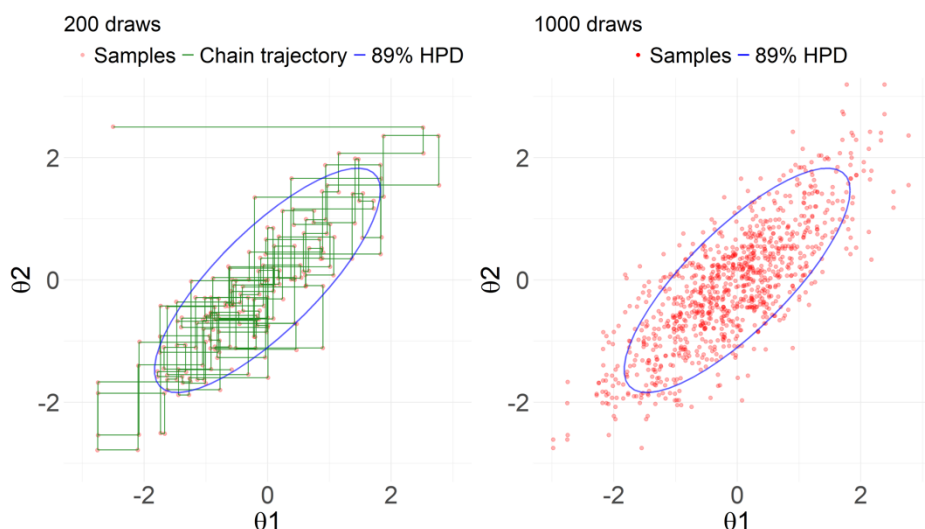


Fig.3.3 Demonstration of Gibbs sampling when sampling the same 2D Gaussian distribution in Fig.3.2. The first column showed the first 200 draws from the initial point. The second column showed 1000 draws after removing the first 50 draws as the warm-up samples. Figures are produced from the adaption of the code in https://github.com/avehtari/BDA_course_Aalto

However, Gibbs sampling is still a “random walk” approach and can only be efficient when sampling independent parameters one by one. Even though reparametrizing the model into subsets that are independent from each other may satisfy this requirement, the statistical concept called “concentration of measure” (McElreath, 2020) will push us to seek more advanced algorithms. This concept is based on the fact that the general goal when solving a model is actually about estimating the statistical expectation of each parameter. The statistical expectation is defined as $\int p(\theta)d\theta$, where $p(\theta)$ is the probability density function (PDF) of parameter θ . On one hand, the further a certain value of θ is to the mode of its PDF (i.e., peak(s) of PDF), the smaller $p(\theta)$ will be (see curve $p(\theta)$ in Fig.3.4). On the other hand, the corresponding $d\theta$ will become larger while θ is departing to the mode of its PDF, especially in a high dimensional space (see curve $d\theta$ in

Fig.3.4). For instance, the geometry of a 3D Gaussian distribution is a ball, then the unit volume ($d\theta$) increases while θ is departing from the mode (i.e., the center of the ball). Hence, the product of $p(\theta)$ and $d\theta$, which is the term $p(\theta)d\theta$ required to calculate the integral $\int p(\theta)d\theta$ for estimating the statistical expectation, is actually maximized as a trade-off between these two terms ($p(\theta)$ and $d\theta$) while increasing the distance ($\theta - \theta_{Mode}$) from a certain value of θ to the mode of its PDF (see curve $p(\theta)d\theta$ Fig.3.4). Therefore, the highest density of the statistical expectation of any parameter does not distribute around the mode of the corresponding distribution. Moreover, this observation is especially true when increasing the dimensionality of the model since the higher the dimensionality of the parameter space, the larger $d\theta$ will be while increasing the distance $\theta - \theta_{Mode}$. This is also the reason why nowadays maximum likelihood or optimization based point estimation is raising some concerns when dealing with high dimensionality models. All in all, these issues led the developers to sample the entire posterior at one time rather than part by part. This introduces the last algorithm, Hamiltonian Monte Carlo, described in the next section and applied in Chapter 7.

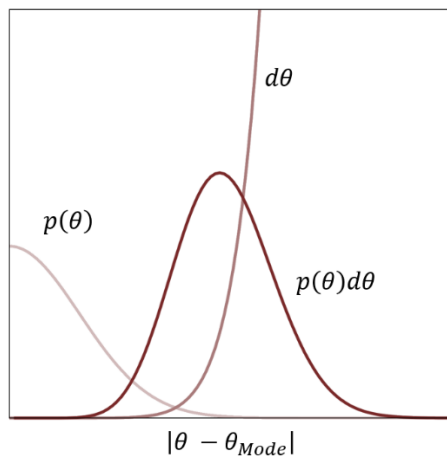


Fig.3.4 Demonstration of the concept called concentration of measure. The horizontal axis shows the distance, $\theta - \theta_{Mode}$, between a certain point on the probability distribution to the mode of it. Each line respectively represents the value of $p(\theta)$, $d\theta$ and $p(\theta)d\theta$ as a function of $\theta - \theta_{Mode}$. The figure is adapted from https://betanalpha.github.io/assets/case_studies/probabilistic_computation.html

3.2.4 Hamiltonian Monte Carlo

Hamiltonian Monte Carlo (HMC) algorithm (Duane *et al.*, 1987) is a brilliant idea to efficiently explore the target distribution with a high acceptance ratio and more independent samples. It

actually considers the target distribution as a physics model involving momentum and kinetic energy. To introduce how HMC works, we could use the toy example presented in Fig3.5a. The target distribution is still the same 2D Gaussian considered in previous sections. Each possible value of the distribution is considered as a coordinate in 2D space, and the log transformation of the density function is considered as a frictionless multi-dimensional surface that can be imagined as a bowl. Then, we assign “gravity” to space by putting the Earth in the center of the distribution (bottom of the bowl). If we initialize the kinetic energy and direction to a little ball (grey arrow in Fig.3.5), it will glide through the target distribution according to the gradient (reflected its corresponding “gravity”) on each location. In the end, the trajectory of the little ball (black curve) will actually follow the exact shape of the target distribution. In practice, the number and size of the sampling step (black dots in Fig3.5a) need to be predefined. It is preferred to enlarge the distance (green arrow) between the current sample and the next accepted proposal, meaning to have more steps in the trajectory (black dots). Therefore, HMC is a unique sampling framework resulting in more independent samples, because the distance from the current sample to the next one is large. However, inappropriate step size may result in the trajectory make a “U-turn” as shown in Fig3.5.b, in which the proposal will be too close or even overlaps with the current sample.

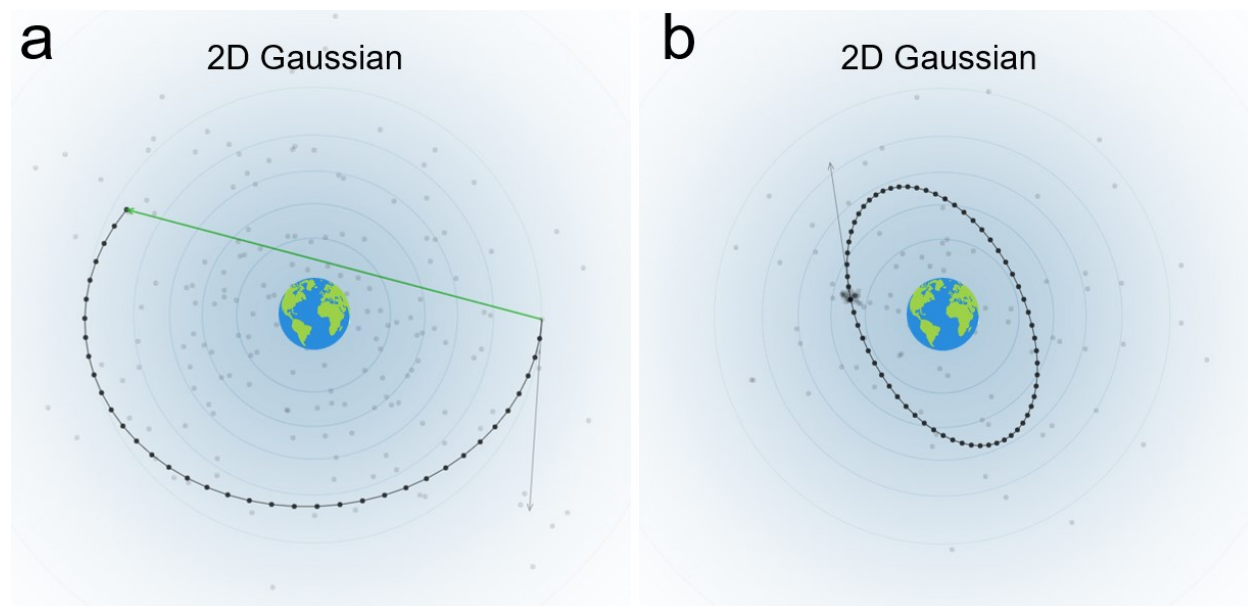


Fig.3.5 Demonstration of Hamiltonian Monte Carlo (HMC) algorithm. a) one sampling proposal made by HMC. The grey arrow showed the location of the current sample and the proposed direction of the kinetic energy to flick the little ball; the black curve illustrates the trajectory of this trial; the green arrow represents an accepted proposal (origin as the current sample and destination as the next sample). b)

demonstration of the problem called U-turn, in which the trajectory made a turn and coincidentally came back to the current sample. The chain will still work but become much less efficient. Simulation adapted from MCMC demos in <https://chi-feng.github.io/mcmc-demo/>

To avoid such circumstances and improve the efficiency of HMC, an advanced algorithm called No-U-Turn Sampler (NUTS) (Hoffman and Gelman, 2014) was developed to adaptively set the step numbers and size of the sampling in the warm-up phase, therefore, preventing the trajectory to make a U-turn. NUTS will launch two trajectories in opposite directions, and sample the posterior at the time when these two trajectories start turning around. This approach will prevent U-Turn, and in the meantime, make sure the distances between neighbor samples are relatively long, therefore, resulting in more independent samples in total. Fig3.6 illustrates this sampling strategy. In this example, NUTS is so efficient that it is actually explores the target distribution by following its exact shape, i.e., a donut, which will be quite challenging for Metropolis-Hastings algorithms. Finally, the most recent implementation of HMC, based on the idea of NUTS, is entitled dynamic HMC (Betancourt, 2017). Dynamic HMC was developed to replace the slice sampling approach with a multinomial sampling approach for each trajectory, therefore achieving massive improvement in the performance and accuracy.

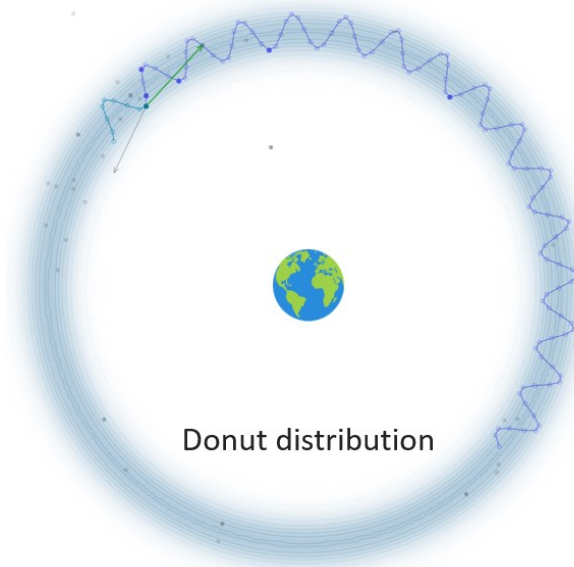


Fig.3.6 Demonstration of No-U-Turn Sampler (NUTS). A donut shape 2D distribution is the target distribution in this case. NUTS can detect when the sampling trajectory is turning and then sample right away. The proposal is not close to the current location, therefore allowing more independent samples.

HMC algorithm allows exploring this complex target distribution efficiently by following its shape. Simulation adapted from MCMC demos in <https://chi-feng.github.io/mcmc-demo/>

In practice, thanks to the drastic improvement in Bayesian data analysis workflow in the last decade, Bayesian inferences have become more accessible, and estimated posterior distributions are also becoming more accurate and reliable. NUTS and dynamic HMC are implemented in a Bayesian statistical modeling and computation platform called Stan (Stan Development Team, 2020b). Not only the functionalities of these samplers but also the diagnostic statistics (introduced in section 3.3) of the resulted HMC chains are provided in Stan, to allow accurate and reliable Bayesian data analysis. In Chapter 7, the R Version 4.0.3 (R Core Team, 2020) distribution of the Stan Probabilistic programming languages (Stan Development Team, 2020b) - RStan package Version 2.21.2 (Stan Development Team, 2020a) was used to program and solve the models with the advanced dynamic HMC.

3.3 Markov Chain Diagnostic statistics

Although sampling algorithms are evolving more efficiently nowadays, the target distribution to estimate may still be complex and challenging to sample. Therefore, diagnostics of the sampling process is a crucial step for evaluating the accuracy and eventual biases of the estimated posterior distributions. In this chapter, we introduce the diagnostic statistics proposed for MCMC sampling. Some of them were designed for general MCMC approaches, whereas others were specifically proposed for HMC.

3.3.1 General MCMC diagnostics

Convergence diagnostic consists in evaluating whether a Markov chain converges, which means the sampled distributions are close enough to the true target distribution. A common approach is to launch multiple chains initialized randomly and visualize if the traces of all chains mixed well, meaning each chain sequence achieves stationarity and no single chain looks different from others. Fig3.7 shows the traces of 4 chains mixed together. In the left column, all four chains mixed well so that none of them looks different and all chains reached stationarity, whereas in the right column, two chains (green and red curves) did not become stationary, and all chains did not mix well. Note that the term stationary means the range of θ value sampled by each chain is not changing while increasing the number of interactions, for instance, the θ values in the left figure stay in the range from -2 to 2 along the whole range of interactions.

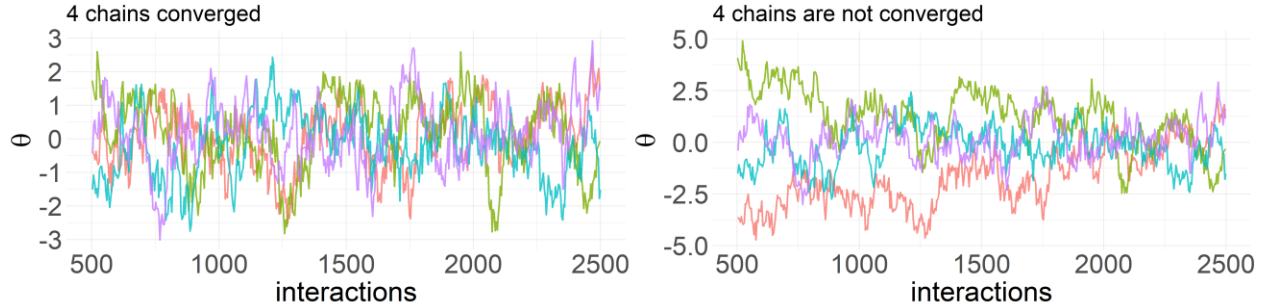


Fig3.7 Visualization of MCMC chain traces to diagnose convergence. Each color represents one chain trace. a) 4 converged chains showing homogenous explorations of the whole range of θ , and there is no obvious difference among all chains, indicating they mixed well, whereas in b) all 4 chains did not converge, each chain preferred to sample the values of θ that are only part of its full range.

Quantitative approaches have been proposed to assess chain convergence, for instance, the \hat{R} metric proposed by Gelman and Rubin, 1992; Brooks and Gelman, 1998. It calculates for each parameter as the ratio of between-chains variance over the within-chain variance,

$$\hat{R} = \sqrt{\frac{\frac{N-1}{N}W + \frac{1}{N}B}{W}} \quad (3.9)$$

where W and B are within- and between- chain variance, respectively and N is the number of samples per chain. In detail, the between-chains variance B is calculated as the standard deviation among all chains, and the within-chain variance W is represented as the weighted sum of the root mean square of the standard deviation within every single chain. If the chains mixed well, this ratio should be close to 1. \hat{R} would be larger than 1 if the chains did not mix well, indicating that one or more chain(s) did not converge. The recommended criteria for convergence is $\hat{R} < 1.05$. For more details of the latest version of \hat{R} estimation used in Chapter 7, i.e., split- \hat{R} , please refer to Vehtari *et al.*, 2020.

The other commonly used diagnostic metric is the effective sample size, i.e., N_{eff} , describing how many independent samples are drawn by chains. It is estimated by the following (Vehtari *et al.*, 2020),

$$N_{eff} = \frac{N}{1 + 2 \sum_{t=1}^{\infty} \rho_t} \quad (3.10)$$

where ρ_t is the estimated autocorrelation at lag t . When all samples are independent from each other, $\rho_t = 0$ at any lag, $N_{eff} = N$. There is no strict threshold for N_{eff} , but it is recommended to have at least 400 independent samples for each parameter (Vehtari *et al.*, 2020).

3.3.2 HMC diagnostic statistics

While sampling a “high curvature” target distribution, meaning the geometry of the parameter space contains areas that are not smooth, an inappropriate large step size could miss-sample these regions. The resulted samples of the target distribution will then be biased. This sampling issue is usually caused by the parameterization of the models, especially when involving multivariate and hierarchical structures. Parameters tend to be dependent from each other in these models, therefore, creating a “high curvature” geometry also called Neal’s Funnel (Neal, 2003), which is difficult to sample. Thanks to the fact that HMC was developed based on a physics model (Neal, 2010; Betancourt and Girolami, 2013), such issues will be diagnosed as “transition divergences”. This diagnostic is specific for HMC sampler, mainly invigilating the miss-match of the step size of the HMC chain (e.g., the resolution of the sampler) and the target distribution geometry. For example, when an overly large step size was assigned to a chain, it will “fly off” while approaching the “high curvature” region, and this pathological behavior can be indicated by infinite energies (Betancourt, 2017) and recorded by the algorithm. Note that reparameterization of the model into non-centred form could primarily reduce the chance of divergence, as we conducted in Chapter 7.

Poorly chosen parameters of the HMC can also decrease the efficiency or even result in the incomplete exploration of the target distribution, especially for distributions with heavy tails. This issue can be diagnosed again by taking advantage of the physics feature of HMC, comparing the marginal energy density (denoted as π_E) and the energy transition density (denoted as $\pi_{\Delta E}$) of the chain. One can visualize it by superimposing the histograms of π_E and $\pi_{\Delta E}$, the higher the efficiency, the more overlapping the two distributions will be. Such diagnosis analysis is also illustrated in Chapter 7. Quantitatively, the Energy-Bayesian Fraction of Missing Information (E-BFMI) (Rubin, 2004) has been proposed as a specific diagnostic for HMC sampler to evaluate the efficiency of the sampling process (Betancourt, 2016). Empirically, an E-BFMI value below 0.3 is considered problematic, please refer to (Betancourt, 2016, 2017) for more detailed explanations and the derivation of E-BFMI indices.

3.4 Bayesian Inferences vs. frequentist inferences

Statistical inferences of the research findings help us to evaluate how plausible an underlying hypothesis can be considered as true and how reliable the findings are. In this section, we will compare Bayesian inferences and conventional frequentist inferences.

3.4.1 Bayesian inferences

Bayesian inferences summarize the parameter in terms of probability conditioned on the observed data and regularized by prior knowledge. Since Bayesian models allow the estimation of the posterior probability distribution, one can then calculate any statistics of interest, such as the mean, variance and assess how plausible it is to have the parameter value within a specific range. Mathematically it can be proven that the uncertainty of the posterior, sd_{Bayes} , is lower than both the uncertainty of prior (sd_{prior}) and data (sd_{data}) as follows (Gelman, Hill and Vehtari, 2020),

$$sd_{Bayes} = \frac{1}{\sqrt{\frac{1}{sd_{prior}^2} + \frac{1}{sd_{data}^2}}} \quad (3.11)$$

Moreover, once the posterior distribution is known, one can estimate the uncertainty of any observed but also unobserved quantity of interest, by a given equation that describes the relationship between the unobserved quantity of interest and observed ones. This unique process is called posterior predictive simulations (Gelman *et al.*, 2013a; McElreath, 2020). It estimates the posterior distribution of any quantity of interest by predicting it via the fitted model and feeding new simulated data. For instance, in Chapter 7, we performed posterior predictive simulations to infer what is the probability distribution of cortical excitability changes of each intervention at both group and individual level; and what would have been the probability distribution of cortical excitability changes when increasing the intensity of TMS pulses if we would have reconducted the experiments. Such a process makes Bayesian inferences substantially flexible and unique, fully exploiting the posterior distributions learned from the observed data and the model. In the end, since it is based on probabilistic modeling, Bayesian inferences could also be updated by involving new real data to improve the estimation (i.e., Bayesian updating) and conveniently performing meta-analysis by sharing models and data between research groups. In terms of open science, it would also be much easier for communications because all we need to share is the model and prior, which encapsulate the hypothesis (prior knowledge) and data analysis, rather than descriptive

analysis pipelines that are difficult to reproduce (Eklund, Nichols and Knutsson, 2016; Botvinik-Nezer et al., 2020).

3.4.3 Comparison with frequentist inferences

Traditional statistical inferences, known as frequentist inferences, are based on only summarizing observed data features, without using priors. To estimate an accurate distribution, independent sampling of the data and a sufficiently large number of observations are required. The most applied frequentist technique in scientific research, especially in the neuroimaging field, is the statistical significance test, which was first proposed by Sir Ronald Fisher (Fisher, 1925, 1955) in the 20th century. It estimates the probability of an effect equal to or larger than a predefined value denoted as the null hypothesis. Since the accuracy of this estimated probability function to the true one is largely affected by the data sampling process and the number of samples, the reliability of the inference is then depends on the randomness of the data sampling and the number of data samples. To reject the null hypothesis, an arbitrary threshold - 95% is often considered (we usually report the type I error threshold so 5% as the probability of detecting an effect when data are following the null hypothesis distribution, i.e., probability of making a false positive error). According to the original work of Sir Ronald Fisher (Fisher, 1925), the selection of this threshold simply considers convenience. Therefore, there is no link of this threshold to a scientific conclusion. This approach achieved success in practice, especially in agriculture studies in which a large number of data samples could be collected; the experimental conditions could be precisely controlled such as the temperature, humidity, soil nutrition, and the experiment outcomes could be accurately quantified such as the plant height, width and the amount of productions.

Recently, many scientific fields are facing a replication crisis, including neuroscience and neuroimaging as reported in several studies (Craig M. Bennett et al., 2010; Carp, 2012; Eklund, Nichols and Knutsson, 2016; Botvinik-Nezer et al., 2020). It has been emphasized by the American Statistical Association (ASA) since (Wasserstein and Lazar, 2016) that the problem of applying significant tests is that they tend to overestimate the effect size in scientific research findings. Nature has published a comment article entitled “Retire statistical significance” (Valentin Amrhein, Sander Greenland, 2019), which gathered more than 800 signatories calls from scientists all over the world. The ASA conducted another special issue (Wasserstein, Schirm and Lazar, 2019) after (Wasserstein and Lazar, 2016) to highlight this problem and provided several

alternative statistical solutions including Bayesian inferences. More importantly, overestimated scientific findings could propagate through the literature reviews and study designs when conducting new projects. These claims remind us to embrace the variation that we cannot reduce, instead of claiming overestimated significant findings.

Arguing on the legitimacy of the statistical significance test was beyond the scope of this thesis, but we are referring here three inspiring points from statistical literature that may kindly remind us what are we concluding when referring to significance inferences,

- 1) With a large enough amount of samples, anything can be statistically significant when compared to a null hypothesis (Gelman, Hill and Vehtari, 2020). To illustrate this point, one can simply perform a simulation: let us draw 1000 samples from a normal distribution $\mathcal{N}(0.01,1)$, these samples are very noisy since the standard deviation is 100 times larger than the mean. Then we conduct a one sample t-test against 0 (i.e., null hypothesis). The resulted p-value is 0.33 indicating the test cannot reject the hypothesis that the true mean is 0. On the other hand, what if we draw 10,000 samples? Then the test will reject the null hypothesis with a p-value equal to 0.0004. Which experiment result is then true? The actual mean is indeed 0.01 according to our simulations. In fact, the effect size, the number of samples, and significance have a so-called “triangle association”, meaning significance can be achieved either by 1) large effect size and small sample size or 2) small effect size and large sample size.
- 2) The difference between “significant” and “not significant” is not itself statistically significant. This is actually the title of the paper published by Gelman and Stern, 2006. One can demonstrate this by an analytical calculation inspired by Gelman, Hill and Vehtari, 2020; McElreath, 2020: suppose two research groups did the same experiment independently, one found an effect of 15 ± 5 (*mean \pm standard error*) and the other obtained 5 ± 5 . The first one is results significantly larger than 0, while the second one is not. Then the difference between the two measures is characterized by 10 ± 7 , since the standard error of the difference between two independent sample sets is $\sqrt{5^2 + 5^2} \approx 7$. Therefore, the difference itself between these two results is not significantly different from zero. Then, if the idea of significant test is strictly followed, we may not want to differentiate the works for publication,

which showing either significant or non-significant results, because the difference between them may be statistically non-significant.

- 3) In section 3.1.1, we mentioned that the significance test approach also makes use of Bayes' rule in a specific way. Let us illustrate this point according to the original investigation (Ioannidis, 2005) and the example in Chapter 3 of McElreath, 2020. When one results in statically significant results, the probability of the corresponding conclusion being true, $Pr(true|sig)$, can be expressed as,

$$\begin{aligned} Pr(true|sig) &= \frac{Pr(sig|true)Pr(true)}{Pr(sig)} \\ &= \frac{Pr(sig|true)Pr(true)}{Pr(sig|true)Pr(true) + Pr(sig|false)Pr(false)} \end{aligned} \tag{3.12}$$

where “*sig*” represents the significant test being positive and “true” means the scientific hypothesis being true. $Pr(sig|true)$ is the probability of significant results conditioned on the true hypothesis, which is actually 0.95 when using the conventional significance threshold. $Pr(sig|false)$ is the false positive rate equal to 0.05 in this case. $Pr(true)$ is the probability of a true (correct) hypothesis being proposed, which is called the “base rate” (Ioannidis, 2005). When conducting the null hypothesis test with a randomly sampled large data set of a well-controlled experiment, we actually assumed $Pr(true) = 0.5$, since it is a binarized test saying whether the hypothesis is true or not. However, the base rate varies a lot in different fields and in general, it is much lower than 0.5. For instance, McElreath, 2020 suggested an empirical base rate of 0.01 in general. Let us assume an even higher base rate than 0.01, e.g., 1 out of 10 hypotheses is true, by substituting it into equation 3.12 with a power of 0.95 and a false positive rate of 0.05, $Pr(true|sig)$ would only be 0.68, meaning the probability of the corresponding conclusion being true is just about 68%. A more detailed demonstration curves of $Pr(true|sig)$ as a function of statistical power, false positive rate and base rate can be found in Ioannidis, 2005.

3.5 Conclusions

This chapter introduced the essential workflow of modern Bayesian data analysis. This workflow consists of 1) probabilistic modeling 2) posterior sampling 3) Markov chain diagnostic and 4)

Bayesian inferences. Probabilistic modeling is the key concept behind MEM reconstruction methodology for NIROT introduced in Chapter 1 and Chapter 4. The whole hierarchical Bayesian workflow was considered in Chapter 7 to handle TMS/NIRS data sets which often consist in small sample sized data and large between-/within-subject variances. When compared to conventional frequentist inferences, Bayesian has unique features, such as 1) the integration of observation and prior knowledge, 2) the estimation of the whole probability density function of the parameter of interest, 3) partial pooling to reduce the uncertainty of the estimation and 4) flexible statistical inferences using posterior predictive simulations. These advantages may bring more insights into analyzing data and inferring results for neuroimaging research.

Chapter 4

Manuscript 1: Diffuse Optical Reconstructions of Functional Near Infra-Red Spectroscopy Data using Maximum Entropy on the Mean

Context

As outlined in Chapter 1, fNIRS measures non-invasively fluctuations of both HbO and HbR in the human head with high temporal resolution (Jöbsis, 1977; Scholkmann, Klein, *et al.*, 2014). Conventional fNIRS data analysis considers so-called channel space analysis applying the mBLL, which makes strong assumptions on homogeneous concentration changes of hemoglobin within the underlying region(s) of interest, hence, inducing systemic errors in the estimations of HbO/HbR concentration changes (O’Leary *et al.*, 1995; Pogue *et al.*, 1995). NIROT has been proposed to provide more accurate estimations, since it does not assume such homogeneity and reconstructs the light intensity changes measured in the channel space along the underneath cortical area. The main technical challenge to conduct NIROT is to solve the inverse problem. It is ill-posed and requires specific regularization to obtain a unique solution. In the NIROT field, most studies are applying a linear reconstruction method – MNE based on Tikhonov regularization. It is well known in EEG/MEG source imaging field that MNE trends smearing the reconstruction maps and provides false positives outside the ground truth region (Ding, 2009). Our lab developed and carefully evaluated a non-linear reconstruction method – MEM, which was shown to provide accurate spatial reconstructions in the context of EEG/MEG source imaging, for several applications (Chowdhury *et al.*, 2016; Heers *et al.*, 2016; von Ellenrieder *et al.*, 2016; Hedrich *et al.*, 2017; Aydin *et al.*, 2020; Pellegrino *et al.*, 2020). In this study, our main objective was to adapt the MEM framework to conduct NIROT reconstructions. This adaptation required two original improvements of the MEM method per se: 1) the implementation of depth weighting in the MEM framework, to compensate potential biases caused by the large reduction of fNIRS sensitivity when increasing cortical depth; 2) the improvement of MEM temporal accuracy, allowing the investigation of fNIRS hemodynamic responses within a broader time window. The proposed new MEM version for NIROT was comprehensively validated using realistic simulations performed considering different true generator locations, sizes, and depths as well as under

different SNRs.

This manuscript is currently in revision in *Scientific Reports* journal, Zhengchen Cai, Alexis Machado, Rasheda Arman Chowdhury, Amanda Spilkin, Thomas Vincent, Ümit Aydin, Giovanni Pellegrino, Jean-Marc Lina, Christophe Grova. Diffuse Optical Reconstructions of Functional Near Infra-Red Spectroscopy Data using Maximum Entropy on the Mean. A preprint is also available on bioRxiv (Cai *et al.*, 2021).

Abstract

Functional near-infrared spectroscopy (fNIRS) measures the hemoglobin concentration changes associated with neuronal activity. Diffuse optical tomography (DOT) consists of reconstructing the optical density changes measured from scalp channels to the oxy-/deoxy-hemoglobin (i.e., HbO/HbR) concentration changes within the cortical regions. In the present study, we adapted a nonlinear source localization method developed and validated in the context of Electro- and Magneto-Encephalography (EEG/MEG): the Maximum Entropy on the Mean (MEM), to solve the inverse problem of DOT reconstruction. We first introduced depth weighting strategy within the MEM framework for DOT reconstruction to avoid biasing the reconstruction results of DOT towards superficial regions. We also proposed a new initialization of the MEM model improving the temporal accuracy of the original MEM framework. To evaluate MEM performance and compare with widely used depth weighted Minimum Norm Estimate (MNE) inverse solution, we applied a realistic simulation scheme which contained 4000 simulations generated by 250 different seeds at different locations and 4 spatial extents ranging from 3 to 40cm² along the cortical surface. Our results showed that overall MEM provided more accurate DOT reconstructions than MNE. Moreover, we found that MEM was remained particularly robust in low signal-to-noise ratio (SNR) conditions. The proposed method was further illustrated by comparing to functional Magnetic Resonance Imaging (fMRI) activation maps, on real data involving finger tapping tasks with two different montages. The results showed that MEM provided more accurate HbO and HbR reconstructions in spatial agreement with the main fMRI cluster, when compared to MNE.

4.1 Introduction

Functional near-infrared spectroscopy (fNIRS) is a non-invasive functional neuroimaging modality. It detects changes in oxy-/deoxy-hemoglobin (i.e., HbO/HbR) concentration within head

tissues through the measurement of near-infrared light absorption using sources and detectors placed on the surface of the head (Scholkmann, Kleiser, *et al.*, 2014; Yücel *et al.*, 2021). In continuous wave fNIRS, the conventional way to transform variations in optical density to HbO/HbR concentration changes at the level of each source-detector channel, is to apply the modified Beer Lambert Law (mBLL, Delpy *et al.*, 1988). This model assumes homogeneous concentration changes within the detecting region, i.e., ignoring the partial volume effects which indicate the absorption of light within the illuminated regions varies locally. This assumption reduces the quantitative accuracy of HbO/HbR concentration changes when dealing with focal hemodynamic changes (Boas, Brooks, *et al.*, 2001; Strangman, Franceschini and Boas, 2003).

In order to handle these important quantification biases associated with sensor level based analysis, diffuse optical tomography (DOT) has been proposed to reconstruct, from sensor level measures of the optical density, the fluctuations of HbO/HbR concentrations within the brain (Arridge, 1999). This technique not only provides better spatial localization accuracy and resolution of the underlying hemodynamic responses (Boas *et al.*, 2004b; Joseph *et al.*, 2006b), but also avoids partial volume effect in classical mBLL, hence achieves better quantitative estimation of HbO/HbR concentration changes (Boas, Brooks, *et al.*, 2001; Strangman, Franceschini and Boas, 2003). DOT has been applied to reconstruct hemodynamic responses in sensory and motor cortex during median nerve stimulation (Dehghani, White, *et al.*, 2009) and finger tapping (Boas *et al.*, 2004b; Yamashita *et al.*, 2016a); to conduct visual cortex retinotopic mapping (Zeff *et al.*, 2007; White and Culver, 2010; Eggebrecht *et al.*, 2012) and to simultaneous image hemodynamic responses over the motor and visual cortex (White *et al.*, 2009).

To formalize DOT reconstruction, one needs to solve two main problems. The first one is the forward problem which estimates a forward model or sensitivity matrix that maps local absorption changes within the brain to variations of optical density changes measured by each channel (Boas *et al.*, 2002b). The second problem is the inverse problem which aims at reconstructing the fluctuations of hemodynamic activity within the brain from scalp measurements (Arridge, 2011). The forward problem can be solved by generating a subject specific anatomical model, describing accurately propagation of light within the head. Such anatomical model is obtained by segmenting anatomical Magnetic Resonance Imaging (MRI) data, typically into five tissues (i.e., scalp, skull, cerebrospinal fluid (CSF), white matter and gray matter), before initializing absorption and scattering coefficients values for each tissue type and for each wavelength (Fang, 2010; Machado

et al., 2018). Solving the inverse problem relies on solving an ill-posed problem which does not provide a unique solution, unless specific additional constraints are added. The most widely used inverse method in DOT is a linear approach based on Minimum Norm Estimate (MNE) originally proposed for solving the inverse problem of Magnetoencephalography (MEG) and Electroencephalography (EEG) source localization (Hämäläinen and Ilmoniemi, 1994). It minimizes the L2 norm of the reconstruction error along with Tikhonov regularization (Boas, Dale and Franceschini, 2004; Zeff *et al.*, 2007; Dehghani, Eames, *et al.*, 2009; Eggebrecht *et al.*, 2012, 2014; Tremblay *et al.*, 2018). Other strategies to solve DOT inverse problem have also been considered, such as sparse regularization using the L1 norm (Süzen, Giannoula and Durduran, 2010; Okawa, Hoshi and Yamada, 2011; Kavuri *et al.*, 2012; Prakash *et al.*, 2014; Tremblay *et al.*, 2018) and Expectation Maximization (EM) algorithm (Cao, Nehorai and Jacobs, 2007). A non-linear method based on hierarchical Bayesian model for which inference is obtained through an iterative process (Shimokawa *et al.*, 2012, 2013a) has been proposed and applied on finger tapping experiments in (Yamashita *et al.*, 2016a).

Maximum Entropy on the Mean (MEM) framework was first proposed by Amblard, Lapalme and Lina, 2004 and then applied and carefully evaluated by our group in the context of EEG/MEG source imaging (Grova, Daunizeau, *et al.*, 2006; Chowdhury *et al.*, 2013). The MEM framework was specifically designed and evaluated for its ability to recover spatially extended generators (Chowdhury *et al.*, 2016; Grova *et al.*, 2016; Heers *et al.*, 2016; Pellegrino, Hedrich, *et al.*, 2016). We recently demonstrated its excellent performances when dealing with focal sources (Hedrich *et al.*, 2017) and when applied on clinical epilepsy data (Chowdhury *et al.*, 2018; Pellegrino *et al.*, 2020). In addition to its unique ability to recover the spatial extent of the underlying generators, we also demonstrated MEM's excellent accuracy in low SNR conditions, with the ability to limit the influence of distant spurious sources (Chowdhury *et al.*, 2016; Heers *et al.*, 2016; von Ellenrieder *et al.*, 2016; Hedrich *et al.*, 2017; Aydin *et al.*, 2020; Pellegrino *et al.*, 2020).

We believe that these important aspects should be carefully considered in the context of fNIRS reconstruction. The first one is the ability to accurately recover the spatial extent of the underlying hemodynamic activity for both focal and extended generators. The second one is to provide robust reconstruction results when data SNR decreases, especially when considering the fact that it is challenging to maintain a good intra-subject consistence using continuous-wave fNIRS due to its relatively low SNR (Chen *et al.*, 2020). Therefore, our main objective was to adapt the MEM

framework for fNIRS reconstruction and carefully evaluate its performance. Moreover, fNIRS reconstruction results tend to be biased towards more superficial regions, because the light sensitivity profile decreases exponentially with the depth of the generators (Strangman, Li and Zhang, 2013). To overcome this bias, we implemented and evaluated a depth weighted variant of the MEM framework.

The article is organized as follows. The methodology of depth weighted MEM for DOT is first presented. Then, we described our validation framework using realistic simulations and associated validation metrics. fNIRS reconstruction using MEM was compared with widely used depth weighted Minimum Norm Estimate (MNE) inverse solution. Finally, illustrations of the methods on finger tapping fNIRS data set acquired with two different montages from 6 healthy subjects are provided and compared with functional Magnetic Resonance Imaging (fMRI) results.

4.2 Material and methods

4.2.1 fNIRS reconstruction

To perform fNIRS reconstructions, the relationship between measured optical density changes on the scalp and wavelength specific absorption changes within head tissue is usually expressed using the following linear model (Arridge, 1999):

$$Y = AX + e \quad (4.1)$$

where Y is a matrix ($p \times t$) which represents the wavelength specific measurement of optical density changes in p channels at t time samples. X ($q \times t$) represents the unknown wavelength specific absorption changes in q locations along the cortex at time t . A ($p \times q$) is called the light sensitivity matrix which is actually the forward model relating absorption changes in the head to optical density changes measured in each channel. Finally, e ($p \times t$) models the additive measurement noise. Solving the fNIRS tomographic reconstruction problem consists in solving an inverse problem which can be seen as the estimation of matrix X (i.e., the amplitude for each location q at time t). However, this problem is ill-posed and admits an infinite number of possible solutions. Therefore, solving the DOT inverse problem requires adding additional prior information or regularization constraints to identify a unique solution.

In DOT studies, anatomical constraints can be considered by defining the reconstruction solution

space (i.e., where q is located) within the gray matter volume (Boas and Dale, 2005) or along the cortical surface (Huppert *et al.*, 2017; Machado *et al.*, 2021). In EEG and MEG source localization studies (Dale and Sereno, 1993; Grova, Daunizeau, *et al.*, 2006; Chowdhury *et al.*, 2013), it also is common to constrain the reconstruction along the cortical surface. In this study, the reconstruction space was considered as the mid surface defined as the middle layer between gray matter/pial and gray/white matter interfaces (Fischl *et al.*, 2002).

4.2.2 Minimum Norm Estimation (MNE)

Minimum norm estimation is one of the most widely used reconstruction methods in DOT (Zeff *et al.*, 2007; Dehghani, White, *et al.*, 2009; White *et al.*, 2009; White, 2010; Eggebrecht *et al.*, 2012, 2014; Yamashita *et al.*, 2016a). Such estimation can be expressed using a Bayesian formulation which solves the inverse problem by estimating the posterior distribution $P(X|Y) = P(Y|X)P(X)/P(Y)$ (i.e., the probability distribution of parameter X conditioned on data Y). A solution can be computed by imposing Gaussian distribution priors on the generators X ($P(X) = N(0, \Sigma_s^{-1})$) and the noise e ($P(e) = N(0, \Sigma_d^{-1})$). Σ_d is the inverse of the noise covariance which could be estimated from baseline recordings. Σ_s is the inverse of the source covariance which is assumed to be an identity matrix in conventional MNE.

The Maximum a Posteriori (MAP) estimator of the posterior distribution $P(X|Y)$ can be obtained using maximum likelihood estimation:

$$\begin{aligned} \widehat{X}_{MNE} &= \operatorname{argmin}(\|(Y - AX)\|_{\Sigma_d}^2 + \lambda\|X\|_{\Sigma_s}^2) \\ &= (A^T \Sigma_d A + \lambda \Sigma_s)^{-1} A^T \Sigma_d Y \end{aligned} \quad (4.2)$$

where \widehat{X}_{MNE} is the reconstructed absorption changes along the cortical surface. λ is a hyperparameter to regularize the inversion using the priori minimum norm constraint $\|X\|_{\Sigma_s}^2$. In this study, we applied the standard L-Curve method to estimate this λ as suggested in (Hansen, 2000).

4.2.3 Depth weighted MNE

Standard MNE solutions assumes $\Sigma_s = I$, which then tends to bias the inverse solution towards the generators exhibiting large sensitivity in the forward model, therefore the most superficial ones (Fuchs *et al.*, 1999). When compared to EEG/MEG source localization, such bias is even more

pronounced in fNIRS since within the forward model light sensitivity values decrease exponentially with the depth (Strangman, Li and Zhang, 2013). This bias can be compensated by scaling the source covariance matrix such that the variances are equalized (van der Sluis, 1969; Fuchs *et al.*, 1999). In the context of DOT, depth weighted MNE has been proposed by (Culver *et al.*, 2003) as an approach to compensate this effect and applied in different studies (Zeff *et al.*, 2007; Dehghani, White, *et al.*, 2009; White *et al.*, 2009; Eggebrecht *et al.*, 2012, 2014). In practice, depth weighting can be formulated differently, here we consider a generalized expression for the implementation of depth weighted MNE as proposed in (Lin *et al.*, 2006). It consists in initializing the source covariance matrix as $\Sigma_s^{-1/2} = \Lambda$, resulting in a so called depth weighted MNE solution, described as follows:

$$\begin{aligned}
 \widehat{X}_{dMNE} &= \operatorname{argmin}(\|(Y - AX)\|_{\Sigma_d}^2 + \lambda\|X\|_{\Sigma_s}^2) \\
 &= (A^T \Sigma_d A + \lambda(\Lambda \Lambda^t)^{-1})^{-1} A^T \Sigma_d Y \\
 \operatorname{diag}(\Lambda) &= \frac{1}{\operatorname{diag}((A^T \Sigma_d A)^\omega)}
 \end{aligned} \tag{4.3}$$

Depth weighted MNE solution takes into account the forward model A for each position in the brain and therefore penalizes most superficial regions exhibiting larger amplitude in A , by enhancing the contribution to deeper regions. ω is a weighting parameter tuning the amount of depth compensation to be applied. The larger is ω , the more depth compensation is considered. $\omega = 0$ would therefore refer to no depth compensation and an identity source covariance model. $\omega = 0.5$ refers to standard depth weighting approach mentioned above. In the present study, we carefully evaluated the impact of this parameter on DOT accuracy with a set of ω values (i.e., $\omega = 0, 0.1, 0.3, 0.5, 0.7$ and 0.9).

4.2.4 Maximum Entropy on the Mean (MEM) for fNIRS 3D reconstruction

MEM framework

The main contribution of this study is the first adaptation and evaluation of MEM method (Amblard, Lapalme and Lina, 2004; Grova, Daunizeau, *et al.*, 2006; Chowdhury *et al.*, 2013) to perform DOT reconstructions in fNIRS. Within the MEM framework, the intensity of x , i.e., amplitude of X at each location q in Eq.4.1, is considered as a random variable, described by the

following probability distribution $dp(x) = p(x)dx$. The Kullback-Leibler divergence or v-entropy of $dp(x)$ relative to a prior distribution $dv(x)$ is defined as,

$$S_v(dp(x)) = - \int_x \log \left(\frac{dp(x)}{dv(x)} \right) dp(x) = - \int_x f(x) \log(f(x)) dv(x) \quad (4.4)$$

where $f(x)$ is the v-density of $dp(x)$ defined as $dp(x) = f(x)dv(x)$. Following a Bayesian approach to introduce the data fit, we denote C_m as the set of probability distributions on x that explains the data on average:

$$Y - [A|I_q] \left[\begin{matrix} E_{dp}[x] \\ e \end{matrix} \right] = 0, \quad dp \in C_m \quad (4.5)$$

where Y represents the measured optical density changes, $E_{dp}[x] = \int x dp(x)$ represents the statistical expectation of x under the probability distribution dp , and I_q is an identity matrix of $(q \times q)$ dimension. Therefore, within the MEM framework, a unique solution of $dp(x)$ could be obtained,

$$dp^*(x) = \operatorname{argmax}_{dp(x) \in C_m} (S_v(dp(x))) \quad (4.6)$$

The solution of $dp^*(x)$ can be solved by maximizing the v-entropy which is a convex function. It is equivalent to minimize an unconstrained concave Lagrangian function i.e., $L(dp(x), \kappa, \lambda)$, along with two Lagrangian constraint parameters, i.e., κ and λ . It is finally equivalent to maximize a cost function $D(\lambda)$ which is described as,

$$D(\lambda) = \lambda^T Y - F_v(A^T \lambda) - \frac{1}{2} \lambda^T \Sigma_d^{-1} (\Sigma_d^{-1})^T \lambda \quad (4.7)$$

where Σ_d^{-1} is the noise covariance matrix. F_v represents the free energy associated with reference $dv(x)$. It is important to mention that $D(\lambda)$ is now an optimization problem within a space of dimension equal to the number of sensors. Therefore, if we estimate $\lambda^* = \operatorname{argmax}_\lambda D(\lambda)$ the unique solution of MEM framework is then obtained from the gradient of the free energy.

$$\hat{X}_{MEM} = \nabla_\xi F_v^*(\xi) |_{\xi=A^T \lambda^*} \quad (4.8)$$

For further details on MEM implementation and theory we refer the reader to (Amblard, Lapalme and Lina, 2004; Grova, Daunizeau, *et al.*, 2006; Chowdhury *et al.*, 2013).

Construction of the prior distribution for MEM estimation

To define the prior distribution $dv(x)$ mentioned above, we assumed that brain activity can be depicted by a set of K non-overlapping and independent cortical parcels. Then the reference distribution $dv(x)$ can be modelled as,

$$dv(x) = \prod_{k=1}^K [(1 - \alpha_k)\delta(x_k) + \alpha_k N(\mu_k, \Sigma_k)] dx_k, \quad 0 < \alpha_k < 1 \quad (4.9)$$

Each cortical parcel k is characterized by an activation state, defined by the hidden variable S_k , describing if the parcel is active or not. Therefore we denote α_k as the probability of k^{th} parcel to be active, i.e., $Prob(S_k = 1)$. δ_k is a Dirac function that allows to “switch off” the parcel when considered as inactive (i.e., $S_k = 0$). $N(\mu_k, \Sigma_k)$ is a Gaussian distribution, describing the distribution of absorptions changes within the k^{th} parcel, when the parcel is considered as active ($S_k = 1$). This prior model, which is specific to our MEM inference, offers a unique opportunity to switch off some parcels of the model, resulting in accurate spatial reconstructions of the underlying activity patterns with their spatial extent, as carefully studied and compared with other Bayesian methods in (Chowdhury *et al.*, 2013).

The spatial clustering of the cortical surface into K non-overlapping parcel was obtained using a data driven parcellation (DDP) technique (Lapalme, Lina and Mattout, 2006). DDP consisted in first applying a projection method, the multivariate source prelocalization (MSP) technique (Mattout *et al.*, 2005), estimating a probability like coefficient (MSP score) between 0 and 1 for each vertex of the cortical mesh, characterizing its contribution to the data. DDP is then obtained by using a region growing algorithm, along the tessellated cortical surface, starting from local MSP maxima. Once the parcellation is done, the prior distribution $dv(x)$ is then a joint distribution expressed as the multiplication of individual distribution of each parcel in Eq.4.9 assuming statistical independence between parcels,

$$dv(x) = dv_1(q_1)dv_2(q_2) \dots dv_k(q_k) \dots dv_K(q_K) \quad (4.10)$$

where $dv(x)$ is the joint probability distribution of the prior, $dv_k(q_k)$ is the individual distribution of the parcel k described as Eq.4.9.

To initialize the prior in Eq.4.9, μ_k which is the mean of the Gaussian distribution, $N(\mu_k, \Sigma_k)$, was set to zero. Σ_k at each time point t , i.e., $\Sigma_k(t)$, was defined by Eq.4.11 according to (Chowdhury *et al.*, 2013),

$$\begin{aligned}\Sigma_k(t) &= \eta(t)W_k(\sigma)^T W_k(\sigma) \\ \eta(t) &= 0.05 \frac{1}{\mathcal{P}_k} \sum_{i \in \mathcal{P}_k} \overline{X_{MNE}^2}(i, t)\end{aligned}\tag{4.11}$$

where $W_k(\sigma)$ is a spatial smoothness matrix, defined by (Friston *et al.*, 2008), which controls the local spatial smoothness within the parcel according to the geodesic surface neighborhood order. The same value of $\sigma = 0.6$ was used as in (Chowdhury *et al.*, 2013). $\eta(t)$ was defined as 5% of the averaged energy of MNE solution within each parcel \mathcal{P}_k at time t . Finally, we can substitute this initialization into Eq.4.9 to construct the prior distribution $dv(x)$, and then obtain the MEM solution using Eq.4.8.

It is worth mentioning that we did not use MNE solution as the prior of μ_k in Eq.4.9 at all, which was actually initialized to 0 in our framework. We only used 5% of the averaged energy of MNE solution, over the parcel k , to set the prior for covariance Σ_k . The posterior estimation of parameter μ_k was estimated from the Bayesian framework by conditioning with data. Moreover, the prior of MEM framework is a mixture of activation probability α_k and a Gaussian distribution (see Eq.4.9), in which the prior for α_k was informed by a spatio-temporal extension of the MSP score (see Chowdhury *et al.*, 2013 for further details). These aspects completely differentiate MEM from approaches that iteratively update reconstruction results initialized by a MNE solution.

Depth weighted MEM

In addition to adapting MEM for fNIRS reconstruction, we also implemented for the first time, depth weighting within the MEM framework. Two depth weighting parameters, ω_1 and ω_2 , were involved in this process. ω_1 was used to apply depth weighting on the source covariance matrix Σ_k of each parcel k in Eq.4.11. ω_2 was applied to solve the depth weighted MNE, as described in Eq.4.3, before using those prior to initialize the source covariance model within each parcel of the

MEM model. Therefore, the standard MNE solution $\widehat{X}_{MNE}(i, t)$ in Eq.4.11 was replaced by the depth weighted version of MNE solution $\widehat{X}_{dMNE}(i, t)$ described by Eq.4.3. Consequently, the depth weighted version of $\Sigma_k(t)$ is now defined as,

$$\begin{aligned}\Sigma_k(t)_{dw} &= \Lambda_{\mathcal{P}_k} \eta(t)_{dw} W_k(\sigma)^T W_k(\sigma) \\ \eta(t)_{dw} &= 0.05 \frac{1}{\mathcal{P}_k} \sum_{i \in \mathcal{P}_k} \widehat{X}_{dMNE}^2(i, t)\end{aligned}\tag{4.12}$$

where $\Lambda_{\mathcal{P}_k}$ is the depth weighting matrix for each parcel k , in which ω_1 was involved to construct this scaling matrix as described in Eq.4.3. This initialization followed the logic that depth weighting is in fact achieved by scaling the source covariance matrix. The other depth weighting parameter, ω_2 , was considered when solving $\widehat{X}_{dMNE}(i, t)$, therefore avoiding biasing the initialization of the source covariance with a standard MNE solution.

To comprehensively compare MEM and MNE and also to investigate the behavior of depth weighting, we first evaluated the reconstruction performance of MNE with different ω_2 (i.e., step of 0.1 from 0 to 0.9). Then two of these values (i.e., $\omega_2 = 0.3$ and 0.5) were selected for the comparison with MEM since they performed better than the others. Note that the following expressions of depth weighted MEM will be denoted as $\text{MEM}(\omega_1, \omega_2)$ to represent the different depth weighting strategies.

Accuracy of temporal dynamics

The last contribution of this study was to improve the temporal accuracy of MEM solutions. In the classical MEM approach (Chowdhury *et al.*, 2013), $\widehat{X}_{MNE}(i, t)$ in Eq.4.12 was globally normalized by dividing by $\max_{i \in \Omega, t \in T} (\widehat{X}_{MNE}(i, t))$, where Ω represents all the possible locations along the cortical surface and T is the whole time segment. Therefore, the constructed prior along the time actually contained the temporal scaled dynamics from MNE solution. To remove this effect, we performed local normalization for $\widehat{X}_{dMNE}(i, t)$ at each time instance t , i.e., by dividing by $\max_{i \in \Omega} (\widehat{X}_{dMNE}(i, t))$. This new feature would preserve the spatial information provided by prior distribution, while allowing MEM to estimate the temporal dynamics only from the data.

4.2.5 Validation of fNIRS reconstruction methods

We evaluated the performance of the two fNIRS reconstruction methods (i.e., MEM and MNE), first within a fully controlled environment involving the use of realistic simulations of fNIRS data, followed by evaluations on real data acquired with a well controlled finger tapping paradigm. Two different fNIRS montages were considered in those two proposed evaluations.

Montage 1: A full Double Density (DD) montage (see Fig.4.1) which is a widely used fNIRS montage, was considered given that it allows sufficient dense spatial coverage of fNIRS channel to allow local DOT (Kawaguchi et al., 2007). One healthy subject underwent fNIRS acquisitions with this DD montage, involving the two following sessions,

- A 10 minutes resting state session was acquired to add realistic physiological noise to be considered in our realistic simulations. The subject was seated in a comfortable armchair and instructed to keep the eyes open and to remain awake. The optodes of the full DD montage (i.e., 8 sources and 10 detectors resulting in 50 fNIRS channels) are presented in Fig.4.1e. The montage composed of 6 second-order distance channels(1.5cm), 24 third-order channels(3cm) and 12 fourth-order channels with 3.35cm distance. In addition, we also added one proximity detector paired for each source to construct close distance channels (0.7cm) in order to measure superficial signals within extracerebral tissues. To place the montage with respect to the region of interest, the center of the montage was aligned with the center of the right "hand knob" area, which controls the left hand movement (Raffin *et al.*, 2015a), projected on the scalp surface and then each optodes were projected on the scalp surface (see Fig.4.1d).
- The subject was asked to sequentially tap the left thumb against the other digits around 2Hz, therefore the main elicited hemodynamic response was indeed expected over the right hand knob area. The finger tapping paradigm consisted in 10 blocks of 30s tapping task and each of them was followed by a 30 to 35s resting period. The beginning/end of each block was informed by an auditory cue.

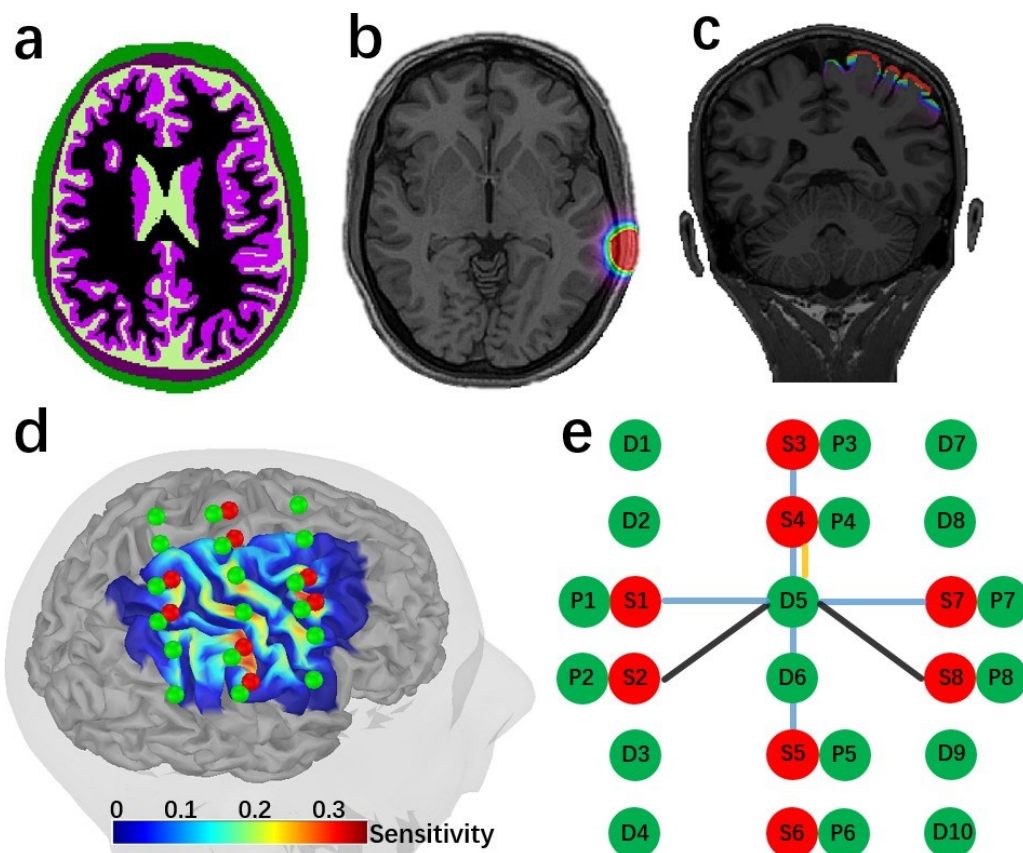


Fig.4.1 *fNIRS measurement montage 1 and the anatomical model considered for DOT forward model estimation.* (a) Anatomical 3D MRI segmented in five tissues, namely, scalp (green), skull (brown), CSF (light green), gray matter (purple) and white matter (black). (b) Optical fluence of one optode calculated through Monte Carlo simulation of Photons within this head model, using MCXLab. (c) Sensitivity profile of the whole montage in volume space. (d) Sensitivity profile, i.e., the summation of sensitivity map of all channels, along the cortical surface. Green dots represent detectors, including one proximity detector 0.7 cm for each source, and red dots represent sources. (e) double density montage 1 considered for this acquisition. There were 50 channels in total, 12 of 3.8 cm (black), 24 of 3 cm (blue), 6 of 1.5 cm (yellow) and 8 of close distance (0.7cm) channels.

Montage 2: A personalized optimal montage (see Fig.4.8) following the methodology we previously reported in Machado *et al.*, 2018. First, the hand knob within right primary motor cortex was drawn manually along the cortical surface and defined as a target region of interest (ROI) using the Brainstorm software (Tadel *et al.*, 2011). Then we applied optimal montage estimation (Machado *et al.*, 2014a, 2018) in order to estimate personalized montages, built to maximize a priori fNIRS sensitivity and spatial overlap between channels with respect to the target ROI. To ensure good spatial overlap between channels for local 3D reconstruction, we constructed

personalized optimal montages composed of 3 sources and 15 detectors (see Fig.7b). The source detector distance was set to vary from 2cm to 4.5cm and each source was constrained such that it has to create channels with at least 13 detectors. Finally, we also manually added 1 proximity channel, located at the center of the 3 sources. Five subjects underwent fNIRS acquisitions with personalized optimal montage during a similar finger tapping task as the one for montage 1, in which 20 blocks were acquired by alternating a task (period of 10s) and a resting state period ranging from 30s to 60s.

All 6 subjects have signed written informed consent forms for this study which was approved by the Central Committee of Research Ethics of the Minister of Health and Social Services Research Ethics Board, Quebec, Canada.

MRI and fMRI Data acquisitions

Anatomical MRI data were acquired on those 6 healthy subjects (25 ± 6 years old, right-handed) and were considered to generate realistic anatomical head models. MRI data were acquired in a GE 3T scanner at the PERFORM Center of Concordia University, Montreal, Canada. T1-weighted anatomical images were acquired using the 3D BRAVO sequence ($1 \times 1 \times 1 \text{ mm}^3$, 192 axial slices, 256×256 matrix), whereas T2-weighted anatomical images were acquired using the 3D Cube T2 sequence ($1 \times 1 \times 1 \text{ mm}^3$ voxels, 168 sagittal slices, 256×256 matrix).

Participants also underwent functional MRI acquisition (without fNIRS) while performing the same finger opposition tasks considered in fNIRS. fMRI acquisition consisted in a gradient echo EPI sequence ($3.7 \times 3.7 \times 3.7 \text{ mm}^3$ voxels, 32 axial slices, TE = 25ms, TR = 2,000ms). fMRI Z-maps were generated by standard first-level fMRI analysis using FEAT from FSL v6.0.0 software (Smith *et al.*, 2004; Jenkinson *et al.*, 2012).

fNIRS Data acquisition

fNIRS acquisitions were conducted at the PERFORM Center of Concordia University using a Brainsight fNIRS device (Rogue Research Inc., Montreal, Canada), equipped with 16 dual wavelength sources (685nm and 830nm), 32 detectors and 16 proximity detectors (for short distance channels). All montages (i.e., double density and optimal montages) were installed to cover the right motor cortex. Knowing a priori the exact positions of fNIRS channels estimated on the anatomical MRI of each participant, we then used a 3D neuronavigation system (Brainsight

TMS navigation system, Rogue Research Inc.) to guide the installation of the sensors on the scalp. Finally, every sensor was glued on the scalp using a clinical adhesive, collodion, to prevent motion and ensure good contact to the scalp (Yücel *et al.*, 2014; Machado *et al.*, 2018).

fNIRS forward model estimation

T1 and T2 weighted anatomical images were processed using FreeSurfer V6.0 (Fischl *et al.*, 2002) and Brain Extraction Tool2 (BET2) (Smith *et al.*, 2004) in FMRIB Software Library (FSL) to segment the head into 5 tissues (i.e., scalp, skull, Cerebrospinal fluid (CSF), gray matter and white matter see Fig.4.1a).

The same optical coefficients used in (Yücel *et al.*, 2014; Machado *et al.*, 2018) for the two wavelengths considered during our fNIRS acquisition, 685nm and 830nm, were assigned to each tissue type mentioned above. Fluences of light for each optode (see Fig.4.1b) was estimated by Monte Carlo simulations with 108 photons using MCXLAB developed by Fang and Boas, 2009; and Yu *et al.*, 2018 (<http://mcx.sourceforge.net/cgi-bin/index.cgi>). Sensitivity values were then computed using the adjoint formulation and were normalized by the Rytov approximation (Arridge, 1999).

For each source detector pair of our montages, the corresponding light sensitivity map was first estimated in a volume space, and then further constrained to the 3D mask of gray matter tissue (see Fig.4.1c), as suggested in (Boas and Dale, 2005). Then, these sensitivity values within the gray matter volume were projected along the cortical surface (see Fig.4.1d and Fig.4.7c) using the Voronoi based method proposed by (Grova, Makni, *et al.*, 2006). We considered the mid-surface from FreeSurfer as the cortical surface. This surface was downsampled to 25, 000 vertices. This volume to surface interpolation method has the ability to preserve sulco-gyral morphology (Grova, Makni, *et al.*, 2006). After the interpolation, the sensitivity value of each vertex of the surface mesh represents the mean sensitivity of the corresponding volumetric Voronoi cell (i.e., a set of voxels that have closest distances to a certain vertex than to all other vertices).

fNIRS data preprocessing

Using the coefficient of variation of the fNIRS data, channels exhibiting a standard deviation larger than 8% of the signal mean were rejected (Schmitz *et al.*, 2005; Schneider *et al.*, 2011; Eggebrecht *et al.*, 2012; Piper *et al.*, 2014). Superficial physiological fluctuations were regressed out at each

channel using the average of all proximity channels' (0.7cm) signals (Zeff *et al.*, 2007). All channels were then band-pass filtered between 0.01Hz and 0.1Hz using a 3rd order Butterworth filter. Changes in optical density (i.e., ΔOD) were calculated using the conversion to log-ratio. Finally, ΔOD of finger tapping data were block averaged around the task onsets. Note that since sensors were glued with collodion, we observed very minimal motion during the acquisitions. Real background signal considered to generate realistic simulations also underwent the same preprocessing.

Realistic Simulations of fNIRS Data

We first considered realistic simulations of fNIRS data to evaluate DOT methods within a fully controlled environment. To do so, theoretical task induced HbO/HbR concentration changes were simulated within cortical surface regions with a variety of locations, areas and depths. Corresponding optical density changes in the channel space were then computed by applying the corresponding fNIRS forward model, before adding real resting state fNIRS baseline signal as realistic physiological noise at different signal to noise ratio (SNR) levels.

As presented in Fig.4.2a, we defined three sets of evenly distributed seeds within the field of view of DOT reconstruction. The locations were selected with respect to the depth relative to the skull, namely we simulated 100 "superficial seeds", 100 "middle seeds" and 50 "deep seeds". The cortical regions in which we simulated an hemodynamic response were generated by region growing around those seeds, along the cortical surface. To simulate generators with different spatial extents (denoted here as Se), we considered four levels of neighborhood orders, growing geodesically along the cortical surface, resulting in spatial extents ranging from $Se = 3, 5, 7, 9$ (corresponding areas of 3 to 40 cm^2). For simplification, these cortical regions within which an hemodynamic response was simulated will be denoted as "generators" in this paper. For each vertex within a "generator", a canonical Hemodynamic Response Function (HRF) was convoluted with a simulated experimental paradigm which consisted in one block of 20s task surrounded by 60s pre-/post- baseline period (Fig.4.2b). Simulated HbO/HbR fluctuations within the theoretical generator (Fig.4.2c) were then converted to the corresponding absorption changes of two wavelengths (i.e., 685nm and 830nm). After applying the forward model matrix A in Eq.4.1, we estimated the simulated, noise free, task induced ΔOD in all channels.

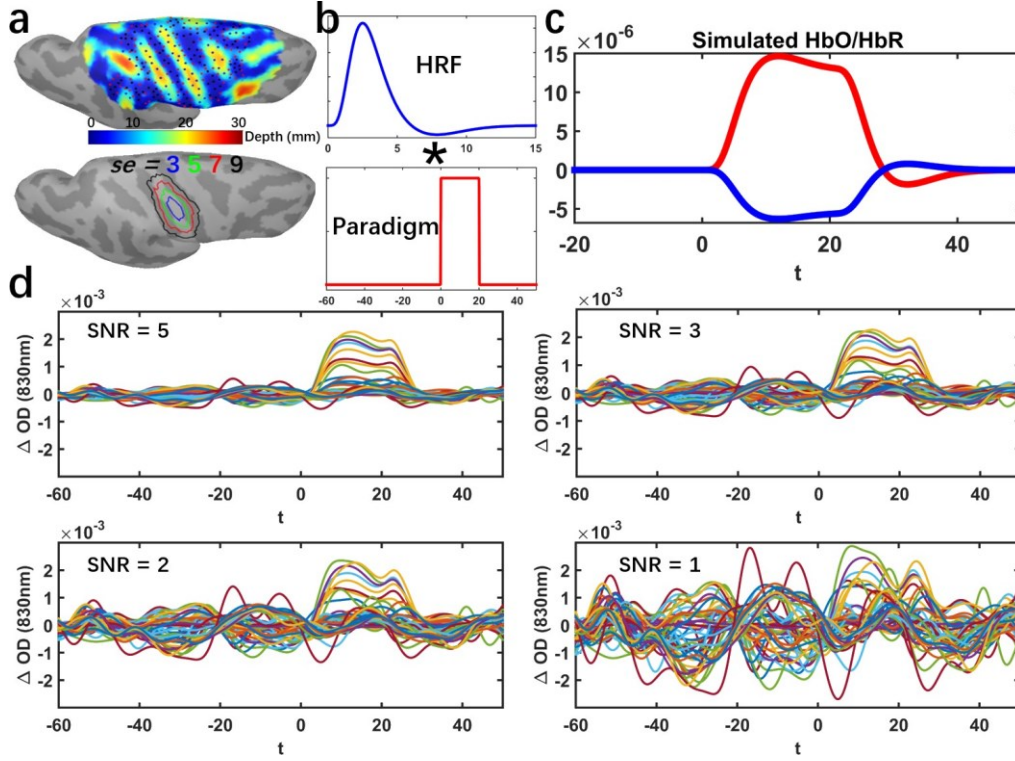


Fig.4.2 Workflow describing our proposed realistic fNIRS simulation framework. (a) 100 Superficial seeds (black dots), 100 Middle seeds (red dots), 50 Deep seeds (blue dots) with spatial extent of $Se = 3, 5, 7, 9$ neighbourhood order within the field of view. (b) Convolution of a canonical HRF model with an experimental block paradigm (60s before and 50s after the onset). (c) Simulated theoretical HbO/HbR fluctuations along the cortical surface within the corresponding generator. (d) Realistic simulations obtained by applying the fNIRS forward model and addition of the average of 10 trials of real fNIRS background measurements at 830nm. Time course of ΔOD of all channels with SNR of 5, 3, 2 and 1 respectively are presented.

ΔOD of real resting state data were then used to add realistic fluctuations (noise) to these simulated signals. Over the 10min of recording, we randomly selected 10 baseline epochs of 120s each, free from any motion artifact by visual inspection. To mimic a standard fNIRS block average response, realistic simulations were obtained by adding the average of these 10 real baseline epochs to the theoretical noise-free simulated ΔOD , at five SNR levels (i.e., SNR = 5, 3, 2, 1). SNR was calculated through the following equation,

$$SNR_{\lambda} = \frac{\max(\text{abs}(\Delta OD_{\lambda}[0, t_1]))}{\text{mean}(\text{std}(\Delta OD_{\lambda}[-t_0, 0]))} \quad (4.13)$$

where $\Delta OD_{\lambda}[0, t_1]$ is the optical density changes of a certain wavelength λ in all channels during the period from 0s to $t_1 = 60s$. $std(\Delta OD_{\lambda}[-t_0, 0])$ is the standard deviation of ΔOD_{λ} during baseline period along all channels. Simulated trials for each of four different SNR levels are illustrated in Fig.4.2d. A total number of 4000 realistic simulations were considered for this evaluation study, i.e., 250 (seeds) \times 4 (spatial extents) \times 4 (SNR levels). Note that resting state fNIRS baseline signal was preprocessed before adding to the simulated signals.

Validation metric

Following the validation metrics described in (Grova, Daunizeau, *et al.*, 2006; Chowdhury *et al.*, 2013, 2015; Hedrich *et al.*, 2017), we applied 4 quantitative metrics to assess the spatial and temporal accuracy of fNIRS 3D reconstructions. Further details on the computation of those four validation metrics are reported in [section 4.6 Supplementary material S1](#).

Area Under the Receiver Operating Characteristic (ROC) curve (AUC) was used to assess general reconstruction accuracy considering both sensitivity and specificity. AUC score was estimated as the area under the ROC curve, which was obtained by plotting sensitivity as a function of (1-specificity). AUC ranges from 0 to 1, the higher it is the more accurate the reconstruction is.

Minimum geodesic distance (Dmin) measuring the geodesic distance in millimeters, following the circumvolutions of the cortical surface, from the vertex that exhibited maximum of reconstructed activity to the border of the ground truth. Low Dmin values indicate better accuracy in estimating the location of the generator.

Spatial Dispersion (SD) assessed the spatial spread of the estimated generator distribution and the localization error. It is expressed in millimeters. A reconstructed map with either large spatial spread around the ground truth or large localization error would result in large SD values.

Shape error(SE) evaluated the temporal accuracy of the reconstruction. It was calculated as the root mean square of the difference between the normalized reconstructed time course and the normalized ground truth time course. Low SE values indicate high temporal accuracy of the reconstruction.

4.2.6 Statistics

Throughout all of the quantitative evaluations among different methods involving different depth weighting factors ω in the results section, Wilcoxon signed rank test was applied to test the

significance of the paired differences between each comparison. For each statistical test, we reported the median value of paired differences, together with its p-value (Bonferroni corrected). We are only showing results at 830nm for simulations, since the ones from 690nm under the same SNR level would have provided similar reconstructed spatiotemporal maps except for the reversed amplitudes. However, reconstruction results on real data indeed involved both wavelengths.

4.3 Results

4.3.1 Evaluation of MEM v.s. MNE using realistic simulations

We first investigated the effects of depth weighting factor ω_2 selection for depth weighted MNE. To do so, we evaluated spatial and temporal performances of DOT reconstruction for a set of ω_2 (step of 0.1 from 0 to 0.9). Based on those results reported in the [Supplementary material S2](#) and Fig.4.S1, we decided to consider that most accurate fNIRS reconstructions were obtained when considering $\omega_2 = 0.3$ and 0.5 for depth weighted MNE. Therefore only those two values were further considered for comparison with MEM reconstructions.

Comparison of the performance of MEM and MNE on superficial realistic simulations are presented in Table.4.1 and Fig.4.3, for 4 levels of spatial extent ($Se = 3,5,7,9$), using boxplot distribution of the 4 validation metrics. We evaluated 3 depth weighted implementations of MEM, namely, MEM ($\omega_1 = 0.3, \omega_2 = 0.3$), MEM(0.3, 0.5) and MEM(0.5, 0.5), as well as 2 depth weighted implementations of MNE, namely, MNE(0.3) and MNE(0.5).

For spatial accuracy, results evaluated using Dmin, we obtained median Dmin values of 0mm for all methods, indicating the peak of the reconstructed map, was indeed accurately localized inside the simulated generator. It is worth mentioning that MEM(0.5, 0.5) provided few Dmin values larger than 0mm in $Se = 3$ and $Se = 5$ cases, which consisted of superficial and focal generators. Since MEM accurately estimated the spatial extent, more depth weighting considered for MEM(0.5, 0.5) could result in focal and deeper reconstruction, hence resulting in non-zero Dmin values. On the other hand, MNE would overestimate the size of the underlying generators, therefore resulting in 0mm Dmin, but larger SD values in similar conditions.

When considering the general reconstruction accuracy using AUC, for focal generators such as $Se = 3$ and 5 , we found significant larger AUC (see Table.4.1) for MEM(0.3, 0.3) and MEM(0.3, 0.5) when compared to the most accurate version of MNE, i.e., MNE(0.3). When considering more

extended generators, i.e., $Se = 7$ and 9 , MEM(0.3, 0.5) and MEM(0.5, 0.5) achieved significantly larger AUC than MNE(0.3). However, the AUC of MNE(0.5) was significantly larger than MEM(0.3, 0.3) for $Se = 7$ as well as significantly larger than MEM(0.3, 0.5) and MEM(0.5, 0.5) for $Se = 9$.

In terms of spatial extent of the estimated generator distribution and the localization error, MEM provided significantly smaller SD values among all the comparisons. Finally, for temporal accuracy of the reconstruction represented by SE, MNE provided significantly lower values, but with a small difference (e.g., 0.01 or 0.02, see results on real data as a reference of this effect size), than MEM among all comparisons when $Se = 3, 5$.

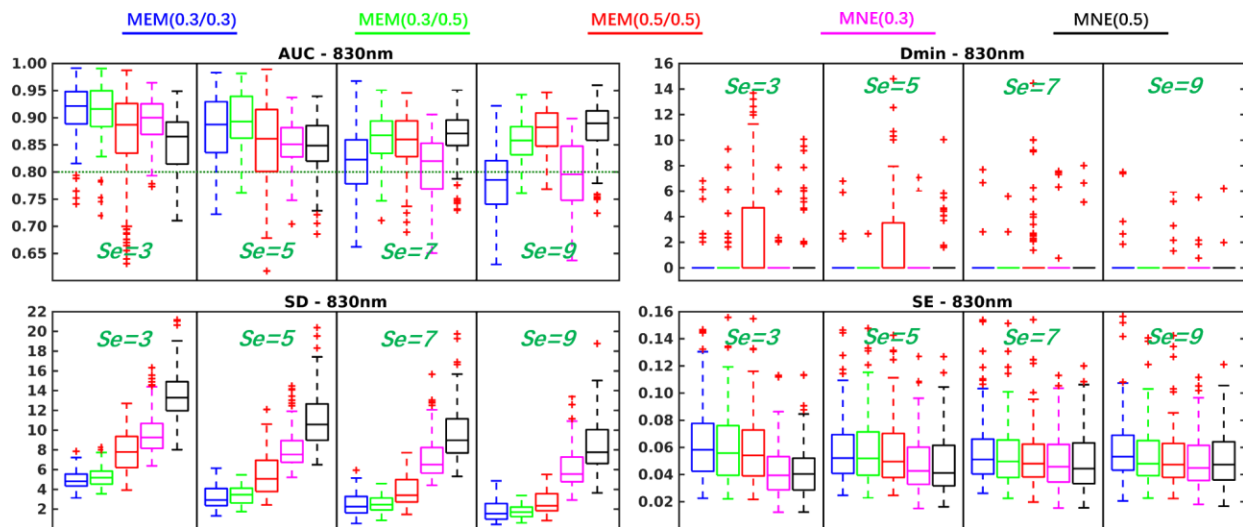


Fig.4.3 Evaluation of the performances of MEM and MNE using realistic simulations involving superficial seeds for different spatial extent ($Se = 3, 5, 7, 9$). Boxplot representation of the distribution of four validation metrics for three depth weighted strategies of MEM and two depth weighted strategies of MNE, namely: MEM(0.3, 0.3) in blue, MEM(0.3, 0.5) in green, MEM(0.5, 0.5) in red, MNE(0.3) in magenta and MNE(0.5) in black. Results were obtained after DOT reconstruction of 830nm ΔOD .

Superficial Seeds		Se = 3		Se = 5		Se = 7		Se = 9	
		MNE (0.3)	MNE (0.5)						
AUC	MEM (0.3, 0.3)	0.02*	0.06**	0.04**	0.03**	0.01	-0.04**	-0.01	-0.10**
	MEM (0.3, 0.5)	0.02*	0.05**	0.05**	0.04**	0.05**	0.00	0.05**	-0.03**
	MEM (0.5, 0.5)	-0.01	0.03	0.00	0.01	0.04**	0.00	0.07**	-0.01
Dmin	MEM (0.3, 0.3)	0.00	0.00	0.00	0.00	0.00	0.00	0.00	0.00
	MEM (0.3, 0.5)	0.00	0.00	0.00	0.00	0.00	0.00	0.00	0.00
	MEM (0.5, 0.5)	0.00	0.00	0.00	0.00	0.00	0.00	0.00	0.00
SD	MEM (0.3, 0.3)	-4.26**	-8.31**	-4.48**	-7.63**	-4.16**	-6.43**	-3.85**	-6.28**
	MEM (0.3, 0.5)	-3.78**	-8.23**	-4.11**	-7.11**	-3.86**	-6.30**	-3.71**	-6.24**
	MEM (0.5, 0.5)	-1.64**	-5.56**	-2.60**	-4.97**	-2.90**	-4.79**	-2.84**	-5.01**
SE	MEM (0.3, 0.3)	0.02**	0.02**	0.01**	0.01**	0.01	0.01	0.01	0.01
	MEM (0.3, 0.5)	0.02**	0.02**	0.01**	0.01**	0.01	0.01	0.00	0.00
	MEM (0.5, 0.5)	0.02**	0.02**	0.01**	0.01**	0.00	0.00	0.00	0.00

Table.4.1. Wilcoxon signed rank test results of reconstruction performance comparison of MEM and MNE in superficial seeds case. Median values of paired difference are presented in the table. *p* values were corrected for multiple comparisons using Bonferroni correction, * indicates $p < 0.01$ and ** represents $p < 0.001$. Median of the paired difference of each validation metrics is color coded as follows: green: MEM is significantly better than MNE, red: MNE is significantly better than MEM and gray: non-significance.

Similar comparisons between MEM and MNE were conducted respectively for middle seed simulated generators and deep seed simulated generators. Results were overall reporting similar trends when comparing MEM and MNE methods for middle and deep seeds, and as expected more depth weighting resulted in more accurate reconstructions (described in details in supplementary material, Fig.4.S2 and Table.4.S1 for middle seeds, Fig.4.S3 and Table.4.S2 for deep seeds).

To further illustrate the performance of MEM and MNE as a function of the depth of the generator, we are presenting some reconstruction results in Fig.4.4. Three generators with a spatial extent of $Se = 5$, were selected for this illustration. They were all located around the right "hand knob" area, and were generated from a superficial, middle and deep seed respectively. The first column in Fig.4.4 shows the location and the size of the simulated generator, considered as our ground truth. The generator constructed from the superficial seed only covered the corresponding gyrus, whereas the generators constructed from the middle seed, included parts of the sulcus and the gyrus. Finally, when considering the deep seed, the simulated generator covered both walls of the sulcus, extended just a little on both gyri. For superficial case, MEM(0.3, 0.3) and MEM(0.3, 0.5) provided similar performances in term of visual evaluation of the results and quantitative

evaluations ($AUC = 0.96$, $D_{min} = 0mm$, $SD = 1.94mm, 2.15 mm$, $SE = 0.03$). On the other hand, for the same simulations, MNE(0.3) and MNE(0.5) resulted in less accurate reconstructions, spreading too much around the true generator, as confirmed by validation metric, exhibiting notably large SD values $AUC = 0.86, 0.8$, $D_{min} = 0mm$, $SD = 9.84mm, 14.63mm$, $SE = 0.02$). When considering the simulation obtained with the middle seed, MEM(0.3, 0.5) retrieved accurately the gyrus part of the generator but missed the sulcus component, since less depth compensation was considered. When increasing depth sensitivity, MEM(0.5, 0.5) clearly outperformed all other methods, by retrieving both the gyrus and sulcus aspects of the generator, resulting in the largest $AUC = 0.98$ and the lowest $SD = 2.93mm$. MNE(0.3) was not able to recover the deepest aspects of the generator, but also exhibited a large spread outside the ground truth area as suggested by a large $SD = 9.69mm$. MNE(0.5) was able to retrieve the main generator, but also exhibited a large spatial spread of $SD = 10.16mm$. When considering the generators obtained from the deep seed, MNE(0.3) only reconstructed part of gyrus, missing completely the main sulcus aspect of the generator, resulting in low AUC of 0.57 and large SD of 10.34mm. MEM(0.3, 0.5) was not able to recover the deepest aspects of the sulcus, but reconstructed accurately the sulci walls, resulting in an AUC of 0.89 and a SD of 2.71mm. MEM(0.5, 0.5) recovered the deep simulated generator very accurately, as demonstrated by the excellent scores ($AUC = 0.97$, $SD = 2.11mm$) when compared to MNE(0.5). For those three simulations, all methods recovered the underlying time course of the activity with similar accuracy (i.e., similar SE values). In supplementary material, we added Video.1, illustrating the behavior of all the simulations and all methods, following the same layout provided in Fig.4.4.

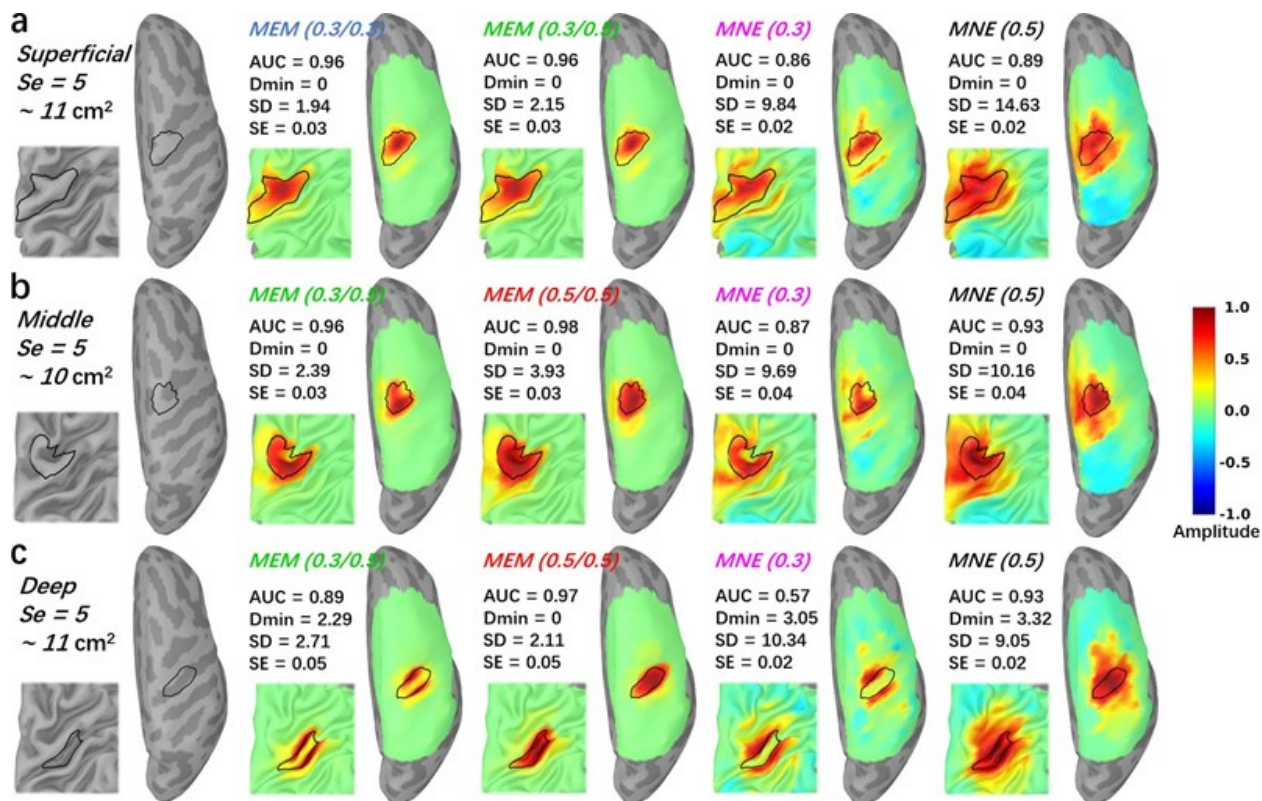


Fig.4.4 Comparisons of the reconstruction maps using MEM and MNE in realistic simulations. Three theoretical regions with spatial extent $Se = 5$ (11cm^2) were selected near the hand knob at different depths. The first column presents the locations and the size of the generator along the cortical surface. (a) Superficial seed case with reconstructed maps reconstructed using all MEM and MNE implementations considered in this study. (b) Middle seed case with reconstructed maps reconstructed using all MEM and MNE implementations considered in this study. (c) Deep seed case with reconstructed maps reconstructed using all MEM and MNE implementations considered in this study. 20% inflated and zoomed maps are presented on the left corner of each figure. 100% inflated right hemisphere are presented on the right side. All the maps were normalized by their own global maximum and no threshold was applied.

Note that for this quantitative evaluation of fNIRS reconstruction methods using a realistic simulation framework, we considered fNIRS data at only one wavelength (830nm). Using single wavelength in the context simulation based evaluation is a common procedure in DOT literature (Dehghani, White, *et al.*, 2009; White, 2010; Okawa, Hoshi and Yamada, 2011; Shimokawa *et al.*, 2012, 2013b; Zhan *et al.*, 2012a; Tremblay *et al.*, 2018), since we may expect overall similar performances for 685nm wavelength under the same SNR level.

4.3.2 Effects of depth weighting on the reconstructed generator as a function of the depth

and size of the simulated generators

To summarize the effects of depth weighting in 3D fNIRS reconstructions, we further investigated the validation metrics, AUC, SD and SE, as a function of depth and size of the simulated generators. Dmin was not included due to the fact that we did not find clear differences among methods throughout all simulation parameters from previous results. In the top row of Fig.4.5, 250 generators created from all 250 seeds with a spatial extent of $Se = 5$ were selected to demonstrate the performance of different versions of depth weighting as a function of the average depth of the generator. Whereas in the bottom row of Fig.4.5, we considered 400 generators constructed from all 100 superficial seeds with 4 different spatial extents of $Se = 3,5,7,9$, to illustrate the performance of different versions of depth weighting as a function of the size of the generator. According to AUC, depth weighting was indeed necessary for all methods when the generator moved to deeper regions ($>2\text{cm}$) as well as when the size was larger than 20cm^2 . Moreover, any version of MEM always exhibited clearly less false positives, as indicated by lower SD values, than all of MNE versions, whatever was the depth or the size of the underlying generator. We found no clear trend and difference of temporal accuracy among methods when reconstructing generators of different depths and sizes.

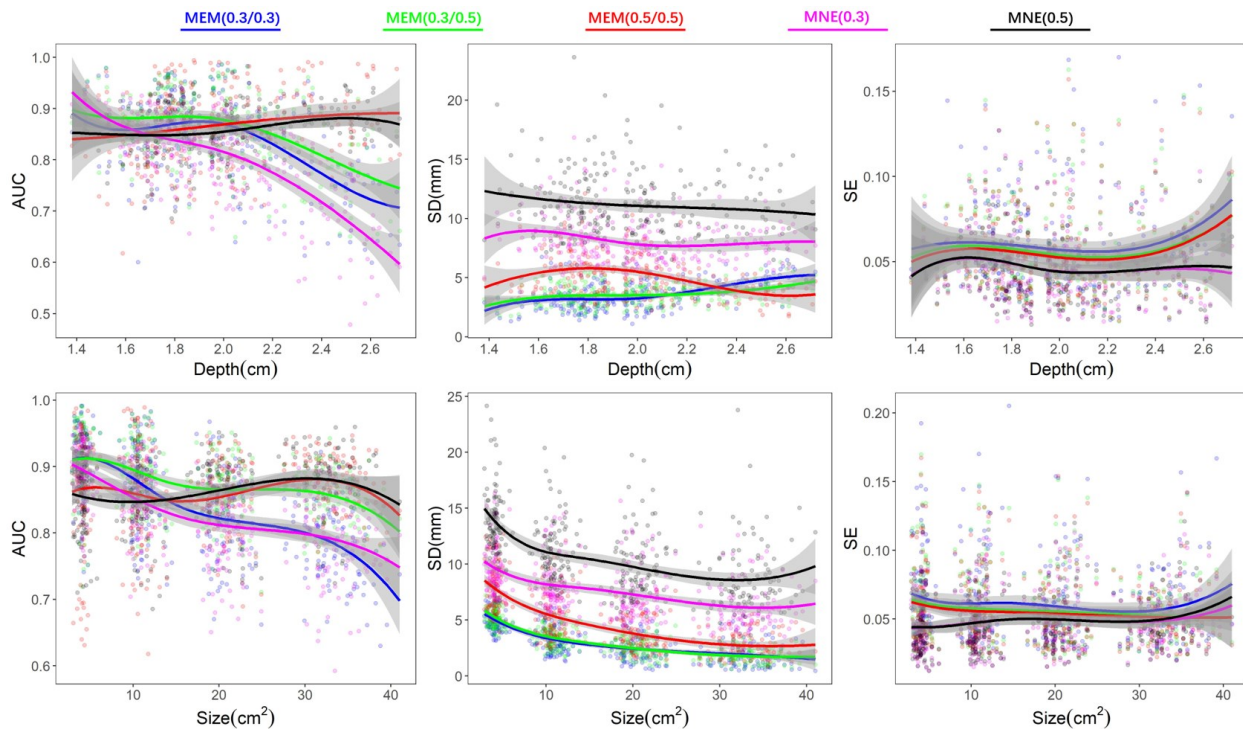


Fig.4.5 Effects of depth weighting on the depth and size of the simulated generators. First row

demonstrates the validation matrices, AUC, SD and SE, as a function of depth of generators. We selected 250 generators created from all 250 seeds with a spatial extent of $SD = 5$. Depth was calculated by the average of minimum Euclidean distance from each vertex, within each generator, to the head surface. Second row demonstrates the validation matrices, AUC, SD and SE, as a function of size of generators. Involving 400 generators which constructed from 100 superficial seeds with 4 different spatial extend of $Se = 3, 5, 7, 9$. Line fittings were performed via a 4 knots spline function to estimate the smoothed trend and the shade areas represent 95% confident interval. Color coded points represent the values of validation matrices of all involved generators.

4.3.3 Robustness of 3D reconstructions to the noise level

All previous investigations were obtained from simulations obtained with a SNR of 5, in this section we compared the effect of the SNR level in Fig.4.6, on depth weighted versions of MNE and MEM, for superficial seeds only and generators of spatial extent $Se = 5$. We only compared MEM(0.3, 0.5) and MNE(0.5) considering the observation from previous results that these two methods were overall exhibiting the best performances in this condition. Regarding D_{min} , paired differences were not significant but MNE exhibited more D_{min} values above 0mm than MEM at all SNR levels, suggesting that MNE often missed the main generators while MEM was more accurate in reconstructing the maximum of activity within the simulated generator. Regarding AUC, MEM(0.3, 0.5) exhibited values higher than 0.8 at all SNR levels, whereas MNE(0.5) failed to recover accurately the generator for $SNR = 1$. Besides, in Table.4.2, we found that the difference of AUC between MEM and MNE increased when SNR level decreased, suggesting the good robustness of MEM when decreasing the SNR level. The difference in SD also increased when SNR levels decreased. Indeed, MEM exhibited stable SD values among most SNR levels (except $SNR = 1$), whereas for MNE SD values were highly influenced by the SNR level. Finally, for both methods, decreasing SNR levels resulted in less accurate time course estimation (SE increased), slightly more for MEM when compared to MNE.

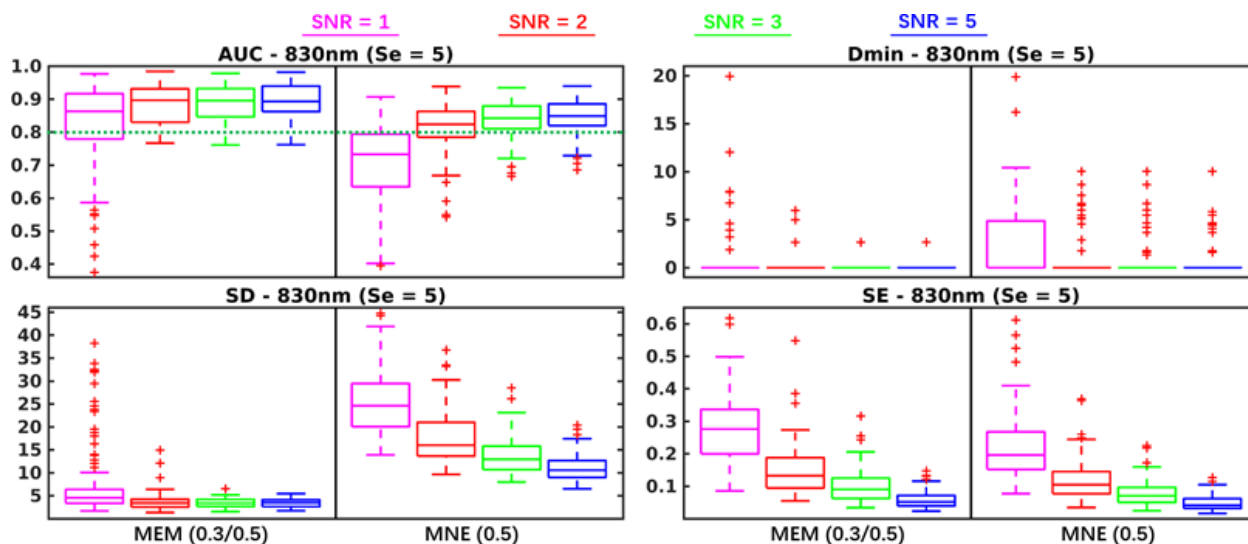


Fig.4.6 Evaluation of the performances of MEM and MNE at four different SNR levels. Boxplot representation of the distribution of four validation metrics for MEM(0.3, 0.5) and MNE(0.5) involving superficial seeds with spatial extent $Se = 5$. SNR levels (SNR = 1, 2, 3, 5) are represented using different colors.

$Se = 5$ ($\sim 11 \text{ cm}^2$)		SNR = 1	SNR = 2	SNR = 3	SNR = 5
		MNE (0.5)	MNE (0.5)	MNE (0.5)	MNE (0.5)
AUC	MEM (0.3, 0.5)	0.14**	0.07**	0.05**	0.04**
Dmin	MEM (0.3, 0.5)	0.00	0.00	0.00	0.00
SD	MEM (0.3, 0.5)	-17.63**	-12.40**	-9.22**	-7.11**
SE	MEM (0.3, 0.5)	0.05**	0.03**	0.02**	0.01**

Table.4.2 Reconstruction performance comparison of MEM and MNE with different SNR levels. Median of paired difference of validation metric (i.e., AUC, Dmin, SD and SE) values of $Se = 5$ are presented in the table following the SNR increase from 1 to 5. ** indicates corrected $p < 0.001$.

4.3.4 Evaluation of MEM and MNE on real fNIRS data

For all finger tapping fNIRS data considered in our evaluations, two wavelengths (i.e., 685nm and 830nm) were reconstructed first and then converted to HbO/HbR concentration changes along the cortical surface using specific absorption coefficients. All the processes from fNIRS preprocessing

to 3D reconstruction were completed in Brainstorm (Tadel *et al.*, 2011) using the NIRSTORM plugin developed by our team (<https://github.com/Nirstorm>). For full double density montage (montage 1), reconstructed HbR amplitudes were reversed to positive phase and normalized to their own global maximum, to facilitate comparisons. In Fig.4.7.a, we showed the reconstructed HbR maps at the peak of the time course (i.e., 31s) for MEM and MNE by considering the 4 depth weighted versions, previously evaluated, i.e., MEM(0.3, 0.3), MEM(0.3, 0.5), MNE(0.3) and MNE(0.5). The two depth weighted versions of MEM clearly localized well the "hand knob" region, while exhibiting very little false positives in its surrounding. On the other hand, both depth weighted version of MNE clearly overestimated the size of the hand knob region and also exhibited some distant possibly spurious activity. The fMRI Z-map obtained during the corresponding fMRI task is presented in Fig.4.7.b, after the projection of the volume Z-map on the cortical surface. Fig.4.7.c showed the time courses within the region of interest representing the "hand knob". Each curve represents the reconstructed time course of one vertex of the hand knob region and the amplitude was normalized by the peak value within the whole region.

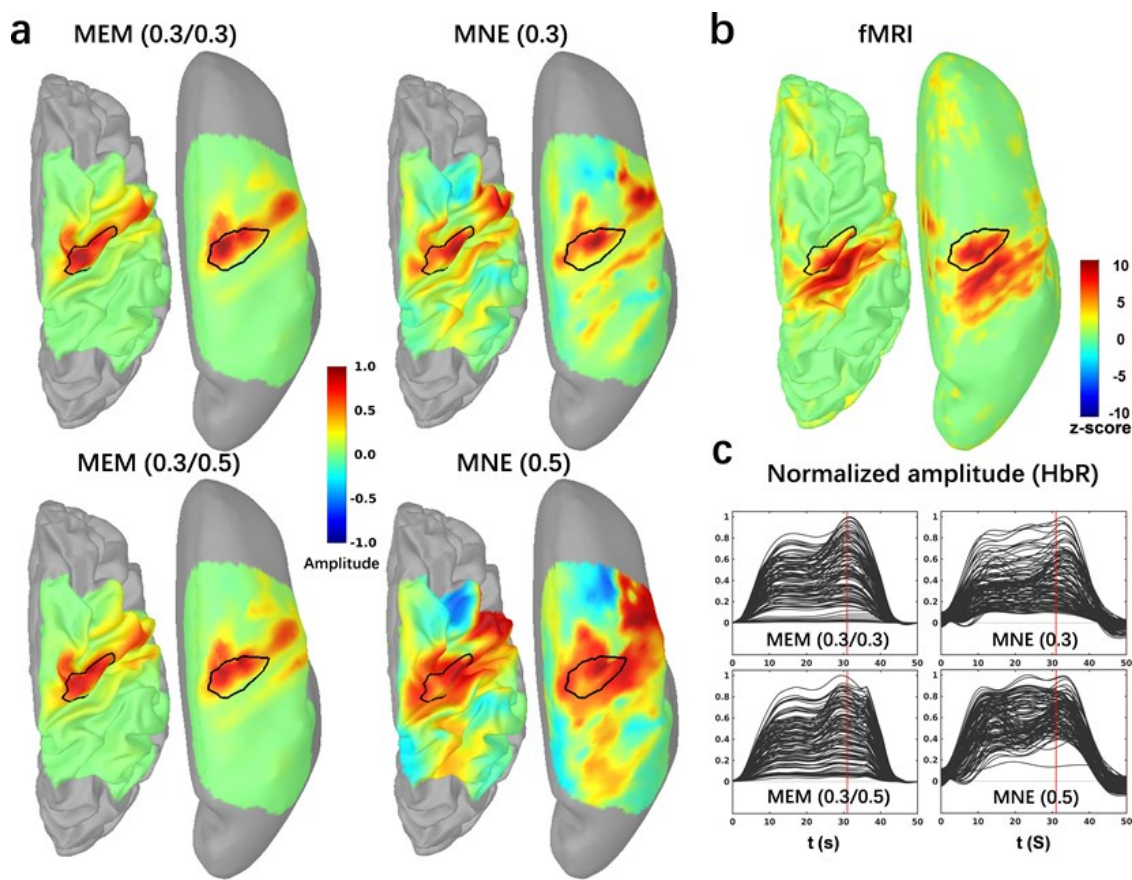


Fig.4.7 Application of MEM versus MNE reconstruction of HbR during a finger tapping task on one

healthy subject. (a) Reconstructed maps of HbR (e.g., 20% inflation on the left and 100% inflation on the right side.) from MEM and MNE with different depth compensations. Each map was normalized by its own global maximum. (b) fMRI Z-map results projected along the cortical surface. (c) Reconstructed time courses of HbR within the hand knob region from MEM and MNE. Note that the hand knob region, represented by the black profile, was also matched well with the mean cluster of fMRI activation map on the primary motor cortex. No statistical threshold was applied on fNIRS reconstructions.

Results obtained on 5 subjects for acquisition involving personalized optimal fNIRS montage (montage 2) and corresponding fNIRS reconstructions are presented in Fig.4.8. For every subject, fMRI Z-maps are presented along the left hemisphere only and thresholded at $Z > 3.1$ ($p < 0.01$, corrected using Gaussian random field theory). The most significant fMRI cluster along M1 and S1 was delineated using a black profile. Reconstruction maps at the corresponding HbO/HbR peaks are then presented. Similar accuracy between MEM and MNE, with good overlap with fMRI results, was found for subjects 4 and 5, while MNE was overestimating the spatial extent of the generator. For subjects 1, 2 and 3, MNE exhibited poor spatial correspondence with fMRI results. Averaged reconstructed time courses within the fMRI main cluster region are shown with standard deviation as the error bar. Comparing to simulation results, MEM exhibited overall very similar time course estimations to MNE in all cases. Considering the task duration was 10s, the reconstructed peak timing of HbO/HbR appeared accurately within the range of 10s to 20s.

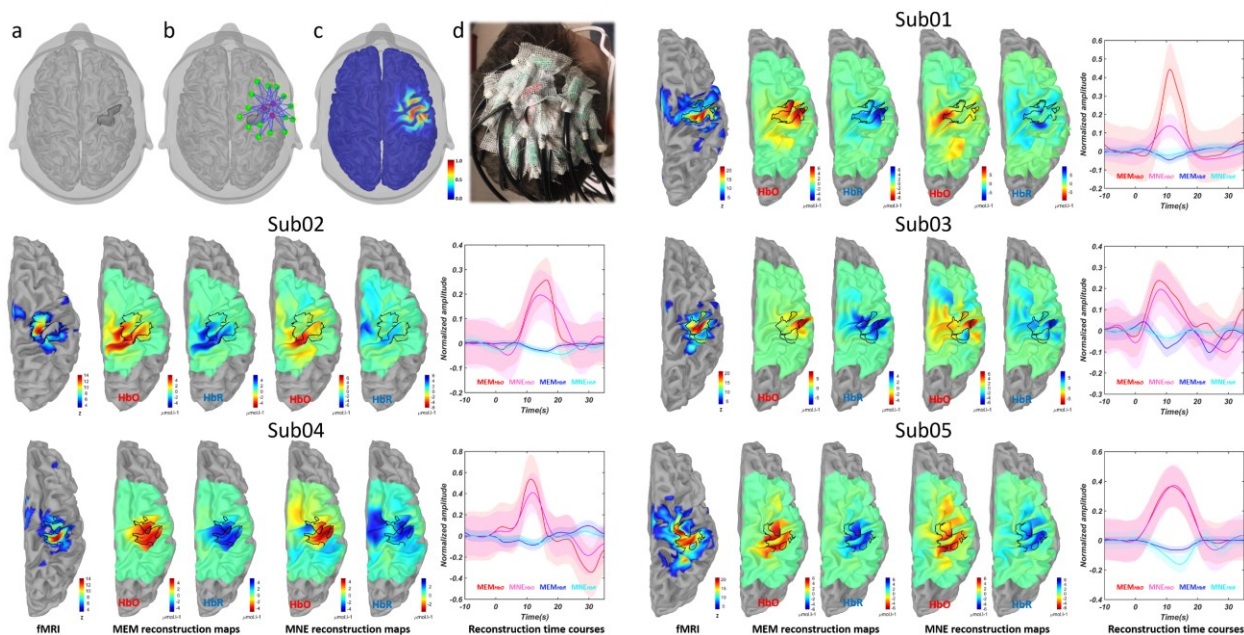


Fig.4.8 Personalized fNIRS montage and comparisons between MEM and MNE reconstructions with

respect to fMRI Z-map at individual level. a) the region of interest defined as the hand knob, b) optimal montage targeting the ROI consisting 3 sources (red) and 15 detectors (green) and one proximity (in the center of sources not shown), c) normalized sensitivity profile of the optimal montage which calculated as the sum of all channels sensitivity along the cortical surface, d) optimal montage glued on the scalp of the one subject, using collodion. fMRI Z-map of each subject during finger tapping task (threshold with $Z > 3.1$, Bonferroni corrected), black profile represents the main cluster along M1 and S1. MEM reconstruction maps at the corresponding HbO/HbR peak times, using depth weighted option 0.3, 0.3. MNE reconstruction maps, at the corresponding HbO/HbR peak times, using depth weighted option 0.3. Reconstructed time courses within the black profile, solid lines represent the main time courses and the shade areas represent standard deviation within the region of interest. Reconstructed time courses were normalized by the maximum amplitude, for each method respectively, before averaging.

4.4 Discussion

4.4.1 Spatial accuracy of 3D fNIRS reconstruction using MEM

In the present study, we first adapted the MEM framework in the context of 3D fNIRS reconstruction and extensively validated its performance. The spatial performance of reconstructions can be considered in two aspects, 1) correctly localizing the peak of the reconstructed map close enough to the ground truth area, 2) accurately recovering the spatial extent of the generator. According to our comprehensive evaluations of the proposed depth-weighted implementations of MEM and MNE methods, accurate localization was overall not difficult to achieve as suggested by our results using Dmin metric. Almost all methods provided median value of Dmin to be 0mm in all simulation conditions except for the lowest $SNR = 1$ condition where more localization error was found. On the other hand, recovering the actual spatial extent of the underlying generator is actually the most challenging task in fNIRS reconstruction. When considering the results of MNE on both realistic simulations and real finger tapping tasks, either from visual inspection (Fig.4.4, Fig.4.7 and Fig.4.8) or quantitative evaluation by SD (Fig.4.3, Table.4.1 and supplementary section S2), we found that MNE overall reconstructed well the main generator but largely overestimated the size of the underlying generator. MEM was specifically developed, in the context of EEG/MEG source imaging, as a method able to recover the spatial extent of the underlying generators, which has been proved not to be the case for MNE based approaches (Chowdhury *et al.*, 2013, 2016; Pellegrino, Hedrich, *et al.*, 2016; Hedrich *et al.*, 2017; Pellegrino *et al.*, 2020). A recent review (Sohrabpour and He, 2021) in the context of EEG/MEG

source imaging has also demonstrated that the Bayesian approach with sparsity constraints is required to accurately estimate the spatial extent. These important properties of MEM were successfully demonstrated in our results on fNIRS reconstructions. These excellent performances were reliable for different sizes and depths of simulated generators, and for real finger tapping fNIRS data as well.

4.4.2 Implementation of depth weighting strategy within the MEM framework

In this study, we are proposing for the first time a depth weighting strategy within the MEM framework, by introducing two parameters: ω_1 acting on scaling the source covariance matrix, and ω_2 tuning the initialization of the reference for MEM. When compared to depth weighted MNE, the MEM framework demonstrated its ability to reconstruct, different depth of focal generators as well as larger size generators, exhibiting excellent accuracy and few false positives (see Fig.4.5). When considering deeper focal generators (depth > 2cm), MEM(0.5, 0.5) clearly outperformed all other methods (see AUC and SD values in Fig.4.5). In summary, for a large range of depths and spatial extents of the underlying generators, MEM methods exhibited accurate results (large AUC values) and less false positives (lower SD values) when compared to MNE methods. In practice, we would suggest to consider either $\omega_2 = 0.3$ or 0.5 for the initialization of MEM in all cases and only tune ω_1 . This is due to the fact that MNE(0.3 or 0.5) provided a generally good reconstruction with larger true positive rate in most scenarios, therefore providing MEM an accurate reference model ($dv(x)$) to start with. Even when considering the most focal simulated generators ($Se = 3$) case (see Fig.4.3, Table.4.1 and Fig.4.5), MEM(0.3, 0.3) and MEM(0.3, 0.5) were actually exhibiting very similar performances. Our proposed suggestion to tune ω_1 and ω_2 parameters was actually further confirmed when considered results obtained from real data. For both montages, MEM(0.3, 0.3) results in excellent spatial agreement with fMRI Z-maps. Note that depth weighting was also considered in DOT studies using MNE (Culver *et al.*, 2003; Deghani, White, *et al.*, 2009; White *et al.*, 2009; Eggebrecht *et al.*, 2012, 2014) and a hierarchical Bayesian DOT algorithm (Shimokawa *et al.*, 2012, 2013a; Yamashita *et al.*, 2016a). A spatially variant regularization parameter β was added to a diagonal regularization matrix featuring the sensitivity of every generator (forward model), and the value of β was tuned according to the sensitivity value of a certain depth. In practice, this strategy would result in similar depth compensation as ours, but we preferred the depth weighting parameter ω which mapped the amount of compensation from 0

to 1 (as described in Eq.4.3) for easier interpretation and comparison. This is also a standard procedure introduced in EEG/MEG source localization studies (Fuchs *et al.*, 1999; Lin *et al.*, 2006). Finally, using the depth weighted MNE solution as the prior is a common consideration in Hierarchical Bayesian framework based fNIRS reconstructions (Shimokawa *et al.*, 2012, 2013b; Yamashita *et al.*, 2016a).

4.4.3 Temporal accuracy of 3D fNIRS reconstruction using MEM

Another important contribution of this study was that we improved the temporal accuracy time courses estimated within the MEM framework, resulting in similar temporal accuracy the one obtained with MNE. For instance, the largest significant SE difference between MEM and MNE was only 0.02 for $Se = 3$ and 0.01 for $Se = 5$. Corresponding time course estimations are also reported for MEM and MNE in real data (Fig.4.7 and Fig.4.8), suggesting again very similar performances. For instance, SE between MEM and MNE HbO time course was estimated as 0.02 for Sub05 in Fig.4.8. Moreover, we found no significant SE differences between MEM and MNE for more extended generators ($Se = 7,9$). These findings are important considering that MNE is just a linear projection therefore the shape of the reconstruction will directly depend on the averaged signal at the channel level. On the other hand, MEM is a nonlinear technique, applied at every time sample, which is not optimized for the estimation of resulting time courses.

4.4.4 Robustness of fNIRS reconstructions to the noise level

To further investigate the effects of the amount of realistic noise in our reconstructions on both reconstruction methods, we performed the comparisons along 4 different SNR levels, i.e., $SNR = 1,2,3,5$. As shown in Fig.4.6 and Table.4.2, we found that MEM was overall more robust than MNE when dealing with simulated signals at lower SNR levels. This is actually a very important result since when reconstructing HbO/HbR responses, one has to consider at least two ΔOD of two different wavelengths exhibiting different SNR levels. For the simulation results, we reported reconstruction results obtained from 830nm data, whereas when considering real data (Fig.4.7 and Fig.4.8), we had to convert the reconstruction absorption changes at 685nm and 830nm into HbO/HbR concentration changes. Therefore, our final results were influenced by the SNR of all involved wavelengths. fNIRS is inherently sensitive to inter-subject variability (Novi *et al.*, 2020), as also suggested in our application on real data presented in Fig.4.8. Data from Sub05 were exhibiting a good SNR level and therefore both MEM and MNE reconstructed accurately the main

cluster of the activation, while MNE presented more spatial spread and false positive activation outside the fMRI ROI. When considering subjects for whom we obtained lower SNR data, e.g., Sub02 and Sub03, MEM still recovered an activation map similar to fMRI map. In those cases, MNE not only reported suspicious activation pattern but also incorrectly reconstruct the peak amplitude outside the fMRI ROI. Our results suggesting MEM robustness in low SNR conditions for DOT are actually aligned with similar findings suggested for EEG/MEG source imaging, when considering source localization of single trial data (Chowdhury *et al.*, 2018; Aydin *et al.*, 2020).

4.4.5 Comprehensive evaluation and comparison of the reconstruction performance using MEM and MNE

To perform a detailed evaluation of our proposed fNIRS reconstructions methods, we developed a fully controlled simulation environment, similar to the one proposed by our team to validate EEG/MEG source localization methods (Chowdhury *et al.*, 2013, 2016; Hedrich *et al.*, 2017). The fNIRS resting state data, acquired by the same montage (montage1) and underwent the same preprocessing as conducted for the real data, was added to the simulated true hemodynamic response for each channel. Indeed such environment provided us access to a ground truth, which is not possible when considering real fNIRS data set. Previous studies validated tomography results (Eggebrecht *et al.*, 2014; Yamashita *et al.*, 2016a) by comparing with fMRI activation map which can indeed be considered as a ground truth, but only for well controlled and reliable paradigms. Since fMRI also measures a signal of hemodynamic origin, it is reasonable to check the concordance between fMRI results and DOT reconstructions. Therefore, as preliminary illustrations, we also compared our MEM and MNE results to fMRI Z-maps obtained during finger tapping tasks on 6 healthy participants, suggesting overall excellent performances of MEM when compared to MNE. Further quantitative comparison between fMRI and fNIRS 3D reconstruction, was out of the scope of this paper and will be considered in future studies.

4.4.6 Availability of the proposed MEM framework

Several software packages have been proposed to provide fNIRS reconstruction pipelines, as for instance NeuroDOT (Eggebrecht *et al.*, 2014; Eggebrecht, Muccigrosso and Culver, 2019), AtlasViewer (Aasted *et al.*, 2015) and fNIRS-SPM (Ye *et al.*, 2009). To ensure an easy access of our MEM methodology to the fNIRS community, we developed and released a fNIRS processing toolbox - NIRSTORM (<https://github.com/Nirstorm>), as a plugin of Brainstorm software (Tadel

et al., 2011), which is a renowned software package dedicated for EEG/MEG analysis and source imaging. Our package NIRSTORM offers standard preprocessing, analysis and visualization as well as more advanced features such as personalized optimal montage design, access to forward model estimation using MCXlab (Fang and Boas, 2009; L. Yu *et al.*, 2018) and the MNE and MEM implementations considered in this study.

4.4.7 Limitations and Perspectives

Previously, Tremblay *et al.*, 2018 had comprehensively compared a variety of fNIRS reconstruction methods using large number of realistic simulations. Since introducing MEM was our main goal of this study, we did not consider such wide range of methodological comparisons. We decided to carefully compare MEM with MNE since MNE remains the main method considered for DOT, and is available in several software packages. As suggested in Tremblay *et al.*, 2018, DOT reconstruction methods based on Tikhonov regularization, such as least square regularization in MNE, usually allow great sensitivity, but performed poorly in term of spatial extent - largely overestimating the size of the underlying generator. On the other hand, L1-based regularization (Süzen, Giannoula and Durduran, 2010; Okawa, Hoshi and Yamada, 2011; Kavuri *et al.*, 2012; Prakash *et al.*, 2014) could achieve more focal solutions with high specificity but much lower sensitivity. As demonstrated in our results, the proposed MEM framework allows reaching good sensitivity and accurate reconstruction of the spatial extent of the underlying generator. Bayesian model averaging (BMA) originally proposed for EEG source imaging by (Trujillo-Barreto, Aubert-Vázquez and Valdés-Sosa, 2004a), also allows accurate DOT reconstructions with less false positives when compared to MNE. Similarly, we carefully compared MEM to Bayesian multiple priors approaches in (Chowdhury *et al.*, 2013) in the context of MEG source imaging. Comparing MEM with more advanced DOT reconstruction methods, including also the one proposed by (Yamashita *et al.*, 2016a), would be of great interest but was out of the scope of this study.

Considering the main contribution of this study was to introduce the MEM framework for 3D fNIRS reconstruction, we decided to first carefully evaluate the performance of MEM, using well controlled realistic simulations. We also included few real data set reconstructions to illustrate the performance of the MEM reconstruction, whereas quantitative evaluation of MEM reconstructions on larger database will be considered in our future investigations. In previously reported studies

(Zeff *et al.*, 2007; White, 2010; Eggebrecht *et al.*, 2012, 2014; Zhan *et al.*, 2012a), a high density montage was considered which was proved to be able to provide high spatial resolution and robustness to low SNR conditions (White, 2010), evaluating the performance of MEM when considering high density fNIRS montage would be of great interest but was out of the scope of this present study.

4.5 Conclusion

In this study, we introduced a new fNIRS reconstruction method entitled Maximum Entropy on the Mean (MEM). We first implemented depth weighting into MEM framework and improved its temporal accuracy. To carefully validate the method, we applied a large number ($n=4000$) of realistic simulations with various spatial extents and depths. We also evaluated the robustness of the method when dealing with low SNR signals. The comparison of the proposed method with the widely used depth weighted MNE was performed by applying four different quantification validation metrics. We found that the MEM framework provided accurate and robust reconstruction results, relatively stable for a large range of spatial extents, depths and SNRs of the underlying generator. Moreover, we implemented the proposed method into a new fNIRS processing plugin - NIRSTORM in Brainstorm software to provide the access of the method to users for applications, validations and comparisons.

4.6 Supplementary material

S1. Validation metrics

Here is a detailed description of the four validation metrics considered in our evaluation. Except for the shape error (SE), other metrics were all calculated at the time instant τ when the simulated ΔOD time course reached its peak value (e.g., 12.2s after onset).

Area Under the Receiver Operating Characteristic (ROC) curve (AUC) was used to assess the overall detection accuracy of the reconstruction methods. We used a specific version of AUC that has been proposed in (Grova, Daunizeau, *et al.*, 2006) in order not to bias results towards false positives. In further detail, ROC curves were generated by plotting the sensibility of the detection as a function of 1-specificity, while thresholding the normalized reconstruction map from 0 to 1 with a certain step value. In the context of source reconstruction, especially when the generator is focal, the region of true positive is usually much smaller than the region of true negative, whereas

non-biased AUC evaluation would require to sample the same amount of active and inactive generators. To overcome this possible bias, we considered a ROC evaluation using the same number of active and inactive generators that were randomly sampled within two different regions: 1) AUC_{close} : inactive generators were sampled within the immediate spatial neighborhood of the ground truth; and 2) AUC_{far} : inactive generators were sampled within the local maxima of the reconstructed activity located far from the ground truth. The final AUC was then the average of AUC_{close} and AUC_{far} .

Minimum geodesic distance (D_{min}) was represented by the geodesic distance, following the circumvolutions of the cortical surface, of the vertex that exhibited maximum of reconstructed activity to the border of the 'generator'. It should be 0 when the peak of the reconstruction map was located inside the simulated cortical region.

Spatial Dispersion (SD) assessed the spatial spread of the estimated 'generator' distribution and the localization error using Eq.4.1. The ideal value (i.e., $SD = 0mm$), was achieved when no activation was reconstructed outside the theoretical 'generator'. The larger the SD was, the more spatially spread were the reconstructed maps.

$$SD = \sqrt{\frac{\sum_{i=1}^K \left(\min_{j \in \Theta} (D^2(i, j)) \widehat{X}^2(i, \tau) \right)}{\sum_{i=1}^K \left(\widehat{X}^2(i, \tau) \right)}} \quad (4.14)$$

where $\min_{j \in \Theta} (D^2(i, j))$ is the minimum Euclidean distance between the vertex i to the vertex j which is located inside the simulated 'generator' (Θ). $\widehat{X}^2(i, \tau)$ is the power of the amplitude of reconstructed time course on vertex i at time τ . K is the total number of vertices within the reconstruction field of view.

Shape error (SE) evaluated the temporal accuracy of the reconstruction. Reconstructed time courses within the simulation 'generator' were averaged and normalized. The root mean square of the difference between this time course and the normalized theoretical time course was estimated and denoted as SE in Eq.4.15 as introduced in (Chowdhury *et al.*, 2013).

$$SE = \sqrt{\frac{1}{T} \sum_t \left(\frac{X_{th}(t)}{\max(|X_{th}(t)|)} - \frac{\text{mean}_{j \in \Theta}(\hat{X}(j, t))}{\max(|\text{mean}_{j \in \Theta}(\hat{X}(j, t))|)} \right)^2} \quad (4.15)$$

where T is the length of the time course. $X_{th}(t)$ is the theoretical time course of the simulation. $\text{mean}_{j \in \Theta}(\hat{X}(j, t))$ is the averaged mean of the reconstructed time courses within the 'generator'.

S2. Effects of depth weighting on MNE

We first investigated the effects of the depth weighting factor ω_2 selection for depth weighted MNE. To do so, we evaluated the spatial and temporal performances of DOT reconstruction. As presented in Fig.4.S1, we compared depth weighted MNE using depth weighting factors $\omega_2 = 0, 0.1, 0.3, 0.5, 0.7, 0.9$ in superficial seeds case. In general, $\omega_2 = 0.3$ and 0.5 provided overall the most accurate results (i.e., median $AUC > 0.8$ and $D_{min} = 0 \text{ mm}$). For focal generators (i.e., $Se = 3, 5$), $\omega_2 = 0.3$ performed better than $\omega_2 = 0.5$ considering it was providing significantly lower SD. However, in extended generators (i.e., $Se = 7, 9$), reconstructions with $\omega_2 = 0.5$ were exhibiting more accurate results, consisting in significantly positive AUC difference (0.05 and 0.08, $p < 0.001$) and significantly positive SD difference (2.24 and 2.06, $p < 0.001$). $\omega_2 = 0$ and 0.1 only provided AUC higher than 0.8 in the case of $Se = 3$, whereas $\omega_2 = 0.7$ and 0.9 failed in all cases and even the median values of D_{min} were significantly larger (median values around 2-3 cm) than other cases. Based on these results, we decided to consider only the depth weighting values $\omega_2 = 0.3$ and 0.5 for depth weighting MNE in the comparisons with MEM reconstructions.

S3. MEM v.s. MNE with realistic simulations involving middle and deep seeds

In Fig.4.S2 and Table.4.S1, we are presenting the comparison of MEM and MNE in middle seeds cases. First of all, we found that more depth compensation was required to provide good reconstructions in all scenarios. Thus, MEM(0.5, 0.5) was compared to the best of MNE - MNE(0.5). Non-significant AUC and D_{min} differences were found between them. However, MEM(0.5, 0.5) provided significant lower SD than MNE(0.5), median value of difference of $SD = -5.3, -4.80, -5.00, -4.95$, $p < 0.001$ for $Se = 3, 5, 7, 9$ respectively. Fig.4.S3 and Table.4.S2 are presenting the comparison of MEM and MNE in the comparison of them in deep seeds case. Similarly, no significant AUC and D_{min} differences were found. MEM(0.5, 0.5) provided

significant lower SD than MNE(0.5), median value of difference of $SD = -6.39, -6.33, -6.97, -5.52$, $p < 0.001$ for $Se = 3, 5, 7, 9$ respectively. For temporal performance in these two cases, similar to Fig.4.3, MNE(0.5) gave significantly lower SE (-0.01 or -0.02, $p < 0.001$) than MEM when $Se = 3, 5$ (small difference). No significant difference in SE was found in $Se = 7, 9$.

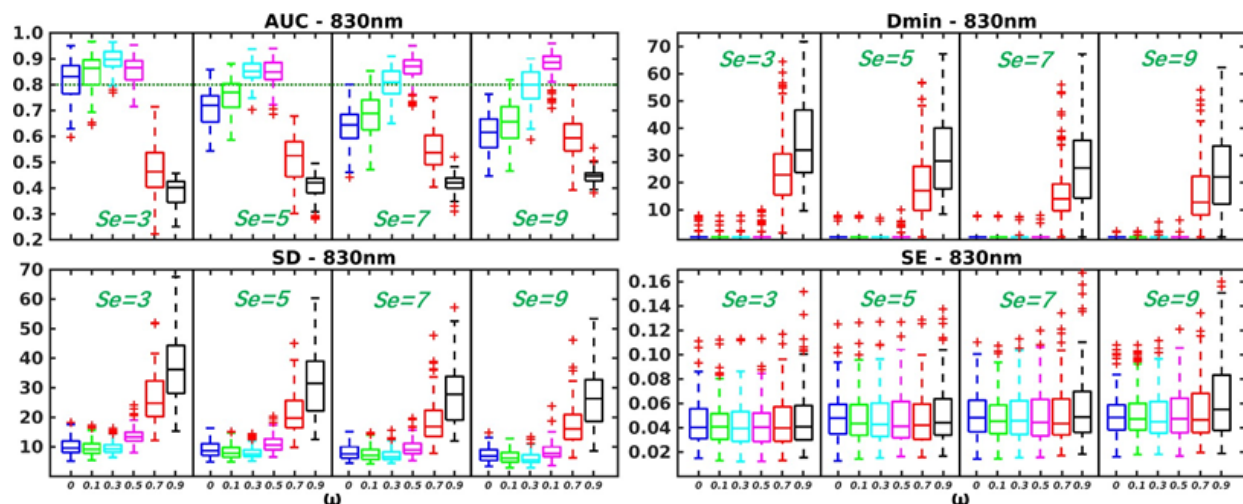


Fig.4.S1. Evaluation of the performances of depth weighted MNE for different depth weighting factors $\omega = 0, 0.1, 0.3, 0.5, 0.7, 0.9$. Distribution of validation metrics (AUC, Dmin, SD and SE) are displayed using boxplot representations, for simulations involving superficial seeds only and for spatial extents $Se = 3, 5, 7, 9$.

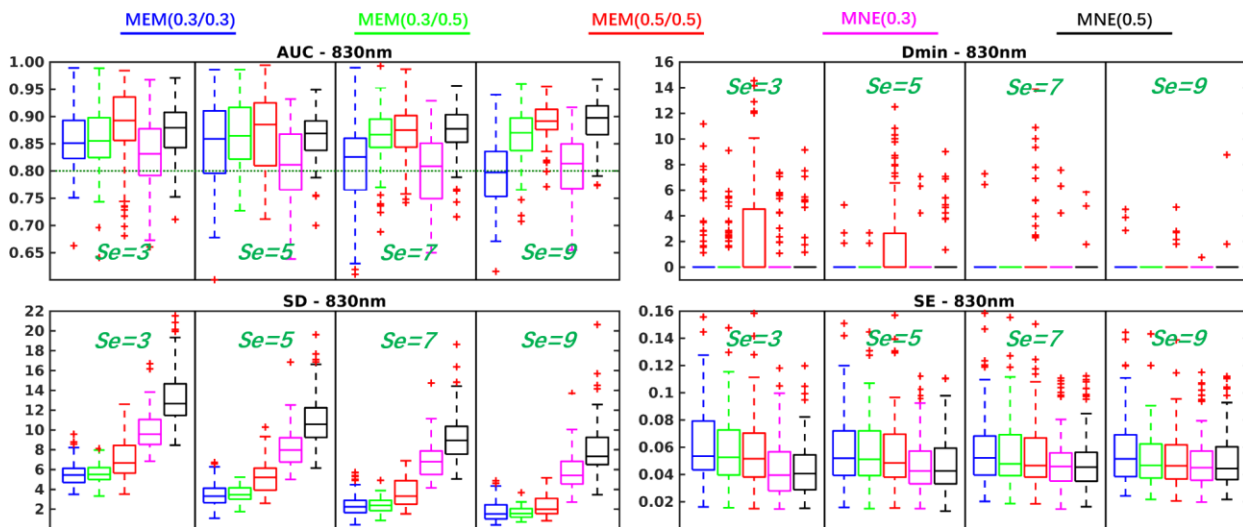


Fig.4.S2 Evaluation of the performances of MEM and MNE using realistic simulations involving middle seeds for different spatial extent ($Se = 3, 5, 7, 9$). Boxplot representation of the distribution of four validation metrics for three depth weighted strategies of MEM and two depth weighted strategies of MNE, namely: MEM(0.3, 0.3) in blue, MEM(0.3, 0.5) in green, MEM(0.5, 0.5) in red, MNE(0.3) in magenta and MNE(0.5) in black.

MNE(0.5) in black. Results were obtained after DOT reconstruction of 830nm ΔOD .

Middle Seeds		Se = 3		Se = 5		Se = 7		Se = 9	
		MNE (0.3)	MNE (0.5)						
AUC	MEM (0.3, 0.3)	0.03**	-0.03	0.03**	0.00	0.02	-0.05**	-0.02	-0.10**
	MEM (0.3, 0.5)	0.03**	-0.03	0.05**	0.01	0.05**	-0.01	0.05**	-0.02**
	MEM (0.5, 0.5)	0.06**	0.02	0.07**	0.01	0.07**	-0.01	0.08**	0.00
Dmin	MEM (0.3, 0.3)	0.00	0.00	0.00	0.00	0.00	0.00	0.00	0.00
	MEM (0.3, 0.5)	0.00	0.00	0.00	0.00	0.00	0.00	0.00	0.00
	MEM (0.5, 0.5)	0.00	0.00	0.00	0.00	0.00	0.00	0.00	0.00
SD	MEM (0.3, 0.3)	-4.05**	-7.21**	-4.27**	-7.25**	-4.10**	-6.40**	-3.58**	-5.43**
	MEM (0.3, 0.5)	-4.00**	-7.06**	-4.09**	-6.90**	-3.96**	-6.40**	-3.65**	-5.45**
	MEM (0.5, 0.5)	-2.54**	-5.33**	-2.46**	-4.80**	-2.85**	-5.00**	-3.08**	-4.95**
SE	MEM (0.3, 0.3)	0.02**	0.02**	0.01**	0.01**	0.01**	0.01*	0.00	0.01
	MEM (0.3, 0.5)	0.01**	0.01**	0.01**	0.01**	0.00	0.00	0.00	0.00
	MEM (0.5, 0.5)	0.01**	0.01**	0.01**	0.01*	0.00	0.00	0.00	0.00

Table.4.S1. Wilcoxon signed rank test results of reconstruction performance comparison of MEM and MNE in middle seeds case. Median values of paired differences are presented in the table. p values were corrected for multiple comparisons using Bonferroni correction, *indicates $p < 0.01$ and ** represents $p < 0.001$. Median of the paired difference of each validation metrics are color coded as follows: green: MEM is significantly better than MNE, red: MNE is significantly better than MEM and gray: non-significance.

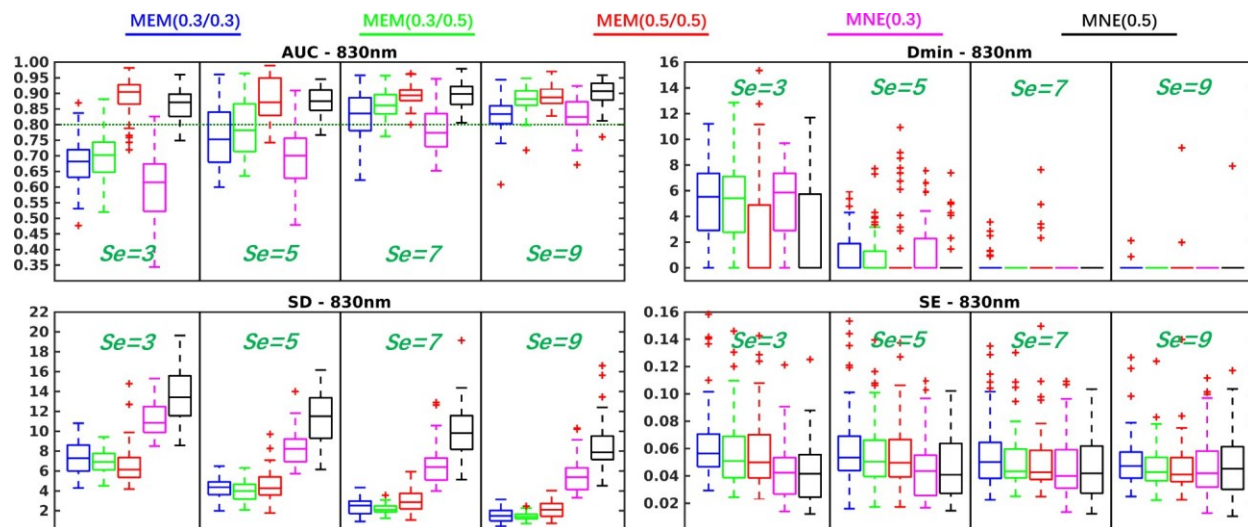


Fig.4.S3. Evaluation of the performances of MEM and MNE using realistic simulations involving deep seeds for different spatial extent ($Se = 3, 5, 7, 9$). Boxplot representation of the distribution of four validation metrics for three depth weighted strategies of MEM and two depth weighted strategies of MNE, namely: MEM(0.3, 0.3) in blue, MEM(0.3, 0.5) in green, MEM(0.5, 0.5) in red, MNE(0.3) in magenta and

MNE(0.5) in black. Results were obtained after DOT reconstruction of 830nm ΔOD .

Deep Seeds		Se = 3		Se = 5		Se = 7		Se = 9	
		MNE (0.3)	MNE (0.5)						
AUC	MEM (0.3, 0.3)	0.08**	-0.20**	0.06**	-0.13**	0.05**	-0.08**	0.00	-0.07**
	MEM (0.3, 0.5)	0.09**	-0.17**	0.08**	-0.08**	0.08**	-0.03*	0.05**	-0.02
	MEM (0.5, 0.5)	0.29**	0.03	0.18**	-0.01	0.13**	-0.01	0.06**	-0.01
Dmin	MEM (0.3, 0.3)	0.00	2.91	0.00	0.00	0.00	0.00	0.00	0.00
	MEM (0.3, 0.5)	0.00	2.16	0.00	0.00	0.00	0.00	0.00	0.00
	MEM (0.5, 0.5)	-3.53	0.00	0.00	0.00	0.00	0.00	0.00	0.00
SD	MEM (0.3, 0.3)	-3.73**	-6.25**	-3.65**	-7.37**	-3.51**	-7.39**	-3.46**	-6.21**
	MEM (0.3, 0.5)	-4.00**	-6.61**	-3.83**	-7.54**	-3.95**	-7.63**	-3.82**	-6.50**
	MEM (0.5, 0.5)	-4.56**	-6.39**	-3.73**	-6.33**	-3.10**	-6.97**	-3.33**	-5.52**
SE	MEM (0.3, 0.3)	0.02**	0.02**	0.02**	0.02**	0.01*	0.01	0.01	0.00
	MEM (0.3, 0.5)	0.01**	0.01**	0.01*	0.01**	0.01	0.01	0.00	0.00
	MEM (0.5, 0.5)	0.01*	0.01**	0.01*	0.01*	0.00	0.01	0.00	0.00

Table.4.S2. Wilcoxon signed rank test results of reconstruction performance comparison of MEM and MNE in deep seeds case. Median values of paired differences are presented in the table. *p* values were corrected for multiple comparisons using Bonferroni correction, * indicates $p < 0.01$ and ** represents $p < 0.001$. Median of the paired difference of each validation metrics are color coded as follows: green: MEM is significantly better than MNE, red: MNE is significantly better than MEM and gray: non-significance.

Chapter 5

Manuscript 2: Evaluation of a Personalized Functional Near Infra-Red Optical Tomography Workflow using Maximum Entropy on the Mean

Context

In Chapter 4, we presented a new version of MEM framework dedicated to NIROT reconstruction. Its performance has also been carefully evaluated using realistic simulations along the cortical surface with different conditions (e.g., location, size, and depth). In source imaging literature for both EEG/MEG and fNIRS, an appropriate way to evaluate the reconstruction method consists of two steps: 1) evaluation with simulation data in which a ground truth is given, completed in Chapter 4; 2) application on real data, usually applied on relatively well-controlled tasks, such as finger tapping (Yamashita *et al.*, 2016b), visual tasks (Zeff *et al.*, 2007; Eggebrecht *et al.*, 2012) and median nerve stimulations (Huppert *et al.*, 2017). Hence, we conducted this second study to further evaluate the proposed MEM reconstructions. Moreover, we opted in this study to introduce a workflow of NIROT, integrating all of our methodology developments. Since in a real data scenario we do not have a ground truth area for fNIRS reconstruction validation, we also performed fMRI acquisitions and considered the resulting individual activation map as the reference for the validation. Task performance during fMRI is known to be variable, especially in terms of the size of the main cluster of activation (Zandbelt *et al.*, 2008; Quiton *et al.*, 2014). Therefore, we proposed to use the size of the main cluster estimated from group level analysis, to inform the expected size of the main cluster of activation at the individual level. Additionally, we also assessed the reliability of NIROT reconstruction performance, using a non-parametric measure called discriminability (Bridgeford *et al.*, 2018; Wang *et al.*, 2020). MEM and also MNE were considered as NIROT methods to conduct performance and reliability comparisons.

This manuscript is published in *Human Brain Mapping* journal, Zhengchen Cai, Makoto Uji, Ümit Aydın, Giovanni Pellegrino, Amanda Spilkin, Edouard Delaire, Chifaou Abdallah, Jean-Marc Lina, Christophe Grova. Evaluation of a Personalized Functional Near Infra-Red Optical Tomography Workflow using Maximum Entropy on the Mean.

Abstract

In the present study, we proposed and evaluated a workflow of personalized Near Infra-Red Optical Tomography (NIROT) using functional Near-Infrared Spectroscopy (fNIRS) for spatio-temporal imaging of cortical hemodynamic fluctuations. The proposed workflow from fNIRS data acquisition to local 3D reconstruction consists of: 1) the personalized optimal montage maximizing fNIRS channel sensitivity to a predefined targeted brain region; 2) the optimized fNIRS data acquisition involving installation of optodes and digitalization of their positions using a neuronavigation system; and 3) the 3D local reconstruction using Maximum Entropy on the Mean (MEM) to accurately estimate the location and spatial extent of fNIRS hemodynamic fluctuations along the cortical surface. The workflow was evaluated on finger-tapping fNIRS data acquired from ten healthy subjects for whom we estimated the reconstructed NIROT spatio-temporal images and compared with functional Magnetic Resonance Imaging (fMRI) results from the same individuals. Using the fMRI activation maps as our reference, we quantitatively compared the performance of two NIROT approaches, the MEM framework and the conventional Minimum Norm Estimation (MNE) method. Quantitative comparisons were performed at both single subject and group-level. Overall, our results suggested that MEM provided better spatial accuracy than MNE, while both methods offered similar temporal accuracy when reconstructing oxygenated (HbO) and deoxygenated hemoglobin (HbR) concentration changes evoked by finger-tapping. Our proposed complete workflow was made available in the Brainstorm fNIRS processing plugin – NIRSTORM, thus providing the opportunity for other researchers to further apply it to other tasks and on larger populations.

5.1 Introduction

Functional Near Infra-Red spectroscopy (fNIRS) non-invasively measures fluctuations of both oxygenated and deoxygenated hemoglobin (i.e. HbO and HbR) in the cerebral cortex with high temporal resolution (Jöbsis, 1977; Scholkmann, Kleiser, *et al.*, 2014; Yücel *et al.*, 2021). fNIRS raw data measured by source-detector pairs called channels refer to light intensity changes at specific wavelengths (e.g., 685nm and 830nm), modulated by local absorption associated with underlying fluctuations of hemoglobin concentrations. Concentration changes in HbO/HbR in each channel are usually estimated via the modified Beer-Lambert Law (mBLL) (Delpy *et al.*, 1988).

Importantly, the channel space analysis assumes homogeneous concentration changes within the underlying region(s) of interest. Such an assumption actually introduces systemic errors when dealing with focal hemodynamic responses (Boas, Gaudette, *et al.*, 2001; Strangman, Franceschini and Boas, 2003). Near Infra-Red Optical Tomography (NIROT) is a powerful alternative to channel space analysis to overcome this issue, as well as to generate hemodynamic images along the cortical surface (Arridge, 1999; Boas, Brooks, *et al.*, 2001). NIROT avoids the homogeneity assumption by reconstructing the light intensity changes measured in the channel space on the underneath cortical area, before converting them into local hemodynamic HbO/HbR fluctuations. NIROT reconstruction actually consists in solving an ill-posed inverse problem that requires specific regularization to obtain a unique solution.

The first step of NIROT involves the definition of a specific fNIRS channel layout, also called the montage, used for data acquisition, which should allow sufficient density and spatial overlap between channels to allow accurate 3D reconstruction (White and Culver, 2010). A high-density montage involving various channel distances and extensive overlapping between channels was initially proposed in (Zeff *et al.*, 2007; White and Culver, 2010) and successfully considered in several NIROT studies (Eggebrecht *et al.*, 2012, 2014; Ferradal *et al.*, 2016; Hassanpour *et al.*, 2017; Fishell *et al.*, 2019). However, fNIRS devices allowing such high-density montages are not widely accessible and are usually custom-made solutions not available commercially. In previous studies (Machado *et al.*, 2014b, 2018), our group has proposed an approach entitled –*personalized optimal montage*, which maximizes the fNIRS channel layout's sensitivity to a targeted region of interest along the cortex, suggesting fNIRS as a technique mainly used to accurately and locally explore hemodynamic processes, rather than a whole brain imaging technique. While avoiding the need for a large high-density montage, our approach could provide a personalized fNIRS montage maximizing the detection efficiency as well as maintaining a sufficient number of channels and spatial overlap to allow local reconstruction of NIROT images.

The other important step when considering NIROT is to solve the inverse problem to reconstruct HbO/HbR maps along the cortex from the channel space measurements. This inverse problem is ill-posed such that there are infinite number of solutions. Therefore, regularization is required to estimate a unique solution. The most widely used inverse problem estimator is the so-called Minimum Norm Estimation (MNE), which was first proposed by (Hämäläinen and Ilmoniemi, 1994) for Electroencephalography (EEG) and Magnetoencephalography (MEG) source

localization and since then applied in several fNIRS reconstruction studies (Zeff *et al.*, 2007; Dehghani, White, *et al.*, 2009; Eggebrecht *et al.*, 2012, 2014). MNE consists of applying Tikhonov regularization to minimize the L2-norm when solving the ill-posed inverse problem.

The Maximum Entropy on the Mean (MEM) framework was first proposed by (Amblard, Lapalme and Lina, 2004), before being adapted and carefully evaluated in the context of EEG/MEG source localization (Grova, Daunizeau, *et al.*, 2006; Chowdhury *et al.*, 2013). A key property of MEM source imaging is its ability to accurately recover the spatial extent of the generators, as demonstrated in the context of: 1) localizing transient epileptic discharges (Chowdhury *et al.*, 2016; Grova *et al.*, 2016; Heers *et al.*, 2016; Pellegrino, Hedrich, *et al.*, 2016; Pellegrino *et al.*, 2020) and oscillations (Pellegrino, Hedrich, *et al.*, 2016; Avigdor *et al.*, 2021); 2) localizing focal sources, such as those evoked by electrical median nerve stimulations (Hedrich *et al.*, 2017); 3) EEG/MEG fusion in the presurgical evaluation of epilepsy (Chowdhury *et al.*, 2018); and 4) MEG resting state connectivity (Aydin *et al.*, 2020). In our previous study (Cai *et al.*, 2021), we adapted the MEM framework to perform fNIRS reconstructions to generate NIROT images and then carefully evaluated MEM performance within a comprehensive and realistic simulation framework. In this study, we opted to combine the above methodology developments as a workflow for conducting NIROT and evaluated its performance using the real data acquired during a motor task.

Here, we introduce a comprehensive NIROT workflow, *the personalized NIROT using MEM*, to accurately reconstruct and assess HbO/HbR fluctuations within targeted brain regions. Our workflow allows: 1) experiment planning and optimal probe design; 2) personalized fNIRS montage installation and digitalization of sensor positions using the neuro-navigation device and 3) reconstruction of hemodynamic images using the MEM method. To evaluate the workflow, we considered a finger tapping task applied on a cohort of 10 healthy participants who performed the task twice, once during fMRI and then during personalized fNIRS data acquisition. fMRI Z-maps served as the reference for validation purposes. Evaluations were conducted by visual inspections of the reconstructed NIROT maps and using several quantitative validation metrics such as Area Under the Receiver Operating Characteristic (ROC) curve (AUC), Minimum geodesic distance (D_{min}), Spatial Dispersion (SD) and reconstructed HbO/HbR peak times. We also compared MEM reconstructions to the conventional MNE approach. Finally, we also assessed the reliability (M. Yu *et al.*, 2018; Zuo, Xu and Milham, 2019) of the performance differences between MEM

and MNE, using a non-parametric measure of discriminability (Bridgeford *et al.*, 2018; Wang *et al.*, 2020).

5.1 Materials and methods

5.2.1 Subject cohort and experiment protocol

Ten healthy subjects (24 ± 5 years old, right-handed) participated in this study. The study was approved by the Central Committee of Research Ethics of the Minister of Health and Social Services Research Ethics Board, (CCER), Québec, Canada. All subjects signed a written informed consent before participating in the study.

The study comprised two sessions for each participant who performed the same task during a fMRI scan and a personalized fNIRS scan. Participants performed a finger-tapping task which consisted of tapping the left thumb to the other four digits sequentially, with a pace at around 2Hz. The duration of the finger tapping block was 10s, and blocks were interleaved with a resting period lasting between 30s to 60s (i.e., one random sampled resting period in this range per block). In the fMRI scan, during the resting period, participants looked at a fixation cross through a mirror placed above the subjects' forehead. They were also asked not to move the head and body while tapping the finger to reduce motion artifacts. The beginning/end of each block was signalled by an auditory cue. The inter-block interval was set so to reduce the influence caused by physiological and systemic fluctuations so to achieve a better estimation of task-evoked brain hemodynamic responses (Aarabi, Osharina and Wallois, 2017). The finger tapping-rest sequence was repeated 20 times, for around 16 minutes scan duration.

5.2.2 Structural and functional MRI acquisitions

Each participant underwent anatomical and functional MRI with a General Electric Discovery MR750 3T scanner at the PERFORM Centre of Concordia University, Montréal, Canada. The anatomical scans were performed for fNIRS head model, optimal montage, and coregistration between anatomical and fMRI data. In details, data were recorded with the following parameters:

- T1-weighted anatomical images with the 3D BRAVO sequence ($1 \times 1 \times 1 \text{ mm}^3$, 192 axial slices, 256×256 matrix).

- T2-weighted anatomical images were scanned using the 3D Cube T2 sequence ($1 \times 1 \times 1 \text{ mm}^3$ voxels, 168 sagittal slices, 256×256 matrix).
- fMRI images with a gradient echo EPI sequence ($3.7 \times 3.7 \times 3.7 \text{ mm}^3$, 32 axial slices, TE = 25ms, TR = 2000ms, 70° flip angle).

5.2.3 Anatomical data processing

High-resolution T1- and T2-weighted images were processed using FreeSurfer 6.0 (Fischl *et al.*, 2002) (<https://surfer.nmr.mgh.harvard.edu/fswiki/FreeSurferWiki>) and SPM12 [Penny *et al.*, 2011] (<https://www.fil.ion.ucl.ac.uk/spm/software/spm12/>) to segment the head into five tissues (i.e., scalp, skull, Cerebrospinal fluid (CSF), gray matter and white matter). Gray matter and white matter masks were generated from the cortical/subcortical segmentation of FreeSurfer. Scalp and skull masks were segmented using SPM. All segmentation processes used both T1 and T2 weighted images to achieve more accurate estimations of the tissue types by taking advantage of their complementary contrasts. Anatomical surfaces such as pial surface, gray/white matter interface and mid surface (i.e. a middle layer of the gray matter) were estimated using FreeSurfer (Fischl and Dale, 2000).

5.2.4 fMRI data processing

fMRI data were processed using FSL v6.0.0 (<https://fsl.fmrib.ox.ac.uk/fsl/>) (Jenkinson *et al.*, 2012). Data pre-processing included the following steps: 1) slice timing correction using interleaved Hanning-windowed interpolation; 2) brain extraction using BET2; 3) head motion correction applying rigid-body transformations (MCFLIRT); 4) spatial smoothing (5 mm FWHM Gaussian kernel); 5) high-pass temporal filtering (45s cut-off) and 6) registration to the individual T1 anatomical image (FLIRT, linear transformation with 6 degrees of freedom), and normalization (linear affine transformation with 12 degrees of freedom) to the MNI (Montreal Neurological Institute and Hospital) 1mm standard brain template (i.e., ICBM152).

The first-level general linear model (GLM) analyses were performed using FEAT v6.0 (Woolrich *et al.*, 2001), employing boxcar (10s) finger-tapping events convolved with the double-gamma Hemodynamic Response Function (HRF). Time series analysis was carried out using FILM (Woolrich *et al.*, 2001) with local autocorrelation correction. The resulting first-level task-evoked

BOLD Z statistic images were thresholded using Gaussian random field theory based maximum height thresholding (Worsley, 2001) with the voxel-wise inference ($p < 0.01$, corrected). To allow visual and quantitative comparison with NIROT, individual images estimated along the cortical surface, individual volumetric fMRI Z-maps were projected onto the mid-surface (downsampled to 25,000 vertices) using a Voronoi-based projection, which is a volume to surface interpolation method able to preserve sulco-gyral morphology (Grova, Makni, *et al.*, 2006). Z-values were averaged within each Voronoi cell and assigned to the corresponding vertex of the cortical surface.

By using each subject's volume-based fMRI first-level results, we conducted a group-level analysis in order to identify a reliable fMRI reference region of interest (ROI) to be considered as our 'ground truth' for NIROT images evaluation. This group-level analysis was performed using a mixed-effects model – FLAME1 in FEAT (Woolrich *et al.*, 2004). The resulted BOLD Z-statistic images were thresholded using Gaussian random field theory based maximum height thresholding (Worsley, 2001) (clusters determined $Z > 3.1$, cluster significance threshold of $p < 0.01$, corrected). The thresholded fMRI group-level Z-map registered on the MNI standard template (see Supplementary Fig.5.S1) was projected onto the mid-surface of the template per se, using the same Voronoi projection method previously mentioned. The significant region on the surface was determined according to the Z threshold of volume-based results.

5.2.5 Personalized fNIRS data acquisition and pre-processing

fNIRS data acquisition was conducted in the Multimodal Functional Imaging Laboratory at PERFORM Center (Concordia University, Montréal, Canada) using a continuous wave Brainsight fNIRS device (Rogue-Research Inc, Montreal, Canada). Personalized fNIRS acquisition strategy consists of estimating a subject-specific optimal fNIRS montage to maximize, a priori, the fNIRS sensitivity to the hemodynamic activity in some targeted brain regions, while ensuring sufficient spatial coverage and overlap to allow accurate local 3D reconstruction (Machado *et al.*, 2014b, 2018). In this study, the hand-knob region within the right primary motor cortex was defined as the individual ROI. It was selected manually along the cortical surface (see Fig.5.1.a), taking into account anatomical landmarks (Raffin *et al.*, 2015a) and using the Brainstorm software (Tadel *et al.*, 2011) (<http://neuroimage.usc.edu/brainstorm>). Then, we estimated a personalized optimal fNIRS montage under the following constraints (see Fig.5.1.b): 1) 3 sources and 15 detectors; 2)

source-detector distance between 2.0cm and 4.5cm; 3) spatial overlap between channels - signal from each source to be detected by at least 13 out of 15 detectors. For each candidate source/detector pair, a fNIRS forward model, computed using MCXLab Monte Carlo Photon simulator (Fang and Boas, 2009; L. Yu *et al.*, 2018) was considered to measure light sensitivity within the target region. The output of the resulting optimization algorithm under proposed constraints, consisted in a set of spatial 3D coordinates indicating the optimal position of the optodes on subject's scalp. Please find further details in (Machado *et al.*, 2014b, 2018; Cai *et al.*, 2021). To monitor systemic fluctuations within superficial layers, we also added one proximity detector (i.e., $\sim 0.7\text{cm}$ to each source), located in the center of the 3 sources of the montage. These optimal 3D coordinates were loaded into a neuro-navigation system (Brainsight TMS navigation system, Rogue-Research Inc, Montreal) to guide the installation of the optodes on the scalp (Machado *et al.*, 2018). fNIRS sensors were then glued on the scalp (see Fig.5.1.d) using a clinical adhesive, called collodion, in order to minimize sensitivity to motion artifacts and to improve fNIRS signal to noise ratio (Yücel *et al.*, 2014; Machado *et al.*, 2018).

Raw fNIRS data were then pre-processed using a conventional pipeline. Channels exhibiting either negative raw amplitude or a coefficient of variation (standard deviation over the signal mean) larger than 8% were classified as low-quality and rejected (Schmitz *et al.*, 2005; Schneider *et al.*, 2011; Eggebrecht *et al.*, 2012; Piper *et al.*, 2014). Superficial physiological fluctuations, also considered here as noise, were modelled by the average signal of all proximity channels and were regressed out from all channels using a linear regression (Zeff *et al.*, 2007). All channels were band-pass filtered between 0.01Hz and 0.1Hz using a 3rd order Butterworth filter. Optical density changes (i.e., ΔOD), normalized for each channel by the mean amplitude of the entire time course, were calculated using the logarithm conversion of the filtered signal. ΔOD epochs with a time window ranging from -10s to 30s around the task onset were extracted, and noisy epochs were rejected through visual inspections (i.e., overall, less than 4 out of 20 epochs were rejected for each subject, mainly caused by motion artifacts). Then, the resulting epochs were averaged. This epoch averaged ΔOD , measured either at 685nm or 830nm, was the input signal of fNIRS reconstruction algorithm to obtain the NIROT images for each subject.

5.2.6 Forward model estimation for NIROT

The subject-specific head model was calculated to estimate how a local change in light absorption elicited by the hemodynamic response at a specific vertex of the cortical area would impact fNIRS signals on scalp channels. Volume-based subject-specific head segmentation (e.g., scalp, skull, CSF, grey matter and white matter), were used to model the light propagation from each optode of the optimal montage within head tissues. We assigned each tissue the same optical coefficients used in (Fang and Boas, 2009; Machado *et al.*, 2018) for the two wavelengths (i.e. 685nm and 830nm). Fluences of each wavelength for each optode were calculated by simulating the propagation of 10^8 photons using MCXLAB (Fang and Boas, 2009; L. Yu *et al.*, 2018) (<http://mcx.space/wiki/index.cgi?MCX>). Each voxel's sensitivity value corresponding to each fNIRS channel was then computed using the adjoint formulation with the Rytov approximation (Arridge, 1999).

To constrain the fNIRS reconstruction space within the cortical region (Boas and Dale, 2005), we applied volume-to-surface interpolation using Voronoi (Grova, Makni, *et al.*, 2006) to generate surface based sensitivity matrix along the mid cortical surface (please see (Cai *et al.*, 2021) for further details).

Finally, to define the field of view (FOV) of fNIRS reconstruction, this surface-based sensitivity was further spatially constrained to be within 3cm to any optode of a specific optimal montage, Euclidean distance calculated from 100% inflated cortical surface to the head surface by Brainstorm.

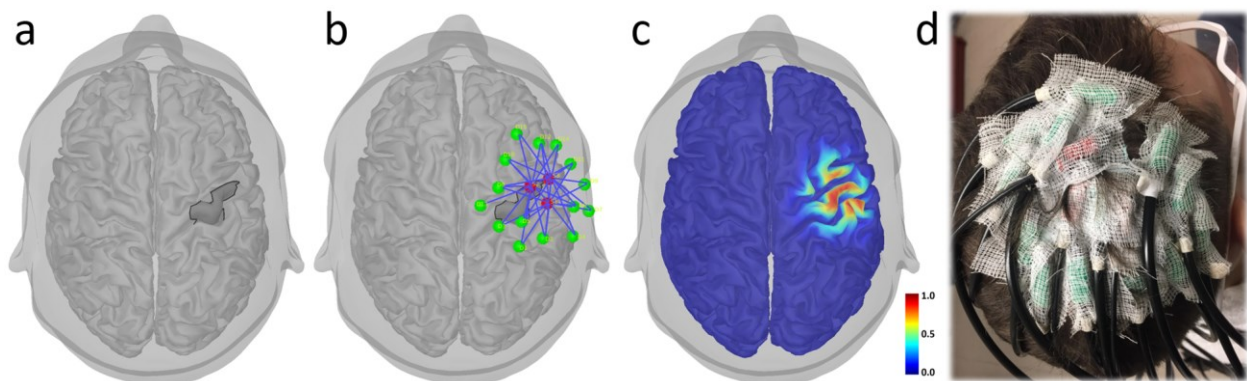


Fig.5.1 Personalized fNIRS investigation using an optimal montage targeting the right motor cortex. a) black profile represents the right ‘hand knob’ targeted region of interest, b) resulting personalized optimal montage targeting this ROI consisting of 3 sources (red), 15 detectors (green) and one proximity (in the center of sources not shown), c) normalized light sensitivity profile of the optimal montage which was

calculated as the sum of all channel's sensitivity along the cortical surface, d) optimal montage glued on the subject's head using collodion. Installation was guided by a neuro-navigation system, and optodes positions were then digitized after the acquisition for coregistration and forward modelling.

5.2.7 NIROT reconstruction

We compared two fNIRS reconstruction methods, one being our previously proposed and validated Maximum Entropy on the Mean (MEM) (Cai *et al.*, 2021) and the other one being the conventional Minimum Norm Estimation (MNE) (Hämäläinen and Ilmoniemi, 1994). MEM offers an efficient nonlinear probabilistic Bayesian framework to incorporate prior knowledge in the solution of the inverse problem. It assumes that brain activity is modelled by cortical parcels that are estimated using a data-driven parcellation of the full field of view considered for NIROT. While fitting the data through relative entropy maximization, MEM has the unique ability to switch off parcels of the model considered as inactive using a hidden variable. In our previous studies in the context of EEG/MEG source imaging, we have demonstrated excellent accuracy of MEM and the ability to be sensitive to the spatial extent of the underlying generators (Chowdhury *et al.*, 2013, 2016; Grova *et al.*, 2016; Heers *et al.*, 2016; Hedrich *et al.*, 2017; Pellegrino *et al.*, 2020), before adapting this framework in the context of NIROT (Cai *et al.*, 2021). As the most conventional inverse procedure considered in NIROT, MNE is a linear method (Hämäläinen and Ilmoniemi, 1994) using Tikhonov regularization to minimize the L2-norm. Please refer to *Appendix.1* for further details on those NIROT methods. In practice, NIROT reconstructions were calculated by our implementations of these two methods in the fNIRS processing plugin - NIRSTORM (<https://github.com/Nirstorm/nirstorm>) in Brainstorm software.

5.2.8 Quantitative evaluation by comparing NIROT to fMRI

To evaluate and compare the spatial accuracy of NIROT reconstructions obtained using either MEM or MNE mentioned above, we proposed to compare the reconstructed HbO/HbR responses along the cortical surface to surface-based fMRI Z-maps, both at the individual and at the group level. To do so, we first defined two cortical regions from the resulted surface-based fMRI Z-map as the ROIs to quantitatively assess the spatial accuracy of NIROT maps.

Determination of the cortical ROIs used for quantitative evaluation

ROIs selected for quantitative evaluation consisted of two cortical regions, extracted from surface-based subject-specific fMRI Z-map response to the finger-tapping task. The first one, fMRI reference ROI#1, corresponded to the ‘activated’ region where the main activation of task-evoked HbO/HbR responses should be expected. The second one, fMRI reference ROI#2, corresponded to the ‘non-activated’ region where no significant HbO/HbR responses were expected. These two fMRI regions were our reference ‘true positives’ and ‘true negatives’ for later NIROT evaluations.

The determination of fMRI reference ROI#1 for each subject was obtained from the first-level Z-map projected on individual mid-surface. We did not directly use the significant region on the projected Z-map (threshold) considering that each subject only went through one fMRI task session, and this might not be enough to estimate a reliable size of the main activation cluster, as suggested by fMRI test-retest reliability studies during motor tasks (Zandbelt *et al.*, 2008; Quiton *et al.*, 2014). Instead, the ROI#1 was defined by thresholding the individual surface-based fMRI Z-map until a predefined size, in order to ensure a similar spatial extent of the activated area of the one found at the group level. The group level analysis provided a more reliable generalized size parameter of the activation pattern, as suggested by (Zandbelt *et al.*, 2008). Therefore, to identify the expected size of fMRI reference ROI#1, we considered from the fMRI group-level map (described in section 2.4) the most significant cluster (Fig.5.2a) projected along the cortical surface. It resulted in 366 vertices shown by the black profile in Fig.5.2a. Consequently, we considered a parameter size of 366 vertices to determine the threshold of each individual map, to estimate the ‘activated’ region at the expected size. It is worth mentioning that such an approach was actually more conservative than the conventional threshold obtained at the single subject volume map (see section 2.4, $p < 0.01$ corrected using Gaussian random field theory). Finally, fMRI reference ROI#2 (‘true negatives’) was directly defined as the ‘non-activated’ region (see Fig.5.2b) on each individual fMRI Z-map on the cortical surface, by identifying vertices that were below the conventional threshold on the single subject volume map ($p < 0.01$ corrected using Gaussian random field theory). The remaining vertices between ROI#1 and ROI#2 could be considered as a region of fMRI uncertainty at the single subject level.

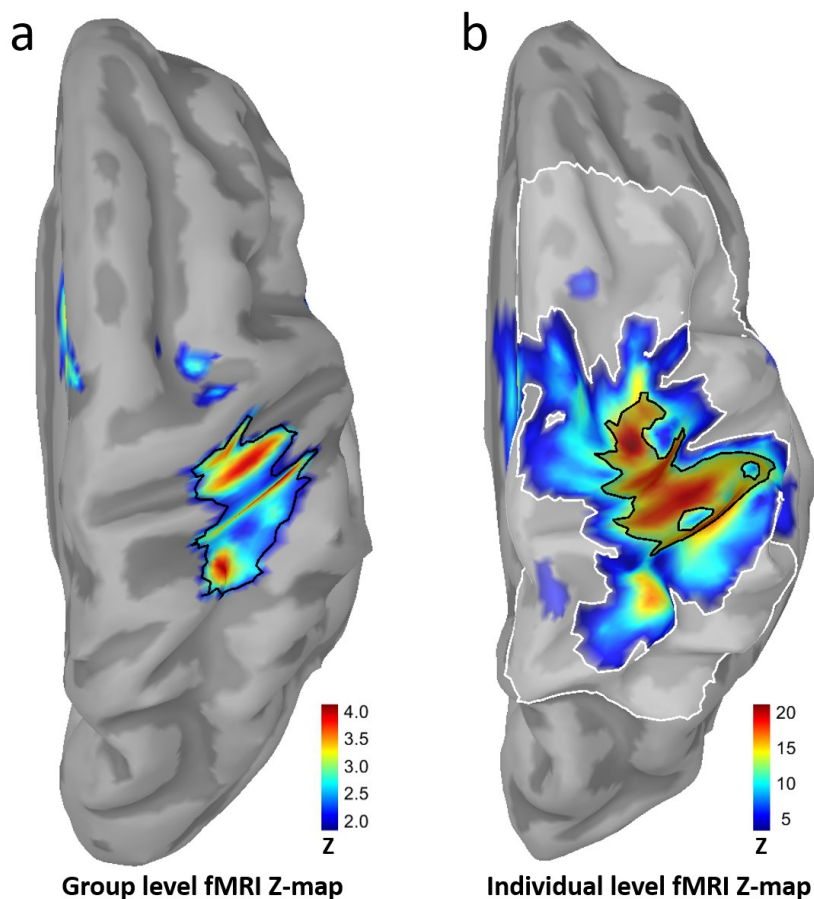


Fig.5.2 Determination of the cortical regions used for quantitative evaluations. a) group-level fMRI Z-map obtained by FSL group-level activation map projected along the mid-surface of MNI template ICBM152. The map was thresholded to only contain the significant activation region along the surface. Black profile represents the most significant cluster, which consists of 366 vertices. b) Determination of fMRI reference ROIs on the individual level surface-based fMRI Z-map of Sub01, projected from FSL first-level activation map on subject's mid-surface. The black profile is the individual fMRI reference ROI#1 which contains 366 vertices when thresholding the individual map by Z values. It represents the 'activated' region used for AUC, SD and Dmin metrics. The white profile is the individual fMRI reference ROI#2 represents the intersection between non-significant region and NIROT reconstruction field of view, which is defined as the 'non-activated' region for AUC calculations. Cortical surfaces are 50% inflated for visualization purposes.

Quantitative validation metrics

To assess the spatial accuracy of NIROT maps, we applied similar validation metrics described in our previous evaluation of MEM source imaging in the context of EEG/MEG data (Grova, Makni,

et al., 2006; Chowdhury *et al.*, 2013, 2016; Hedrich *et al.*, 2017). Each reconstructed NIROT image is actually a spatio-temporal map of the whole hemodynamic response, whereas the fMRI Z-map consists of a statistical static map assessing the presence of a modelled canonical hemodynamic response. To select a single NIROT map to evaluate, from the spatio-temporal estimates of each subject using each reconstruction method, we first averaged the reconstructed HbO/HbR time courses within the fMRI reference ROI#1, and then extracted the HbO/HbR maps at the time point of HbO versus HbR peaks on these averaged time courses. Moreover, since we have no ground truth for the reconstructed time course in fNIRS and since fNIRS is considered a relative measurement compared to baseline activity, we considered only the shape of the reconstructed fNIRS response by normalizing each selected spatial-temporal HbO/HbR map by this selected peak amplitude.

Using the 2 previous selected fMRI reference ROIs, defining our reference ‘true positives’ and ‘true negatives’, we proposed the following four validation metrics to evaluate NIROT spatial and temporal accuracy, for both MNE and MEM:

- **Area Under the Receiver Operating Characteristic (ROC) curve (AUC)** was used to assess the detection ability of the reconstruction methods. ROC analysis consists of assessing the sensitivity and specificity of NIROT maps, when varying the threshold from 0 to maximum amplitude of normalized NIROT maps at their peak. The ROC curve is obtained by plotting sensitivity as a function of (1- specificity). AUC score is then estimated as the area under this ROC curve. It is considered as a measure of detection accuracy, assessing the sensitivity of NIROT map to the underlying spatial extent of the hemodynamic response. We used the two ROIs defined in the previous section to calculate sensitivity and specificity. Sensitivity was calculated when considering fMRI reference ROI#1 as the ‘true positive (TP)’ region, and specificity was calculated when considering fMRI reference ROI#2 as the ‘true negative (TN)’ region. Moreover, we applied a random and homogeneous parcellation on ROI#2 to have the size of each cluster similar to the size of ROI#1. Then the fictive generators were sampled cluster wise within ROI#2, instead of vertex wise when calculating the True Negative rate. This approach was considering the fact that if the fictive generators would have sampled vertex wise, the number of samples for calculating True Negatives would have been much larger than for calculating True Positive. This procedure is consistent with (Grova, Daunizeau,

et al., 2006) on AUC calculation to fit the context of a distributed source model - generating as many “fictive” sources in the TN region as the number of vertices of the TP region. Therefore, our approach to estimate AUC prevented underestimation of the True Negative rate. Please note that the remaining vertices between selected ROI#1 and ROI#2 were not considered by our proposed ROC analysis, but they were actually taken into account in the following Dmin and SD metrics.

- **Minimum geodesic distance (*Dmin*)** was calculated as the minimum geodesic distance, following the circumvolutions of the cortical surface, from the vertex that exhibited maximum of reconstructed activity to the closest border from the individual fMRI reference ROI#1. The Dmin score would therefore be *0mm* if the peak of the HbO/HbR reconstruction map was located inside the fMRI reference ROI#1.
- **Spatial Dispersion (*SD*)** assessed the spatial spread of the estimated activation region distribution and the localization error using the following equation,

$$SD = \sqrt{\frac{\sum_{i=1}^N (\min_{j \in \Theta} (D^2(i, j)) \hat{X}^2(i, \tau))}{\sum_{i=1}^N (\hat{X}^2(i, \tau))}}$$

where $\min_{j \in \Theta} (D^2(i, j))$ is the minimum squared Euclidean distance between the vertex i to a vertex j located inside the fMRI reference ROI#1 represented by Θ . $\hat{X}^2(i, \tau)$ is the power of the peak amplitude of the reconstructed time course on vertex i at the peak time τ . N is the total number of vertices within the reconstruction field of view. The ideal value (i.e., $SD = 0mm$) would be achieved when no activation is reconstructed outside the fMRI reference ROI#1. The larger the SD is, the more spatially spreading or mislocalized the reconstructed maps are.

- **Peak times** of reconstructed HbO/HbR time course and the delay between HbO and HbR peak times were compared when reconstructing NIROT images using MEM and MNE. The average of the reconstructed time course of HbO/HbR within fMRI reference ROI#1 was first calculated to extract corresponding peak times (i.e., $Peak_{HbO}$ and $Peak_{HbR}$). The delay between HbO and HbR peak times was then calculated as $Peak_{HbR} - Peak_{HbO}$.

To conduct group-level evaluation for NIROT, individual NIROT maps at their corresponding peak amplitude were first normalized to [-1, 1]. FreeSurfer spherical registration was used to project normalized individual HbO/HbR maps onto the mid surface of ICBM152 template. Group-

level HbO/HbR reconstruction maps were then estimated by averaging the projected individual maps. AUC, SD and Dmin were calculated by comparing to the group-level fMRI Z-map. We also conducted in the supplementary materials a group-level Z map, in which the Z score was calculated for each vertex, using the mean amplitude divided by the standard deviation among 10 subjects, instead of considering only the average.

Additionally, AUC was also calculated under three different scenarios to answer the following questions specific to the use of personalized fNIRS reconstructions.

- ***Was MEM more accurate than MNE at different time instants other than only the peak of the hemodynamic response?*** AUCs of the reconstructed HbO/HbR maps using MEM and MNE were evaluated at different time instants ranging from 5s to 20s with a step size of 0.5s.
- ***Would it be possible to further threshold MNE reconstruction maps to achieve a similar spatial accuracy than the one obtained when using MEM?*** AUCs of HbO/HbR peak maps were calculated by considering different initial thresholds, as a percentage of the peak amplitude of each corresponding map, ranging from 0% to 50% with an increment of 1%, instead of standard AUC starting with a threshold of 0%.
- ***Was the 3D reconstruction obtained by using the combination of personalized optimal montage and MEM reconstruction primarily biased by the local forward model (i.e. sensitivity map), since the optimal montage was optimized to a targeted ROI in the motor region?*** We assumed the sensitivity profile of each subject, obtained by summing up the sensitivity of all channels of the corresponding optimal montage, to mimic a fully ‘montage-biased’ reconstruction map. Therefore, computing the AUC score of this sensitivity profile and comparing it to the reconstruction results obtained from either MEM or MNE can evaluate whether the local forward model plays a role in biasing the reconstruction.

5.2.9 Reliability of the performance differences between MEM and MNE

Considering reliability is the basis for individual difference research, especially on personalized methods (M. Yu *et al.*, 2018; Zuo, Xu and Milham, 2019), we also evaluated the reliability of reconstruction performance of both MEM and MNE individually, and more importantly, when considering the paired performance differences between the two methods. To do so, we considered the discriminability measure, which was proposed as a novel non-parametric approach for

assessing reliability, proved to be more robust than traditional intraclass correlations and fingerprinting approaches (M. Yu *et al.*, 2018; Wang *et al.*, 2020). Considering a reliability study design, pair-wised distances of the measurement of interest are first calculated for all experiment sessions (within- and between-subjects), and discriminability is then defined as the proportion of the number of cases in which within-subject distances are smaller than between-subject distances. We applied the Multiscale Graph Correlation (MGC) package (Bridgeford *et al.*, 2018; Vogelstein *et al.*, 2019) (available at <https://github.com/neurodata/r-mgc>) to estimate discriminability. Euclidean distance was considered as the default distance measurement to construct within- vs. between-subject distance matrices (Wang *et al.*, 2020) (see Fig.5.A2).

Although we did not have multiple sessions of the same task for each subject, we considered random sub-averaged 16 non-overlapping blocks out of a total of 20 blocks to mimic the task performance variability within each subject. To ensure good coverage of within-subject variance, we sorted all sub-averaged trials by decreasing SNR values and selected 10 trials with a step of 10 SNR value increments around the median SNR value. The selection of 10 sub-averaged trials was to ensure the same degree of freedom of within-subject when compared to between-subject variance, which was 10 subjects in our case. The selection of 16 blocks was to ensure not reducing SNR too much after averaging. This number was empirically defined according to the observation that usually there were less than 4 artifacts contaminated blocks in one finger tapping session. Selecting sub-averaged trials around the median SNR ensured a good representation of fNIRS responses, while discarding artifacts in the meantime. For instance, in artifacts contaminated data, large motion artifacts would result in high SNR of sub-averaged trials. We then performed both MEM and MNE reconstructions on all data samples (e.g., 100 = 10 within-session sub-averaged \times 10 subjects) and applied the same evaluations for the reconstructed hemodynamic maps. Discriminability was then estimated for each validation metric AUC, SD and Dmin, considering either MEM and MNE individually, or paired performance differences between them.

5.2.10 Data availability

The original raw data supporting the findings of this study are available upon reasonable request to the corresponding authors.

5.2 Results

5.3.1 Reconstruction performance comparisons at the individual-level

Statistical summary of individual level results is presented in Fig.5.3. Paired two sample t-tests were considered when comparing performance between the two methods (MEM vs. MNE). When reconstructing HbO responses, MEM provided significantly larger AUC values than MNE (0.79 vs. 0.68, $p < 0.01$). Moreover, MEM also showed significantly lower spatial dispersion (SD) than MNE (5.11mm vs. 9.83mm, $p < 0.01$). Both methods reconstructed the peak amplitude very closely from the fMRI main cluster as quantified using Dmin, with no significant difference between MEM and MNE (2.17mm vs. 3.00mm, $p > 0.05$). Similar performances were also observed when reconstructing HbR responses. MEM provided significantly larger AUC (0.80 vs. 0.70, $p < 0.05$), significantly lower SD (5.93mm vs. 8.97mm, $p < 0.05$) and similar Dmin values (3.33mm vs. 2.90mm, $p > 0.05$).

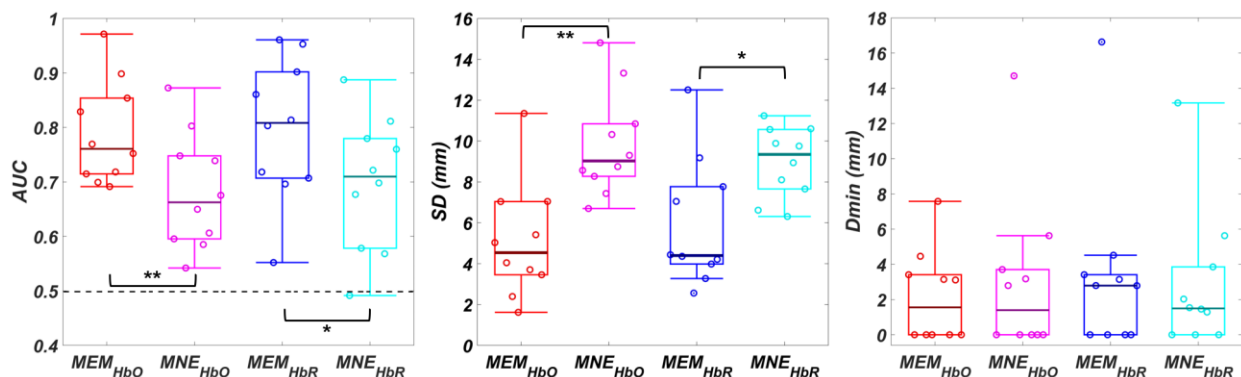


Fig.5.3 Quantitative evaluation of the performances of MEM and MNE reconstructions. a) Distribution of AUC values for MEM and MNE NIROT reconstructions, for HbO and HbR responses respectively, b) Distribution of SD (in mm) comparison between MEM and MNE in the context of reconstructed HbO/HbR, c) Distribution of Dmin (in mm) comparison between MEM and MNE in the context of reconstructed HbO/HbR. Each circle represents the index of one subject, superimposed on a boxplot representation of the distribution, * represents significant paired two sample t-test at $p < 0.05$ and ** for $p < 0.01$

Fig.5.4 and Fig.5.5 present all the individual level reconstruction maps and time courses calculated using MEM and MNE for each of 10 subjects. Fig.5.4a and Fig.5.5a showed the individual fMRI Z-map along with the individual fMRI reference ROI#1 represented by a black profile. All subjects showed clear fMRI activations along M1 and S1 areas, evoked by the finger tapping task. Columns b and c of Fig.5.4 and Fig.5.5 showed NIROT maps normalized by the peak amplitude of HbO/HbR reconstructed using MEM and MNE, respectively, together with validation metric

values. For Sub02, 03, 05, 07, 08, 09 and 10, MEM reconstructed accurately HbO/HbR responses with high AUC values ($[Q_1, Q_3] = [0.73, 0.89]$ for HbO, $[0.74, 0.94]$ for HbR among all maps, Q_1, Q_3 referring to the 1st and 3rd quartile of the distributions, respectively) and small spatial spread (low SD values, $[Q_1, Q_3] = [3.52mm, 6.63mm]$ for HbO, $[3.45mm, 6.37mm]$ for HbR). On the other hand, for these selected 7 subjects, MNE provided less accurate reconstructions characterized by lower AUC values ($[Q_1, Q_3] = [0.60, 0.75]$ for HbO, $[0.60, 0.77]$ for HbR) and larger SD values ($[Q_1, Q_3] = [7.64mm, 10.46mm]$ for HbO, $[8.31mm, 10.59mm]$ for HbR). For Sub01, MEM and MNE were both able to provide accurate HbO/HbR reconstructions when comparing to fMRI results. For Sub06, MEM and MNE provided similar reconstruction results, all maps were able to recover the main cluster but spread out toward more anterior regions. For Sub04, only MEM provided a good reconstruction only for HbO, resulting in an $AUC = 0.7$ and $Dmin = 0mm$. Column d of Fig.5.4 and Fig.5.5 illustrated the averaged reconstructed HbO/HbR time courses within the fMRI reference ROI#1. Temporal fluctuations of averaged reconstruction time courses of HbO/HbR were similar between MEM and MNE in most of the subjects, except that the amplitudes were larger for MEM in Sub 04, 07 and 08, because MNE did not reconstruct the spatial map accurately within the expected region.

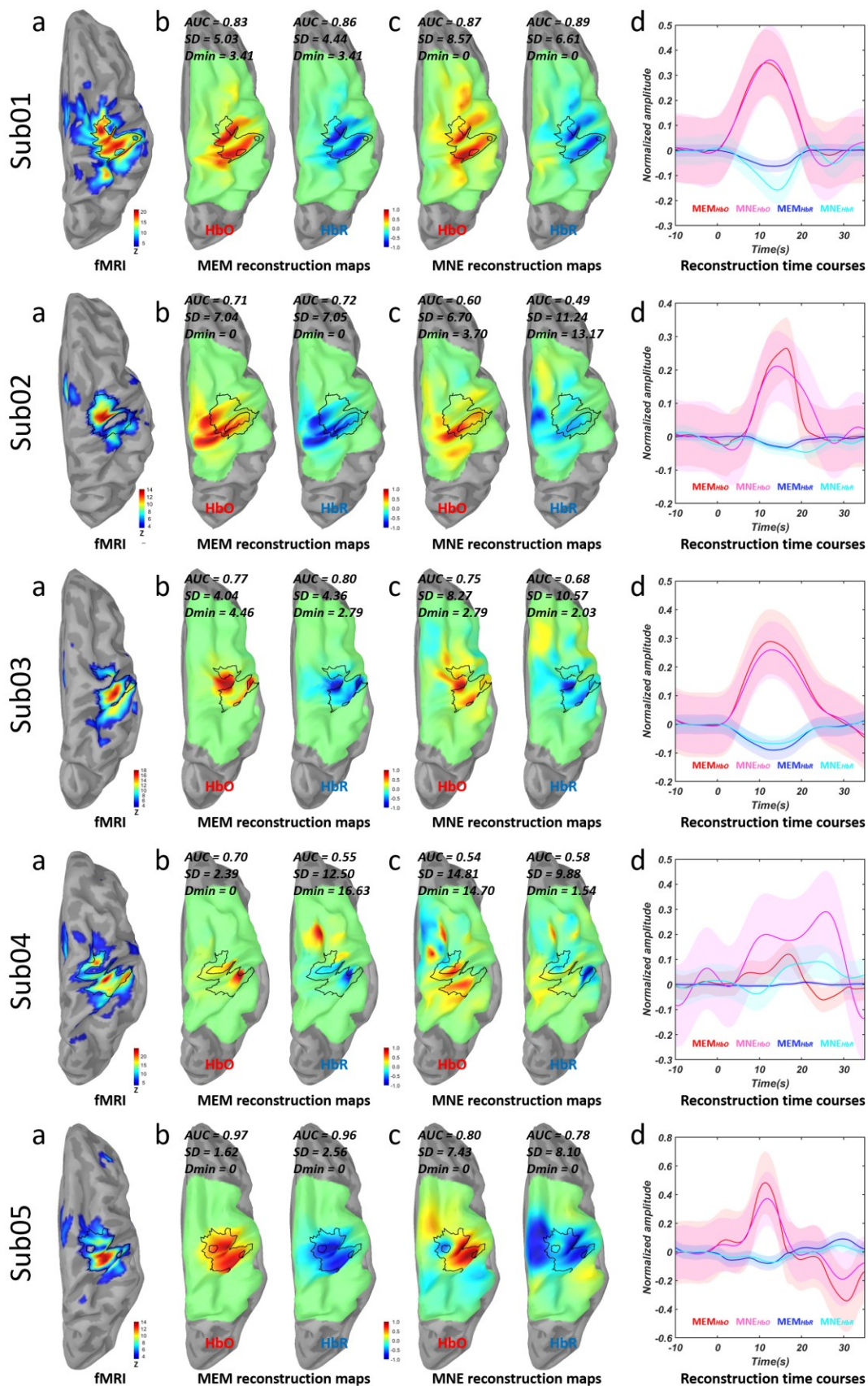


Fig.5.4 Visual and quantitative evaluation for NIROT images at the individual level (subjects 1 to 5). a) individual level fMRI Z-map thresholded to only contain the significant activation of each subject during finger tapping task, black profile represents the fMRI reference ROI#1 ('true positive'), non thresholded grey area (non-significant) within the reconstruction FOV represents the fMRI reference ROI#2 ('true negatives'). b) MEM reconstructed NIROT maps at HbO/HbR peak amplitude, respectively, c) MNE reconstructed NIROT maps at HbO/HbR peak amplitude, respectively, d) reconstructed time courses within the black profile, solid lines represent the averaged time courses, and the shaded areas represent standard deviation within the ROI#1. Quantitative evaluation metric results are showed on top of each map, respectively. AUCs were calculated by setting black profiles (fMRI reference ROI#1) as the 'activated' region and grey area (fMRI reference ROI#2) as the 'non-activated' region. SD and Dmin only considered fMRI ROI#1 as the 'activated' region. Note that each subject's map was normalized by its own peak, and time courses were normalized by the maximum HbO amplitude across two methods before averaging within the black profile.

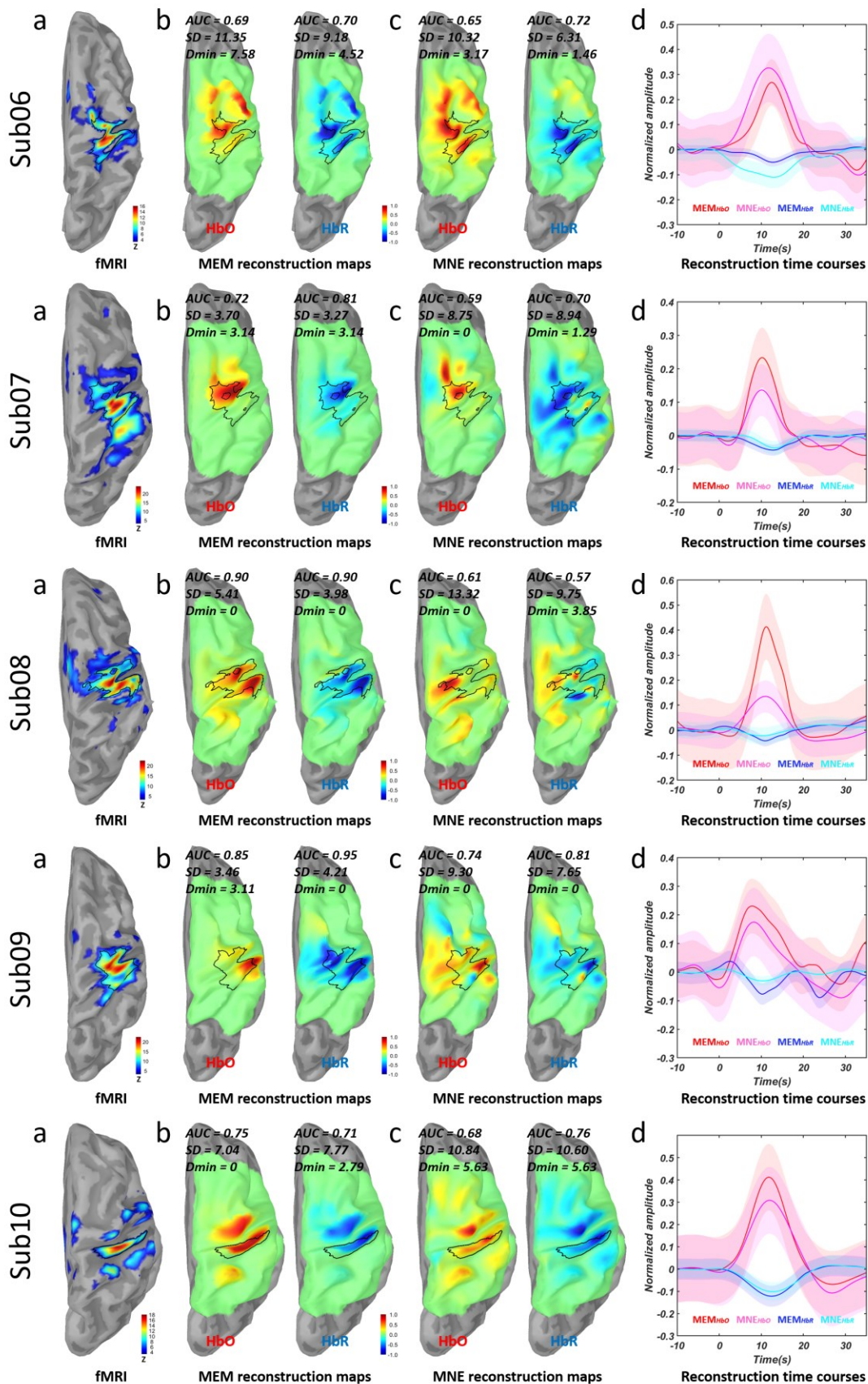


Fig.5.5 Visual and quantitative evaluation for NIROT images at the individual level (subjects 6 to 10).

a) individual level fMRI Z-map thresholded to only contain the significant activation of each subject during finger tapping task, black profile represents the fMRI reference ROI#1 ('true positives'), non thresholded grey area (non-significant) within the reconstruction FOV represents the fMRI reference ROI#2 ('true negatives'). b) MEM reconstructed NIROT maps at HbO/HbR peak amplitude, respectively, c) MNE reconstructed NIROT maps at HbO/HbR peak amplitude, respectively, d) reconstructed time courses within the black profile, solid lines represent the averaged time courses, and the shaded areas represent standard deviation within the ROI#1. Quantitative evaluation metric results are showed on top of each map, respectively. AUCs were calculated by setting black profiles (fMRI reference ROI#1) as the 'activated' region and grey area (fMRI reference ROI#2) as the 'non-activated' region. SD and Dmin only considered fMRI ROI#1 as the 'activated' region. Note that each subject's map was normalized by its own peak, and time courses were normalized by the maximum HbO amplitude across two methods before averaging within the black profile.

Table.5.1 summarized the statistical comparison of the peak times of HbO/HbR extracted from the above averaged reconstruction time courses within the fMRI reference ROI#1. When comparing MEM and MNE results, there were no significant differences in the peak times of HbO/HbR (paired two sample t-test, $p = 0.71$ and 0.17 for HbO and HbR, respectively). Both NIROT methods demonstrated a significant (one sample t-test against 0, $p < 0.05$) delay between the peak time of HbR and HbO ($0.9s \pm 0.3s$ and $1.9s \pm 0.7s$ for MEM and MNE, respectively). Moreover, there was no significant difference (paired two sample t-test, $p = 0.27$) between the delays estimated by MEM and MNE. Note that Sub04 was rejected from this analysis since it was exhibiting a very noisy reconstructed time course and therefore was considered as an outlier (Fig.5.4.d).

	MEM			MNE		
	$Peak_{HbO}(s)$	$Peak_{HbR}(s)$	$Peak_{HbR-HbO}(s)$	$Peak_{HbO}(s)$	$Peak_{HbR}(s)$	$Peak_{HbR-HbO}(s)$
mean \pm se	11.7 ± 0.7	12.7 ± 0.5	0.9 ± 0.3	11.6 ± 0.5	13.5 ± 1.0	1.9 ± 0.7
$[Q_1, Q_3]$	[11.0, 12.5]	[11.7, 13.3]	[0.1, 2.0]	[10.8, 12.6]	[12.1, 13.8]	[0.8, 2.4]
mean > 0	—	—	$p = 0.03$	—	—	$p = 0.03$
MEM vs. MNE	$p = 0.71$	$p = 0.17$	$p = 0.27$	—	—	—

Table.5.1 Statistical comparison of reconstructed HbO/HbR peak times. The first row showed the mean \pm standard error of each corresponding peak time in seconds. $Peak_{HbR-HbO}$ indicated the time delay between peak time of HbR ($Peak_{HbR}$) and HbO ($Peak_{HbO}$). The second row listed the 1st quartile

(Q_1) to 3rd quartile (Q_3) of each peak time and delay. The third row indicated the p -value of one sample t -test against 0s of peak time delay estimated by MEM and MNE. The last row demonstrated the p -value of paired two sample t -test, when comparing MEM and MNE results, for each peak time and delay. ‘-’ represented the cases in which no statistical test was conducted since we consider it was not necessary to test whether $Peak_{HbO}$ or $Peak_{HbR}$ itself were significantly larger than 0. Red background indicated significant differences with $p < 0.05$.

5.3.2 Reconstruction performance comparisons at the group-level

Fig.5.6 reports fMRI versus NIROT comparisons at the group-level. Validation metrics were calculated on the group averaged NIROT HbO and HbR maps, when using either MEM or MNE. Similar trends were found when considering group-level comparisons by visualization. When compared to MNE results (Fig.5.6, using fMRI group-level activation as a reference), MEM provided similar AUC (0.73 vs.0.72 for HbO and 0.74 vs.0.74 for HbR), lower SD (7.52 mm vs.10.52mm for HbO and 7.48mm vs.11.18mm for HbR) and similar Dmin (6.14mm vs.6.14mm for HbO and 2.99mm vs.2.76mm for HbR). When comparing the group averaged reconstructed HbO/HbR time course within the fMRI main cluster region, as a nonlinear method MEM provided almost identical ones to MNE. As a reference, we also illustrated the expected fMRI time course (black dash line in Fig.5.6d) by convolving a standard canonical hemodynamic response function (HRF) (Penny *et al.*, 2011) and a 10s boxcar stimuli. It followed well both MEM and MNE reconstructed HbR mean time courses and laid within the shaded areas, demonstrating the good temporal accuracy of our NIROT workflow.

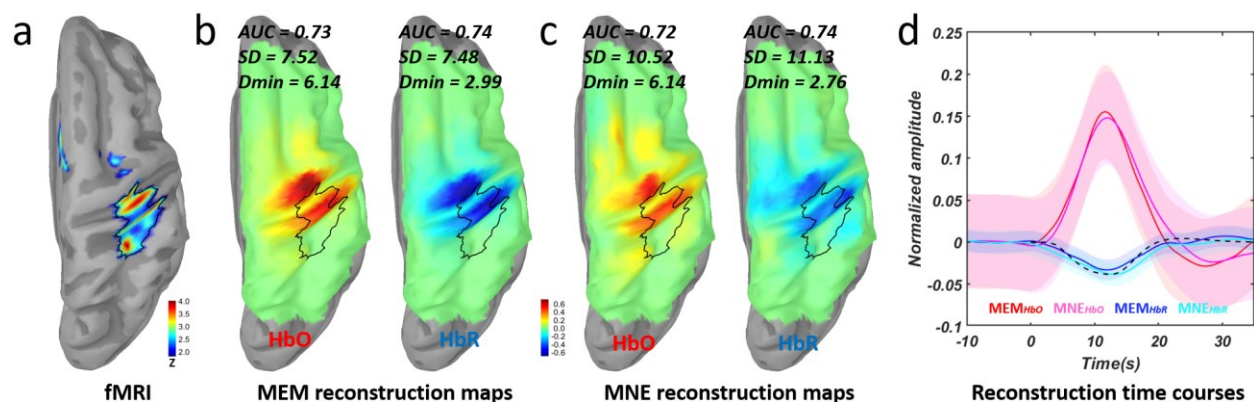


Fig.5.6 Comparisons of MEM and MNE group averaged reconstructions with fMRI Z-maps at the group-level, 10 subjects included. a) group-level fMRI Z-maps estimated by FSL group-level activation map projected along the mid-surface of ICBM152 mid-surface. The black profile represents fMRI the most

significant cluster projected on the cortical surface. Maps were thresholded to exclude the non-significant regions along the cortical surface. b) group averaged MEM reconstruction peak maps, individual peak maps were extracted at the peak times of HbO/HbR in native space and then projected onto the ICBM152 mid-surface, c) group averaged MNE reconstruction peak maps, individual peak maps were extracted at the peak times of HbO/HbR in native space and then projected onto the ICBM152 mid-surface. d) group-level reconstructed time courses within the black profile, solid lines represent the averaged time courses, and the shaded areas represent standard deviation within the black profile. The black dash line represents the expected fMRI time course resulting from the convolution of the standard canonical HRF and a 10s boxcar representing the task stimuli. The amplitude was reversed for better comparison with HbR time courses.

5.3.3 NIROT performance along time

Fig.5.7a illustrates the comparison of AUC values obtained for MEM and MNE reconstructions when considering NIROT maps at different time samples between 5s to 20s by steps of 0.5s. Overall, AUC values corresponding to HbO and HbR reconstructions, when considering either MEM or MNE, were following the temporal fluctuation of the expected task-evoked hemodynamic responses from 5s to 20s. Within this temporal window, MEM always provided larger AUC values when compared to MNE, for both HbO and HbR reconstructions. The differences were statistically significant (paired two sample t-test at each time sample, $p < 0.05$ for both HbO and HbR comparisons) within the range 8.5s to 14.5s. Additionally, AUC values of HbR were also slightly larger than HbO for both reconstruction methods.

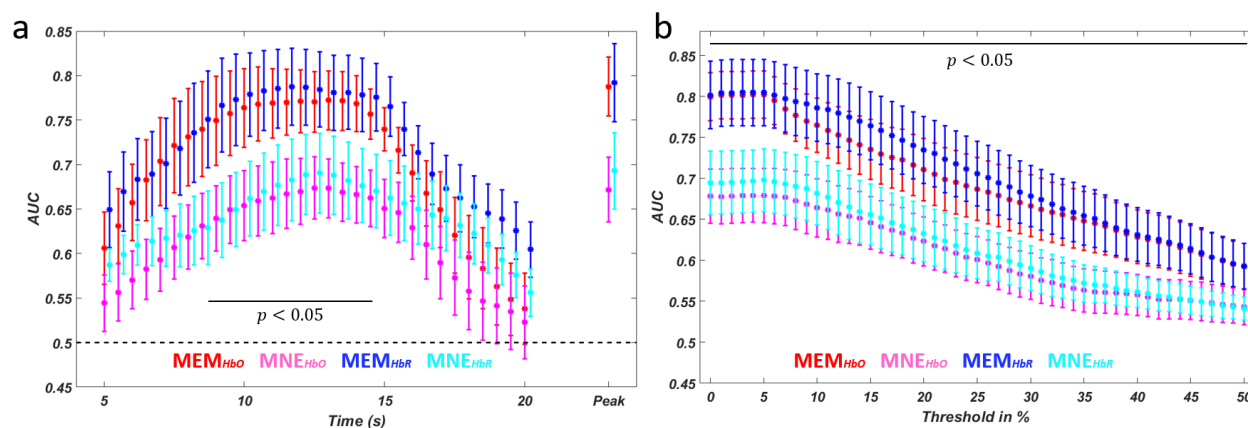


Fig.5.7 AUC comparisons of MEM and MNE reconstructions with respect to time and amplitude threshold value. a) AUC comparison between MEM and MNE, for both HbO and HbR reconstructions. AUC values (mean \pm standard error) were estimated within the time range 5s – 20s with increments

of 0.5s. The last column denoted as 'Peak' reports the distribution of AUC values considered at the peak of the hemodynamic response, within the ROI#1, b) AUC comparison between MEM and MNE, for both HbO and HbR reconstructions, AUC values (mean \pm standard error) were estimated within a percentage threshold of the peak amplitude of each NIROT maps ranging from 0% to 50% with an increment of 1%. Error bars represented the standard error within 10 subjects. Horizontal black bars indicated a significant difference of AUC between MEM and MNE, paired two sample t-test at each time sample or percentage threshold, $p < 0.05$ for both HbO and HbR comparisons.

5.3.4 NIROT performance when applying spatial thresholding on reconstruction maps

Fig.5.7b illustrates AUC as a function of different initial percentage thresholds (percentage relative to the peak amplitude of each NIROT map) applied on reconstructed HbO/HbR maps. ROC analyses were estimated from a specific starting percentage amplitude threshold from 0 up to 50%, in order to assess the impact of initial thresholding on detection accuracy. As expected, AUC values decreased when thresholding the reconstruction map with a larger initial percentage threshold. Overall, MEM provided larger AUC than MNE under all the thresholding scenarios, and the difference was statistically significant (paired two sample t-test at each percentage threshold, $p < 0.05$ for both HbO and HbR comparisons) within the whole threshold range. Results of this analysis, as illustrated in Fig.5.7b, showed that additional thresholding of the MNE results does not improve the estimation accuracy of the activity map, when compared to MEM.

5.3.5 AUC of the sensitivity profile of the optimal montage

The last column of Fig.5.8 demonstrates the AUC values calculated when assessing detection accuracy only on the light sensitivity profile (SP) resulting from the personalized optimal montage of each subject. The mean AUC value among 10 subjects was 0.64, significantly lower than the mean AUC value of MEM reconstructed HbO (0.76, $p < 0.01$, paired two sample t-test, Bonferroni corrected) and HbR (0.81, $p < 0.01$, paired two sample t-test, Bonferroni corrected). This AUC measure was also lower than MNE reconstructed HbO (0.66) and HbR (0.71) map but the difference was not statistically significant. These results suggest that our detection accuracy is slightly influenced by the installation of the optimal montage, but MEM reconstruction still significantly improves NIROT accuracy within the targeted brain region.

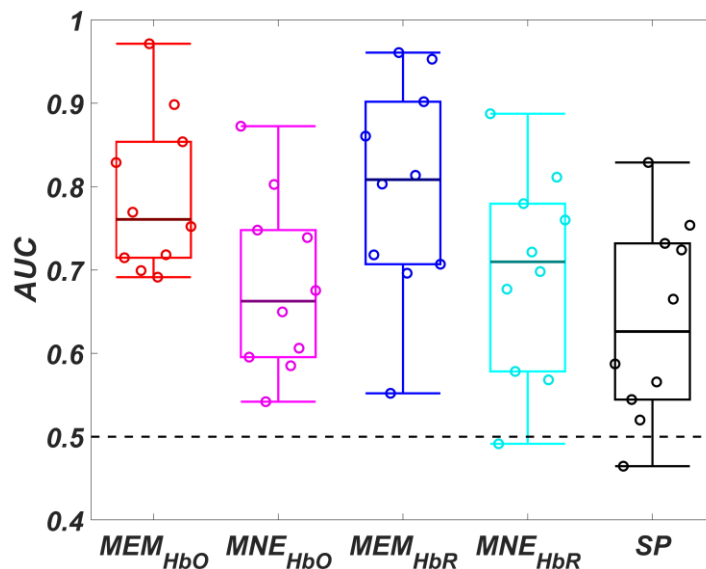


Fig.5.8 Distribution of AUC values estimated for MEM and MNE local reconstructions with the personalized optimal montage, in comparison to the AUC values obtained when considering only the montage light sensitivity profile (SP) for each subject. Exactly the same calculations of AUC for reconstruction methods were applied considering the light sensitivity profile (forward problem) as the reconstructed map. Paired two sample *t*-test showed significant higher AUC of MEM reconstructed HbO (mean = 0.76) and HbR (mean = 0.81) than ‘SP’ (mean = 0.64), $p < 0.01$, Bonferroni corrected for multiple comparison). AUC of ‘SP’ was lower than MNE reconstructed HbO (mean = 0.66) and HbR (mean = 0.71) but not significant.

5.3.6 Reliability of performance differences between MEM and MNE

Over 100 reconstructions, including 10 within-subject resampled sessions and 10 subjects, all three validation metrics (AUC, SD and Dmin) showed significantly better performances using MEM, when compared to MNE. The 95% confidence interval (CI) of the paired differences (MEM-MNE) was [0.13, 0.17] for AUC, [-5.50, -4.31] for SD (in mm) and [-2.76, -0.23] for Dmin (in mm) (see distributions reported in Fig.5.A1). Discriminability of these performance differences was estimated as 0.68 for AUC, 0.70 for SD and 0.68 for Dmin (see Fig.5.A2), indicating that MEM was exhibiting reliably better performances than MNE. When considering the performance of MEM and MNE individually, the discriminability of MEM was estimated as 0.71 for AUC, 0.66 for SD and 0.64 for Dmin, whereas the discriminability of MNE was estimated as 0.85 for AUC, 0.88 for SD and 0.73 for Dmin.

5.4 Discussion

The present study proposed and evaluated a workflow of personalized NIROT using MEM for spatio-temporal imaging of cortical hemodynamic fluctuations evoked by a motor task. This workflow attempted to optimize the reconstruction accuracy considering 1) fNIRS montage planning using personalized optimal montage (Machado *et al.*, 2014b, 2018), which aimed to maximize the fNIRS probing ability of the hemodynamic responses within a targeted ROI along the cortical surface; 2) data acquisition involving the neuro-navigation-guided optode installation using collodion, which ensured accurate positioning, excellent contact to the scalp and minimized motion artifacts (Yücel *et al.*, 2014; Pellegrino, Machado, *et al.*, 2016; Machado *et al.*, 2018), digitalization of the positions of the sensors along with more than 150 head points, accurate coregistration with the anatomical head model, and therefore minimizing potential errors when calculating the forward model of NIROT; 3) reconstruction using MEM, which is sensitive to the spatial extent of the generators in the context of EEG/MEG source location (Chowdhury *et al.*, 2013, 2016; Grova *et al.*, 2016; Heers *et al.*, 2016; Hedrich *et al.*, 2017; Pellegrino *et al.*, 2020) and fNIRS reconstructions with realistic simulations (Cai *et al.*, 2021). We evaluated the spatial accuracy of the NIROT workflow by comparing the HbO/HbR maps to fMRI Z-maps. Our results showed that MEM provided overall better spatial accuracy than MNE, while both NIROT methods exhibited similar temporal features when estimating the fNIRS hemodynamic responses.

5.4.1 Evaluation of the performance of personalized NIROT using MEM

Individual and group analysis revealed that MEM recovers more accurately the hemodynamic responses for both HbO and HbR, when compared to MNE (significantly larger AUC). MEM was sensitive to the spatial extent of the generator (significantly lower SD), in agreement with our previous EEG/MEG results (Chowdhury *et al.*, 2013, 2016; Grova *et al.*, 2016; Heers *et al.*, 2016; Hedrich *et al.*, 2017; Pellegrino *et al.*, 2020). Additionally, when assessing the reliability of our measures using discriminability (M. Yu *et al.*, 2018; Wang *et al.*, 2020) through bootstrap resampled sub-averaged task responses, we found that MEM provided reliably better reconstruction performance than MNE. When evaluating the discriminability of MEM and MNE individually, MNE exhibited very large reliability values (e.g., 0.85 for AUC, 0.88 for SD), which were even larger than the known largest reliability values reported in neuroimaging fields – 0.8 for morphological measures of the human brain (Zuo, Xu and Milham, 2019). This finding might be

explained since MNE is known to spatially smear the reconstruction map, therefore reducing sensitivity and specificity (Ding, 2009), hence resulting in reliable but less accurate results when compared to MEM. On the other hand, the reliability of MEM only (0.71 for AUC, 0.66 for SD and 0.64 for Dmin) was overall good.

MEM reconstructed temporal fluctuations of HbO and HbR were similar to MNE (last column of Fig.5.4 and Fig.5.5). The statistical analysis of the reconstructed HbO/HbR peak times in Table.5.1 further proved this point as no significant differences were found between MEM and MNE regarding the HbO/HbR peak times and the delay between them. Moreover, both methods provided significant delay around 1-2s between HbR and HbO peak times consistent with previous literature (Jasdzewski *et al.*, 2003; Steinbrink *et al.*, 2006). In the end, our group level reconstructed HbR time courses (see Fig.5.6d) estimated by MEM and MNE were almost identical to the expected fMRI time course estimated through the convolution of a 10s boxcar with the standard canonical HRF. To the best of our knowledge, this is the first study reproducing this aspect by investigating reconstructed time courses rather than measures in the channel space. It is important to note that the time course reconstructed by MNE directly depends on the averaged signal at the channel level as it is a linear projection. Conversely, MEM is a nonlinear technique applied at every time sample, and not originally optimized for the estimation of resulting time courses. The temporal similarity to MNE further validated our previous improvement of MEM (Cai *et al.*, 2021) on temporal accuracy of fNIRS reconstruction.

5.4.2 Comparison of MEM and MNE reconstruction performance along time

Most of the spatial accuracy comparisons in this study were performed with the NIROT maps extracted at the HbO/HbR peak. Would MEM outperform MNE at other time points? We also assessed detection accuracy using AUC along the time course of the hemodynamic response, and our results demonstrated that MEM outperformed MNE at any time instance along the elicited hemodynamic response from 5s to 20s after the task onset (Fig.5.7).

5.4.3 Comparison of MEM and MNE reconstruction performance with spatial thresholding

MNE tends to spatially spread the reconstructions out of the ‘true positive’ region due to the use of L2-norm for the regularization when solving the inverse problem (Ding, 2009). Could *post-hoc* thresholding on the reconstruction map achieve a better spatial extension estimation in MNE? As illustrated in Fig.5.7.b, when increasing the initial thresholding in ROC analysis, MNE still

provided smaller *AUC* values than MEM along all percentage thresholding values from 0% to 50%. Therefore, thresholding the MNE map does not solve the typical rate of false positives introduced by the method. While both methods were localizing accurately the maximum of the underlying activity (see *Dmin* results), MNE did not recover the underlying spatial extent of the active region, whereas MEM did. This result further supported the study of (Ding, 2009), which demonstrated that MNE reconstruction cannot retrieve the spatial extent of the underlying generator.

5.4.4 Assessment whether the local forward model of personalized optimal montage was biasing NIROT reconstructions

We also carefully assessed if the use of a local forward model (light sensitivity profile map) obtained from an optimal personalized montage targeting a specific ROI, could bias NIROT reconstruction towards this targeted region. We found that the optimal montage maximized the sensitivity with respect to a targeted ROI, but this does not mean that it was ‘blind’ to the other surrounding areas. As shown in Fig.5.1c, the optimal montage used in this study provided sensitivity covering not only the ROI (‘hand knob’) but also surrounding areas such as the pre-central and post-central cortex. To assess this critical issue, we estimated what would be the detection accuracy of the personalized sensitivity profile of each individual optimal montage using *AUC* (see Fig.5.1c), assuming that the sensitivity profile itself could be considered as a reconstruction result entirely biased by the optimal montage sensitivity. Our results reported in Fig.5.8 demonstrated that MEM reconstruction of data from personalized optimal montage provided significantly larger *AUC* values than the ones estimated when considering only the sensitivity profile as the solution. These results are indeed suggesting that the reconstruction performance is dominated by the process of solving the inverse problem rather than the sensitivity. If optimizing the sensitivity could simply lead the MEM reconstructed activation easily showing up in the targeted ROI, such a clear difference of *AUC* between sensitivity profile and real reconstructions conducted by MEM should not have been observed. Besides, the apparent difference we found between MEM and MNE reconstruction should not have been observed either. On the other hand, MNE was showing slightly larger *AUC* when compared to the sensitivity profile (non-significant), further demonstrating the inability of the MNE operator to recover accurately the spatial extent. This indicated MNE reconstruction is actually not far from a simple projection

of the channel space data onto the cortical surface (Ding, 2009). In the end, these reconstruction results also support our previous conclusion (Machado *et al.*, 2018) that local reconstruction, comparing to NIROT using the high density montage (Zeff *et al.*, 2007; White and Culver, 2010), is possible given appropriate spatial sampling of the montage.

5.4.5 Using fMRI as the reference for NIROT evaluation

Using fMRI as the reference to evaluate the accuracy of NIROT reconstructions has been conducted in previous studies (White and Culver, 2010; Eggebrecht *et al.*, 2012, 2014; Zhan *et al.*, 2012a; Yamashita *et al.*, 2016a; Huppert *et al.*, 2017; Tremblay *et al.*, 2018). Mainly three types of reconstruction errors have been considered in these evaluation studies, as follows:

- **The first evaluation criterion** was the overall localization accuracy, as assessed in our study using AUC, also considered in the simulation study (Tremblay *et al.*, 2018) and in a motor task study (Yamashita *et al.*, 2016a), which considered both the reconstructed map sensitivity and specificity when compared to the fMRI activation map. (Tremblay *et al.*, 2018) used the theoretical ground truth defined in the simulation as the ‘true positive’ region. On the other hand, for real data reconstructions, the calculation of AUC requires the definition of the ‘true positive’ and the ‘true negative’ regions referring to the fMRI activation map. Yamashita *et al.*, 2016 (Yamashita *et al.*, 2016a) defined the ‘true positive’ region on the fMRI t-map, thresholded at $p < 0.05$ (Family-wise error rate (FEW) corrected), and the ‘true negative’ regions with the other voxels exhibiting p values below this threshold. However, in our study, we decided to propose a different approach to determine more robust ROIs from fMRI results as our proposed NIROT validation references.

Our ‘true positive’ region, denoted fMRI reference ROI#1, consisted in two features, which are respectively size and shape. We proposed a robust approach to define the size of it from the group-level fMRI Z-map for the following reasons: 1) each subject only went through one fMRI task session, and this is not enough to estimate a robust size of the main activation cluster, as suggested by fMRI test-retest reliability studies during motor tasks (Zandbelt *et al.*, 2008; Quiton *et al.*, 2014). 2) Group-level analysis involved more sessions, although collected from different subjects, therefore likely to result in a more robust estimation of the spatial extent of the activated map. This important finding was demonstrated by (Zandbelt *et al.*, 2008) who showed a highly stable group-wise spatial activation pattern and BOLD signal changes but substantial variations at the individual level. Then, the shape of the ‘true positive’ region was automatically defined when thresholding

the individual fMRI Z-map until the resulted region was exhibiting a similar size to the one defined from the group-level analysis. In the end, the ‘true positive’ region for each individual map was following its own spatial pattern, along the individual level fMRI Z-map, but constrained by a robust cluster size parameter estimated from group-level fMRI analysis. Our resulting threshold informed by the group-level size parameter was usually higher (more conservative) than the conventional threshold considered at the single subject level ($p < 0.01$, corrected using Gaussian random field theory).

When defining the ‘true negative’ region, denoted fMRI reference ROI#2, we did not simply use the area that is outside the ‘true positive’ region defined above. Instead, we rather referred to the significance test results of conventional FSL individual voxel-wise fMRI analysis ($p < 0.01$, corrected using Gaussian random field theory). The non-significant fMRI regions projected on the cortical surface were then considered as our ‘true negative’ reference. Our results (Fig.5.2, Fig.5.4 and Fig.5.5) showed that this region was always more extended than the areas outside the ‘true positive’ region. We believe that this proposed approach, discarding the vertices between ROI#1 and ROI#2 from ROC analysis, was fair regarding the evaluation of MNE, since it is known that MNE tends to spatially spread the reconstruction along the cortical region (Ding, 2009). On the other hand, those “in between” vertices were actually taken into account in our other validation metrics (SD and Dmin).

- **The second evaluation criterion** was the localization error (LE) which can be estimated as suggested in (Yamashita *et al.*, 2016a) by the distance between the peak of fNIRS reconstruction map and the peak of fMRI Z-map. On the other hand, other authors (White and Culver, 2010; Eggebrecht *et al.*, 2012, 2014; Huppert *et al.*, 2017) proposed a center of mass error calculated by the distance between the center of mass of two maps (fMRI and NIROT), while others (Zhan *et al.*, 2012a; Tremblay *et al.*, 2018) considered the Euclidean distance between reconstruction peak to the peak of the stimulated ground truth. In our study, we defined Dmin as the minimum geodesic distance, following the circumvolutions of the cortical surface, from the vertex that exhibited maximum of reconstructed activity to fMRI reference ROI#1. Overall, we believe that there was little difference between these different localization error metrics, given the fact that reconstructing HbO/HbR peak inside the ‘true positive’ region was not so challenging, resulting in our case of Dmin values mostly close to 0 mm.

- A *third validation criterion* was the false positive or spatial extent reported by the reconstructions. The square root of the area exhibiting amplitudes higher than half maximum, i.e., – an estimate of the full width at half maximum (FWHM), was proposed by (White and Culver, 2010). Similarly, a focality measurement was considered by (Zhan *et al.*, 2012a), which calculates the ratio between localized full volume half maximum (LVHM) and full volume half maximum (FVHM). FVHM is determined as the volume of all voxels along the whole reconstruction field of view that exhibit amplitude larger than half of the peak amplitude. LVHM is defined similarly but only considering the voxels within the single cluster that contains the peak. (Yamashita *et al.*, 2016a) estimated a false-positive amount metric defined as the average amount of negative HbR results in the fMRI non-significant region, and finally (Tremblay *et al.*, 2018) considered a measurement of blurring using the root mean squared of the gradient of the reconstructed map. In our study, we considered the Spatial Dispersion metric (SD), originally proposed by (Molins *et al.*, 2008) when studying EEG/MEG source imaging results. SD consists in weighting the distance of the spread of the reconstructed activity around the ‘true positive’ region, by the reconstructed energy in such a region. SD distance in mm is therefore sensitive to how much the reconstructed map is spreading around the ‘true positive’ region but also to eventual mislocalization errors. In our study, by considering SD metric, we are not weighting in a similar manner a false positive activation reported close to the ‘true positive’ region, as opposed to the same amplitude false-positive activation reported far away from the reference region. Therefore, SD is handling correctly such an issue by weighted the distance to the ‘true positive’ region by reconstructed amplitude. When considering only the spatial extent around the peak of the activation, SD also serves similarly as a FWHM measure to quantify the PSF of the reconstructions (Hedrich *et al.*, 2017).

In our previous studies in the context of EEG/MEG source imaging, AUC and SD metrics appeared overall as key metrics to assess how a source localization or NIROT reconstruction technique could accurately recover the spatial extent of the underlying generators (Chowdhury *et al.*, 2013, 2016; Hedrich *et al.*, 2017; Pellegrino *et al.*, 2020; Cai *et al.*, 2021) therefore they were considered in this study, exhibiting very informative trends in NIROT maps.

5.4.6 Difference between NIROT and fMRI maps

Our results also suggested that NIROT images exhibit activations maps more superficial than fMRI Z-maps, both at the individual and group-level analysis. This is in agreement with findings from a

simultaneous fMRI/fNIRS study investigating electrical median nerve stimulation (Huppert *et al.*, 2017). This observation is due to the limited ability of fNIRS to detect the deeper areas, a standard limitation of the technique itself (Scholkmann, Kleiser, *et al.*, 2014) which can be partially compensated by introducing depth weighting when solving the inverse problem. We investigated the impact of depth weighting, in both MEM and MNE, in fNIRS reconstruction in our previous study (Cai *et al.*, 2021). The optimal depth weighting parameters identified in our previous study were actually the ones considered for this study. Therefore, we believe that our reconstructed results should not overcompensating the effect of the depth of the cortical region.

Although fMRI results were considered as our ‘ground truth’, fMRI and fNIRS signals still have different physical and physiological origins. fMRI measures the Blood-Oxygen-Level-Dependent (BOLD) signal which is a combination of blood flow changes, blood volume changes and deoxygenated hemoglobin concentration changes (Ogawa *et al.*, 1990; Buxton, 2012). On the other hand, using infra-red light absorption in two wavelengths, fNIRS measures the relative oxy-/deoxygenated hemoglobin concentration changes evoked by a task or during the resting state (Scholkmann, Kleiser, *et al.*, 2014). Previous studies have provided conflicting results on whether BOLD signals exhibit the highest correlation with HbO or HbR (Strangman *et al.*, 2002; Huppert *et al.*, 2006; Steinbrink *et al.*, 2006; Cui *et al.*, 2011; Eggebrecht *et al.*, 2012, 2014; Wijekumar *et al.*, 2017). HbR is physically closer to fMRI BOLD signal but the correlation is biased by variability resulted from systemic errors (Strangman *et al.*, 2002). We did not fully investigate this aspect, but HbR reconstruction maps showed overall a better consensus with fMRI Z-map (see Fig.5.4 and 5). For similar reasons, (Yamashita *et al.*, 2016a) decided to compare only HbR maps in their comparison with fMRI results.

5.4.7 Comparison with other NIROT workflows

Most references reported on NIROT results were performed in the context of high-density fNIRS montage (Zeff *et al.*, 2007; Eggebrecht *et al.*, 2014). Increasing the density of the fNIRS montage is expected to improve the power of the reconstruction accuracy and the resolution (White and Culver, 2010). Along with our previous work (Machado *et al.*, 2018; Cai *et al.*, 2021) and the present study, we showed that our approach allows accurate local reconstruction of NIROT images even when considering fewer well-positioned channels. Moreover, we believe that optimal montage can also be beneficial for studies which require more portability.

Other NIROT strategies have also been reported in the literature. Other linear approaches using L1-norm based regularization (Süzen, Giannoula and Durduran, 2010; Okawa, Hoshi and Yamada, 2011; Kavuri *et al.*, 2012; Prakash *et al.*, 2014) have been used to obtain more focal localization with high specificity but with much lower sensitivity. Bayesian model averaging (Tremblay *et al.*, 2018) proposed by (Trujillo-Barreto, Aubert-Vázquez and Valdés-Sosa, 2004b) and a hierarchical Bayesian model applied by (Shimokawa *et al.*, 2012, 2013a; Yamashita *et al.*, 2016a) reported more accurate sparse reconstructions with both higher sensitivity and specificity than L1- and L2-norm based regularizations. It would be of great interest to compare our MEM framework with these other NIROT Bayesian methods, as we previously completed in the context of MEG source imaging (Chowdhury *et al.*, 2013), either on realistic simulations or on well controlled experimental data, however such analysis was out of the scope of this study.

Regarding the statistical analysis of NIROT maps, a hierarchical random-effects cortical surface reconstruction model proposed by Abdelnour, Genovese and Huppert, 2010 was applied by Huppert *et al.*, 2017 to estimate a group level hemodynamic responses evoked by parametric median nerve stimulations. Individual channel space optical density changes and forward model (sensitivity) were concatenated into a single inverse model so that the group-level inference can be made directly by solving this model. In our study, we mainly focused on the paired comparison of the reconstruction performance between MEM and MNE at the individual-level, not on statistical inferences at the group-level. However, in addition to standard evaluation of the grand average group-level responses (average of individual NIROT maps) presented in Fig.5.6, we also investigated group-level evaluation when considering group-level Z maps of MEM and MNE reconstructions (see Supplementary Fig.5.S2). In this case, the Z score was estimated for each vertex along the cortical surface among 10 subjects' reconstruction maps, using the mean of the normalized amplitude divided by the standard deviation of 10 subjects, therefore resulting in a random effect group-level analysis. Our results further demonstrated a good estimation of the main activation cluster using MEM, when compared to MNE.

5.4.8 Implementation of the workflow in an open-source toolbox

Our personalized NIROT workflow is publicly available. All methods described in this study have been implemented in an fNIRS processing plugin - NIRSTORM (<https://github.com/Nirstorm/nirstorm>) in Brainstorm software. Brainstorm (Tadel *et al.*, 2011)

(<https://neuroimage.usc.edu/brainstorm/>) is an open-source software dedicated to analyzing multimodality brain recordings such as MEG, EEG, fNIRS, Electrocorticography, depth electrodes and multiunit electrophysiology. Researchers could apply our proposed NIROT workflow in NIRSTORM starting with designing a personalized optimal montage using individual MRI or a template MRI (Colin 27). If gluing optodes on any possible location is not feasible, our optimal montage can also be estimated on a discrete set of free optodes positions available on a specific cap. fNIRS data pre-processing using the conventional pipeline, and finally reconstruction NIROT spatio-temporal images using depth weighted versions of MEM and MNE are all available in NIRSTORM.

5.4.9 Limitations and future directions

The subject cohort involved in this study was still relatively small – 10 subjects. This could reduce the power of our statistical analysis. However, the design of the study was fully within-subject, with paired comparisons which typically grants more statistical power. The input to each reconstruction method contained the exact same variances of hemodynamic responses between- and within-subjects, meaning the paired comparisons or contrasts involved in this study are not biased by such variances. When studying the reliability of fNIRS 3D reconstruction performances, within-subject variability was conducted using a resampling sub-averaged approach. Although it was beyond the scope of this study, it would be of great interest to perform such reliability evaluation with a well designed test-retest reliability study. It is worth noting that a recent fNIRS reproducibility study has demonstrated the importance of involving montage spatial information, which specifically increased the within-subject reproducibility (Novi *et al.*, 2020), hence taking advantages of the personalized optimal montage our proposed workflow is expected to provide high reliability in a test-retest reliability evaluation study.

Although the same task was performed by the same cohort, fMRI and fNIRS acquisitions were not conducted simultaneously. Within-subject task performance variability might also cause some potential differences between the NIROT and fMRI images, including influence of other processes like attention or arousal (Novi *et al.*, 2020). Concurrent fMRI/fNIRS acquisitions (Huppert *et al.*, 2017; Wijekumar *et al.*, 2017) might be used to address this problem but this was beyond the scope of this study. Overall, we believe there should be great interest to apply the proposed NIROT workflow into different experiments designs, involving a variety of tasks.

5.5 Conclusion

In the present study, we demonstrated and evaluated our proposed workflow for personalized NIROT using MEM. Finger tapping data acquired from 10 subjects were used to reconstruct NIROT images and validating the results by comparing them to the fMRI Z-maps obtained from the same task and cohort. Conventionally used reconstruction method – MNE - was compared with MEM. Our results showed that MEM provides better spatial accuracy and similar temporal features as compared with MNE, when reconstructing both HbO and HbR responses evoked by a finger tapping task. Our proposed workflow is publicly available, and all the processing functionalities have been implemented and validated in the fNIRS processing plugin - NIRSTORM (<https://github.com/Nirstorm/nirstorm>) in Brainstorm software.

5.6 Appendices

A1. fNIRS reconstruction using Minimum Norm Estimate (MNE) and Maximum Entropy on the Mean (MEM)

NIROT reconstruction can be modelled as a linear problem, $Y = AX + e$, where Y ($p \times t$) is the pre-processed ΔOD at a specific wavelength for a specific channel p at a time sample t ; A is the sensitivity matrix ($p \times q$) estimated when solving NIROT forward problem between the vertex q and the channel p . X is a ($q \times t$) matrix representing the reconstructed amplitude at vertex q along the cortical surface at time t , and e is the reconstruction error (same dimension as Y). Solving X by knowing Y and A involves solving an ill-posed inverse problem, which requires regularization. In the MNE approach (Hämäläinen and Ilmoniemi, 1994), Tikhonov regularization was used to minimize the L2-norm, thus the estimated reconstruction spatial-temporal matrix \hat{X}_{MNE} as,

$$\hat{X}_{MNE} = \operatorname{argmin}(\|(Y - AX)\|_{\Sigma_d}^2 + \lambda\|X\|_{\Sigma_s}^2) = (A^T\Sigma_d A + \lambda\Sigma_s)^{-1}A^T\Sigma_d Y$$

where Σ_d and Σ_s are the inverse of noise covariance and source covariance, respectively, λ is the hyperparameter to regularize the inversion. Σ_d was estimated as a full noise covariance matrix from baseline recordings (i.e. -10s to 0s). Σ_s is assumed to be an identity matrix in conventional MNE. In our implementation, λ was estimated by the standard L-Curve method, as suggested in (Hansen, 2000).

In our proposed MEM method, which is a probabilistic framework, the probability distribution of the amplitude of X , described as $dp(x) = p(x)dx$, can be estimated by Bayesian inference, starting from a predefined prior distribution of X denoted $d\nu(x)$. The peak of the posterior of $dp(x)$ represented by $dp^*(x)$ is estimated by maximizing the Kullback-Leibler divergence or ν -entropy to the prior as following,

$$S_\nu(dp(x)) = - \int \log\left(\frac{dp(x)}{d\nu(x)}\right) dp(x) = - \int f(x) \log(f(x)) d\nu(x)$$

$$dp^*(x) = \operatorname{argmax}_{dp(x) \in \mathbb{C}_m} (S_\nu(dp(x)))$$

where $S_\nu(dp(x))$ is the ν -entropy of $dp(x)$ to prior $d\nu(x)$, \mathbb{C}_m is the set of probability distributions of x that explains the data Y on average, meaning

$$Y - [A|I] \begin{bmatrix} E_{dp}[x] \\ e \end{bmatrix} = 0, \quad dp \in \mathbb{C}_m$$

where $E_{dp}[x]$ is the statistical expectation of x under the probability distribution dp , I is the identity matrix with the dimension of the number of vertices involved in the reconstruction.

Then, assuming that brain activity could be described by K non-overlapping and independent cortical parcels, we proposed the following reference distribution $d\nu(x)$ model,

$$d\nu(x) = \prod_{k=1}^K [(1 - \alpha_k)\delta(x_k) + \alpha_k N(\mu_k, \Sigma_k)] dx_k, \quad 0 < \alpha_k < 1$$

where the hidden variable S_k defines the activation state (active or not) of each cortical parcel k . α_k is the probability of k^{th} parcel to be active, i.e. $Prob(S_k = 1)$. δ_k is a Dirac function that allows to ‘switch off’ the parcel when considered as inactive (i.e. $S_k = 0$). $N(\mu_k, \Sigma_k)$ is a Gaussian distribution, describing the distribution of absorptions changes within the k^{th} parcel, when the parcel is considered as active, $S_k = 1$. Note that the multiplication in the definition of $d\nu(x)$ is referring to the assumption that all parcels are statistically independent.

A data driven parcellation (DDP) technique (Lapalme, Lina and Mattout, 2006) was used to parcellate the cortical surface into K non-overlapping parcel. The probability of each parcel to be active (α_k) was initialized as the median Multivariate Source Pre-localization (MSP) (Mattout *et al.*, 2005) score from all the sources within the parcels.

To initialize the $N(\mu_k, \Sigma_k)$ in prior $d\nu(x)$, μ_k was set to zero. $\Sigma_k(t)$ at each time point t was defined according to (Chowdhury *et al.*, 2013),

$$\Sigma_k(t) = \eta(t)W_k(\sigma)^T W_k(\sigma)$$
$$\eta(t) = 0.05 \frac{1}{\mathcal{P}_k} \sum_{i \in \mathcal{P}_k} \hat{X}_{MNE}^2(i, t)$$

where $W_k(\sigma)$ is a spatial smoothness matrix, defined by (Friston *et al.*, 2008), which controls the local spatial smoothness within the parcel according to the geodesic surface neighborhood order. $\eta(t)$ was defined as 5% of the averaged energy of MNE solution within each parcel.

Note that for NIROT reconstruction, we also applied a depth-weighted version of MEM and MNE, as described and evaluated in (Cai *et al.*, 2021). Please refer to this work for further methodological details.

A2. The reliability of performance differences between MEM and MNE

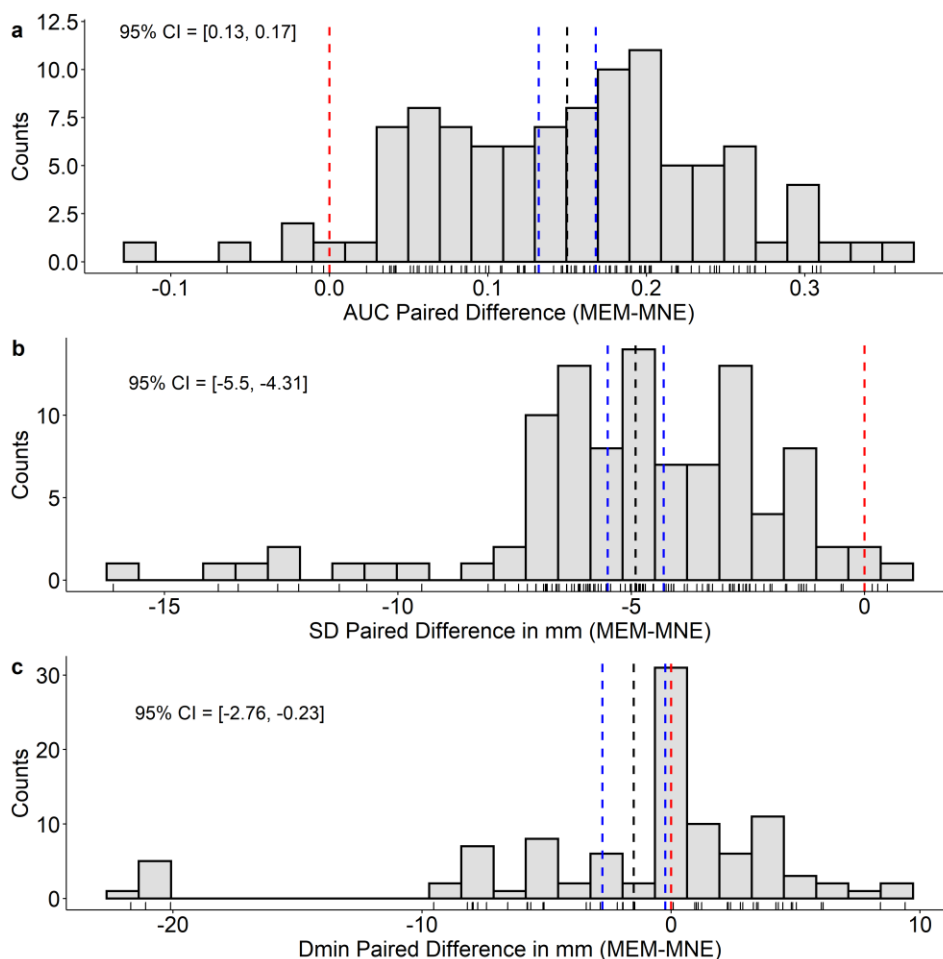


Fig.5.A1. Histograms of paired evaluation metric differences between MEM and MNE estimated over 100 sessions (10 within subject resampled sessions \times 10 subjects). The blue dashed lines indicated the 95% confidence interval (CI) of the estimated paired differences on a) AUC, b) SD (in mm) and c) Dmin (in mm). Red dashed lines showed 0 difference and black dashed lines represented the mean of the corresponding differences. Based on all sessions including within- and between-subjects variability, MEM provided significantly higher AUCs (overall better sensitivity and specificity), smaller SDs (less amplitude weighted spatial spread) and smaller Dmin (closer to the main fMRI cluster) than MNE.

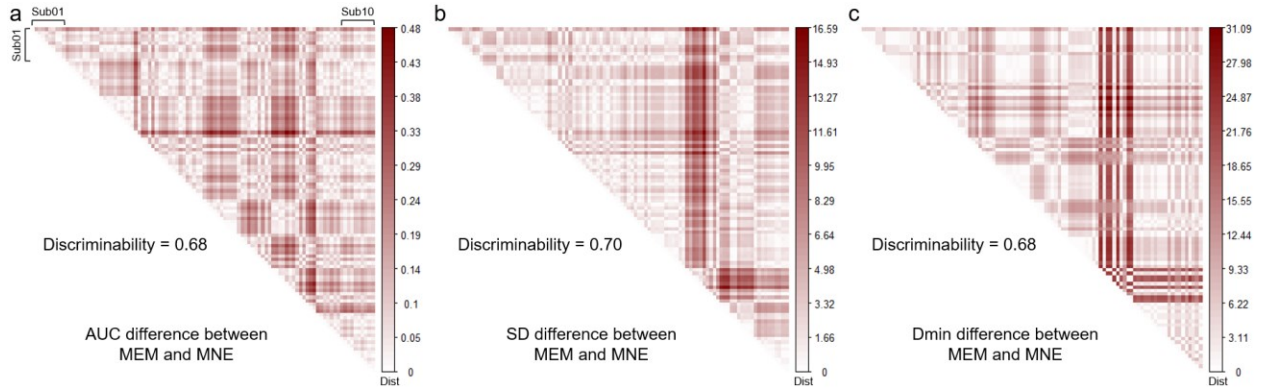


Fig.5.A2. Evaluations of reliability of performance differences between MEM and MNE using discriminability. Each diagonal matrix demonstrated the within-subject and between-subject Euclidean distances of the pair-wised performance differences (MEM–MNE) for a) AUC, b) SD (in mm) and c) Dmin (in mm). MEM showed reliably better reconstruction performance than MNE indicated by a discriminability measure of 0.68 for AUC, 0.70 for SD and 0.68 for Dmin, as illustrated in the figure showing that within-subject distances (block diagonal terms) were overall smaller than between-subject distances (off diagonal terms).

5.7 Supplementary Materials

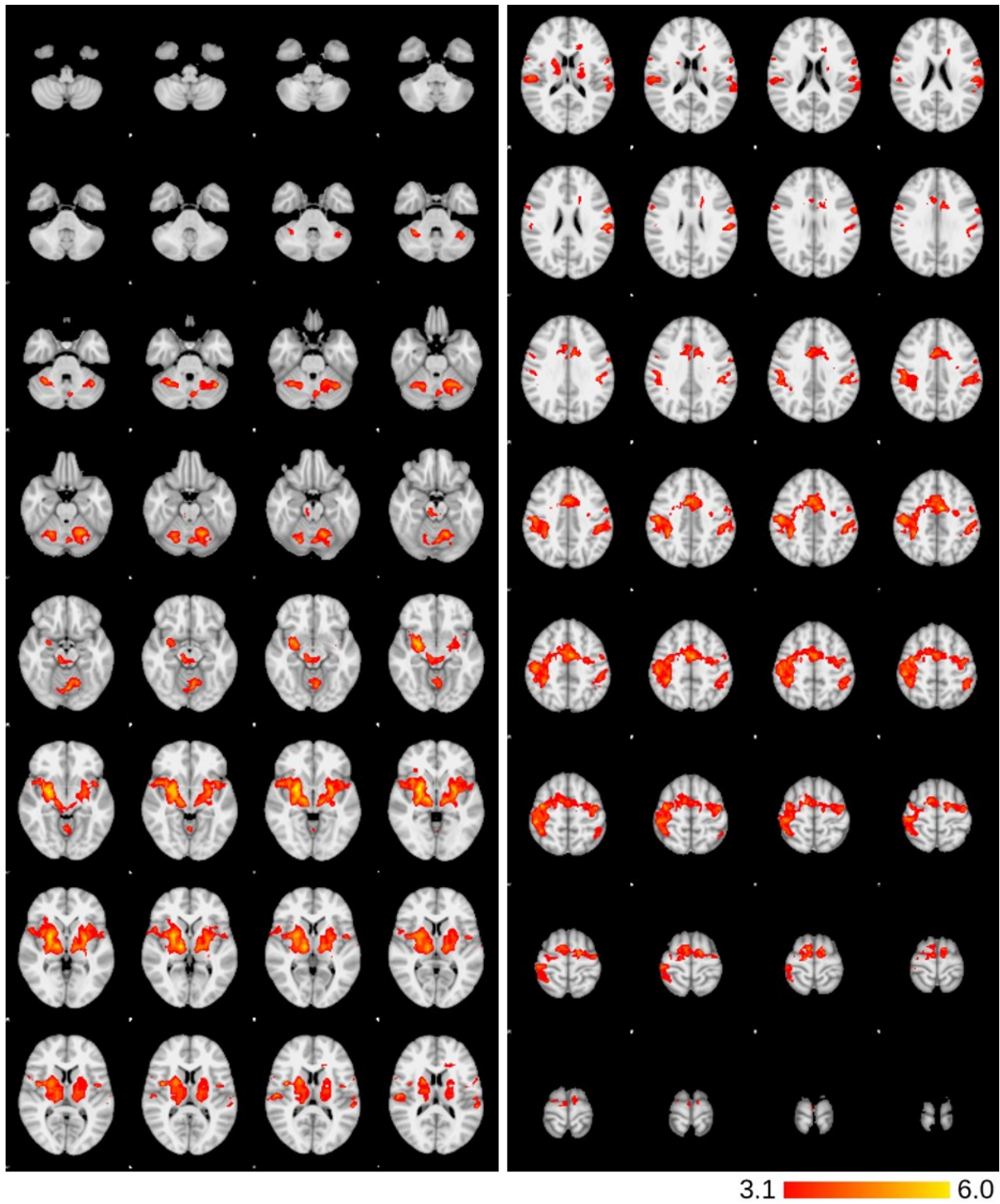


Fig.5.S1. FSL group-level fMRI activation maps of each slice thresholded by $Z > 3.1$ (cluster-wise inference, $p < 0.01$, corrected).

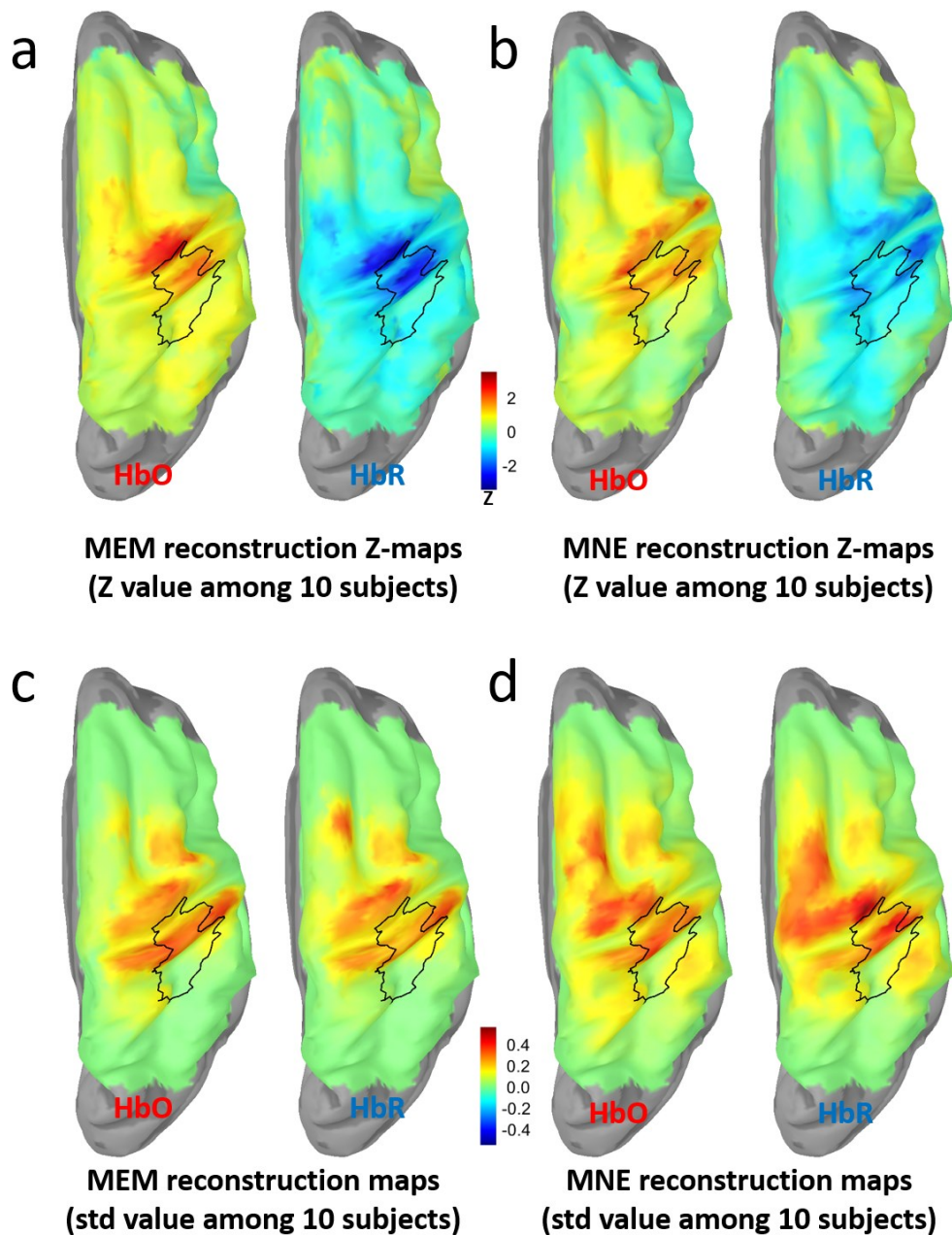


Fig.5.S2. Group-level NIROT Z-maps and standard deviation maps. a) group-level NIROT Z-maps of HbO and HbR reconstructed by MEM. Individual peak maps were first normalized by its own peak amplitude to $[-1,1]$ in the native space, then projected to the mid-surface of the ICBM152 template using FreeSurfer spherical registration. Z values were calculated for each vertex using the mean amplitude divided by the standard deviation among 10 subjects. Black profile represents the group-level fMRI main

cluster. b) same illustrations as a) but reconstructed by MNE. c) and d) demonstrate the standard deviation used for the calculation of Z-maps of the corresponding reconstruction results.

Chapter 6

Manuscript 3: Hemodynamic Correlates of Fluctuations in Neuronal Excitability: A Simultaneous Paired Associative Stimulation (PAS) and functional Near Infra-Red Spectroscopy (fNIRS) Study

Context

In Chapter 2, we introduced the advantages of combining TMS and fNIRS when investigating the correlation between hemodynamic activity and cortical excitability. Corresponding literature is also briefly reviewed in that chapter, reporting some inconsistent findings. Whereas combined TMS/fNIRS features some technical advantages from the data acquisition perspective, addressing research questions remains challenging, especially for the following aspects: 1) brain stimulation techniques are known for inducing variable and sometimes unpredictable effects. [López-Alonso et al., 2014](#) showed that only 39% of subjects exhibited an expected response to PAS25, and 43% of subjects showed an expected response to iTBS. This intrinsic variability of PAS effect depends upon multiple factors, including genetic susceptibility and the position of the coil ([Ziemann and Siebner, 2015](#)); 2) task-evoked hemodynamic response measured using fNIRS also contains considerable levels of variability ([Novi et al., 2020](#)). These sources of variability may explain some reported non-reproducible fNIRS/TMS results. So far, all fNIRS/TMS studies considered traditional fNIRS cap/patch, i.e., fNIRS sensors layout which is not personalized to the subject anatomy, and data analyses were mostly using the basic channel space approach. Not considering spatial information included in fNIRS montage has been shown to impact the reliability of the results ([Novi et al., 2020](#)), and may result in inaccurate hemodynamic response estimations by mBLL, when assuming homogenous HbO/HbR concentration changes along the light pathway (see Chapter 1). To address these limitations, in this chapter, we are applying our previously developed and evaluated personalized NIROT workflow in the context of a simultaneous fNIRS/TMS study to investigate the effects of PAS.

This manuscript is currently in preparation, Zhengchen Cai, Giovanni Pellegrino, Amanda Spilkin, Edouard Delaire, Makoto Uji, Chifaou Abdallah, Jean-Marc Lina, Shirley Fecteau, Christophe

Grova. Hemodynamic Correlates of Fluctuations in Neuronal Excitability: A Simultaneous Paired Associative Stimulation (PAS) and functional Near Infra-Red Spectroscopy (fNIRS) Study.

Abstract

Background: The relationship between task-related hemodynamic activity and brain excitability is poorly understood in humans as it is technically challenging to combine simultaneously non-invasive brain stimulation and neuroimaging modalities. Cortical excitability corresponds to the readiness to become active and as such it may be linked to metabolic demand.

Hypotheses: Cortical excitability and hemodynamic activity are positively linked so that increases in hemodynamic activity correspond to increases in excitability and vice-versa.

Methods: Fluctuations of excitability and hemodynamic activity were investigated via simultaneous Transcranial Magnetic Stimulation (TMS) and functional Near Infrared Spectroscopy (fNIRS). Sixteen healthy subjects participated in a sham-controlled, pseudorandomized, counterbalanced study with PAS (PAS10/PAS25/Sham) on the right primary motor cortex (M1). The relationship between M1 excitability (Motor Evoked Potentials, MEP) and hemodynamic responses to finger tapping reconstructed via personalized fNIRS was assessed.

Results: Hemodynamic activity exhibited a significant correlation with cortical excitability: increased HbO and HbR (absolute amplitude) corresponded to increased excitability and vice-versa ($r=0.25$; $p=0.03$ and $r=0.16$; $p=0.17$, respectively). MEP ratios (post-PAS/pre-PAS) showed a significant linear relationship with HbO and HbR ratios ($r=0.82$, $p<0.001$ and $r=0.88$, $p<0.001$, respectively), when considering sessions with concordant PAS effects on MEP, HbO and HbR.

Conclusions: TMS-fNIRS is a suitable technique for simultaneous investigation of excitability and hemodynamic responses and indicates a relationship between these two cortical properties. PAS effect is not limited to cortical excitability but also impacts hemodynamic processes. These findings have an impact on the application of neuromodulatory interventions in patients with neuropsychiatric disorders.

6.1 Introduction

The relationship between cortical excitability and elicited hemodynamic activity is poorly understood in humans. Such investigation requires simultaneous measurements of excitability and hemodynamic activity (Siebner *et al.*, 2009). Transcranial Magnetic Stimulation (TMS) is a versatile technique that allows the assessment and modulation of primary motor cortex (M1) excitability. Cortical excitability assessment is easily achieved via single pulse TMS (spTMS) by measuring the amplitude of the Motor Evoked Potentials (MEPs). M1 excitability modulation can be obtained by repetitive TMS (rTMS) and related techniques, such as Paired Associative Stimulation (PAS). PAS was established about two decades ago (Stefan, 2000) and consists in combining TMS with peripheral electrical stimulation such as Median Nerve Stimulation (MNS). It relies on the principle that repetitive stimulations delivered with proper timing and pace induce long-term potentiation and long-term depression like plasticity, exploiting the concept of spike-timing-dependent plasticity (Levy and Steward, 1983; Rossini *et al.*, 2015b). PAS effects can last for 30 minutes or more (Stefan, 2000; Lee *et al.*, 2017; Suppa *et al.*, 2017). This technique is therefore well-suited to manipulate cortical excitability by tuning the timing of the interstimulus intervals (ISI), because it can generate either an excitability increase, when applying a 25ms time-interval between MNS and TMS pulses (PAS25), or an excitability decrease, when applying a 10ms time-interval between pulses (PAS10). A PAS sham has also been described and validated (Loo *et al.*, 2000; Gow *et al.*, 2004; Michou *et al.*, 2014b).

A standard approach to non-invasively map brain functions is to measure the fluctuations of brain hemodynamic signals elicited by neuronal activity. Functional magnetic resonance imaging (fMRI) is typically the tool of choice for its reliability, ease of use, high spatial resolution and sensitivity to deep brain regions (Bandettini *et al.*, 1992; Kwong *et al.*, 1992; Glover, 2011). Nevertheless, bringing TMS within the MRI environment is challenging (Hallett *et al.*, 2017). MRI compatible TMS coils have been developed (Navarro De Lara *et al.*, 2015; Wang, Xu and Butman, 2017) and applied to investigate the TMS induced hemodynamic responses (Navarro de Lara *et al.*, 2017), but the majority of studies have had an “offline” approach, meaning that no continuous fMRI measurement during TMS is usually performed (Siebner *et al.*, 2009).

Functional Near InfraRed Spectroscopy (fNIRS) is a non-invasive neuroimaging modality, which allows monitoring changes in oxy- and deoxy-hemoglobin (i.e., HbO/HbR) in the cerebral cortex (Jöbsis, 1977; Scholkmann, Kleiser, *et al.*, 2014; Yücel *et al.*, 2021). It measures light intensity changes, modulated by local absorption associated with underlying hemoglobin concentration

fluctuations, via source-detector pairs placed on the scalp. fNIRS has high temporal resolution and acceptable spatial resolution with no electromagnetic interference (Siebner *et al.*, 2009; Vasta *et al.*, 2017; Curtin, Tong, *et al.*, 2019). It allows the estimation of both HbO and HbR concentration changes in cortical regions. It is relatively portable and permits prolonged scans, with little or no discomfort for the participants (Scholkmann, Kleiser, *et al.*, 2014; Pellegrino, Machado, *et al.*, 2016; Gramigna *et al.*, 2017). The drawback of combining fNIRS and TMS is that when both techniques are applied to the same cortical area, the optodes (fNIRS sensors) introduce some additional space between the TMS coil and the scalp. This requires higher TMS stimulation intensities as the strength of the magnetic field decays sharply when increasing the coil distance to the target region (Parks, 2013; Curtin, Tong, *et al.*, 2019). Nevertheless, we are proposing combining PAS and fNIRS as a promising way to assess the relationship between cortical excitability and hemodynamic responses.

We conducted here the first PAS-fNIRS investigations of the relationship between cortical excitability and task-related hemodynamic response. Cortical excitability corresponds to the cortical readiness to become active and as such it may be linked to metabolic demand. We first hypothesized that fluctuations of cortical excitability are positively correlated with fluctuations of hemodynamic activity. This hypothesis was tested by estimating the correlation between MEP peak-peak amplitude and task-related HbO/HbR response, regardless of the PAS interventions (PAS25, PAS10, Sham). Second, we hypothesized that PAS affects cortical task-related hemodynamic responses in addition to cortical excitability, and such modulations of excitability and hemodynamic positively correlate. In other words, when PAS increases cortical excitability, it results in enhanced task-related hemodynamic response, whereas when PAS decreases cortical excitability, it results in reductions of the hemodynamic response to the task. This hypothesis was tested by estimating the correlation between MEP and HbO/HbR ratios calculated as the post- over pre-intervention amplitudes. As PAS is known to induce variable effects (López-Alonso *et al.*, 2014; Suppa *et al.*, 2017), this second analysis was restricted to cases showing concordant PAS effects on MEP, HbO and HbR.

6.2 Material and methods

6.2.1 Subjects and study design

This study was approved by the Central Committee of Research Ethics of the Minister of Health and Social Services Research Ethics Board, (CCER), Québec, Canada. All subjects signed a written informed consent before participation. Only subjects meeting the following inclusion/exclusion criteria were considered: 1) age between 18 and 40 years old; 2) right-handed male; 3) no present or past neurological disorders; 4) no medications acting on the central nervous system; 5) no contraindications to MRI or TMS (Rossi *et al.*, 2009; Suppa *et al.*, 2017). Nineteen subjects (24 ± 5 years old, mean \pm SD) participated in the study. Subjects were instructed to have a regular sleep cycle for the days before the experiments and to not consume caffeine for at least 90 minutes before the experiment.

The experimental design and setup are illustrated in Fig.6.1 and Fig.6.2, respectively. Every participant had 1) an anatomical head MRI scan (T1- and T2-weighted, 1mm³ isotropic) for neuronavigated TMS; calculate personalized fNIRS optical head model (Machado *et al.*, 2014b, 2018); and install optodes, followed by 2) somatosensory evoked potentials recording during electrical stimulation of the median nerve at the wrist to measure N20 latency and tune PAS accordingly. We then conducted three experimental sessions corresponding to three different PAS interventions: PAS25, PAS10, and sham. These sessions were performed at least two days apart to minimize potential carryover effects. As this study included three sessions, we decided to consider male participants to minimize the confounding of cortical excitability changes due to the menstrual cycle (Hattemer *et al.*, 2007; Lee *et al.*, 2017). Experimental sessions were performed with a pseudorandomized order, counterbalanced across subjects, which consisted of the following components:

- PAS was performed with 100 pairs of MNS and TMS with a fixed interval of 10s according to the guidelines (Suppa *et al.*, 2017), for a total duration of 18 minutes (Fig.6.1c). MNS was delivered at the left wrist and with the following parameters: intensity = 300% perceptual threshold, square wave and 0.2ms duration. TMS intensity was 120% of the resting motor threshold (RMT). The ISI between MNS and TMS were then set to be individual N20+5ms for PAS25 and N20-5ms for PAS10, respectively (Carson and Kennedy, 2013). Sham was the same as PAS25, except TMS was not delivered, whereas its sound was provided via a stereo speaker (Zangrandi *et al.*, 2019).

Before and after each intervention,

- Cortical excitability was measured via M1 spTMS, applying 75 stimuli (ISI ranging between 5s and 25s) to the right hand-knob (Fig.6.1b). MEPs were recorded by bipolar electromyography (EMG) electrodes attached on the right abductor pollicis brevis (APB), with a standard belly-tendon montage (Fig.6.2d). The RMT was defined with the TMS Motor Threshold Assessment Tool (Awiszus *et al.*, 1999; Ah Sen *et al.*, 2017). All TMS procedures followed the recommendations of the International Federation of Clinical Neurophysiology, and no participants reported any severe discomfort or side effects (Rossi *et al.*, 2009).
- A finger tapping task was performed to activate M1 and estimate its task-related hemodynamic activity. Subjects were instructed to tap the left thumb to the other digits sequentially, at a pace of about 2Hz (Fig.6.1a). The movement was performed in short blocks of 10s interleaved with a resting period jittered between 30s to 60s. This time-constraint was meant to avoid task events phase locking to undergoing physiological hemodynamic oscillations (Aarabi, Osharina and Wallois, 2017). Movement onset and offset were instructed by auditory cues. The duration of the motor task was about 18 minutes and consisted of 20 blocks.

fNIRS data were acquired using a Brainsight fNIRS machine (Rogue-Research Inc, Montreal Canada), sampling at 10Hz. MEPs were recorded by a BrainAmp ExG bipolar system (Brain Products GmbH, Germany). Please refer to Appendix A for further detailed experiment protocol. From the nineteen subjects, one was excluded due to low sensitivity to TMS and two due to poor fNIRS signal quality. Four subjects dropped out after the first session due to personal reasons, resulting in 16 PAS25, 12 PAS10 and 12 sham sessions. Ten subjects completed all 3 sessions.

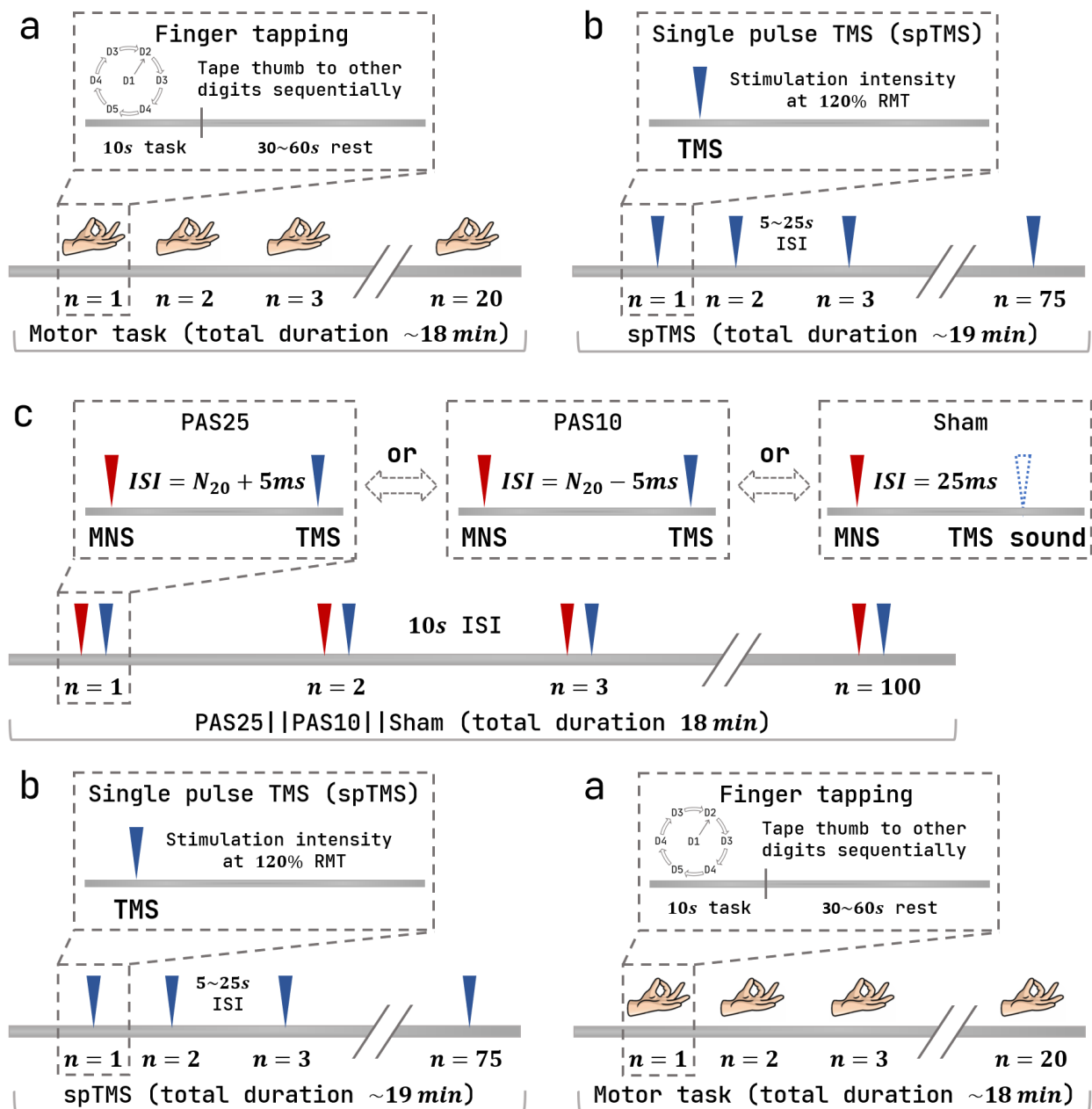


Fig.6.1 Study design. Each acquisition session described above contains sections following the order of **a, b, c and b, a**. (a) Finger tapping task: subjects were asked to tap the left thumb (D1) to the other four left digits (D2-D5) sequentially, at around 2Hz. Each tapping block lasted 10s and was followed by 30s to 60s jitter rest. Start and stop signals were delivered by auditory cues. 20 blocks were performed for 18 minutes total duration. (b) A single pulse TMS was delivered onto the “hot spot” at 120% of individual RMT. 75 pulses were delivered with a 5s to 25s jittered ISI for a total duration of about 19 minutes. (c) Three PAS simulations were performed on different days separated by at least 2 days and presented in a pseudorandomized order. ISI between peripheral (MNS) and TMS was set to individual $N_{20}+5ms$ (PAS25)

and N20-5ms (PAS10) for excitatory and inhibitory PAS, respectively. Sham was similar to PAS25, same MNS followed by a 0 intensity TMS, whereas the TMS click was reproduced via speakers. MNS intensity was set to 3x individual perceptual threshold. PAS pairs were separated by a 10s interval. In total, 100 pairs were delivered in 18 minutes. Note that fNIRS signal was acquired during the whole experiment session.

6.2.2 Personalized fNIRS using the optimal montage

In order to maximize the sensitivity of fNIRS channel layout (i.e., montage) to M1 hemodynamic activity, we applied a personalized optimal montage, previously developed and validated by our group. Specifically, this montage maximizes fNIRS sensitivity along the cortical surface with good spatial overlap between channels (Machado *et al.*, 2014b, 2018, 2021; Pellegrino, Machado, *et al.*, 2016). The T1-/T2-weighted images were processed by FreeSurfer 6.0 to segment the head (i.e., scalp, skull, cerebrospinal fluid, gray matter and white matter) and generate a mid-cortical surface (i.e., a middle layer of the gray matter, between pia mater and gray-white matter interface) (Fischl *et al.*, 2002). The target area for the optimal montage (see Fig.6.2a) corresponded to the right hand-knob and was manually defined for each participant along the mid-surface (Raffin *et al.*, 2015b). The personalized optimal montage was estimated imposing the following constraints: 1) 3 light sources and 15 detectors (see Fig.6.2b); 2) distance between source-detector pairs ranging from 2.0cm to 4.5cm and 3) large spatial overlap between channels, e.g., each source must construct at least 13 channels among 15 detectors. The output of the optimal montage procedure is a set of fNIRS optode positions along the scalp to probe the right hand-knob with the highest sensitivity. Finally, a proximity detector for recording physiological hemodynamics of the scalp was added at the center of the 3 sources (Zeff *et al.*, 2007; Gregg *et al.*, 2010).

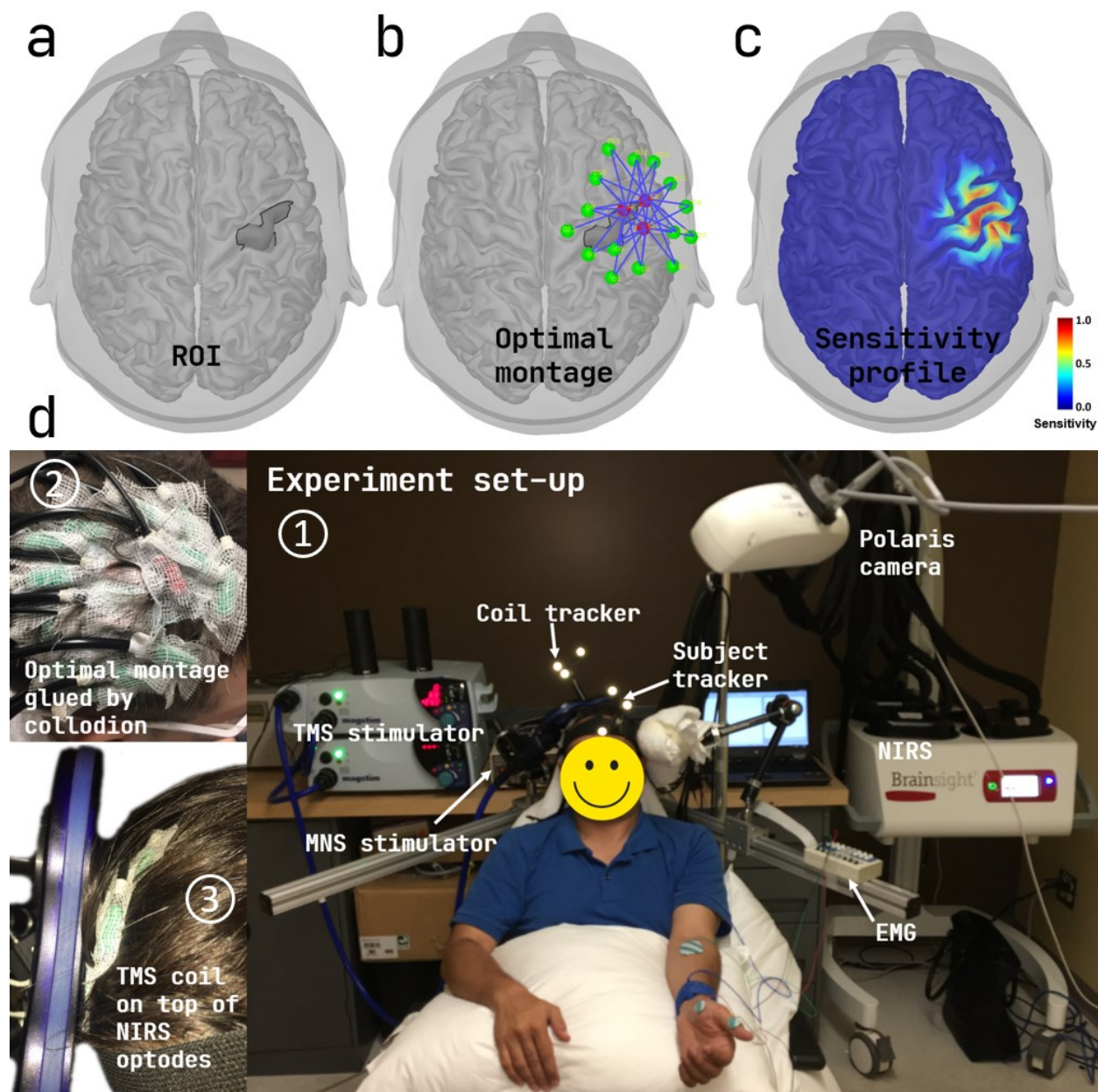


Fig.6.2 Personalized optimal montage and simultaneous PAS-fNIRS acquisition setup. (a) The right M1 hand region (“hand knob”) was pre-defined as the target ROI of personalized optimal fNIRS montage. This area was manually selected on each subject’s cortical surface extracted from individual MRI. (b) Example of the optimal montage estimated for Sub06. The montage was constrained to have 3 sources (red), 15 detectors (green) and 1 proximity detector (placed in the middle of sources, not shown). (c) Normalized light sensitivity profile of the optimal montage expressed as the sum of all channels’ sensitivity along the individual cortical surface. (d) PAS and fNIRS acquisition setup. (1) Participants sat on a comfortable TMS armchair. Four different machines were involved: a Brainsight-fNIRS for fNIRS data acquisition and neuronavigation; Magstim 200² TMS stimulators for spTMS and PAS; a Digitimer DS7A for MNS and PAS;

and a BrainAmp ExG bipolar system for recording MEPs. (2) Low-profile (thin) optodes were attached on the subject's head using collodion based on their optimal positions defined in (b). (3) A figure-8 TMS coil was placed on top of the optodes, guided with the neuronavigation system, held with a mechanical arm.

6.2.3 Excitability data analysis

EMG data collected during spTMS were analyzed using the Brainstorm software (Tadel *et al.*, 2011) and R 4.0.3 (R Core Team, 2020). They were filtered between 3 and 2000Hz. MEP trials were extracted within a time window from -10ms to 100ms around the stimulation and baseline corrected (-10ms to 0ms). Run specific (e.g., pre-PAS 25 of Sub01) excitability was expressed as the average of MEP peak-peak amplitudes across spTMS. Session specific (e.g., PAS 25 of Sub01) excitability change was measured as the post-/pre-PAS ratio of averaged MEP peak-peak amplitudes.

6.2.4 fNIRS data processing

The details of the following procedures are provided in Appendix. B. Briefly, fNIRS data processing was performed applying 3D reconstructions with the Maximum Entropy on the Mean (MEM) framework, as described in (Cai *et al.*, 2021). The goal was to extract HbO/HbR amplitude from spatiotemporal maps reconstructed from the channel space data to the underlying cortical surface. fNIRS data pre-processing involved the following steps: bad channel rejections; physiological noise regression using proximity channels (Zeff *et al.*, 2007; Gregg *et al.*, 2010); band-pass filter between 0.01Hz and 0.1Hz, and epochs extraction with a time window of -10s to 30s around the task onset. To extract robust and reliable HbO/HbR amplitude for further estimation of PAS effects on hemodynamic, we introduced in this study an original approach which comprises three steps: 1) selection of 101 trials centred around the median signal to noise ratio (SNR) of “all the possible” sub-averaged 16 out of 20 fNIRS epochs. This procedure aimed to exclude eventual motion artifacts contaminated epochs from sub-averaging and resulted in a distribution representing the variability of task-evoked fNIRS signal changes specific for each run (e.g., pre-PAS25 of Sub01); 2) fNIRS 3D reconstructions of each sub-averaged trial using the MEM framework, resulted in 101 spatiotemporal hemodynamic responses maps for each task run; 3) extraction/identification of a data-driven ROI which exhibited significant task-related hemodynamic responses for each session (e.g., PAS25 of Sub01). Importantly, since this procedure was data-driven, fNIRS analysis was blind to PAS interventions. Finally, the measure of HbO/HbR

was defined as the averaged amplitude within a 5s window centred around the peak of the reconstructed time course, extracted by averaging reconstructed time courses within the ROI defined in 3). Therefore, 101 HbO/HbR amplitudes were extracted for each run. Run specific hemodynamic responses were expressed as the averaged HbO/HbR amplitude among all 101 trials. Session specific PAS effects on task-related hemodynamic response were represented by the post-/pre-intervention ratios of averaged HbO/HbR measures. To demonstrate group-level intervention effects on reconstructed HbO/HbR maps, individual maps selected at their respective peak were first coregistered on the mid-surface of MNI ICBM152 (Fonov *et al.*, 2009, 2011) template using FreeSurfer spherical registration, and then averaged over all subjects.

6.2.5 Statistical analysis

To assess the relationship between fluctuations of cortical excitability and task-related hemodynamic activity regardless of PAS intervention, we pooled together subjects' data of all runs (before and after PAS) and calculated Pearson's correlations (r) between MEPs amplitude and HbO responses (HbR, respectively). Furthermore, as cortical excitability is usually estimated on 20 or fewer MEPs while we had 75 measures, we applied a procedure to keep within-subject variability, that would have been lost by collapsing all trials in a single average. We then performed a bootstrap so that 2000 correlations were computed considering averaged amplitudes of 20 MEPs, 20 HbO and 20 HbR trials randomly selected for each run. The resulting r empirical distribution allowed the estimation of an average r -value and a confidence interval.

To estimate the effect of PAS on excitability (MEPs), HbO and HbR responses, we considered post-/pre- ratios. The effects of PAS across interventions were tested with a one-way ANOVA applied independently for MEPs, HbO and HbR ratios, whereas the effect of each intervention was tested with a one-sample t-test against 1.

To estimate the relationship between PAS-related excitability and hemodynamic changes, linear regressions were performed between MEP and HbO ratios (HbR, respectively). The regression was conducted on three classes: 1) pooling all sessions; 2) sessions exhibiting concordant effects only, defined as MEP and HbO and HbR ratios simultaneously larger or smaller than 1; and 3) sessions with discordant effects (see Appendix. C).

6.3 Results

6.3.1 Correlation between cortical excitability and task-related hemodynamic responses

Fig.6.3 illustrates the relationship between excitability (MEPs amplitude) and task-related hemodynamic activity (HbO and HbR). We found a significant positive linear correlation between MEP and HbO amplitude ($r = 0.25$, $p=0.03$) and a non-significant negative linear relationship between MEP amplitude and HbR ($r = -0.16$, $p=0.171$), meaning that an increased level of excitability corresponded to higher task-related HbO concentration and lower HbR concentration. These relationships were robust when considering the variability of the three amplitudes, as demonstrated by the bootstrapped correlation histograms (Fig.6.3c and d). The 95% confident interval of correlation value was $[0.16, 0.33]$ for HbO and $[-0.24, -0.08]$ for HbR. In both cases, the confidence interval did not cross the zero line, meaning that the variability of excitability and hemodynamic activity measures within subjects and across trials did not influence the sign of the correlation.

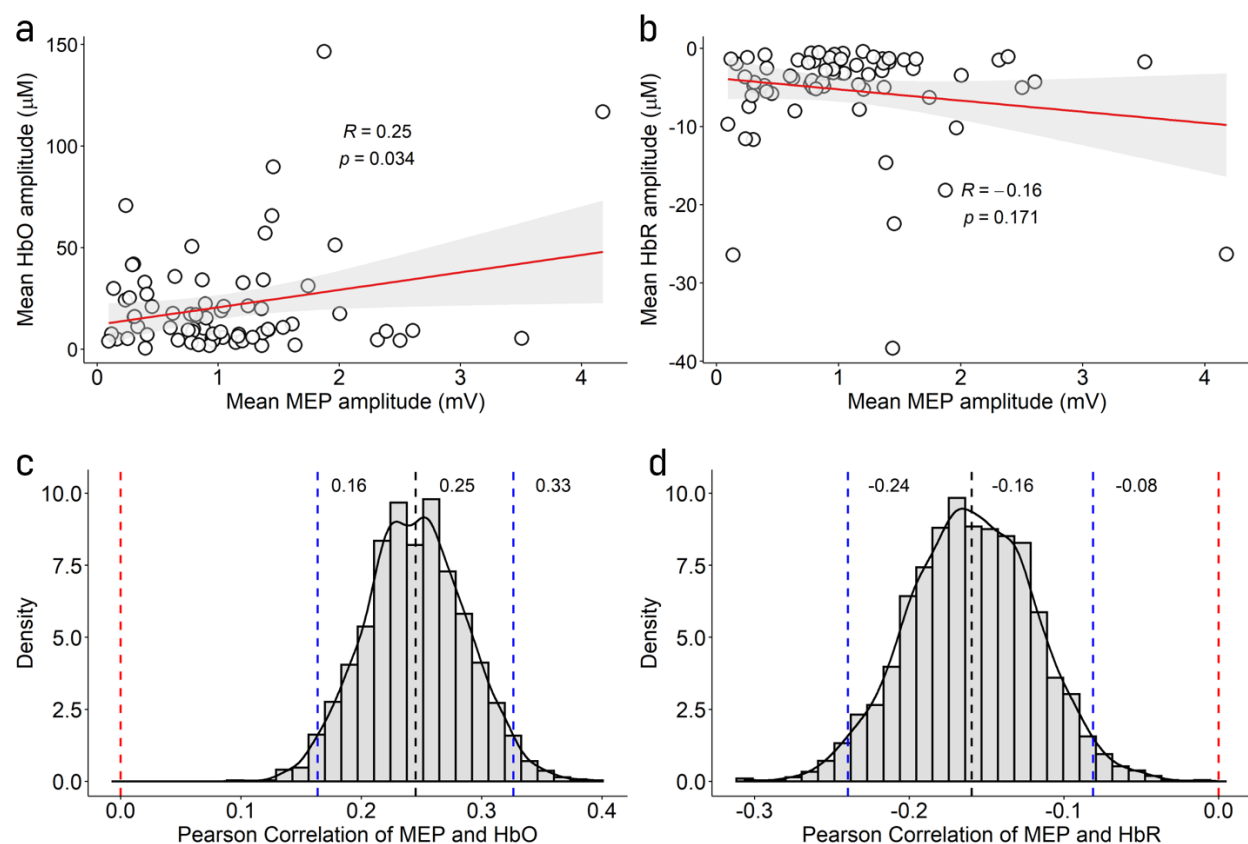


Fig.6.3 Correlation between MEP peak-peak amplitude and task-related HbO/HbR amplitudes. (a) scatterplot of HbO amplitude as a function of MEP amplitude. Each dot corresponds to a run (average over all MEPs amplitudes and all HbO trials). There was a significant positive linear relationship (Pearson's $r =$

0.25, $p=0.03$). Red lines represent the estimated regression line, and the gray area indicated the 95% confidence interval. (b) There was a negative linear relationship between HbR and MEPs amplitude which did not reach statistical significance when considering run averages of all MEPs and HbR amplitudes. (c) and (d) the histogram of the correlation between MEP and HbO/HbR amplitudes, respectively, estimated from the bootstrap procedure (selecting 20 out of 75 MEP, HbO and HbR trials). Black curves represented the estimated density functions; black dashed lines showed the resulting mean correlation value; blue dashed lines indicated the 95% confidence interval estimated from the histograms; red dashed lines indicated $r=0$.

6.3.2 PAS effects on cortical excitability and task-related hemodynamic activity

Fig.6.4 shows the group-level MEP, HbO and HbR ratios for the PAS25, PAS10 and sham sessions. Overall, PAS produced similar effects for excitability and hemodynamic, with an overall increase of MEP, HbO and HbR ratios after PAS25, a decrease of MEP and HbO ratios after PAS10, and the ratio of sham was always in between PAS25 and PAS10. Table.6.1 summarizes the corresponding ratio values. Of note, all measures and especially fNIRS measures showed rather high variabilities, which likely prevented from reaching statistical significance ($p>0.05$ for the ANOVA and one-sample t-test) for the planned comparisons.

Fig.6.5 illustrates the single subject level (Sub02) PAS effects on reconstructed HbO and HbR. Following PAS25 and PAS10, absolute HbO and HbR amplitude were exhibiting increases and decreases, respectively. These effects were concordant with MEP amplitude changes (detailed values in Fig.6.5 caption). Fig.6.6 presented the group-level reconstruction maps. HbO peak amplitude (mean within the ROI, $\mu\text{mol. l}^{-1}$) increased after PAS25 and decreased after PAS10. HbR peak amplitude within the ROI decreased after PAS25 and also decreased after PAS10 (detailed values in Fig.6.6).

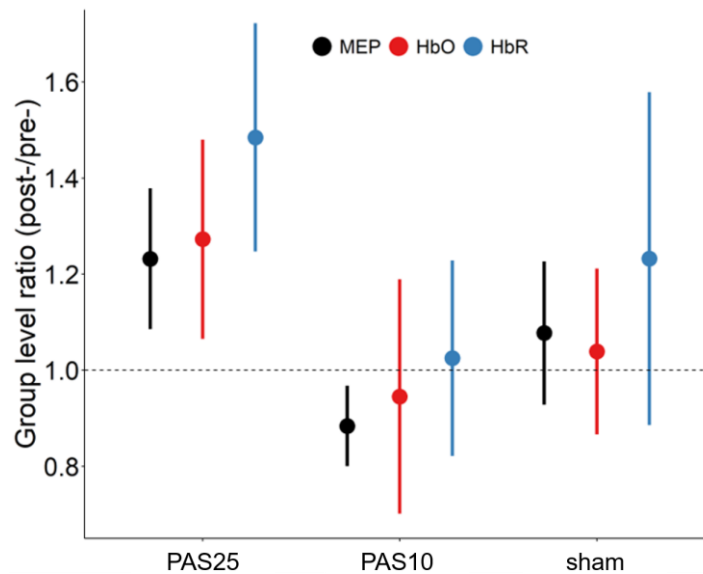


Fig.6.4 Group-level PAS effects on cortical excitability and hemodynamic activity. Effects of PAS25, PAS10 and sham on M1 cortical excitability (MEP amplitude) and M1 task-related hemodynamic activity (HbO and HbR) expressed as mean±SEM (standard error of the mean). PAS produced similar effects for excitability and hemodynamic activity, with an increase of MEP amplitude, HbO and HbR following PAS25, and a decrease of MEP amplitude and HbO following PAS10, a slight increase of the three measures after sham. All measures, and especially fNIRS measures, showed rather high variabilities (see standard error of the mean in the figure).

Table.6.1 Group-level PAS effects on cortical excitability and hemodynamic activity.

	Ratio (Mean±SEM)		
	PAS25	PAS10	Sham
MEP	1.23 ± 0.15	0.88 ± 0.08	1.08 ± 0.15
HbO	1.27 ± 0.21	0.95 ± 0.24	1.04 ± 0.17
HbR	1.48 ± 0.24	1.02 ± 0.20	1.23 ± 0.35

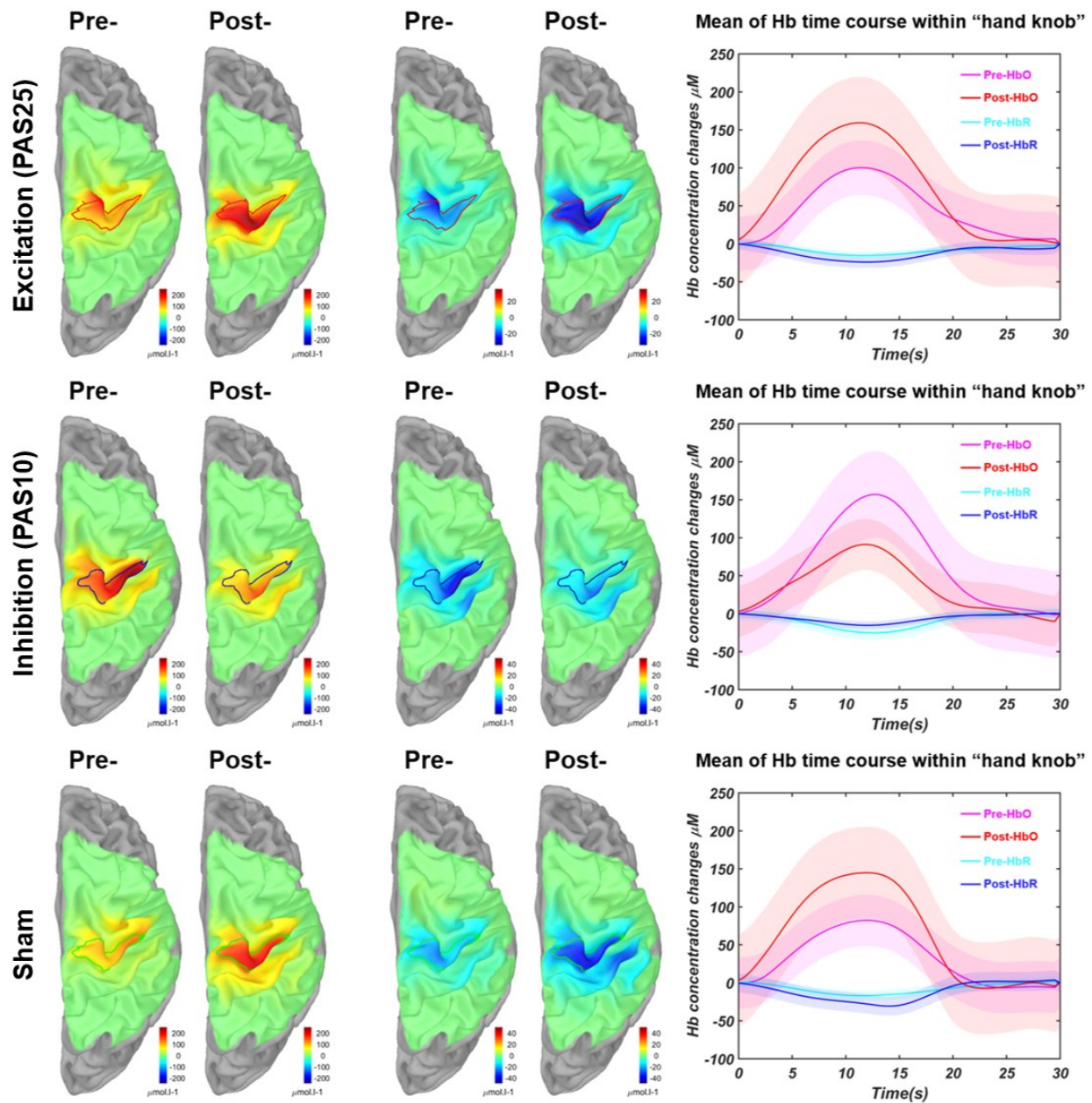


Fig.6.5 PAS effects on task-related hemodynamic responses using personalized fNIRS tomography for Sub02. Individual-level reconstructed fNIRS maps of HbO and HbR responses for each experimental session, pre- or post-intervention, PAS25 (1st row), PAS10 (2nd row), sham (3rd row). Each map demonstrated the spatial distribution pattern of the task-related hemodynamic responses at its own peak timing of the reconstructed time courses showed in the last column. The red, blue and green profiles represented the extracted specific ROIs exhibiting significant hemodynamic responses at the peak amplitudes (see method section for details) for PAS25, PAS10 and sham, respectively. The averaged time course of HbO and HbR within each selected ROI for each session is presented in the last column by the

solid lines, within a time window from 0s (the task onset) to 30s. All HbO and HbR time courses demonstrated the typical hemodynamic responses evoked by a 10s duration task. The shaded area represented the standard deviations of the time course within the ROI. Both the absolute amplitudes of HbO and HbR showed expected increase (after PAS25) and decrease (after PAS10) patterns within the selected ROIs. However, sham session also resulted in increased HbO and decreased HbR. The corresponding ratios of HbO and HbR were also in agreement with the mean MEP ratios, e.g., MEP ratio = 1.37, HbO ratio = 1.62 and HbR ratio = 1.56 for PAS25; then 0.85, 0.58 and 0.61 for PAS10, respectively. Colour maps for pre- and post- maps were fixed for specific hemoglobin and session (e.g., HbO in PAS25). HbO amplitudes generally exhibit a larger range than HbR amplitudes.

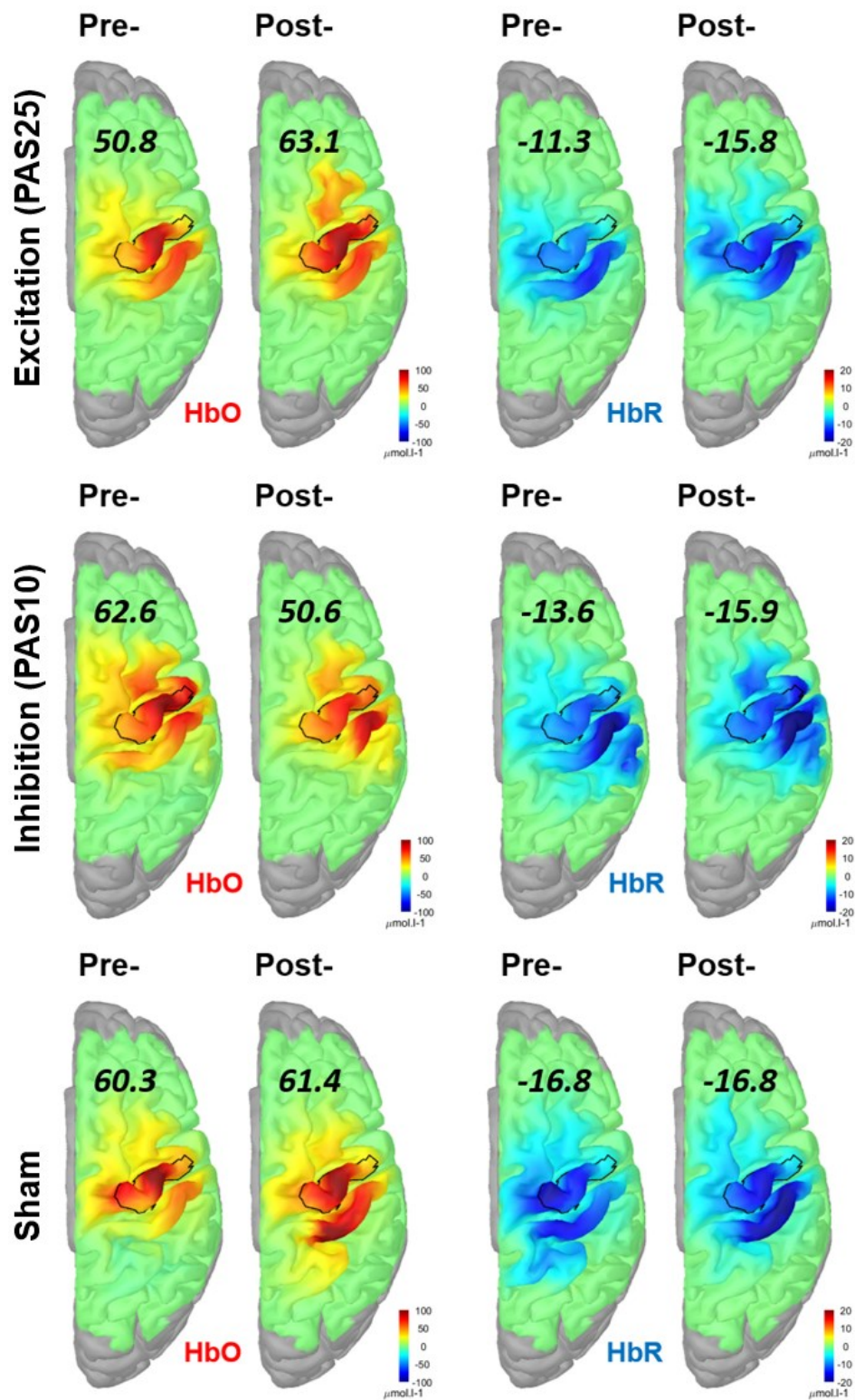


Fig.6.6 Group-level PAS effects on task-related hemodynamic responses. Group level reconstructed maps of HbO and HbR of each experimental session, pre- or post-, were shown in each row for PAS25,

PAS10 and sham, respectively. Each map demonstrated the averaged corresponding individual-level task-related hemodynamic responses. Individual HbO/HbR maps selected at their respective peak were first coregistered on the mid-surface of the MNI ICBM152 template using Freesurfer spherical registration and then averaged over all subjects. The numbers indicated on every map are reporting the mean HbO or HbR amplitude within the corresponding ROI. This group-level ROI was defined manually along the M1 cortex of the template cortical surface to cover the hand knob region. Note that these maps were mainly considered for the visualization of PAS effects, whereas the statistical summary of hemodynamic changes was extracted at the individual levels. Colour maps for pre- and post- maps were fixed for specific hemoglobin and session (e.g., HbO in PAS25). HbO amplitudes generally exhibit a larger range than HbR amplitudes.

6.3.3 Relationship between PAS-related excitability and hemodynamic changes

When pooling all sessions together (Fig.6.7a), the resulted linear regression between HbO ratio (HbR, respectively) and MEP ratio presented a positive relationship, but no significant association (MEP-HbO ratios, $r=0.19$, $p=0.29$; MEP-HbR ratios, $r=0.18$, $p=0.30$). Fig.6.7b illustrated the linear regression for sessions with concordant PAS effects (e.g., MEP and HbO and HbR ratios were simultaneously larger or smaller than 1), resulting in significant positive linear corrections between MEP ratio and both HbO ($r = 0.82$, $p<0.001$) and HbR ($r=0.88$, $p<0.001$) ratios. No significant linear correlations were found when considering sessions with non-concordant PAS effects (Fig.6.7c). For the sessions with concordant PAS effects, the probability of obtaining such correlation results in Fig.6.7b by chance was respectively 0%, 0%, 0.8% and 1.1%, when simulating null hypothesis distributions of correlation values using respectively 1000, 100, 50, 40 samples (see Appendix. C).

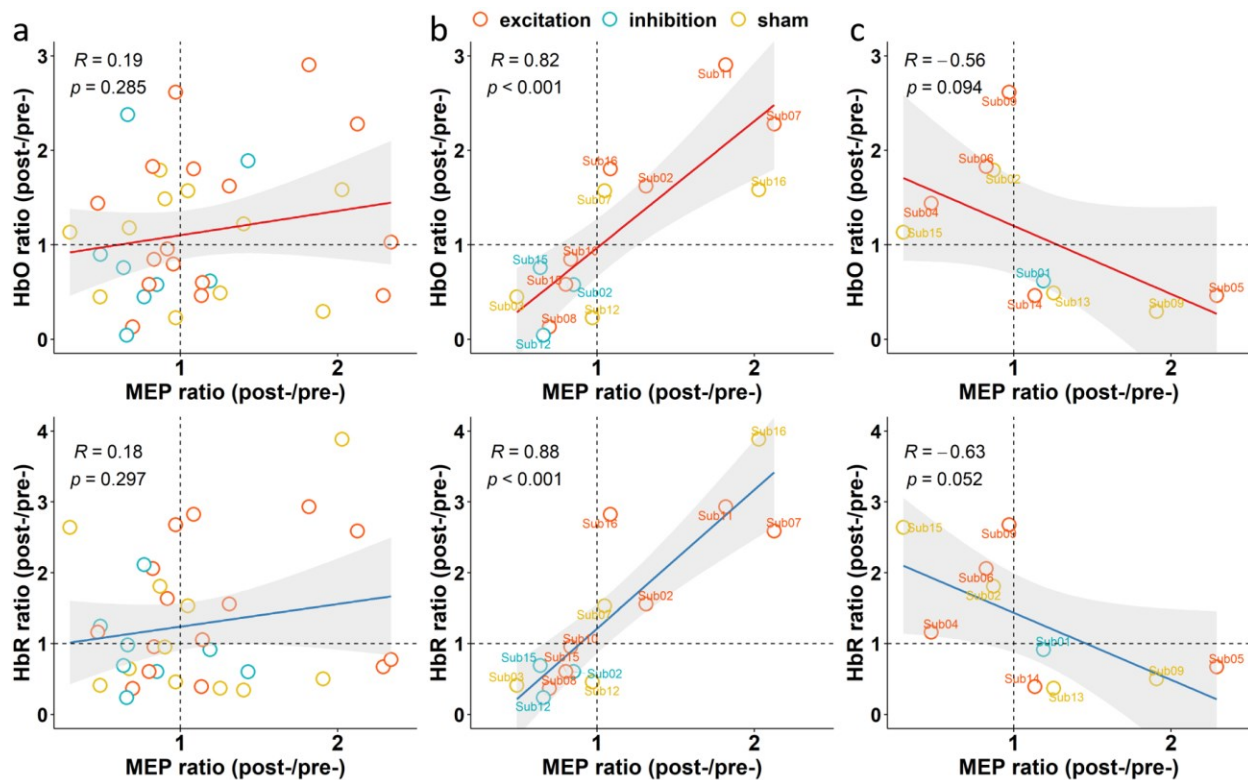


Fig.6.7 Correlates of task-related hemodynamic changes and PAS modulated excitability changes.

The 1st row presented HbO ratio as a function of MEP ratio and 2nd row showed HbR ratio as a function of MEP ratio. Each point represented a session (e.g., PAS25 for Sub01, post-/pre- ratios). Sessions were color coded as red for PAS25, blue for PAS10 and yellow for sham. (a) linear regression between MEP ratios and HbO/HbR ratios when considering all sessions. We found positive Pearson's correlations, $r=0.19$ and $r=0.18$ between MEP-HbO and MEP-HbR ratios, respectively, but none of them were statistically significant. (b) Linear regression for the PAS concordant sessions, in which MEP and HbO and HbR ratios were all larger than 1, or all smaller than 1. Both MEP-HbO and MEP-HbR cases demonstrated significant positive linear correlations ($r=0.82$ and $r=0.88$, $p<0.001$ in both cases). Besides, both fitted lines were not far from the point (1,1), e.g., HbO ratio = 0.96 and HbR ratio = 1.16, when fixing MEP ratio at 1, which is consistent with our prior knowledge. (c) Linear regression for the PAS non-concordant cases acting as a control in which none of the correlations were statistically significant. Two lines were also slightly more distant from the point (1,1), e.g., HbO ratio = 1.18 and HbR ratio = 1.43, when fixing MEP ratio at 1.

6.4 Discussion

Our study is the first one investigating the relationship between excitability and hemodynamic activity with simultaneous PAS-fNIRS in humans. We took advantage of this novel approach to

achieve two main results: 1) fluctuations of cortical excitability were positively correlated with fluctuations of hemodynamic responses to the task; 2) there was a significant linear relationship between effects of PAS on excitability and hemodynamic activity, when considering sessions with concordant PAS effects on MEP, HbO and HbR. Our results provide a unified view on two fundamental properties of cortical function and highlight that they represent two faces of the same coin. In addition, the demonstration of the effects of PAS on hemodynamic activity is relevant for the application of non-invasive brain stimulation techniques for the treatment of neuropsychiatric disorders. Finally, the tight link between excitability and hemodynamic activity may suggest that the effects on hemodynamics might be monitored via the standard spTMS technique.

6.4.1 Correlation between cortical excitability and hemodynamic activity

We demonstrated a link between excitability and task-related hemodynamic activity. Since PAS is known to induce variable effects across subjects, we pooled together all runs (before and after interventions) to investigate relationships between excitability and hemodynamic activity independently from specific PAS effects. Finger tapping is known to increase the metabolic demand and is therefore associated to increase HbO, decrease HbR and increase blood volume (Kashou *et al.*, 2016; Novi *et al.*, 2020). Moreover, finger tapping itself is known to increase cortical excitability (Koenke *et al.*, 2006). The correlation that we found underlines that metabolic demands linked to finger tapping depend on the excitability state when the task was performed. In other words, the metabolic demands seem state-dependent, where brain state corresponded here to cortical excitability. State dependency is a very well-known concept in cortical function and involves multiple measures of neuronal activity such as activity, oscillations and connectivity (Gonçalves *et al.*, 2006; Romei *et al.*, 2008; Silvanto and Pascual-Leone, 2008; Silvanto, Muggleton and Walsh, 2008; Giambattistelli *et al.*, 2014).

6.4.2 PAS effects on hemodynamic activity

In the field of non-invasive human brain stimulation, two previous studies investigated the effect of M1 cortical excitability modulation on task-related hemodynamic activity. Krivánková *et al* (2013) combined PAS and “offline” fMRI and reported no definite effects of PAS on either the task-related BOLD signal of the sensorimotor regions or resting-state functional connectivity. They reported that BOLD fluctuations following PAS were rather unpredictable, with almost no change after excitatory PAS, BOLD increase after inhibitory PAS and BOLD decrease after sham.

Comparing these results to ours is challenging, but the low sampling frequency of fMRI might have contributed to their negative results. A low sampling rate means limited temporal sampling which might dilute small effects of excitability changes that we identified mostly around the peak of the hemodynamic response. Although PAS effects on HbO and HbR were also not significant in our study, we did find expected trends in some individuals and at the group level (Fig.6.4, 5 and 6). Our results are certainly in agreement with those reported by [Chiang et al., \(2007\)](#), who combined rTMS and fNIRS. They found that 1Hz rTMS over M1 induced an expected HbO increase in the contralateral cortex lasting up to 40 minutes, likely related to reciprocal inhibition mechanisms ([Di Lazzaro et al., 2014](#)). Such cortical excitability effects on hemodynamic were also observed in other cortical regions. 5Hz rTMS on the right parietal cortex during the retention period of a match-to-sample task significantly increased HbO levels during the task period ([Yamanaka et al., 2010](#)); whereas continuous theta-burst stimulation (cTBS) applied on the left dorsolateral prefrontal cortex (DLPFC) reduced Emotional Stroop task-evoked HbO levels bilaterally ([Tupak et al., 2013](#)); cTBS on the right-DLPFC also reduced HbO during the dictator game ([Maier et al., 2018](#)).

Further development of our simultaneous fNIRS-TMS protocol may open new avenues for understanding the mechanism of PAS per se. For instance, the sparse rhythmic stimulation involved during PAS will allow investigating pulses-related hemodynamic effects and their build-up. Such analysis was out of our scope and will be considered in future investigations.

6.4.3 Correlation between PAS effects on excitability and PAS effects on hemodynamic activity

We also evaluated the correlation between excitability changes and hemodynamic activity changes modulated by interventions. Such analysis was challenging as the modelling involved dealing with the variabilities of MEP amplitudes, hemodynamic activity and PAS effects. Similar to other neuromodulatory techniques, PAS is known for inducing variable and sometimes unpredictable or even reversed effects ([Ziemann and Siebner, 2015](#); [Suppa et al., 2017](#)), depending upon multiple factors, including state of the brain, genetic susceptibility, position of the coil, and much more ([Ziemann and Siebner, 2015](#)). Using fMRI and PAS, [Krivánková et al., \(2013\)](#) did not report any significant relationship between PAS related excitability changes and finger-tapping related BOLD changes. We found similar results regarding the correlation between MEP ratios and HbO

(HbR, respectively) ratios when considering all sessions. However, this correlation reached significance when taking into consideration sessions with concordant PAS effects on MEP, HbO and HbR ratios. This proposed strategy simply regulates the influences of PAS variability on the correlation of ratios by claiming that the correlation should have existed in sessions where those three measurements varied in the same direction after PAS. The constrain itself does not guarantee high and significant correlations, as demonstrated when compared to a null hypothesis distribution obtained using simulations (see Appendix. C). This finding underlines the complexity of non-invasive brain stimulation effects, which are often only investigated in the domain of excitability, but always involve also hemodynamic activity, electromagnetic activity, connectivity, and much more (Pellegrino *et al.*, 2018, 2019). This finding also underlines the tight link between these cortical properties and may offer new opportunities for patients' treatment whenever the target action is a modulation of blood and hemoglobin supply.

6.4.4 Reliability and robustness

We did our best to acquire and analyze data in a robust way, including only male subjects, tuning PAS on individual N20, applying neuronavigation on individual MRI, collecting many MEPs (75 vs usual 20 trials). We considered personalized fNIRS data acquisition targeting the hand-knob using an optimal montage (Machado *et al.*, 2014b, 2018; Pellegrino, Machado, *et al.*, 2016) computed on the individual MRI. Physiological noise such as heartbeats, respiration and Mayer wave were minimized by filtering and regression using short-distance channels that only probe hemodynamics in the scalp (Zeff *et al.*, 2007). Optodes were positioned with neuronavigation and glued on head skin via collodion to ensure good contact and optimal probe design. We extracted HbO/HbR features after 3D reconstructions along the cortical surface. fNIRS 3D reconstructions have been shown to provide more accurate quantification (Arridge, 1999; Boas, Gaudette, *et al.*, 2001) of HbO/HbR than sensor level analyses applied in most fNIRS involved TMS studies (Oliviero *et al.*, 1999; Thomson *et al.*, 2011, 2013; Curtin, Ayaz, *et al.*, 2019; Curtin, Tong, *et al.*, 2019). More importantly, rigorous statistical procedures were conducted considering variabilities of data at different levels: 1) a bootstrap procedure to pool together data from all recordings instead of simply taking averages to investigate the relationship between excitability and hemodynamic activity; and 2) a resampling technique ensured to extract reliable, robust and data driven (intervention type blind) HbO/HbR measures from fNIRS reconstructions. Finally, most of fNIRS involved TMS studies only reported results on HbO. However, we showed consensus results when

considering both HbO and HbR signals, as recommended in a recent fNIRS guideline paper (Yücel *et al.*, 2021).

6.4.5 Limitations

The small number of subjects and unbalanced data set are the main limitations of this study. However, considering the main contribution of this study was investigating the correlation, the number of sessions involved in the correlation analysis (Fig.6.3 and Fig.6.7) was sufficient. Secondly, the finger-tapping task and the spTMS session were not conducted at the same time, but within a few minutes. To be noted, applying TMS during the task would have answered different biological questions than the ones assessed here. Nonetheless, the time gap between TMS and motor tasks may have introduced some noise when investigating the correlation between MEP and HbO/HbR because of the fluctuations of both measures over time.

6.5 Conclusion

In conclusion, we demonstrated a linear relationship between brain excitability and task-related hemodynamic activity measured using personalized fNIRS. We also demonstrated that PAS may have effects on hemodynamic activity in addition to those on excitability and also influences the relationship between excitability and activity. These effects are not necessarily PAS-specific and may characterize other non-invasive brain stimulation techniques as well. Finally, our findings may further expand the field of non-invasive brain stimulation application for treating brain disorders by targeting those areas for which a modulation of hemodynamic activity is desired.

6.6 Appendices

A. Experiment design and Data acquisition

Anatomical MRI

To guide TMS procedure and to calculate the head model for fNIRS acquisitions and analyses, MR brain images were acquired for each participant, using a General Electric Discovery MR750 3T scanner at the PERFORM Center of Concordia University, Montréal, Canada. T1-weighted images were acquired using the 3D BRAVO sequence and the following parameters: $1 \times 1 \times 1$ mm³, 192 axial slices, 256×256 matrix. T2-weighted anatomical images were acquired using the

3D Cube T2 sequence and the following parameters: $1 \times 1 \times 1 \text{ mm}^3$ voxels, 168 sagittal slices, 256×256 matrix.

fNIRS data acquisition

fNIRS data were acquired using a Brainsight fNIRS machine (Rogue-Research Inc, Montréal, Canada) sampling at 10Hz. A neuro-navigation system (Rogue-Research Inc, Montréal) with individual MRI images guided the installation of the optodes according to the previously estimated optimal montage (see Fig.6.2). Optodes were glued over the subject's scalp with collodion, taking care to remove the hair between skin and sensor, thus allowing reducing motion artifacts during prolonged recordings (Fig.6.2) (Yücel *et al.*, 2014; Pellegrino, Machado, *et al.*, 2016; Machado *et al.*, 2018).

Measurement of M1 cortical excitability

TMS was delivered with a Magstim 200² stimulator (Magstim Company, Carmarthenshire, Wales, UK) connected to a figure-8 coil (Magstim double 70mm remote control coil). Subjects were sitting in a comfortable armchair with the support of the left arm and neck (see Fig.6.2.d). To reduce potential motion, we placed the head of the participant between a mechanical arm wrapped with a soft cushion and the TMS coil (see Fig.6.2.d). TMS procedures were guided by the neuro-navigation system Brainsight (Rogue-Research Inc, Montréal, Canada). TMS coil was placed tangential to the scalp and with a 45° angle to the midline of the head (Thomson *et al.*, 2013). MEPs were recorded by a BrainAmp ExG bipolar system with 2 TECA disposable 20mm disk electromyography (EMG) electrodes attached on the right abductor pollicis brevis (APB), with a standard belly-tendon montage (Fig2.d). The TMS “hot spot” was found for each session as the location with the maximal Motor Evoked Potentials (MEP). Resting motor threshold (RMT) was defined efficiently using the TMS Motor Threshold Assessment Tool (MTAT 2.0, <http://www.clinicalresearcher.org/software.html>) based on maximum-likelihood parameter estimation by sequential testing approach (Awiszus *et al.*, 1999; Ah Sen *et al.*, 2017).

Somatosensory evoked potentials

Electrical stimulation (Digitimer DS7A, Letchworth Garden City, U.K) at the left wrist (e.g., Median Nerve) was performed after the MRI scan. Two bipolar EEG (BrainAmp ExG, Brain Products GmbH, Germany) electrodes located at CP3 and CP4 were used to measure subject

specific N20 latency. Stimulation was delivered slightly above the motor threshold at 4Hz for 2 minutes. N20 latency was visually estimated via the online segment averaging functionality of the BrainVision Recorder (BrainAmp ExG, Brain Products GmbH, Germany).

B. Reliable and robust estimation of task-related hemodynamic responses using fNIRS 3D reconstructions and resampling technique

To conduct a reliable and robust task-related hemodynamic response estimation to compare hemodynamics before and after interventions, we combined fNIRS 3D reconstruction and resampling techniques to appropriately handle variability between trials and influence of eventual motion artifacts. The workflow consisted of 3 steps: a) resampling of “all the possible” averaged optical density time courses; b) fNIRS 3D reconstruction along the cortex using the MEM and c) definition of a session specific spatial ROI for HbO/HbR features extraction.

- a) We conducted a resampling of “all the possible” averaged optical density time course (-10s to 30s) as the input for further fNIRS 3D reconstructions. First, for every 20 blocks of pre-processed optical density data, we sub-averaged all 16 out of 20 blocks, resulting in a total of $C_{20}^{16} = 4845$ possible combinations. These averaged trials were then sorted by the averaged signal-to-noise ratio (SNR) for two wavelengths. SNR was calculated by the largest amplitude among all channels from 0s to 30s, normalized by the mean of standard deviation over all channels during the baseline [-10s, 0s]. Finally, we selected 101 out of 4845 sub-averaged blocks centred around the median SNR of all sub-averages. The selection of 16 trials for sub-averaging was empirically defined according to the observation that usually there were around 4 artifacts contaminated blocks per condition (i.e., containing eventual motion artifacts). For artifacts contaminated data, large motion artifacts would then result in large SNR of sub-averaged trials. On the other hand, for data that are not contaminated by artifacts, the SNR distribution will be flat. Therefore, selecting sub-averaged trials around the median SNR should ensure a good representation of fNIRS responses, discarding artifact sub-averages. We finally chose 101 sub-averaged trials to ensure a good representation of the underlying distribution of SNR values, while being sensitive to the inherent variability of task-evoked fNIRS responses.
- b) fNIRS 3D reconstruction along the cortex was conducted using the MEM method applied to each of 101 sub-averaged trials specific for task run (e.g., pre-PAS25 of Sub01). We,

therefore, took into account the variability of the hemodynamic response, instead of considering only one averaged response. “All the possible” spatiotemporal maps of HbO and HbR along the cortical surface were reconstructed using MEM from these 101 resampled sub-averaged trials. MEM is an efficient nonlinear probabilistic Bayesian framework to incorporate prior knowledge in the solution of the inverse problem for 3D reconstruction (Amblard, Lapalme and Lina, 2004). We have demonstrated the excellent accuracy of MEM, especially its high sensitivity and specificity to the spatial extent of the underlying generators in the context of electro-/magneto-encephalogram source imaging (Chowdhury *et al.*, 2013, 2016; Grova *et al.*, 2016; Heers *et al.*, 2016; Hedrich *et al.*, 2017; Pellegrino *et al.*, 2020) as well as for fNIRS 3D reconstructions (Cai *et al.*, 2021).

- c) A session specific (e.g., PAS25 of Sub01) spatial ROI was finally defined along the cortical surface, to extract the reconstructed HbO/HbR time courses features from MEM reconstructed spatiotemporal maps. To do so, we first extracted the task run specific (e.g., pre-PAS25 of Sub01) HbO/HbR peak maps, at the peak timing estimated from the reconstructed time courses within the hand knob. This resulted in 101 HbO/HbR peak spatial maps for each task run. Then, a one-sample t-test of HbO (respectively HbR) amplitude for each vertex of the map was performed across 101 maps for each task run. Regions exhibiting a significant response ($p < 0.05$, false discovery rate corrected) were kept as the cortical area, which contained significant hemodynamic responses of one task run. For each session (e.g., PAS25 of Sub01), this analysis resulted in 4 regions exhibiting significant hemodynamic responses, i.e., HbO and HbR response t-maps, in pre- and post-intervention conditions. The final ROI was defined as the intersection between these 4 statistically significant regions to ensure reliability and robustness. Note that this final ROI was confirmed to be within the M1 cortical area for all participants. Two PAS10 sessions and 1 sham session were rejected due to the empty intersection regions (no overlapping between the 4 regions), suggesting a lack of reliability of the resulting hemodynamic responses. We defined this ROI for each intervention session rather than for each subject, considering the variability of task performance within each subject, since the intervention sessions of each subject were performed on different days.

c. PAS effects and relationship between cortical excitability and hemodynamic activity

PAS effects on cortical excitability and hemodynamic activity

As shown in Fig.6.C1, PAS exerted the expected group level effect with average MEP ratios (mean±SEM) of 1.23 ± 0.15 , 0.88 ± 0.08 and 1.08 ± 0.15 for PAS25, PAS10 and Sham, respectively. Such group level trends were also manifested in HbO and HbR ratios. For instance, the group level effect with average HbO ratios (mean±SEM) were 1.27 ± 0.21 , 0.95 ± 0.24 and 1.04 ± 0.17 for PAS25, PAS10 and Sham, respectively; and the group level effect with average HbR ratios (mean±SEM) were 1.48 ± 0.24 , 1.02 ± 0.20 and 1.23 ± 0.35 for PAS25, PAS10 and Sham, respectively. However, these effects did not reach statistical significance (one-sample t-test against 1, $p>0.05$). There were also no significant differences among 3 interventions (ANOVA test $p>0.05$).

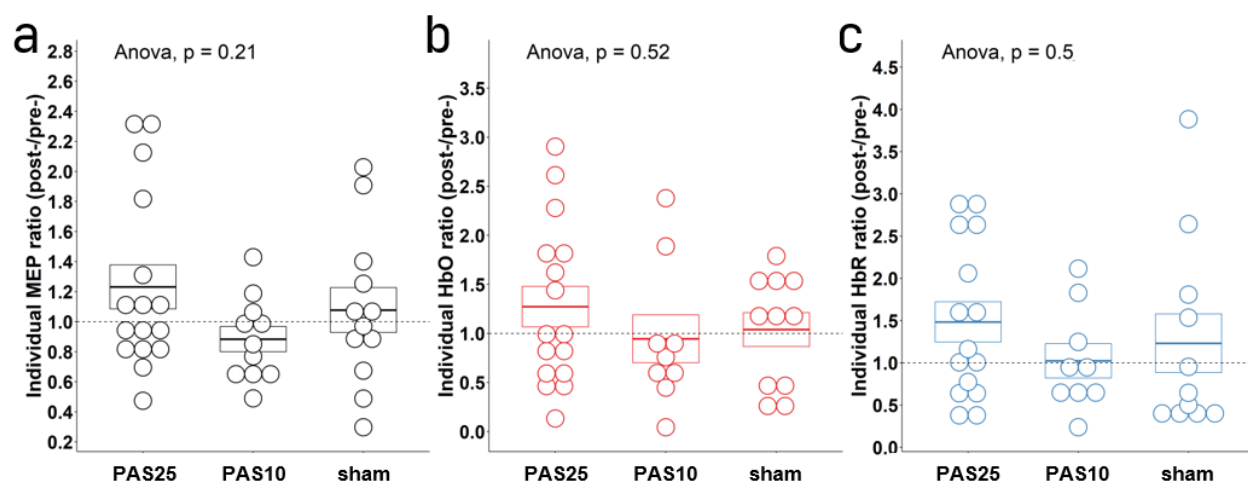


Fig.6.C1. PAS effects on cortical excitability and hemodynamic activity. At the group level, Mean±SEM (standard error of the mean) for the excitatory, inhibitory and sham session were: (a) 1.23 ± 0.15 , 0.88 ± 0.08 and 1.08 ± 0.15 for MEP ratios; (b) 1.27 ± 0.21 , 0.95 ± 0.24 and 1.04 ± 0.17 for HbO ratios; and (c) 1.48 ± 0.24 , 1.02 ± 0.20 and 1.23 ± 0.35 for HbR ratios. Even if trends were observed, none of these ratios were significantly different from 1 based on a one-sample t-test. The individual ratios represented by each dot demonstrated a relatively large variance of the ratios for each scenario. Boxes showed the Mean±SEM in each case. Note that one MEP session (e.g., Sub16, PAS10) was rejected from the whole analysis due to a high ratio of 2.81; and one HbR session (e.g., Sub12, PAS25, HbR) was rejected from the whole analysis due to a high ratio of 5.45. A similar process was also considered in [Krivánková et al \(2013\)](#).

Simulation of null hypothesis distributions of the correlation between concordant MEP and HbO/HbR PAS effects

To further justify our approach of considering concordant effects only for linear regression analyses presented in Fig.6.7, we simulated several null hypothesis distributions of the correlation between concordant MEP and HbO/HbR ratios. To do so, different numbers (e.g., 1,000, 500, 50 and 40) of points, mimicking a pair of MEP ratio and HbO/HbR ratio, were randomly drawn on the MEP – HbO/HbR ratio plane following a 2D Gaussian distribution with 0 correlation (Null distribution). The marginal distributions (i.e., 1D Gaussian for either MEP or HbO/HbR ratio) were defined using the same mean and standard deviation of the respective ratios estimated on our real data. Then, we performed the same linear fit as the one proposed for real data, between these simulated MEP and HbO/HbR ratios. Note that this analysis was also only conducted between concordant MEP and HbO/HbR ratios (1st and 3rd quadrants), considered to assess the linear regression. This process was repeated 1,000 times to obtain 1,000 Pearson's correlation values, to estimate empirically a null hypothesis distribution of the linear correlations when considering only the 1st and 3rd quadrants of the MEP – HbO/HbR ratios plane. Finally, we compared the actual correlation values obtained from real data and this null hypothesis distribution, to evaluate the reliability of our real data fitting results (see Fig.6.C2). Simulations involving 50 and 40 points were similar to the dimensionality of our real data, whereas 1,000 and 500 points represented more ideal scenarios. Since these points were drawn randomly from a 0 correlation 2D Gaussian, the distribution of the correlation values can be inferred as a null hypothesis of the correlation between concordant MEP and HbO/HbR ratios. Therefore, the likelihood of obtaining our resulted correlation by chance between concordant MEP and HbO/HbR ratios can be quantified.

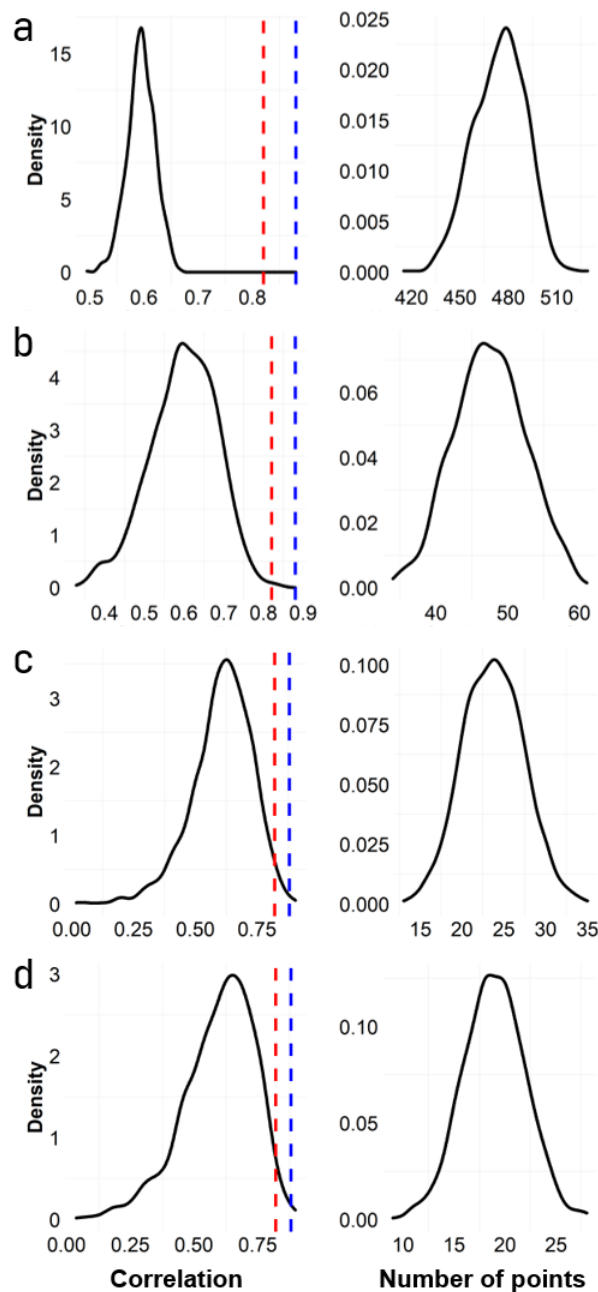


Fig.6.C2. Simulated Pearson correlation distribution of the concordant MEP and HbO and HbR ratios. In the first columns, simulated Pearson correlation distributions of the concordant MEP and HbO ratios were shown along with the actual Pearson's correlation values from Fig.6.7b. The red vertical dash line represented the Pearson's correlation (e.g., 0.82) of the actual MEP-HbO fit, and the blue vertical dash line represented the case of the actual MEP-HbR fit (e.g., 0.88). On the right side of each correlation density plot, we showed the distribution of the number of points within 1st and 3rd quadrants. There were originally (a)1000, (b)100, (c)50 and (d)40 randomly drawn points in the whole MEP-HbO/HbR plane, and such

processes were repeated 1000 times. When sampling the null distributions with 100 and 1000 points, the chance to have a significant Pearson correlation equal to or larger than 0.82 was 0%. When consider similar dimensionality as in our data set (simulating 50 or 40 points), the chance to have a significant Pearson correlation equal to or larger than 0.82 was 0.8% (for 50 points) and 1.1% (for 40 points), respectively. This indicated that the linear fits shown in Fig.7b were not acquired by chance. Note that to make the fair comparison, 0.8% and 1.1% were calculated when conditioning the simulated fits to 1) provide a significant ($p < .05$) Pearson correlation, as well as 2) the interaction of the fitted lines on the vertical line (MEP ratio = 1) has to be within a range of [0.9, 1.1].

Chapter 7

Manuscript 4: Hierarchical Bayesian Modeling of Task Related Hemodynamic Correlates of Neuronal Excitability Changes: a simultaneous fNIRS/TMS study

Context

In Chapter 6, we reported two types of correlations between M1 excitability and task-related hemodynamic response. First, we found a significant positive correlation between fluctuations of cortical excitability and the fluctuations of HbO activity, whatever was the PAS intervention considered. The second correlation was tested by estimating the correlation between MEP and HbO/HbR ratios calculated as the post- over pre-intervention amplitudes. We found that when PAS increased cortical excitability, it resulted in enhanced task-related hemodynamic response, whereas when PAS decreased cortical excitability, it resulted in reductions of the hemodynamic response to the task. This correlation was only significant when constraining the data to concordant PAS effects (e.g., MEP and HbO and HbR ratios were either both larger or smaller than 1). This constraint can be considered as a simple way to regularize intrinsic variability of the data, such as PAS effects on both cortical excitability and task-related hemodynamic responses. To further improve this evaluation of PAS effects on cortical excitability and hemodynamic response, it is necessary to carefully consider the variability of the data at the different levels in the analysis. Therefore, in this chapter, we are proposing hierarchical Bayesian modeling to further analyze the data set presented in Chapter 6. The rationale to apply hierarchical models was considering the fact that the so-called “involvement of variability in the analysis” was all about modeling the heterogeneity of the variables of interest (e.g., MEP, HbO/HbR) at each stage of the analysis. The hierarchical Bayesian model is indeed a good candidate to encode inter-/intra-subject heterogeneity within the data. On the other hand, the difficulty of solving a hierarchical model is often underestimated, especially when dealing with the identifiability of the models (Papaspiliopoulos, Roberts and Sköld, 2007). This means that without a proper model solver, the estimation of the parameters of the model could be biased and therefore leading to biased inferences. Fortunately, Bayesian data analysis is a good candidate to solve these issues by

sampling the distribution of each parameter before making any summary statistics and inferences. More importantly, the unique diagnostic statistics available when evaluating the sampling process, ensure robust and reliable inferences. We found significant correlations between PAS effects on MEP and PAS effects on HbO/HbR, such correlation is mainly exhibited around the peak of the hemodynamic responses.

This manuscript is being finalized for submission, Zhengchen Cai, Giovanni Pellegrino, Jean-Marc Lina, Habib Benali, Christophe Grova. Hierarchical Bayesian Modeling of Task Related Hemodynamic Correlates of Neuronal Excitability Changes: a simultaneous fNIRS/TMS study.

Abstract

Background: Investigating the relationship between task-related cortical hemodynamic activity and brain excitability is challenging for the following reasons: 1) it requires simultaneous measurement of brain hemodynamic activity, while applying non-invasive brain stimulation; 2) both brain stimulation and task-related hemodynamic responses are associated with considerable inter-/intra-subject variability.

Methods: We performed a study on 16 healthy subjects with simultaneous Paired Associative Stimulation (PAS) and functional Near-Infrared Spectroscopy (fNIRS) on the right primary motor cortex (M1). PAS was applied to conduct excitability modulation along with sham control. Before and after each intervention, cortical excitability was measured by motor evoked potentials (MEPs), and the motor task-related hemodynamic response was measured using fNIRS. We proposed hierarchical Bayesian modeling to improve statistical inference by taking into account variability in the data at the individual and group levels. We constructed three models to encode 1) PAS effects on the M1 excitability; 2) PAS effects on the whole-time course of fNIRS hemodynamic responses to finger tapping tasks, and 3) the correlation between PAS effects on M1 excitability and PAS effects on task-related hemodynamic responses. Dynamic Hamiltonian Monte Carlo (HMC) was considered to sample the posterior distributions of parameters involved in these models. Posterior predictive simulations were performed to conduct Bayesian inferences of PAS effects.

Results: Significant increase of the cortical excitability was found after PAS25, whereas a small reduction of the cortical excitability was shown after PAS10 and no changes after sham. PAS

elicited modulation of M1 excitability effects could be more pronounced when increasing the spTMS intensity. We found PAS effects on finger tapping evoked HbO/HbR within M1, around the peak of the hemodynamic time courses. Both HbO and HbR absolute amplitudes increased after PAS25 and decreased after PAS10. Cortical excitability changes and task-related HbO/HbR changes showed a high probability of being positively correlated, 77.2% and 79.2%, respectively. The corresponding Pearson's correlations were 0.58 ($p < .0001$, HbO with MEP) and 0.56 ($p < .001$, HbR with MEP), respectively.

Conclusion: Our results showed that PAS modulates task-related cortical hemodynamic responses in addition to M1 excitability. The fact that PAS effects on hemodynamic response were exhibited mainly around the peak of the hemodynamic time course may indicate the intervention only increases metabolic demanding rather than modulating hemodynamic response function per se. Moreover, the positive correlation between PAS modulations of excitability and hemodynamic brings insights to understand the fundamental properties of cortical function and cortical excitability.

7.1 Introduction

Investigation of the association between hemodynamic response and excitability of the corresponding cortical region helps to understand the relationship between cortical metabolic demand and cortical readiness. Therefore, expanding the field of application of non-invasive brain stimulation for treating brain disorders in which targeting areas may require modulation of hemodynamic activity. In this context, when considering invasive animal studies using optical imaging, *Allen et al., (2007)* reported immediate increases of tissue oxygenation followed by a prolonged reduction of oxygenation during around 2 minutes after inhibiting the anesthetized cat's visual cortex using low-frequency repetitive Transcranial Magnetic Stimulation (rTMS). A recent study on healthy rats combining functional Magnetic Resonance Imaging (fMRI) and proton Magnetic Resonance Spectroscopy (MRS) showed increases in resting-state connectivity, GABA, glutamine and glutamate levels following high frequency rTMS and reduced connectivity and glutamine levels after low frequency rTMS stimulations (*Seewoo et al., 2019*).

When considering the human brain, similar investigations have been considered using neuroimaging and non-invasive brain stimulation approaches. fMRI (*Bandettini et al., 1992*;

Kwong *et al.*, 1992; Glover, 2011) can be considered to measure the cortical hemodynamic processes during or after TMS interventions, but simultaneous fMRI/TMS acquisitions are challenging and require specific coil and fMRI sequence developments (Navarro De Lara *et al.*, 2015; Wang, Xu and Butman, 2017). Therefore most studies consisted in fMRI sessions before and after TMS interventions (Siebner *et al.*, 2009). Alternatively, as a wearable/bedside neuroimaging approach, functional Near-Infrared Spectroscopy (fNIRS) non-invasively measures fluctuations of both oxygenated- and deoxygenated-hemoglobin (i.e., HbO and HbR) concentration changes in the human head with a high temporal resolution (Jöbsis, 1977; Scholkmann, Kleiser, *et al.*, 2014). fNIRS relies on optical absorption signals which are independent of electromagnetic signals, as opposed to fMRI, therefore, fNIRS appears as an interesting alternative offering better compatibility for simultaneous acquisition during TMS (Curtin, Tong, *et al.*, 2019).

Regarding the modulation of cortical excitability, TMS pulses repeated in a train following a certain frequency – the repetitive TMS (rTMS) (Ridding and Rothwell, 2007; Di Pino *et al.*, 2014) – were applied to induce the cortical plasticity. A simultaneous rTMS and fMRI study demonstrated increases in functional connectivity with the anterior cingulate cortex 15 minutes after applying high frequency rTMS stimulation over the left dorsolateral prefrontal cortex (Navarro De Lara *et al.*, 2015; Tik *et al.*, 2017). Studies using low frequency rTMS and fNIRS reported an increase in HbO over 20s to 40s after rTMS train followed by a prolonged reduction in HbO (Thomson *et al.*, 2012, 2013). When conducting a match-to-sample task, significant increases in HbO over the frontal lobe were observed, when increasing right parietal excitability using 5Hz rTMS (Yamanaka *et al.*, 2010). Chiang *et al.*, (2007) applied 1Hz rTMS over M1 and reported HbO increases in the contralateral cortex lasting up to 40 minutes according to reciprocal inhibition mechanisms (Di Lazzaro *et al.*, 2014).

Another neurostimulation approach entitled Paired Associative Stimulation (PAS) has also been proposed by Mariorenzi *et al.*, 1991; Stefan, 2000. PAS is inspired by the concept of Spike Timing Dependent Plasticity (Levy and Steward, 1983; Rossini *et al.*, 2015b). It consists of pairs of cortical TMS and peripheral electrical Median Nerve Stimulation (MNS) delivered with proper timing – around 25ms or 10ms interstimulus intervals (ISI) to excite (PAS25) or to inhibit (PAS10) motor cortical areas, respectively. In this study, we decided to choose PAS rather than rTMS to change cortical excitability. Indeed, using simultaneous TMS/fNIRS, Näsi *et al.* (2011) reported that

physiological fluctuations measured using photoplethysmography (PPG) amplitude and heart rate measured using electrocardiogram were largely influenced by trains of TMS pulses (0.5 to 2Hz). Therefore, these systemic physiological fluctuations evoked by TMS trains may influence hemodynamic fluctuations in both scalp and brain signals, resulting in additional confounds when investigating the hemodynamic correlates of TMS. Even if fNIRS short distance channel regression approach can be applied to remove scalp components of systemic physiological fluctuations (Zeff *et al.*, 2007; Gregg *et al.*, 2010), TMS trains may still introduce additional confounding signals in the brain. This brings the advantage of applying PAS rather than rTMS when investigating neurostimulation and hemodynamic, since the frequency of stimulation pairs in PAS is often suggested to be 0.1Hz or less (Suppa *et al.*, 2017), therefore PAS intervention is likely introducing significantly less or even no systemic physiological fluctuations when compared to rTMS.

The relationship between the primary motor cortex (M1) excitability and Blood-Oxygen-Level-Dependent (BOLD) signal was investigated using PAS stimulation and “offline” fMRI acquisition in Krivánková *et al.*, (2013). They reported no significant effect of PAS interventions neither on task-related (motor and sensory) BOLD response nor on resting-state functional connectivity. In Chapter 6, we conducted the first simultaneous PAS-fNIRS study to investigate the relationship between motor task-evoked cortical hemodynamic response and M1 excitability. We found a significant and positive correlation between fluctuations of cortical excitability and fluctuations of HbO responses to the task. When comparing PAS modulated excitability changes and PAS modulated hemodynamic changes, we demonstrated significant correlations between motor evoked potential (MEP) post-/pre-intervention ratios and HbO/HbR amplitude post-/pre-intervention ratios, only when restricting our analyses to concordant sessions, in which all three post-/pre-intervention ratios, MEP, HbO and HbR, were simultaneously larger or smaller than 1.

However, inconsistency between results on hemodynamic correlates of excitability reported either in rTMS or PAS literature can mainly be explained by the variability of brain stimulation efficiency. Although the ability of PAS in eliciting significant changes in cortical excitability has been replicated by several studies (Stefan, 2000; Wolters *et al.*, 2005b; Tsang, Bailey and Nelson, 2015; Lee *et al.*, 2017; Suppa *et al.*, 2017), PAS efficiency has also been investigated in López-Alonso *et al.*, 2014, in which only 39% of 56 subjects showed expected MEP amplitude increase

after conducting PAS25. A lower than 50% efficiency of PAS was also suggested in a review study (Suppa *et al.*, 2017). Similarly, inter-subject variability of the task-evoked hemodynamic response has also been reported, whether measured using fMRI (Witt, Laird and Meyerand, 2008) or fNIRS (Novi *et al.*, 2020). Therefore, it seems essential to carefully take into account intrinsic variability of both cortical excitabilities elicited by non-invasive brain stimulation and hemodynamic responses to tasks, when investigating the correlation between both effects.

To conduct accurate and robust investigations of PAS elicited cortical excitability (measured using MEP) and hemodynamic responses to finger tapping task (measured using HbO/HbR), we propose to consider the variability of data within a hierarchical Bayesian model to infer PAS effects on both cortical excitability and hemodynamic response, as well as their correlation. Hierarchical Bayesian modeling allows taking into account heterogeneity of the variables of interest (MEP, HbO/HbR) at every stage (inter-/intra-subject, intervention type) of the analysis (Papaspiliopoulos, Roberts and Sköld, 2007; Betancourt and Girolami, 2015). Moreover, when considering a hierarchical structure, partial pooling can decrease the uncertainty of estimated parameters (Gelman *et al.*, 2013b; McElreath, 2020). This means the group-level and individual-level estimations could inform each other to regularize the uncertainty of each parameter. In this context, Bayesian data analysis allows estimating the statistical expectation of each parameter of the model by sampling the joint posterior distributions. Thanks to the developments in Bayesian data analysis workflow during the last decade, Bayesian inferences have become more accessible and can provide accurate and reliable estimations of the posterior distribution. For instance, the most recent implementations of the Hamiltonian Monte Carlo (HMC) algorithm (Duane *et al.*, 1987) called the dynamic HMC (Betancourt, 2017, 2019) is available as an open source Bayesian statistical modeling and computation platform called Stan (Stan Development Team, 2020b). This technique not only accurately and efficiently samples the joint posterior distribution, but also provides robust estimations by quantitatively diagnosing pathological behaviours of Markov Chain Monte Carlo (MCMC) chains that are used to sample the joint posterior distributions (Betancourt and Girolami, 2015; Betancourt, 2017).

In this study, we propose to revisit our analysis of a TMS/fNIRS dataset first reported in Chapter 6, using a Bayesian data analysis workflow (Gabry *et al.*, 2019; Gelman *et al.*, 2020) to investigate whether cortical excitability and hemodynamics are directly linked to each other. We hypothesize

that enhanced brain excitability should be associated with higher hemodynamic activity elicited by a finger tapping task, and decreased excitability should be associated with a reduced hemodynamic response to the task. We first summarized the study design and data acquisition. Data preprocessing was then conducted to prepare the inputs of our proposed Bayesian framework. We evaluated the relevance of three hierarchical models to investigate: 1) PAS effects on M1 excitability measured using MEP; 2) PAS effects on the whole-time course of task-related hemodynamic responses measured using fNIRS, and 3) the correlation between PAS modulated excitability changes and PAS modulated hemodynamic changes. The variability of each measurement was carefully considered in each model and at each level (i.e., at the individual and group levels) to conduct reliable estimations of the intervention effects and correlations. Statistical inferences were made via posterior predictive simulations (McElreath, 2020). Diagnostic of the models were conducted to ensure the robustness of the estimated posterior distributions.

7.2 Material and methods

7.2.1 Study design and subjects

Nineteen subjects (24 ± 5 (mean \pm sd) years old, male and right-handed) with no history of neurological disorders were selected to participate in the study. We only included male participants in order to minimize the confounding of cortical excitability changes due to the menstrual cycle (Hattemer *et al.*, 2007; Lee *et al.*, 2017). This study was approved by the Central Committee of Research Ethics of the Minister of Health and Social Services Research Ethics Board (CCER), Québec, Canada. All subjects signed written informed consent prior to the data acquisition. They also went through a screening procedure to confirm no contraindications to MRI or TMS (Rossi *et al.*, 2009; Suppa *et al.*, 2017), and no medication related to the central nervous system was taken. Subjects were instructed to have a regular sleep cycle for the days and not to take caffeine for at least 90 minutes before the data acquisition.

The experiment paradigm of this study is illustrated in Fig.7.1a. To modulate M1 cortical excitability and inducing brain plasticity, three different intervention sessions were performed at least two days apart to minimize carryover effects. Each session consisted of five time-ordered sections, defined as follows:

- 1) *A block designed finger-tapping task composed of 20 blocks, 10s of finger-tapping followed by 30s ~ 60s of resting was conducted within each block.* Subjects were informed to tap their

left thumb to the other 4 digits sequentially around 2Hz (Fig.7.1a). This long-range jitter was designed to prevent the task responses from phase locking to the undergoing physiological hemodynamic oscillations (Aarabi, Osharina and Wallois, 2017), therefore, reducing the physiological confounding on the task-related response at the stage of experiment paradigm design. Tapping onsets/offsets were instructed by auditory cues.

- 2) ***An event-related designed single pulse TMS (spTMS) composed of 75 events, jittered from 5s to 25s (Fig.7.1a).*** Guided along with subject specific anatomical MRI using a Brainsight neuro-navigation system (Rogue-Research Inc, Canada), we placed a figure-8 coil (Magstim double 70mm remote control coil) targeting M1, tangential to the scalp and with a 45° angle to the midline of the head (Fig.7.1c) to maximize stimulation efficiency (Thomson *et al.*, 2013). The individual ‘hot spot’ was defined for each session as the location which maximally twitched the left thumb, therefore, resulting in the largest Motor Evoked Potentials (MEPs) amplitude measured on the left thumb using electromyography (EMG). A Magstim 200² stimulator (Magstim Company, U.K.) was used to generate accurate stimulation intensity, defined as 120% of the subject-specific resting motor threshold (RMT). This RMT was determined based on the maximum-likelihood parameter estimation by sequential testing approach (Awiszus *et al.*, 1999; Ah Sen *et al.*, 2017), implemented as a toolbox called TMS Motor Threshold Assessment Tool (MTAT 2.0, <http://www.clinicalresearcher.org/software.html>), as an approach to find efficiently the right intensity more efficiently than traditional methods. All TMS procedures followed the recommendations of the International Federation of Clinical Neurophysiology (Rossi *et al.*, 2009) and no participants reported any considerable discomfort or side effects.
- 3) ***A PAS intervention session attempted to modulate the M1 cortical excitability temporally (Fig.7.1a).*** The PAS intervention consisted either in PAS25, PAS10 or sham-PAS. PAS was conducted with 100 pairs of electrical median nerve stimulation (MNS) on the left wrist, followed by TMS pulse delivered over the right M1, with a fixed interval of 10s between paired stimulations, for a total intervention of 18 minutes, as suggested in Suppa *et al.*, (2017). MNS was delivered with a Digitimer (Digitimer DS7A, U.K.) at the left median nerve and with the intensity equals 300% of the subject-specific perceptual threshold. TMS intensity was the same as the spTMS - 120% of RMT. After estimating subject-specific N20 response to electrical MNS using bipolar electroencephalogram (EEG) (BrainAmp ExG, Brain Products

GmbH, Germany) on CP3 and CP4 electrodes, the interstimulus intervals (ISI) between MNS and TMS were determined to be pre-measured individual N20+5ms for PAS25 and N20-5ms for PAS10 (Carson and Kennedy, 2013). Sham parameters (e.g., MNS intensity, coil position, ISI) were the same as PAS25, but TMS was not delivered, and instead, its sound ('TMS click') was played via a stereo speaker.

- 4) *Repetition of the event-related designed spTMS (Fig.7.1a) after the intervention.* By comparing the MEPs measured during pre-intervention and post-intervention sessions, PAS intervention effects on M1 cortical excitability can be assessed.
- 5) *Repetition of the block designed finger tapping task (Fig.7.1a) after the intervention.* Similarly, the corresponding effects on task-evoked hemodynamic responses can be estimated by comparing HbO/HbR concentration changes measured during pre-intervention and post-intervention sessions.

7.2.2 Data acquisitions

Anatomical MRI

Individual anatomical MRI was acquired to guide TMS and to calculate the head model required for fNIRS acquisition planning and fNIRS reconstructions. A General Electric Discovery MR750 3T scanner at the PERFORM Center of Concordia University, Montréal, Canada, was used to scan: 1) T1-weighted images using the 3D BRAVO sequence ($1 \times 1 \times 1 \text{ mm}^3$, 192 axial slices, 256×256 matrix) and 2) T2-weighted images using the 3D Cube T2 sequence ($1 \times 1 \times 1 \text{ mm}^3$ voxels, 168 sagittal slices, 256×256 matrix).

Motor Evoked Potentials

MEPs induced by spTMS pulses were measured to assess the M1 cortical excitability. A BrainAmp ExG bipolar system (BrainAmp ExG, Brain Products GmbH, Germany) was used to record EMG of the right abductor pollicis brevis (APB) muscle, with 2 TECA disposable 20mm disk electromyography (EMG) electrodes attached with a standard belly-tendon montage (Fig1.c).

functional Near-Infrared Spectroscopy

fNIRS data were acquired to estimate the finger-tapping evoked hemodynamic responses (i.e., HbO/HbR). fNIRS data were acquired at 10Hz using a Brainsight fNIRS system (Rogue-Research

Inc, Canada), which consists of two wavelengths – 685nm and 830nm. fNIRS optodes were attached to the subject’s scalp using a clinical adhesive called collodion (Fig.7.1.c) to reduce motion artifacts (Yücel *et al.*, 2014; Pellegrino, Machado, *et al.*, 2016; Machado *et al.*, 2018) and to ensure better contact to the skin, when compared to standard fNIRS caps. A personalized optimal montage developed by our group (Machado *et al.*, 2014b, 2018; Pellegrino, Machado, *et al.*, 2016) was used to maximize the sensitivity of fNIRS channels to a predefined region of interest (ROI) - the individual ‘hand knob’ region (see Fig.7.1b) manually defined along the right M1 cortical surface which controls the left hand movement (Raffin *et al.*, 2015b). The resulted personalized optimal montage consisted of 3 sources and 15 detectors (see Fig.7.1b). The distance between each source-detector pair was constrained to range from 2.0 cm to 4.5 cm. Each source was positioned to construct at least 13 channels among the 15 detectors ensuring a high spatial overlap between channels, to allow accurate local reconstruction along the cortical surface. A proximity detector was added at the center of 3 sources to record the physiological hemodynamics fluctuations within the scalp. Brainsight neuro-navigation system coregistered with subject specific T1 MRI was used to guide the installation and to digitize the position of fNIRS sources and detectors glued at their optimal positions. Additional 150 points were digitized on the head surface to allow accurate montage registration with the anatomical MRI, as a prerequisite for computing the fNIRS forward model. fNIRS data were acquired continuously during the whole experimental session, as described in Fig.7.1a.

From the nineteen subjects selected for this study, one was excluded due to low sensitivity to TMS and two were excluded because they exhibited poor fNIRS signal qualities. Four subjects dropped out after the first session due to personal reasons, resulting in 16 PAS25, 12 PAS10 and 12 sham sessions. Please note that starting from here, we will denote 1) “**Session**” as one specific acquisition, consisted in any PAS intervention type, of one subject including experiments 1 to 5 as illustrated in Fig.7.1a (e.g., PAS25 for Sub01); “**Run**” as one specific experiment (spTMS or finger tapping), before or after any PAS intervention type, of one subject (e.g., pre-PAS25 spTMS for Sub01); and “**Time**” to differentiate whether one specific experiment was conducted before or after the intervention (e.g., pre-PAS25 vs. post-PAS25).

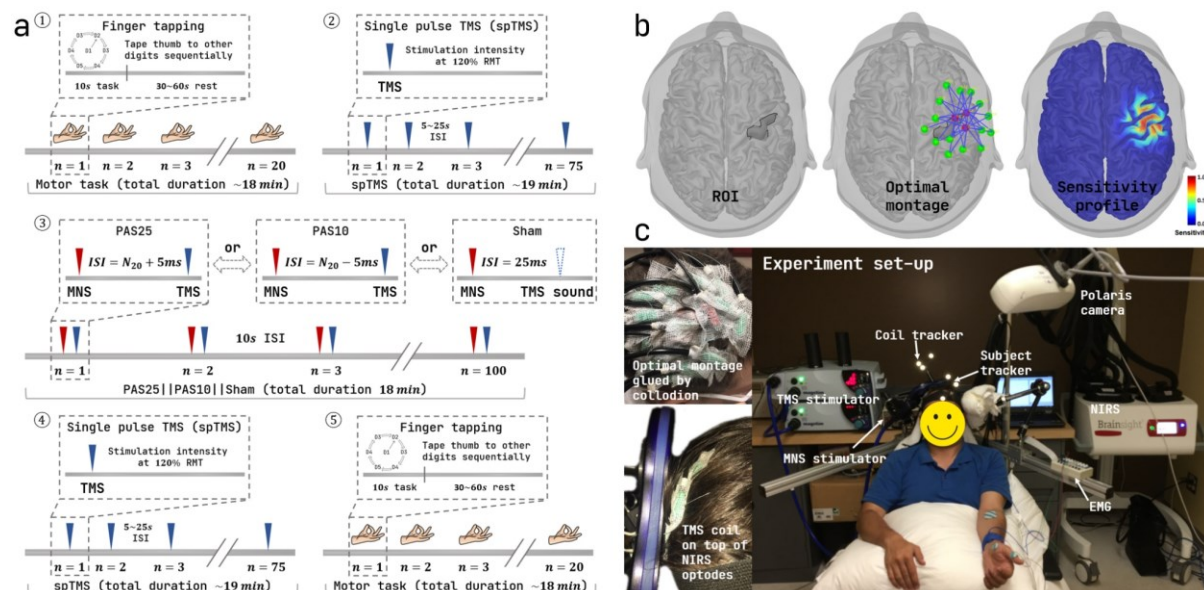


Fig.7.1 Experimental paradigm and set-up (adapted from Chapter 6). a) experiment paradigm ordered by time: 1) is a block designed finger-tapping task consisted of 20 blocks, each contained 10s task and 30s to 60s rest; subjects were informed to tapping their left thumb to the other 4 digits sequentially at around 2Hz; 2) is an event-related designed single pulse TMS (spTMS) Run consisted of 75 events jittered from 5s to 25s. 3) PAS25/PAS10/sham-PAS consisted of 100 pairs of stimulations, interleaved by 10s; 4) and 5) repeated 2) and 1), respectively, after the PAS intervention. b) personalized optimal montage for fNIRS acquisition. 3 sources (red dots) and 15 detectors (green dots) were selected to optimize the sensitivity of fNIRS montage to a predefined ROI, the right M1 hand knob (outlined using a black profile) along the cortical surface. c) an overview of the experimental set-up, the personalized optimal montage was glued on the scalp using clinical adhesive – collodion; TMS coil was placed on top of the fNIRS optodes to target the ‘hot spot’ which corresponded to subject’s left thumb, note that the low-profile feature of the fNIRS optodes allowed less TMS intensity decreases when departing from the scalp surface; a neuro-navigation system was used to guild the placement of the TMS coil and the digitization of the fNIRS optodes.

7.2.3 Data preprocessing

EMG data processing

EMG data collected during spTMS Runs were processed using Brainstorm software (Tadel *et al.*, 2011) (<https://neuroimage.usc.edu/brainstorm/>) to extract MEP amplitudes. Raw EMG data were first band-pass filtered between 3 and 2000Hz. A time window from -10ms to 100ms around the stimulation onset was defined to extract MEP trials. These trials were then baseline corrected (-10ms to 0ms), and the peak-to-peak amplitude of each MEP trial was calculated. Note that

throughout the analysis reported in this study, none of the single MEP trials was excluded to preserve the intrinsic variability of MEP peak-to-peak amplitude measures. *From here, for convenience, we will denote as “MEP”, the actual MEP peak-to-peak amplitude, as often considered in TMS literature.*

At the end, the output of the whole EMG data preprocessing section was a set of 75 MEPs estimated for each participant (specified by subject ID from 1 to 16), each intervention (PAS25, PAS10 or sham) and Time (pre-PAS or post-PAS).

fNIRS data preprocessing

fNIRS data processing was performed using our fNIRS processing plugin - NIRSTORM (<https://github.com/Nirstorm/nirstorm>) implemented in Brainstorm software (Tadel *et al.*, 2011) (<https://neuroimage.usc.edu/brainstorm/>). fNIRS data analysis consisted of the following three parts (further details are provided in Chapter 5)

- 1) Raw fNIRS data were first preprocessed following standard recommendations (Yücel *et al.*, 2020): a) bad channel rejections of channels exhibiting either a negative raw amplitude during the whole time course and a coefficient of variation (CV) larger than 8% (Schmitz *et al.*, 2005; Schneider *et al.*, 2011; Eggebrecht *et al.*, 2012; Piper *et al.*, 2014); b) linear regression of superficial physiological fluctuations using the average of all proximity channels (Zeff *et al.*, 2007); c) band-pass filtering (i.e., 0.01Hz to 0.1Hz) using a 3rd order Butterworth filter (zero-phase); d) conversion in optical density changes (i.e., ΔOD) using logarithm conversion; e) ΔOD epochs extraction within a time window ranging from -10s to 30s around task onsets. Instead of the conventional process averaging extracted ΔOD epochs, we then conducted a resampling process to estimate not one but a set of ‘possible’ averaged ΔOD s (see also Chapter 6). Our rationale was to propose an evaluation preserving the intrinsic variance of averaged ΔOD related to the underlying physiological fluctuations and eventual measurement errors such as motion artifacts. To do so, we first averaged 16 out of 20 preprocessed ΔOD epochs for all possible unique combinations (i.e., $C_{20}^{16} = 4845$ possibilities). Then, the averaged signal to noise ratio (SNR) of the resulting averaged ΔOD s, for each wavelength, was estimated as the peak amplitude over the averaged standard deviation of baseline (within -10s to 0s) among all channels. Lastly, we selected 101 of these resampled averaged ΔOD s, distributed around the median SNR (50 averaged below and 50 averaged above the median

SNR), to obtain a distribution of ‘possible’ responses evoked by one finger-tapping Run. The selection of 16 blocks out of 20 trials and 101 resampled averaged Δ ODs maintained a good coverage of the data distribution. This number was empirically defined according to the observation that usually there were less than four blocks contaminated with artifacts in one finger-tapping Run. Selecting sub-averaged trials around the median SNR ensured a good representation of fNIRS responses, while discarding artifacts in the meantime. Indeed, in artifacts contaminated data, large motion artifacts would result in high SNR of corresponding sub-averaged trials.

- 2) We applied our 3D fNIRS reconstruction workflow using personalized optimal montage and maximum entropy on the mean (MEM), as further described and validated in Chapter 5, to the 101 sub-averaged Δ ODs. Therefore, ‘all possible’ HbO/HbR responses for each finger-tapping Run were reconstructed as spatiotemporal maps along the cortical surface. To do so, the subject-specific fNIRS forward model was first estimated as the following steps: a) 5 tissues head segmentation (e.g., scalp, skull, Cerebrospinal fluid, grey matter and white matter) calculated using FreeSurfer6.0 (Fischl *et al.*, 2002) (<https://surfer.nmr.mgh.harvard.edu>) and SPM12 (Penny *et al.*, 2011) (<https://www.fil.ion.ucl.ac.uk/spm/software/spm12/>); b) light fluences at each optode location, and for each wavelength (i.e., 685nm and 830nm), were calculated by simulating 10^8 photons, using MCXLAB toolbox - a Monte Carlo photon simulator for modeling light transport in 3D turbid media, developed by Fang and Boas, 2009 and Yu *et al.*, 2018; c) sensitivity of each voxel was computed using the adjoint formulation and was normalized by Rytov approximation (Arridge, 1999); d) surface space sensitivity was finally obtained by projecting volumetric sensitivity map to subject’s cortical surface (i.e., mid-surface, a middle layer of the gray matter, between pia mater and gray-white matter interface, 25,000 vertices) using the Voronoi based method proposed by Grova *et al.*, 2006. Finally, each of 101 averaged Δ OD epoch was down-sampled to 2Hz and MEM method proposed previously by our group for fNIRS reconstruction (Cai *et al.*, 2021) was applied to estimate the HbO/HbR spatiotemporal maps (0s to 30s) along the subject-specific cortical surface.
- 3) After the fNIRS 3D reconstruction using MEM, the HbO/HbR spatiotemporal maps of each subject during each finger-tapping Run (e.g., 101 HbO maps for Sub01 during pre-PAS25 finger-tapping) were co-registered to the mid-surface of the MNI ICBM152 template (Fonov

et al., 2009, 2011), using FreeSurfer spherical transformation. An ROI was defined along the template surface as the ‘hand knob’, to cover the expected activation regions. Finally, reconstructed HbO/HbR time courses (0s to 30s) within this “hand knob” ROI were averaged to represent the hemodynamic responses of each specific finger-tapping Run.

The output of the whole fNIRS data preprocessing section was a set of 80 Runs (i.e. 40 Sessions (16 PAS25+12 PAS10+12 sham) \times 2 Times) of 101 reconstructed HbO/HbR time course ranging from 0s to 30s, for each Run specified by Subject (ID 1 to 16), Intervention (PAS25, PAS10 or sham) and Time (pre-PAS or post-PAS).

7.2.4 Hierarchical Bayesian Modeling

To clarify the notation used in the following model equations, we used small letters to denote a scale variable (e.g., μ for the mean of a Gaussian distribution) and capital letters to denote a matrix (e.g., Σ for the covariance matrix of a multivariate Gaussian distribution). A list of scalar values from one specific variable is represented by a small letter along with a subscript letter, for instance, a symbol μ_s refers to a list of means, and the subscript s represents each individual element of this list (mean for the s^{th} Session). The dimensionality of each list is given by the range of s (e.g., $s = 1, 2, 3, \dots, 40$, for s^{th} session). If subscript letter(s) is contained in square brackets, it means the individual element of this list variable is differentiated by the model using index variables. Such as, i in $intercept_{[i=1,2,3]}$ indicates our model differentiates the intercept parameter for each intervention type by index variable $i = 1, 2, 3$, 1 for PAS25, 2 for PAS10 and 3 for sham.

Hierarchical Bayesian Model #1: Assessment of PAS effects on cortical excitability

We proposed a first hierarchical Bayesian model to assess PAS effects on M1 cortical excitability, which was evaluated using the MEPs measured during spTMS Runs before and after each PAS intervention. This model consists of two parts: 1) a measurement error model taking into account the variability of MEPs within each spTMS Run and 2) a multivariate hierarchical linear model describing post-intervention MEP as a function of pre-intervention MEP.

1) A model of measurement error

We assume the “empirical” mean of the observed MEP in each Run to be drawn from a Gaussian distribution with the mean equals to the ‘true’ MEP amplitude and the scale equals to the standard

error of all MEPs trials. The ‘true’ and observed (‘obs’) MEP of the pre-PAS spTMS Run can be expressed as follows,

$$\begin{aligned} MEP_{obs,s}^{pre} &\sim \mathcal{Normal}(MEP_{true,s}^{pre}, MEP_{se,s}^{pre}) \\ MEP_{true,s}^{pre} &\sim \mathcal{Normal}(0.5, 1) \\ s &= 1, 2, 3, \dots 40, \text{ for } s^{th} \text{ session} \end{aligned} \quad (7.1)$$

where $MEP_{true,s}^{pre}$ is the ‘true’ value of the pre-PAS mean MEP for Session s . $MEP_{obs,s}^{pre}$ is the “empirical” mean of the observed MEP from the same Run expressed as,

$$\begin{aligned} MEP_{obs,s}^{pre} &= \frac{\sum_{k=1}^N MEP_{k,s}^{pre}}{N} \\ k &= 1, 2, 3, \dots 75, \text{ for } k^{th} \text{ trial} \end{aligned} \quad (7.2)$$

where $MEP_{k,s}^{pre}$ represents the pre-PAS MEP of the k^{th} trial from a total of $N=75$ trials in Session s . The corresponding measurement error $MEP_{se,s}^{pre}$ is then represented by the standard error of the MEP among all 75 trials, estimated by,

$$MEP_{se,s}^{pre} = \sqrt{\frac{\sum_{k=1}^N (MEP_{k,s}^{pre} - MEP_{obs,s}^{pre})^2}{N(N-1)}} \quad (7.3)$$

Finally, substituting (7.2) and (7.3) into (7.1), both empirical mean and variance estimated over the 75 observed pre-PAS MEPs of a specific Session were modeled to estimate the ‘true’ corresponding amplitude. For the prior distribution of $MEP_{true,s}^{pre}$, we applied a weakly informed prior (Gelman *et al.*, 2008; Gelman, Simpson and Betancourt, 2017; Gabry *et al.*, 2019) consisting in a Gaussian distribution $\mathcal{Normal}(0.5, 1)$. Note that all observed MEPs ($MEP_{obs,s}^{pre,post}$ and $MEP_{se,s}^{pre,post}$, for 40 Sessions \times 2 Times (pre –/post – PAS) = 80) were normalized by the global maximum value of $MEP_{obs,s}^{pre,post}$ to ensure a [0, 1] range. Then, 0.5 appears as an appropriate prior of the mean when nothing is known about the MEP amplitude, but only the range (i.e., $(0 + 1)/2 = 0.5$).

The ‘true’ MEP in the post-PAS spTMS Run was then modeled as follows,

$$\begin{aligned}
 MEP_{obs,s}^{post} &\sim \text{Normal}(MEP_{true,s}^{post}, MEP_{se,s}^{post}) \\
 MEP_{obs,s}^{post} &= \frac{\sum_{k=1}^N MEP_{k,s}^{post}}{N} \\
 MEP_{se,s}^{post} &= \sqrt{\frac{\sum_{k=1}^N (MEP_{k,s}^{post} - MEP_{obs,s}^{post})^2}{N(N-1)}}
 \end{aligned} \tag{7.4}$$

Note that the prior distribution of the parameter $MEP_{true,s}^{post}$ is introduced in the next section, within the context of hierarchical multivariate linear regression.

2) Hierarchical multivariate linear regression

PAS effects on M1 cortical excitability were then modeled using a multivariate linear regression model, in which $MEP_{true,s}^{post}$ and $MEP_{true,s}^{pre}$ were considered as the dependent and predictor variables, respectively.

$$\begin{aligned}
 MEP_{true,s}^{post} &\sim \text{Normal}(\mu_s, \sigma) \\
 \mu_s &= \text{intercept}_{[i]} + (\text{group}_{[i]} + \text{actor}_{[a,i]}) \cdot MEP_{true,s}^{pre} \\
 i &= 1, 2 \text{ and } 3, \text{ for } i^{\text{th}} \text{ intervention} \\
 a &= 1, 2, 3, \dots 16, \text{ for } a^{\text{th}} \text{ subject} \\
 s &= 1, 2, 3, \dots 40, \text{ for } s^{\text{th}} \text{ session}
 \end{aligned} \tag{7.5}$$

where μ_s is the mean of $MEP_{true,s}^{post}$, predicted by $MEP_{true,s}^{pre}$ using the following linear model: $\mu_s = \text{intercept}_{[i]} + (\text{group}_{[i]} + \text{actor}_{[a,i]}) \cdot MEP_{true,s}^{pre}$, and σ is the error of the linear regression (i.e., the scale of the normal distribution). We added the following index variables to differentiate Subject, Intervention (PAS25/PAS10/sham) and Time (pre-/post-PAS) in the model. $\text{intercept}_{[i]}$ is the intercept of the linear regression, for the i^{th} intervention, in which $i = 1, 2 \text{ and } 3$ refers to PAS25, PAS10 and sham, respectively. The slope parameter is modeled using two parts, a group-level slope parameter $\text{group}_{[i]}$, specific for each intervention i , and a parameter modeling inter-subject variability, denoted as $\text{actor}_{[a,i]}$, for each intervention i and each subject a , associated with the following prior model:

$$\begin{aligned}
 \begin{bmatrix} actor_{[a,i=1]} \\ actor_{[a,i=2]} \\ actor_{[a,i=3]} \end{bmatrix} &\sim \text{MultiNormal} \left(\begin{bmatrix} 0 \\ 0 \\ 0 \end{bmatrix}, \Sigma \right) \\
 \Sigma &= \Sigma_{actor} \cdot Rho \cdot \Sigma_{actor} \\
 &= \begin{pmatrix} \sigma_1 & 0 & 0 \\ 0 & \sigma_2 & 0 \\ 0 & 0 & \sigma_3 \end{pmatrix} \begin{pmatrix} 1 & \rho_{12} & \rho_{13} \\ \rho_{21} & 1 & \rho_{23} \\ \rho_{31} & \rho_{32} & 1 \end{pmatrix} \begin{pmatrix} \sigma_1 & 0 & 0 \\ 0 & \sigma_2 & 0 \\ 0 & 0 & \sigma_3 \end{pmatrix}
 \end{aligned} \tag{7.6}$$

where $\text{MultiNormal}(\cdot)$ is a multivariate Gaussian distribution to model the interaction, which allows the effects of each specific intervention to vary for each subject, meaning each subject can respond to each intervention differently. We defined this multivariate Gaussian prior distribution to have zero means (3 elements vector) therefore assuming all the subjects to have zero mean deviation around the group-level slope parameter $group_{[i]}$. Rho and Σ_{actor} denote respectively the correlation matrix and the scale matrix of the covariance matrix Σ of the multivariate Gaussian distribution. $\sigma_{1,2,3}$ is the scale among all subjects within each intervention group, for example, σ_3 is the scale of the vector $actor_{[a,i=3]}$ for sham. ρ is the correlation between pair-wised interventions, for instance, ρ_{12} represents the correlation between $actor_{[a,i=1]}$ for PAS25 and $actor_{[a,i=2]}$ for PAS10.

Weakly informed priors were assigned to the parameters in (5) and (6) as follows,

$$\begin{aligned}
 intercept_{[i]} &\sim \text{Normal}(0, 0.1) \\
 group_{[i]} &\sim \text{logNormal}(\log(1), 0.5) \\
 \rho &\sim \text{LKJcorr}(2) \\
 \sigma &\sim \text{HalfNormal}(0, 1)
 \end{aligned} \tag{7.7}$$

$\text{Normal}(0, 0.1)$ was chosen for $intercept_{[i]}$ considering that when $MEP_{true,s}^{pre} = 0$, the corresponding $MEP_{true,s}^{post}$ should not be too much apart from 0. $\text{logNormal}(\log(1), 0.5)$ was selected for the group-level slope to ensure it is a positive value with a median of 1. Therefore, without knowing any intervention type, the slope should be equal to 1, assuming there is no averaged PAS effect among subjects when the intervention type is not known. $\text{LKJcorr}(\eta = 2)$, the Lewandowski-Kurowicka-Joe distribution (Lewandowski, Kurowicka and Joe, 2009), is a weakly informative prior for the correlation parameter ρ that does not prioritize extreme

correlation values such as ± 1 . η is a positive value, $\eta = 1$ denotes uniform density of ρ . The larger η is (when compared to 1), the least likely the extreme correlation values to occur (sharper probability density distribution), and vice versa. We selected $\eta = 2$ as a weakly informed prior commonly considered in Bayesian data analysis (McElreath, 2020). Finally, $HalfNormal(0,1)$ was used for variance parameters to ensure a positive value, whereas its likelihood decreased following the positive half of a $Normal(0, 1)$ distribution, when variance increases. As denoted previously, we normalized all data $MEP_{k,s}^{pre}$ and $MEP_{k,s}^{post}$ within the range $[0,1]$, therefore $Normal(0, 1)$ is considered as a conservative (“flat”) enough prior, not reducing the variance.

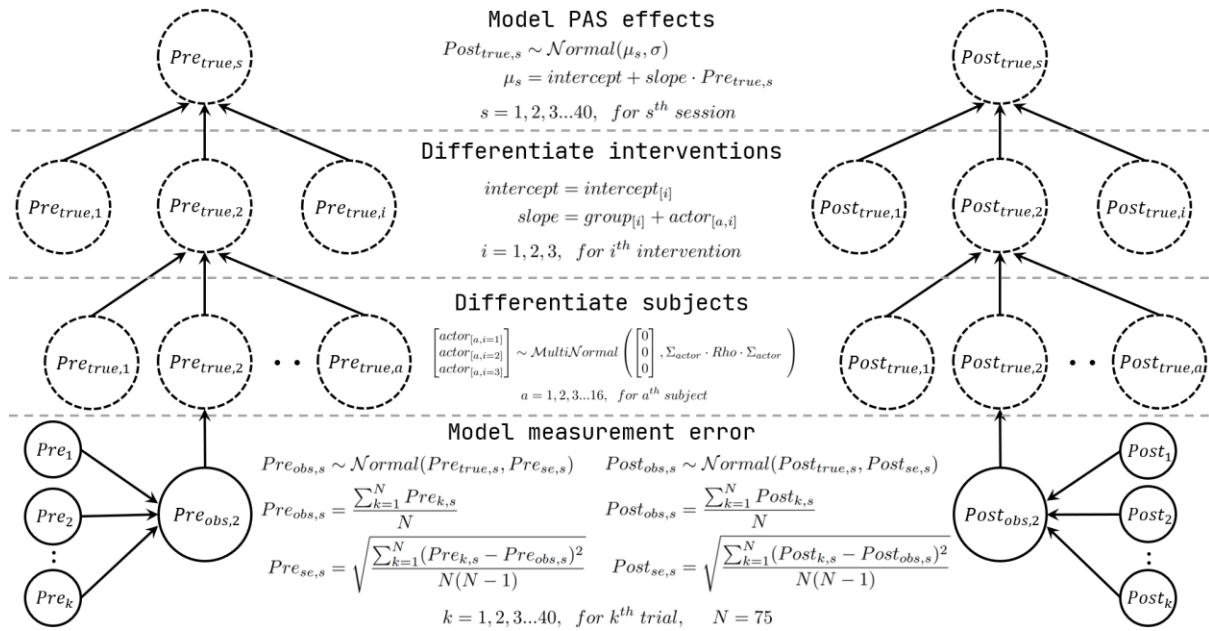


Fig.7.2 The hierarchical model of PAS effects on either cortical excitability (MEP) or hemodynamic responses (Hb). From bottom to top, 1) a measurement error model assuming the mean of the variable of interest (either the observed MEPs, e.g., $MEP_{se,s}^{pre}$; or a spline weight of HbO/HbR time course, e.g., $w_{obs,s,n}^{pre}$ of each Run at a different Time (pre-/post-) is drawn from a Gaussian distribution. The mean of this Gaussian distribution is the ‘true’ value of the variable of interest, and the scale is the corresponding standard error; 2) each subject and intervention were differentiated using index variables; 3) PAS effects were modeled by linear regression in which the ‘true’ post- variable of interest was predicted by the ‘true’ pre- variable of interest. Solving this hierarchical model by Bayesian allows partial pooling on each parameter to reduce the uncertainty.

Hierarchical Bayesian Model #2: Assessment of PAS effects on task-related HbO/HbR

A similar hierarchical multivariate linear regression model is proposed to assess PAS effects on task-related fNIRS hemodynamic responses. This model is very similar to previous Model#1, the main difference being that the input variables to the model are now ‘features’ representing hemodynamic responses during the finger-tapping task. Instead of extracting amplitudes at a particular time sample of HbO/HbR time courses, for instance the hemodynamic peak amplitude, or performing a local average within a specific time window, in this Model #2, we conducted a procedure to model the PAS effects over the whole time course of HbO/HbR responses to finger tapping.

To do so, after 3D reconstruction using MEM of all 101 sub-averaged of the fNIRS responses, HbO/HbR time courses were first averaged within the selected M1 ROI along the selected time range [0s, 30s]. To lower the dimension of the input to the model, resulting time courses were then projected on B-splines temporal basis functions (Boor, 2001; Gelman *et al.*, 2013b; Hastie, 2017). Therefore, hemodynamic responses were expressed as a weighted linear combination of those basis functions, considering the hierarchical model summarized in Fig.7.3. Please note that Hb refers to either HbO or HbR in the model, which was fitted separately for each chromophore,

$$\begin{aligned}
 Hb_{obs,s,t}^{pre} &\sim Normal(\mu_{s,t}^{pre}, Hb_{sd,s,t}^{pre}) \\
 \mu_{s,t}^{pre} &= w_{obs,s,n}^{pre} \times B_{n,t} \\
 w_{obs,s,n}^{pre} &\sim Normal(0,10) \\
 Hb_{obs,s,t}^{post} &\sim Normal(\mu_{s,t}^{post}, Hb_{sd,s,t}^{post}) \\
 \mu_{s,t}^{post} &= w_{obs,s,n}^{post} \times B_{n,t} \\
 w_{obs,s,n}^{post} &\sim Normal(0,10) \\
 n &= 1, 2, 3, \dots 10, \text{ for } n^{th} \text{ weight} \\
 t &= 0s \text{ to } 30s \text{ with a step of } 0.5s \\
 s &= 1, 2, 3, \dots 40, \text{ for } s^{th} \text{ session}
 \end{aligned} \tag{7.8}$$

where $Hb_{obs,s,t}^{pre}$ is the observed empirical mean of pre-PAS HbO/HbR responses among all 101 sub-averaged time courses, for a specific finger-tapping Run (e.g., finger-tapping Run in pre-PAS25 of Sub01) of a specific Session s at a specific time point t . $Hb_{obs,s,t}^{pre}$ is assumed to follow a Gaussian distribution with a mean of $\mu_{s,t}^{pre}$ and a scale of $Hb_{sd,s,t}^{pre}$, where $Hb_{sd,s,t}^{pre}$ is the corresponding standard deviation estimated among all 101 sub-averaged time courses. Note that

all pre- and post-PAS HbO/HbR time courses in one Session were normalized by the global maximum amplitude to be within the range $[-1,1]$. Then, $\mu_{s,t}^{pre}$ representing the mean time course of the true pre-PAS HbR/HbO for time sample t and session s , was defined as a linear combination of $n = 10$ B-spline basis functions $B_{n,t}$ using the corresponding weight $w_{obs,s,n}^{pre}$. Each basis function $B_{n,t}$ was defined as a 3rd order polynomial function. A similar model structure was applied to data and parameters corresponding to the post-PAS finger-tapping Run. To model the temporal response using B-spline, we selected 10 knots pivoted at the percentiles of time sequence $t = 0s$ to $30s$ with a step of $0.5s$; therefore, 10 corresponding weights and basis functions, as illustrated in the second column of Fig.7.3. Using this Bayesian spline model, not only the averaged time course of HbO/HbR, but also their corresponding standard deviation over the 101 sub-averaged, for each time point, were projected in the ‘spline space’. This means the averaged time course of HbO/HbR can be recovered by the linear combination of the mean of each weight (over 101 sub-averaged) and basis functions $B_{n,t}$, whereas the standard deviation of HbO/HbR time course is reflected by the linear combination of the standard deviation of each weight (over 101 sub-averaged) and $B_{n,t}$. Note that the use of spline basis functions in this study was mainly to reduce the dimensionality of the HbO/HbR time course from 60 sampling points to 10 weights, while preserving the variability structure to be modeled. Therefore, selecting 10 spline knots was a trade-off between: 1) choosing fewer knots that would result in eventual distortion of the HbO/HbR time courses, involving too much temporal smoothness; 2) adding more knots that would increase the dimensionality of the data after projection. Hence, our empirical choice ensured accurate representation of the whole HbO/HbR time courses with a minimum dimensionality span. Importantly, projecting to spline space also preserved the autocorrelation of the HbO/HbR time courses per se, which could not be achieved when simply applying the same hierarchical model on each of 60 data points independently. Finally, $Normal(0,10)$ is considered as a weakly informative prior for spline weight considering the HbO/HbR time course was normalized within the range $[-1,1]$.

We then embedded this spline model of the hemodynamic response within the same hierarchical model proposed in the previous section (Model#1), for instance, replacing the $MEP_{obs,s}^{pre}$ with the spline weights $w_{obs,s,n}^{pre}$ as follows, also illustrated in the third column of Fig.7.3.

$$\begin{aligned}
 w_{obs,s,n}^{post} &\sim \text{Normal}(w_{true,s,n}^{post}, w_{sd,s,n}^{post}) \\
 w_{obs,s,n}^{pre} &\sim \text{Normal}(w_{true,s,n}^{pre}, w_{sd,s,n}^{pre}) \\
 w_{true,s,n}^{post} &\sim \text{Normal}(\mu_s, \sigma) \\
 \mu_s &= \text{intercept}_{[i]} + (\text{group}_{[i]} + \text{actor}_{[a,i]}) \cdot w_{true,s,n}^{pre} \\
 w_{true,s,n}^{pre} &\sim \text{Normal}(0,10)
 \end{aligned} \tag{7.9}$$

where $w_{obs,s,n}^{post}$, $w_{obs,s,n}^{pre}$, $w_{sd,s,n}^{post}$ and $w_{sd,s,n}^{pre}$ were all calculated from the corresponding posterior of spline weights estimated from equation (7.8). In total, 10 models were considered for 10 pairs of weights (pre- and post-PAS) to encode the PAS effects for either HbO or HbR separately. $w_{obs,s,n}^{post}$ and $w_{obs,s,n}^{pre}$ are referring to the empirical mean of each spline weight for either pre- or post-PAS HbO/HbR for Session s , estimated from the corresponding posterior of spline weights in equation (7.8). The scale of Gaussian distribution in the measurement error model was then $w_{sd,s,n}^{post}$ and $w_{sd,s,n}^{pre}$, respectively. Note that equation (7.8) resulted the estimated posterior distribution of $w_{obs,s,n}^{post}$ and $w_{obs,s,n}^{pre}$ after projecting HbO or HbR time course to the spline space, then scales of Gaussian distributions used for measurement error model in (7.9) were directly reflected by the standard deviation of the posterior distribution (denoted as sd in subscript). Finally, the intervention, subject index variables and priors to be considered for this model, were similar to those previously introduced for Model#1, so the PAS effects on HbO/HbR whole time course were then encapsulated in the hierarchical model of spline weights.

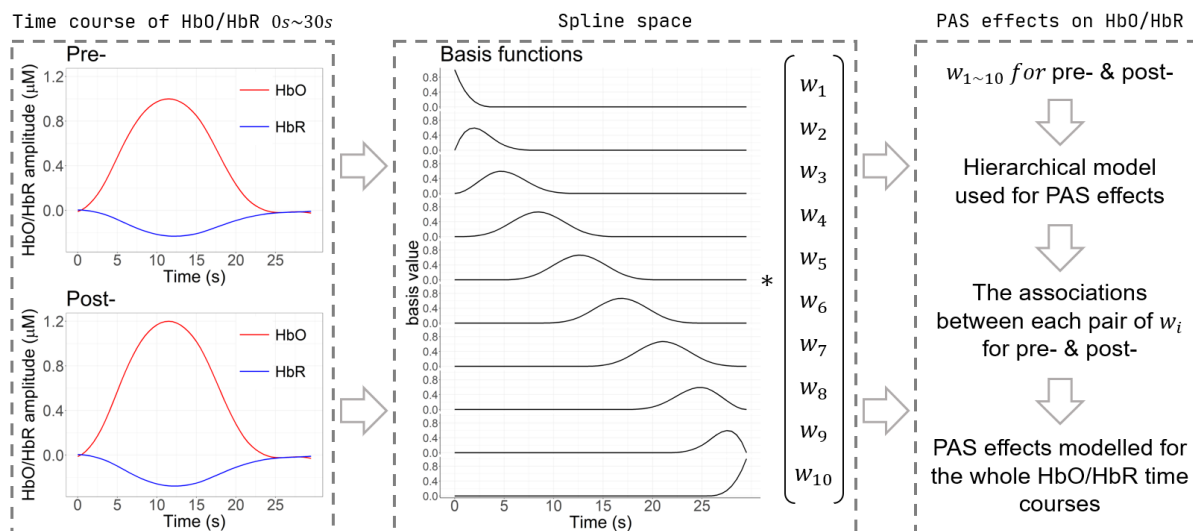


Fig.7.3 The hierarchical Bayesian spline model for PAS effects on the whole HbO/HbR time course. HbO/HbR time courses, from 0s to 30s, before and after each intervention Session were selected as the inputs of the model. They were projected into the spline space which is composed of 10 predefined basis functions (3rd order polynomial with 10 knots). The linear combination of basis function using 10 corresponding weights $w_{1\sim 10}$ can fully recover the HbO/HbR time course. The resulting pre- and post-PAS spline weights were then fed into the hierarchical model, similar to model #1 to estimate the PAS effects on each weight. Therefore, the associations between each pair of weights encapsulated the PAS effects on the whole time course of HbO/HbR.

Hierarchical Bayesian Model #3: Relationship between PAS effects on task-related M1 hemodynamic activity and PAS effects on M1 excitability

In this third model, we propose to investigate the interactions between (i) PAS effects on M1 excitability (PAS effects on MEP, represented by the slope parameter in Model#1) and (ii) PAS effects on reconstructed hemodynamic finger tapping responses (PAS effects on HbO/HbR, represented by the slope parameter in Model#2 for a specific weight w_n). We assumed the relationship between task-related M1 hemodynamic activity and M1 excitability was not intervention specific, then the previous hierarchical models (i.e., Model#1 and Model#2) were modified to be only Session specific, i.e., only index variable of Session s was used, whereas intervention and subject index i and a were ignored.

$$\begin{aligned} \begin{bmatrix} slope_{[s]}^{MEP} \\ slope_{[s]}^{Hb} \end{bmatrix} &\sim \text{MultiNormal} \left(\begin{bmatrix} 0 \\ 0 \end{bmatrix}, \Sigma_{slope} \right) \\ \Sigma_{slope} &= \Sigma_{session} \cdot Rho_{slope} \cdot \Sigma_{session} \\ &= \begin{pmatrix} \sigma_{MEP} & 0 \\ 0 & \sigma_{Hb} \end{pmatrix} \begin{pmatrix} 1 & \rho_{MEP-Hb} \\ \rho_{Hb-MEP} & 1 \end{pmatrix} \begin{pmatrix} \sigma_{MEP} & 0 \\ 0 & \sigma_{Hb} \end{pmatrix} \\ &s = 1, 2, 3, \dots 40, \text{ for } s^{th} \text{ session} \end{aligned} \quad (7.10)$$

The interactions were modeled using a multinormal distribution, in which the parameter ρ_{MEP-Hb} in the Rho_{slope} matrix denotes the correlation between the two slopes (representing the PAS effects in both linear models). The same model was fitted separately when investigating either the relationship between MEP and HbO or between MEP and HbR. $slope_{[s]}^{MEP}$ is the Session specific slope parameter in Model#1. Similarly, $slope_{[s]}^{Hb}$ (either HbO or HbR) is the Session specific slope parameter in Model#2 for one of the corresponding spline weights $w_{1\sim 10}$. σ_{MEP} and σ_{Hb} are the

standard deviations of $slope_{[s]}^{MEP}$ or $slope_{[s]}^{Hb}$, respectively. Note that this model was fitted for each spline weight separately - 10 correlation investigations between MEP and each spline weight were conducted. Therefore, the posterior distribution ρ_{MEP-Hb} inferred for a specific spline weight can be interpreted as the correlation between brain excitability and task-related cortical hemodynamic activity at a specific period (e.g., w_5 reflecting HbO/HbR fluctuations around the peak time point of the hemodynamic response). For the parameters of the Multinormal distribution, we considered the same weakly informed priors as those proposed in Model#1 and Model#2.

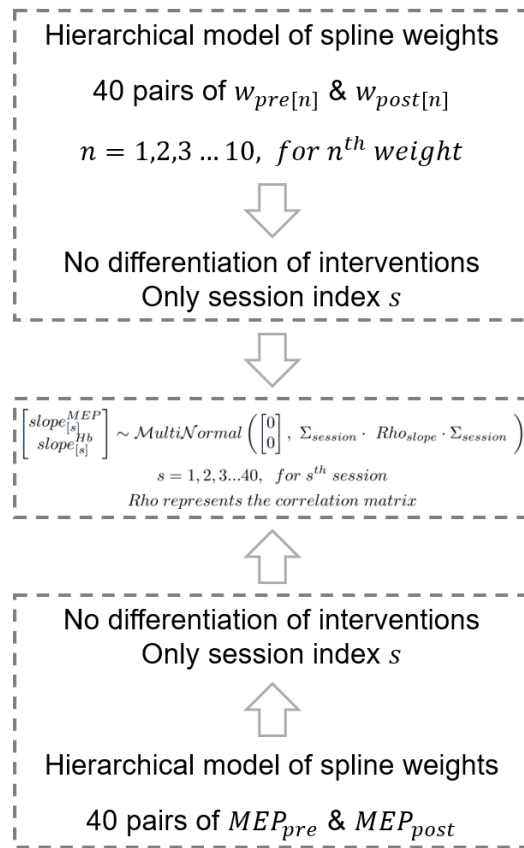


Fig.7.4 Modeling the relationship of task-related M1 hemodynamic activity and M1 excitability. For MEP, which represented the M1 excitability, the previous Model #1 was modified to be Session-specific only. For spline weights, which represented the features of task-related HbO/HbR time course, the previous ‘Model #2 was also modified to be Session-specific only. The association between the $slope_{MEP}$ in MEP model and $slope_{Hb}$ represented by any of the spline weight of the HbO/HbR time course model were described by a multinormal distribution.

7.2.5 Prior predictive simulation

To justify the choices of ‘weakly informed’ prior, a prior predictive simulation was conducted in Fig.7.3. The prior predictive simulation consists in a generative process simply checking what kind of data we would expect to generate from our hierarchical models, when applying all possible values of the parameters considering the proposed prior distributions of the model. Then by comparing the distribution of data generated by our model, to the domain knowledge, one can assess whether the proposed priors could be overregulating or not objective (e.g., too strongly informed). In our study, PAS effects were modeled using linear regression. To perform prior predictive simulation, we considered prior predictive simulation to draw 1000 lines following the prior distributions of the intercept and slope in the normalized pre-MEP vs. post-MEP amplitude plane. Then the distribution of generated regression lines was compared to three reference lines summarizing our knowledge of the problem. The three reference lines were featuring a slope of 0.2, 1 and 3, respectively and an intercept of 0. When the intercept is set to 0, the slope just refers to the ratio of post- over pre-PAS MEP amplitude, which was used in our previous conventional analysis to represent the PAS effects. Whereas a slope of 1 would then correspond to no effect (post-/pre-PAS ratio of 1), the reference slopes of 0.2 and 3 represented the thresholds for outliers of extremely small or large MEP ratios reported in [Krivánková et al., 2013](#).

7.2.6 Hierarchical Bayesian model fitting

Using Bayes’ theorem ([Laplace, 1810](#)), the posterior density of the conditional probability distribution, $p(\theta|y)$, of all parameters (θ), knowing the data y , can be expressed as follows,

$$p(\theta|y) = \frac{p(\theta)p(y|\theta)}{p(y)} \quad (7.11)$$

where $p(y|\theta)$ is considered as the likelihood of the data y , when parameters θ are known and $p(\theta)$ is the prior distribution of those parameters. $p(y)$ is then the average likelihood of the data over all possible values of θ . $p(\theta|y)$ was sampled from the joint posterior distribution $p(\theta)p(y|\theta)$ using Markov Chain Monte Carlo (MCMC) ([Neal, 1993](#); [Gelman et al., 2013b](#)), while omitting the normalization factor $p(y)$, therefore,

$$p(\theta|y) \propto p(\theta)p(y|\theta) \quad (7.12)$$

In this study, we used the R Version 4.0.3 (R Core Team, 2020) distribution of the Stan Probabilistic programming languages (Stan Development Team, 2020b) - RStan package Version 2.21.2 (Stan Development Team, 2020a) to implement and solve the proposed Bayesian models. Specifically, the joint posterior distribution was sampled using the implementation of dynamic HMC in Stan (Betancourt, 2017, 2019), as an improved version of HMC algorithm (Neal, 2010; Betancourt and Girolami, 2015). In total, 4 MCMC chains were used to sample each model and they were initialized randomly to ensure a better exploration of the joint posterior distribution, while allowing diagnostic of the convergence. Each chain consisted of 2000 samples, including a first half warm-up phase (1000 samples) for the adaptation of the HMC parameters. Therefore, when combining all 4 chains, we obtained 4000 samples of each parameter of the models mentioned above, drawn respectively to estimate the corresponding posterior distributions. Regarding computation time, using an Intel 10750H laptop CPU and parallel computation (one core per chain), dynamic HMC took 66s for sampling once Model#1, 59s for Model#2 and 53s for Model#3 (including compiling time and calculation of the diagnostics).

Diagnosing the HMC sampling process is a crucial step when evaluating the accuracy and biases of the estimated posterior distributions. This is also known as a unique and advanced feature of HMC when compared to other MCMC algorithms (Roberts and Rosenthal, 2004). In this study, we considered the diagnostic approach recommended by Stan to evaluate pathological behaviours of HMC sampling (Betancourt, 2017; Gabry *et al.*, 2019; Gelman *et al.*, 2020),

- 1) ***Divergent transitions for real samples drawn after the warm-up phase.*** This diagnostic statistic is specific for the HMC sampler, mainly invigilating the miss-match between the step size of the MCMC chain and the target distribution geometries (Betancourt *et al.*, 2017). While sampling a ‘high curvature’ region of the target distribution, an inappropriate large step size may miss-sample it, therefore biasing the resulted posterior distribution. MCMC chains will approach infinite energy immediately – called divergent transitions – when approaching such regions (Neal, 2010; Betancourt, 2017). These divergences are recorded and reported by Stan. Note that divergence is usually related to the parameterization of the model, especially when involving multivariate and hierarchical structures. Parameters may usually be dependent on each other in these models, therefore, creating a ‘high curvature’ distribution landscape, also denoted as Neal’s Funnel (Neal, 2003), which is difficult to sample. In order to reduce the

chances of such divergences, in our study, we considered reparameterization of the model into non-centred forms when sampling with HMC.

- 2) ***The Energy-Bayesian Fraction of Missing Information (E-BFMI) is a specific diagnostic statistic for HMC sampler, evaluating the efficiency of the sampling process*** (Betancourt, 2016). Poorly chosen parameters of the HMC can decrease the efficiency of the sampling process or even result in incomplete exploration of the target distribution, especially when considering distributions with heavy tails. Such a behaviour can be diagnosed by taking advantage of the physics feature of HMC, by comparing the marginal energy density (denoted as π_E) and energy transition density (denoted as $\pi_{\Delta E}$) of the chain. When superimposing the histograms of π_E and $\pi_{\Delta E}$, the higher the efficiency, the more overlap between the two distributions. The Energy Bayesian Fraction of Missing Information (E-BFMI) (Rubin, 2004) is used in Stan to quantify such comparison, by calculating the statistical expectation of the variance of $\pi_{\Delta E}$ over the variance of π_E . Empirically, an E-BFMI value below 0.3 is considered as problematic (Betancourt, 2016, 2017).
- 3) ***\hat{R} as a general and primary diagnostic statistic when evaluating convergence of MCMC chains*** (Gelman and Rubin, 1992; Brooks and Gelman, 1998). \hat{R} is estimated for each parameter of the model as the ratio of between-chains variance over the within-chain variance. In detail, the between-chains variance is calculated as the standard deviation among all chains, whereas the within-chain variance is calculated as the weighted sum of the root mean square of the standard deviation within each single chain. The recommended criteria for convergence is $\hat{R} < 1.05$ (Gabry *et al.*, 2019; Vehtari *et al.*, 2020).

Finally, we used tidyverse package (Wickham *et al.*, 2019) in R (R Core Team, 2020) for general data wrangling and visualization. Tidybayes package (Kay, 2020) was used for visualizing the posterior distributions whereas bayesplot package (Gabry *et al.*, 2019; Gabry and Mahr, 2020) was used for visualizing the diagnostics of HMC chains.

7.2.7 Statistical inferences

In general, two types of statistical inferences were made in this study:

- 1) When investigating the effect of PAS on MEP, we first made inferences by answering the question - what would be the distribution of MEP after a certain PAS intervention when giving

a specific pre-PAS MEP? This approach is more direct and convenient comparing the process checking the posterior distribution of each parameter of the model one by one. This technique is referred as the posterior predictive simulation (Gabry *et al.*, 2019; Gelman *et al.*, 2020). For instance, ***to infer the PAS effects on the M1 cortical excitability***, we used the averaged MEP (i.e., equals to 1.0mV, in the original data scale before normalizing) among all pre-PAS Runs to represent the group-level pre-PAS M1 cortical excitability. This amplitude was then substituted into the fitted Model#1 along with all posterior distributions of parameters (e.g., intervention-specific intercepts and slopes) to estimate a group-level post-PAS MEP distribution. By comparing the distributions of the percentage change of this post-PAS MEP distribution relative to the pre-PAS MEP amplitude, the effects of each intervention can be inferred. We also performed this inference using a set of different pre-PAS MEPs values, such as 0.2mV, 0.6mV, 1.2mV, 2.2mV and 2.8mV according to the observed range of all individual pre-PAS MEP (i.e., ranging from 0.1mV to 3.0mV), to investigate how PAS effects could be related to the pre-PAS MEP amplitude. Note that these pre-PAS MEP amplitudes were also scaled by dividing the global maximum value of $MEP_{obs,S}^{pre,post}$ before being feed into the model, and posterior predicted post-PAS MEP amplitudes were rescaled back to the original data scale.

Similarly, ***the PAS effects on task-related hemodynamic*** were statistically inferred using the following steps: 1) select any preferred pre-PAS HbO/HbR time course (e.g., the averaged HbO/HbR of all pre-PAS Runs demonstrated in the results); 2) calculate the 10 weights (variable) corresponding to this specific time courses; 3) inferring the 10 post-weights along with their variance by posterior predictive simulations of the fitted hierarchical Model#2; 4) apply a linear combination of 10 post-weight and basis functions to obtain the distribution of post-PAS HbO/HbR time course. Note that we also calculated the PAS effects on HbO/HbR by contrasting post-PAS25 or post-PAS10 hemodynamic response to the one obtained in post-sham condition. To do so, we subtracted from the posterior predicted distributions of post-PAS25 HbO/HbR time courses (or post-PAS10) the posterior predicted post-sham HbO/HbR time courses.

- 2) ***The correlation between M1 cortical excitability and task-related hemodynamic response*** can be inferred directly from the posterior distribution of the correlation parameter ρ_{MEP-Hb}

per se. Note that this correlation distribution was estimated for each spline weight separately, therefore, the resulted posteriors can be used to infer the excitability association for each specific time point of the HbO/HbR time course. For instance, the posterior distribution of the correlation between $slope_{[s]}^{MEP}$ and $slope_{[s]}^{Hb(w_5)}$ indicated the relationship between the peak period (e.g., few seconds around the expected peak timing of the response) of task-related HbO/HbR and M1 cortical excitability. We also conducted typical frequentist inferences of this relationship using the linear fit and Pearson's correlation over all 40 Sessions on the resulted mean of $slope_{[s]}^{MEP}$ and $slope_{[s]}^{Hb(w_5)}$, for both HbO and HbR.

Note that for quantified statistics, we reported median and the median absolute deviation (i.e., mad_{sd}), which was suggested by Gelman et al., 2020a and estimated as follows: $mad_{sd} = 1.483 \cdot median_{i=1}^n |z_i - M|$, where z_i is a certain value of a set of values $z_{i=1,2,3...n}$ and M is the median of all z_i . The mad_{sd} is a more universal representation of the variance, which is comparable to the standard deviation, without considering the parametric/nonparametric distribution of z_i and is more computationally stable.

7.3. Results

7.3.1 Prior predictive simulation

As illustrated in Fig.7.5, resultant prior predictive simulation lines were distributed symmetrically around the control line suggesting no PAS effect (i.e., intercept = 0, slope =1). This means our priors exhibited no preference towards a slope < 1 or >1. Moreover, within the post-PAS MEP versus pre-PAS MEP plane, the area spanned by all simulated lines covered a larger area than the area enfolded by the reference lines (0 intercepts, a slope spanning from 0.2 to 3.0). These results are confirming that priors in our hierarchical model are not biased to the expected PAS effect and are more conservative than the conventional MEP ratio thresholding approach. This prior predictive simulation result also applies to PAS effects on HbO/HbR, since fNIRS data were normalized similarly as MEP values and the priors in the multivariate linear regression models were the same.

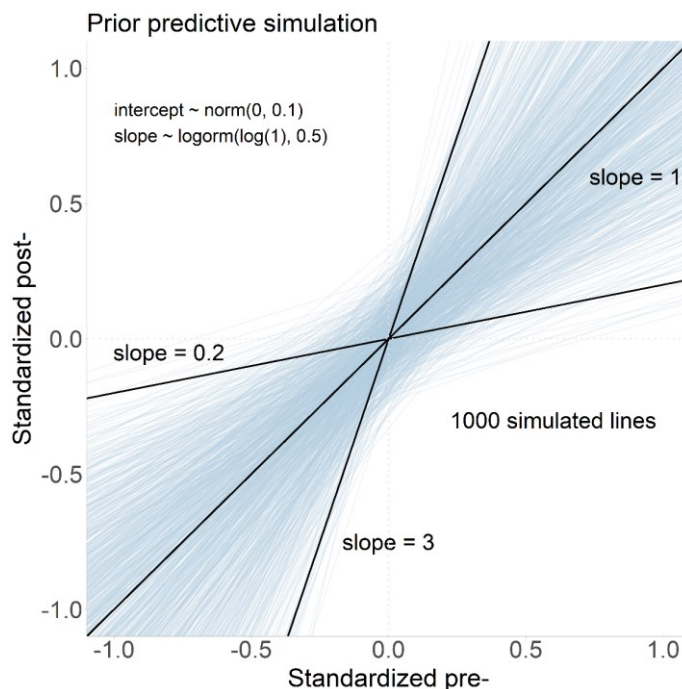


Fig.7.5 Prior predictive simulations for the hierarchical model of PAS effects on cortical excitability. Each blue line represents one prior predictive simulation obtained by drawing simultaneously the intercept and the slope parameters when considering only the priors proposed in Model#1. For comparison purposes, as a reference, we first represented a control line suggesting no PAS effect (intercept of 0, slope of 1), then two lines referring to MEP ratio outliers (intercept of 0 and slope of 0.2 and 3 respectively).

7.3.2 Diagnosis of HMC

All of the models resulted in 0 divergences reported by Stan, indicating they were well parameterized, and HMC chains explored sufficiently well the target distribution. Fig.7.6 reports the evaluation of diagnostic statistics for the two metrics \hat{R} and E-BFMI. In each column of Fig.7.6, a specific model sampling process for a specific model is being diagnosed (see further details in Fig.7.6 caption). The first row illustrates the histogram of \hat{R} for all parameters in each corresponding model. No parameters resulted $\hat{R} > 1.05$ indicating the corresponding HMC chains indeed well converge. The second row demonstrated the superimposed histograms of π_E (i.e., marginal energy density) and $\pi_{\Delta E}$ (i.e., energy transition density), which overlapped well for all models. This evaluation was also quantified by reporting E-BFMI values for each model, which were all smaller than 0.3. Therefore, we can conclude that the HMC chains used to sample the

parameters of the key models involved in this study were robust and reliable according to these reported diagnostic statistics.

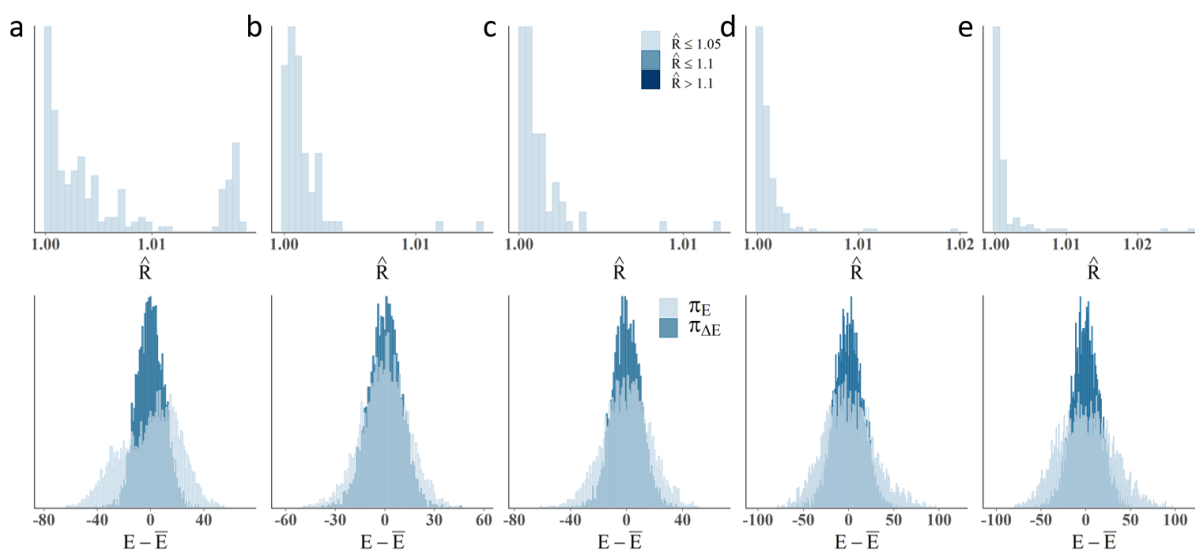


Fig.7.6 Diagnostic statistics of key features of the models considered in this study. Diagnostic statistics for a) Model#1 - PAS effects on MEP amplitude, b) Model#2 - PAS effects on w_5 of task-evoked HbO, c) Model#2 - PAS effects on w_5 of task-evoked HbR, d) Model#3 - correlation between PAS effects on MEP and PAS effects on w_5 of task-evoked HbO and e) Model#3 - correlation between PAS effects on MEP and PAS effects on w_5 of task-evoked HbR. The first row presents the histogram of \hat{R} values for all parameters among all chains of each model. No \hat{R} value was above 1.05, suggesting that all chains converged well. The second row presents the superimposed distributions of the marginal energy density π_E and the energy transition density $\pi_{\Delta E}$ for all HMC chains sampled for each model. The corresponding quantification metric E-BFMI was smaller than 0.3, indicating a good overlapping between the two distributions.

7.3.3 PAS effects on cortical excitability

When considering Model#1, the estimated regression lines (using the averaged intercept and slope parameters calculated from their posterior distributions) linking pre- and post-PAS MEPs for each intervention are reported in Fig 7a. The regression line estimated for sham intervention (black line) was found as expected - between the regression lines estimated for PAS25 (red line) and PAS10 (blue line), and it was almost identical to the reference line reporting no effect (intercept=0, slope=1). Observed pairs of post-PAS MEP and pre-PAS MEP mean amplitude over all trials are presented as solid pints (observed data), whereas corresponding estimated ‘true’ amplitudes are presented as empty points. The black lines connecting each pair of solid (observed mean) and

empty (estimated ‘true’ mean) points illustrate the shrinkage process, also known as the result of partial pooling obtained when considering hierarchical Bayesian modeling. This demonstrated the regularization property of the model, where the estimated ‘true’ MEPs corresponding to each intervention group shrank toward the corresponding regression line. Moreover, when considering the variance of the MEPs, the larger the MEP variability of a certain Run, the more shrinkage there was. Results of posterior predictive simulation at the group-level, when considering a pre-PAS MEP amplitude of 1.0mV is illustrated in Fig.7.7b, as the posterior distribution of relative changes of post-PAS MEP amplitudes (in %) after each intervention. PAS25 intervention resulted in a substantial relative increase of post-PAS MEP amplitude ($\text{median} \pm \text{mad}_{sd} = 30.6\% \pm 14.6\%$), consisting of a posterior probability of 0.97 for obtaining an increase in MEP amplitude. The posterior distribution of sham post-PAS MEP amplitude exhibits a nice symmetric pattern around a 0% increase (an increase of $2.3\% \pm 14.5\%$). The effects of PAS10 were subtle, showing a slight shift towards the negative side consisting in a relative decrease of $-1.80\% \pm 11.0\%$, and a probability of 0.57 of obtaining a decrease in MEP amplitude. Individual-level inferences are presented in Fig.7.S1, where both PAS25 and PAS10 effects are showing a large between-subject variability, as addressed in the introduction. When reporting individual level results, posterior predictive simulations were obtained by considering the same averaged pre-PAS MEP amplitude over 40 Sessions as the input for all subjects, taking full benefit of hierarchical modeling, allowing to compare individual-level results within the appropriate framework.

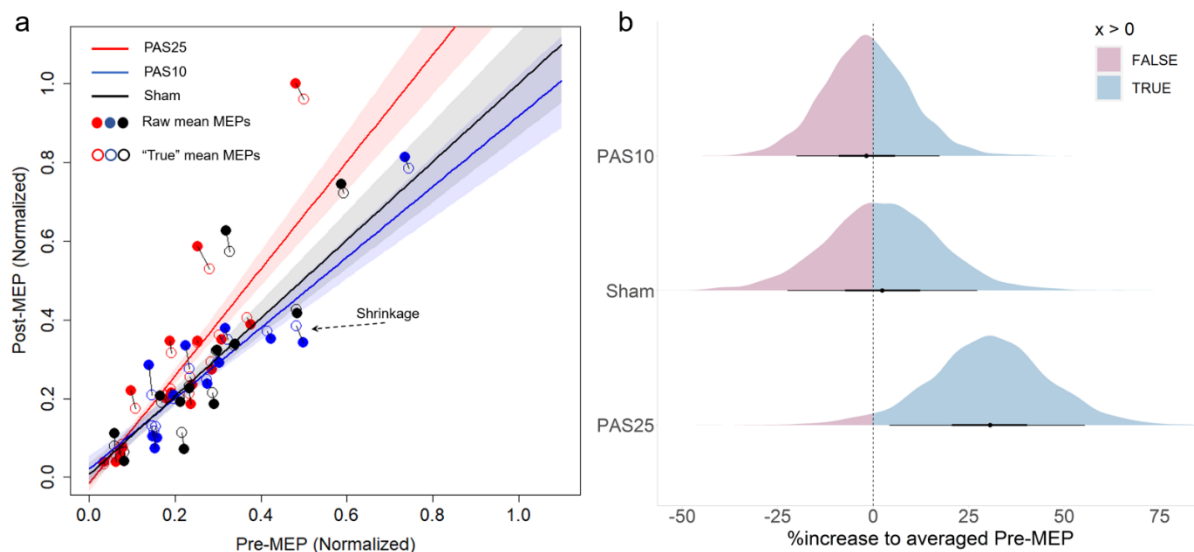


Fig.7.7 PAS effects on cortical excitability. a) the regression lines of each intervention estimated by the mean of intercept and slope from the corresponding posterior distribution, PAS25 (red), PAS10 (blue) and sham (black). Pre- and post-PAS MEP amplitudes were normalized by dividing by the global maximum amplitude of all 80 MEP values. Shadow areas represent the 50% interval estimated from the posterior distribution of the regression parameters. Solid points correspond to pairs of averaged pre-/post-PAS MEP amplitudes over all trials of each specific Run. Empty points represent the 'true' amplitude of the corresponding pre-/post-PAS MEP pair estimated using the proposed hierarchical Bayesian Model#1. The black bar connecting each solid point to the corresponding empty point illustrates the shrinkage process of Bayesian inference of the hierarchical model; b) Posterior predictive simulations of post-PAS MEP amplitudes obtained when considering a given pre-PAS MEP amplitude of 1mV as input, corresponding to the averaged pre-PAS MEP amplitude over all 40 Sessions. The blue area represents the probability of obtaining a relative increase (in %) for the post-PAS MEP amplitude when compared to the pre-PAS MEP amplitude, whereas the pink area represents the probability of obtaining a relative decrease (in %). The black dot represents the median of each posterior distribution, and the surrounding bars show the corresponding 50% and 90% credibility intervals.

Fig.7.8 presents the effects of simulating different pre-PAS MEP amplitudes as inputs, on the relative change of post-PAS MEP amplitude for each intervention, at the group level. For both PAS25 and PAS10, the higher the pre-PAS MEP amplitude was, the higher the relative change in MEP amplitude was. In further details, PAS25 resulted in an increase of post-PAS MEP amplitude of $+26.2\% \pm 15.7\%$ ($Prob = 0.95$), $+31.4\% \pm 15.1\%$ ($Prob = 0.97$), $+33.5\% \pm 17.7\%$ ($Prob = 0.96$) and $+33.9\% \pm 18.7\%$ ($Prob = 0.95$) when considering an input pre-PAS MEP amplitude of 0.6mV, 1.2mV, 2.2mV and 2.8mV respectively. Similarly, PAS10 resulted in an increase of post-PAS MEP amplitude of $+4.2\% \pm 18.9\%$ ($Prob = 0.59$), when considering an input pre-PAS MEP amplitude of 0.6mV, followed respectively by decreases of $-3.1\% \pm 10.5\%$ ($Prob = 0.62$), $-6.5\% \pm 12.6\%$ ($Prob = 0.70$) and $-7.51\% \pm 13.8\%$ ($Prob = 0.71$) when considering an input pre-PAS MEP amplitude of 1.2mV, 2.2mV and 2.8mV. This important finding of our proposed Bayesian Model#1 suggests that even without increasing the TMS stimulation intensity during PAS, simply increasing the spTMS intensity considered to measure changes in excitability can reveal the expected PAS effects more clearly, while reducing some variability in the data. On the other hand, when assessing this effect on sham, we obtained similar distributions of relative changes in post-PAS MEP amplitude, all symmetric around 0%, consisting in relative changes of 4.6%, 2.0%, 0.6% and 0.2%, when considering a pre-PAS MEP amplitude

of 0.6mV, 1.2mV, 2.2mV and 2.8mV, respectively. Importantly, the higher the pre-PAS MEP amplitude was, the closer to 0% the median of relative change in post-PAS MEP amplitude was. Overall, when considering pre-PAS MEP amplitude of 0.2mV for each intervention, we found a large level of uncertainty in spTMS responses, suggesting that small MEP amplitude induced by spTMS should be avoided when assessing the level of brain excitability.

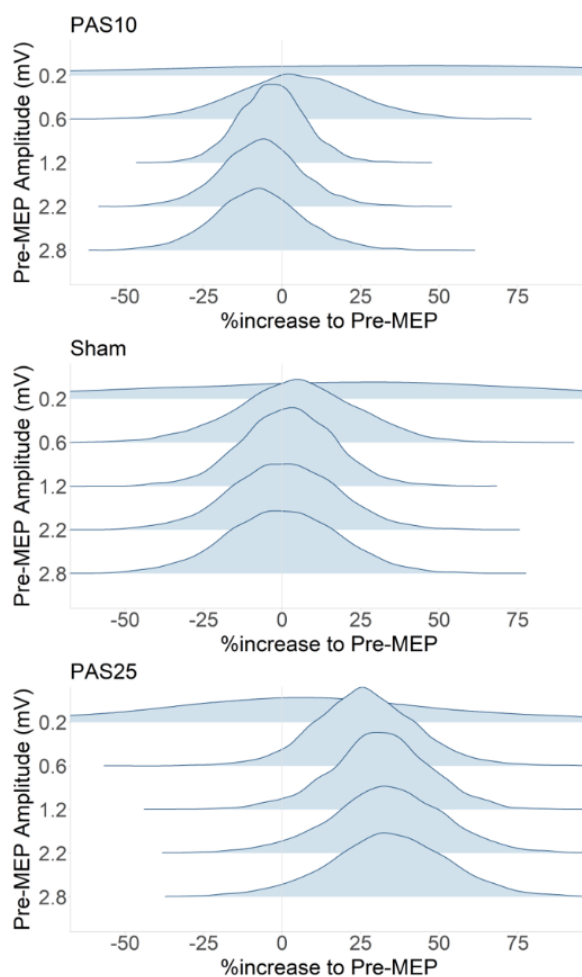


Fig.7.8 Effects of spTMS intensity on PAS assessment. We used posterior predicting simulations applied to five levels of pre-PAS MEP amplitudes, to evaluate the impact of five levels spTMS intensities. Posterior distributions of the corresponding relative changes in post-PAS MEP amplitude relative to pre-PAS MEP amplitudes are presented in each row. The expected effects of PAS25 (positive % increase) and PAS10 (negative % decrease) became clearer when increasing the spTMS intensity. On the other hand, when considering the sham intervention, we found no effect of relative changes in post-PAS MEP amplitude, exhibited at all intensity levels, as well as symmetric distributions around 0%.

7.3.4 PAS effects on task-related HbO/HbR responses

Fig.7.9 showed the PAS effects on the whole time course HbO/HbR, as a contrast (i.e., subtraction of posterior distributions) between the intervention of interest (PAS25 or PAS10) and sham condition. When considering the group level averaged pre-PAS HbO/HbR responses (normalized to $[-1, 1]$) as input for posterior predictive simulations (dashed red and blue curves for HbO and HbR), we observed that PAS25 (Fig.7.9a) resulted in a relative increase of HbO amplitude (solid red curve) and HbR amplitude (solid blue curve), mainly around the expected peak of the hemodynamic response (from 8s to 16s). When comparing absolute peak amplitudes, the probability of increasing the hemodynamic response after PAS25 was 80% for HbO response and 82% for HbR response. After PAS10 (Fig.7.9b), our results are suggesting at the group level a subtle relative decrease of HbO and HbR absolute amplitudes around the peak of the hemodynamic response. The probability of obtaining a relative decrease in absolute peak amplitudes after PAS10 was 66% for HbO response and 48% for HbR response. Interestingly, PAS10 demonstrated a clear absolute amplitude decrease within a period ranging from the peak to the end of the response (11s to 25s) for both HbO and HbR.

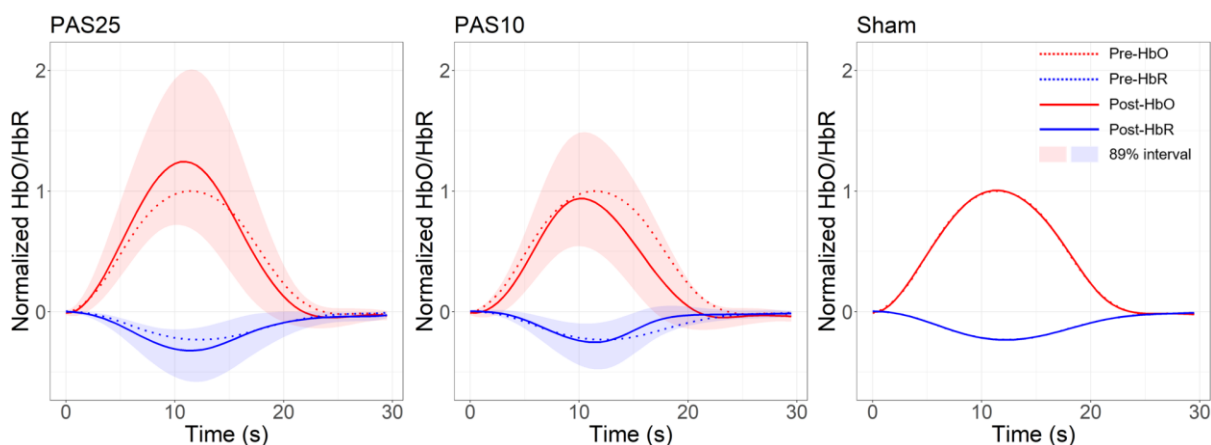


Fig.7.9 PAS effects on the whole time course of HbO/HbR. Posterior predictive simulations of post-PAS HbO/HbR time course (solid curves: HbO in red and HbR in blue) when considering pre-PAS HbO/HbR template input defined as the group-level averaged pre-PAS HbO/HbR response (normalized to $[-1, 1]$) over all 40 Sessions (dash curves). The shadow area represents the 89% credibility interval of resulted post-PAS HbO/HbR responses. Note that sham effects were subtracted from the PAS25 and PAS10 to obtain so-called ‘unbiased’ effects. The overlappings of lines in the sham panel are shown as a sanity check of the contrast.

7.3.5 Relationship between PAS effects on task-related cortical hemodynamic activity and PAS effects on M1 excitability

Fig.7.10a presents inferences on the relationship between PAS effects on task-related cortical hemodynamic activity and PAS effects on M1 excitability, represented by the posterior distribution of correlations between the slope of MEP amplitudes (post-PAS versus pre-PAS) and the slope of spline weight w_5 (post-PAS versus pre-PAS) for either HbO or HbR task-related responses. Since our previous observations of the PAS effects were conducted for the whole HbO/HbR time course (Fig.7.9), we selected w_5 as the spline weight of interest considering it corresponded to the spline basis function exhibiting a peak at 12.5s, therefore consisting in the closest temporal pattern when compared to the expected hemodynamic response. The probability of obtaining a positive correlation between PAS effects on MEP amplitude and PAS effects on HbO response was 77%; and 79% for a positive correlation between PAS effects on MEP amplitude and PAS effects on HbR response. The corresponding 89% highest posterior density interval (HPDI) of this correlation was [-0.26, 0.89] for HbO; and [-0.20, 0.84] for HbR. Fig.7.10b presents the linear fits between the averaged $slope_{[s]}^{MEP}$ and the averaged $slope_{[s]}^{Hb(w_5)}$ obtained for each Session s among all 40 Sessions. The corresponding estimated Pearson's correlation was 0.58 for MEP vs. HbO ($p < .0001$, $CI_{95\%} = [0.33, 0.75]$) and 0.56 for MEP vs. HbR ($p < .001$, $CI_{95\%} = [0.30, 0.74]$).

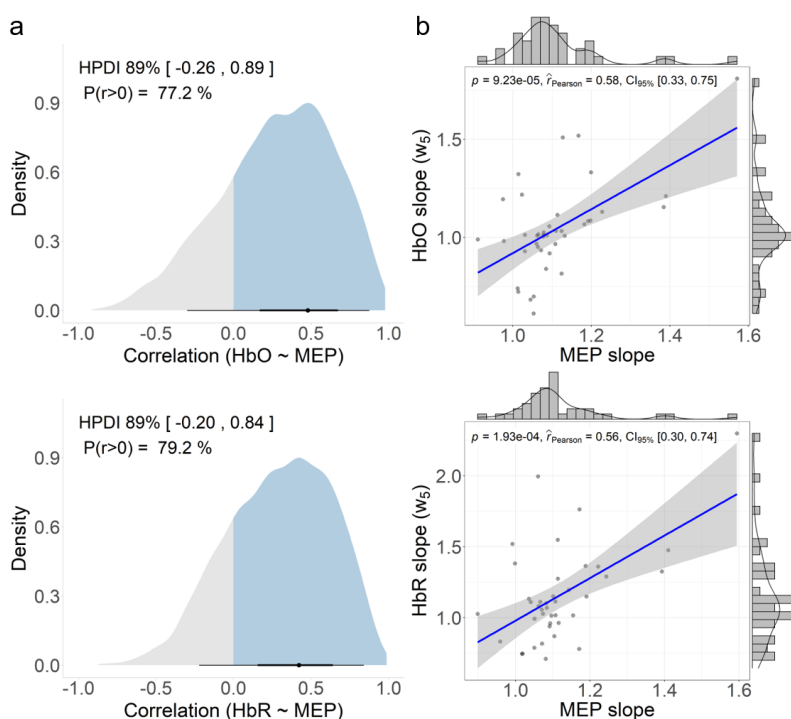


Fig.7.10 The relationship between task-related cortical hemodynamic activity and M1 excitability. a) the posterior distribution of the correlation between $\text{slope}_{[s]}^{\text{MEP}}$ and $\text{slope}_{[s]}^{\text{Hb}(w_5)}$ for HbO (top) and HbR (bottom). The blue area represents the probability of observing a positive correlation ($\rho > 0$). The black dot represents the median of each posterior distribution, and the surrounding bars show the corresponding 50% and 90% credibility intervals. b) Linear fit (blue line) between the averaged $\text{slope}_{[s]}^{\text{MEP}}$ and the averaged $\text{slope}_{[s]}^{\text{Hb}(w_5)}$ obtained for all 40 sessions (each represented by a grey dot). The grey area indicates the 95% confidence interval of the regression. Estimated Pearson's correlation between $\text{slope}_{[s]}^{\text{MEP}}$ and $\text{slope}_{[s]}^{\text{Hb}(w_5)}$ over the 40 sessions together with corresponding p-values and 95% confident intervals are shown on top of each panel. The marginal histograms and fitted density functions are shown on the side of each corresponding marginal axis.

Fig.7.11 illustrates the posterior distribution of the correlation between $\text{slope}_{[s]}^{\text{MEP}}$ and $\text{slope}_{[s]}^{\text{Hb}(w_n)}$, when considering each spline weight for $n = 2,3,4,5,6,7$ and 8. The closer the corresponding peak of the spline basis function associated with the weight w_n was to the expected peak of the HbO/HbR response, the higher the correlation between $\text{slope}_{[s]}^{\text{MEP}}$ and $\text{slope}_{[s]}^{\text{Hb}(w_n)}$ was. In further details, the median of these correlation values was respectively -0.05, 0.13, 0.28, 0.31, 0.13, -0.10 and 0.01 when considering $w_{n=2,3,4,5,6,7,8}$ for HbO; and a median value of 0.06, 0.17, 0.31, 0.32, 0.15, -0.06 and 0.03 when considering $w_{n=2,3,4,5,6,7,8}$ for HbR, therefore confirming this trend. Our results are suggesting that the expected positive correlation between PAS effects on task-related hemodynamic response and PAS effects on M1 excitability appeared mostly around the peak of HbO/HbR time course (e.g., w_5), in agreement with PAS effects reported previously in Fig.7.9. On the other hand, for the earliest aspects of the hemodynamic response (modeled using $w_{2,3}$) as well as for the end of the response (modeled using $w_{7,8}$), we found a posterior correlation with a median close to zero, suggesting no relationship between $\text{slope}_{[s]}^{\text{MEP}}$ and $\text{slope}_{[s]}^{\text{Hb}(w_n)}$ for the corresponding time periods.

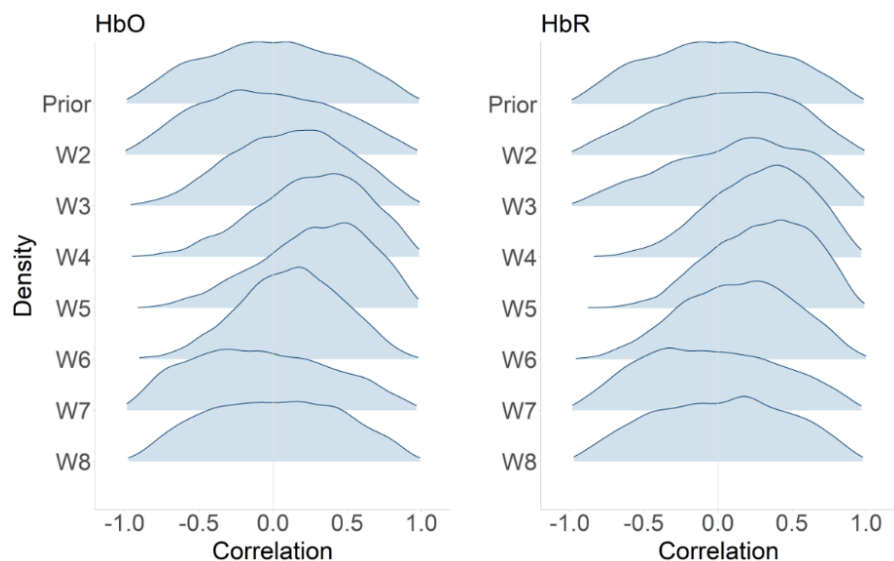


Fig. 7.11 Posterior distributions of the correlations between $\text{slope}_{[s]}^{\text{MEP}}$ and several selected $\text{slope}_{[s]}^{\text{Hb}(w_n)}$.

The posterior distribution of the correlation between $\text{slope}_{[s]}^{\text{MEP}}$ and $\text{slope}_{[s]}^{\text{Hb}(w_n)}$, when considering each spline weights for $n = 2, 3, 4, 5, 6, 7$ and 8 for HbO (left) and for HbR (right). The prior distribution of the correlation (i.e., LKJ(2)) on the first row demonstrates a perfect symmetric to the 0 correlation. There was a trend showing the closer the corresponding peak of the spline basis function associated with the weight w_n was to the expected peak of the HbO/HbR response, the higher the correlation between $\text{slope}_{[s]}^{\text{MEP}}$ and $\text{slope}_{[s]}^{\text{Hb}(w_n)}$ was. w_5 showed the highest correlation values for both HbO and HbR as it corresponded to the spline basis function exhibiting the peak at 12.5s, therefore the closest temporal pattern when compared to the expected hemodynamic response. In contrast, the earliest aspects of the hemodynamic response (modeled using $w_{2,3}$) and the end of the response (modeled using $w_{7,8}$), showed almost identical distributions when comparing to the prior.

7.4. Discussion

7.4.1 PAS effects on cortical excitability

Using hierarchical Bayesian modeling, we first investigated PAS effects on cortical excitability, which was measured using MEP amplitude induced by spTMS. Probability distributions of the relative changes (in %) of post-PAS MEP amplitudes when compared to pre-PAS MEP amplitudes were estimated using posterior predictive simulations. Our results showed a substantial increase of MEP amplitude after PAS25, a subtle decrease after PAS10 and no changes after control (sham). These results are consistent with previous PAS studies (Stefan, 2000; Wolters *et al.*, 2005b; Tsang,

Bailey and Nelson, 2015; Lee *et al.*, 2017; Suppa *et al.*, 2017). These studies considered conventional MEP analysis, calculating the ratio between the averaged MEP amplitude after PAS over the one before PAS. Therefore, when MEP ratio was larger than 1, it indicated an excitability increase and vice versa. In contrast, here we applied for the first time a full Bayesian workflow using an advanced sampling algorithm. The benefits of this procedure are: 1) multivariate linear regression allowed the differentiation of interventions and subjects, hence modeling the heterogeneity of intervention effects exhibited in different groups of data; 2) involving intercept in linear regression reduced the influences of low MEP amplitudes Runs when compared to the conventional ratio calculation of post- over pre-PAS MEPs; 3) the variability of MEP amplitudes were considered in the estimation of the PAS effects rather than only using the averaged amplitudes of each Run and ignore the variance; 4) parameters of the model were estimated by Bayesian inferences using dynamic HMC algorithm sampling posterior distributions using a hierarchical structure and weakly informed priors, therefore, allowing partial pooling to reduce the estimation uncertainty; 5) flexible and intuitive statistical inferences of the modeled PAS effects were obtained by conducting posterior predictive simulations from the model learned from the data. This means by giving any pre-PAS MEP amplitude and intervention index, the distribution of the corresponding group-level post-PAS MEP amplitude could be estimated; Finally, 6) the estimated PAS effects were reliable and informative, as suggested by their posterior probability distributions, rather than considering only a statistical significance test providing a binary output. Moreover, our model also allowed inferring the effects of MEP amplitude itself on the effect size of the resulted excitability changes modulated by PAS. In Fig.7.8, we reported a pattern suggesting that the higher the MEP amplitude was, the larger was the effect size of both PAS25 and PAS10. This pattern was not biased when comparing to the sham session, which showed no effects for different pre-PAS MEP amplitudes. It is important to mention that when considering posterior predictive simulation, the intensity of the TMS pulse during the intervention session (PAS25 or PAS10 or sham) did not change. This means the underlying intervention effects did not change. Then considering spTMS as the assessment procedure to measure brain excitability, our results are suggesting that a high enough spTMS intensity might help to measure more accurately PAS effects.

7.4.2 PAS effects on the whole HbO/HbR time course of finger tapping responses

To our best knowledge, our study demonstrated for the first time PAS effects on the whole time course of task-related HbO/HbR time courses. In contrast, few time segments along selected time windows were considered in previous studies, then HbO or HbR amplitudes were just averaged within each time segment and compared before and after interventions (Chiang *et al.*, 2007; Yamanaka *et al.*, 2010). In our previous study (Chapter 6), we also simply averaged the HbO/HbR amplitude within a 5s long time window centred around the peak of the hemodynamic response to represent the total amount of hemoglobin delivered to the region of interest. The Bayesian approach proposed in this study brings more insights into the investigation of PAS effects on hemodynamics, considering not only the peak amplitude before and after interventions, but whole HbO/HbR time courses. For instance, visual inspections of results presented in Fig.7.9 are suggesting that PAS effects are indeed more pronounced around the peak of the expected hemodynamic response. This is expected if we can assume that the hemodynamic response function (HRF) is not much affected by interventions, then the expected task-related hemodynamic response would result from a convolution with a higher or lower amplitude boxcar function representing excited or inhibited neuronal activity patterns (Sotero and Trujillo-Barreto, 2007). Therefore, the effect of intervention should appear mostly around the peak, and the closer to the peak the higher the effect size. Consequently, averaging HbO or HbR amplitude within a certain time window would ‘dilute’ the estimation of the effect of interest, especially when considering the effect size was not large, for instance around 25% increase for HbO after PAS25 is shown in Fig.7.9.

The fact that PAS intervention effects could be observed mainly around the peak of hemodynamic time courses may also explain the difficulty of investigating similar questions using fMRI. Indeed, a typical BOLD signal is sampled around 0.5Hz using standard fMRI sequences. Such low temporal resolution may not be sufficient to sample well the effects around the peak and could possibly explain why no PAS effects were found on BOLD signal changes in the PAS and fMRI study reported by Krivánková *et al.*, 2013. Besides, depending on how well fMRI BOLD samples and the actual peak of the hemodynamic response are phased-locked, the mismatch between the time of BOLD signal sampling and the actual peak of the response may introduce some confounds, when comparing BOLD signal changes before and after PAS interventions. Another benefit of modeling accurately the whole HbO/HbR time course is the possibility to offer alternative interpretations of PAS effects. For instance, our results in Fig.7.9 showed a slight time shift for

HbO after PAS25 and a larger one after PAS10 (e.g., the peak time of HbO shifted from 12s to 10s after PAS10). The decrease of HbO amplitudes after PAS10 was also mainly exhibited from 11s to 25s of the response time course. These observations may suggest a more complex mechanism of the effect of neuronal plasticity on neurovascular coupling. Further analysis using the deconvolution technique (Machado *et al.*, 2021) to estimate HRFs that are related to these hemodynamic responses may help us to better investigate such a potential mechanism but it is beyond the scope of this study.

It is important to mention that we did not perform a specific analysis for every time sample of the hemodynamic response. We regularized and reduced the dimensionality of the problem by projecting HbO/HbR responses on B-splines as temporal basis functions. Therefore, PAS effects on hemodynamic were modeled by only 10 weights instead of 60 data points, whereas the actual post-PAS HbO/HbR time courses could then be fully retrieved from the estimated weights and the spline basis functions. The choice of the number and locations of knots might have limited the ‘resolution’ of our proposed correlation analysis. There are more advanced Bayesian spline approaches, such as the penalized spline (P-spline) (Eilers and Marx, 2010; Ventrucchi and Rue, 2016), which introduces an extra prior to regularize the number of effective knots. This approach was mainly designed to smooth a time course and prevent overfitting rather than considering an accurate representation of the time course. Non-parametric time series modeling techniques were also proposed in this context, without assuming the location of the knots along the time course. For instance, Gaussian process regression (Neal, 1998) characterizes the time course, such as the hemodynamic response, as an unknown function. Samples of the time course are then drawn from a multinormal distribution providing a full covariance matrix of all time samples. Our analysis could benefit from these non-parametric approaches to avoid eventual limitations associated with the choice of the knots, but this was beyond the scope of this study.

It is also worth noting that these results of PAS effects on the whole HbO/HbR time courses were also benefiting from accurate time courses estimated by our previously proposed fNIRS reconstruction workflow (Chapter 5). In this workflow, the fNIRS acquisition montage was personalized and the detection sensitivity of it was maximized to the individual ROI. Meanwhile, the MEM framework adapted from our previous works in the context of electro-/magneto-encephalogram source imaging (Chowdhury *et al.*, 2013, 2016; Grova *et al.*, 2016; Heers *et al.*, 2016; Hedrich *et al.*, 2017; Pellegrino *et al.*, 2020) for conducting fNIRS reconstruction (Cai *et*

al., 2021) also ensured accurate estimation of HbO/HbR time courses from reconstructed spatiotemporal maps. For instance, delays between HbO and HbR peak times were around 1s shown in Fig.7.9, which is consistent with our previous finding (Chapter 5) and fNIRS literature (Jasdzewski *et al.*, 2003; Steinbrink *et al.*, 2006).

7.4.3 Relationship between PAS effects on task-related hemodynamic and PAS effects on M1 excitability

We also investigated for the first time the relationship between PAS effects on task-related hemodynamic activity and PAS effects on cortical excitability along the whole HbO/HbR time course. When compared to standard frequentist analysis of the correlation between $slope_{[s]}^{MEP}$ and $slope_{[s]}^{Hb(w_n)}$ reported in Fig.7.10b, our proposed Bayesian analysis was more informative since we could estimate the whole posterior distribution of such a correlation, instead of providing a single correlation value estimated from the mean effects while ignoring the variance. Even if the sample size was not large and we acknowledge the influences from large variability of PAS effects and variability of task-evoked hemodynamic responses, our proposed hierarchical Bayesian models were able to demonstrate a high probability of positive correlations between MEP and hemodynamic slopes (representing the PAS effects), around the peak of HbO and HbR responses. This finding is consistent with previous results reported in animal studies, suggesting a positive correlation between hemodynamic responses and cortical excitability. For instance, Allen *et al.*, 2007 demonstrated decreased oxygenations in anesthetized cat's visual cortex after applying inhibitory rTMS; increased fMRI resting-state connectivity, GABA, glutamine and glutamate levels after performing excitatory rTMS. Reduced connectivity and glutamine levels after applying inhibitory rTMS on healthy rat's right hemisphere were reported by Seewoo *et al.*, 2019. The reliability of our proposed model was further confirmed by the fact that no correlation was found between PAS effects on MEP and hemodynamic responses, when considering other time windows, such as the initial aspects and the end of the hemodynamic response. The further the analyzed time period was to the expected hemodynamic peak, the closer to the prior was to the posterior distribution of the correlation, with no preference on either positive or negative correlations.

7.4.4 HMC sampling and diagnostic

Taking advantage of dynamic HMC to sample the hierarchical Bayesian models in this study, we were able to carefully diagnose the pathological behaviour of MCMC sampling chains

(Betancourt, 2017, 2019). This diagnostic procedure is an essential step when applying Bayesian data analysis (Gelman *et al.*, 2020). To allow accurate and reliable inferences, MCMC chains must explore well the typical set of the posterior distributions, in which most of the probability density is contained. For instance, the convergence of MCMC chains needs to be confirmed and quantified to ensure such full explorations. When inappropriate parameters of the chain are chosen (e.g., the step size), abnormalities such as divergences should be detected to avoid eventual sampling biases. In our study, we reported several diagnostic statistics for all key components of three models using both visualization and quantified metrics, following the recommendations of the Stan team (Gelman *et al.*, 2013b; Gabry *et al.*, 2019; Stan Development Team, 2020b). The proposed diagnostic statistics considered here also constitute a unique feature of HMC sampling, when compared to conventional MCMC algorithms such as Gibbs sampling (Geman and Geman, 1984; Gelfand and Smith, 1990). HMC is also considered to be more accurate by taking advantage of sampling all parameters at the same time, comparing to Gibbs that often samples parameters alternatively one after the other which may bias the resulted posterior distribution due to the inherent correlations between parameters. Overall, the diagnostic analysis of the sampling process in this study is suggesting that our inferences are built upon well-sampled posterior distributions, reasonably accurate and unbiased. Similar HMC sampling and diagnostic approaches were also reported in several recent studies, such as a Bayesian virtual epileptic patient to model the spread of epileptic activity (Hashemi *et al.*, 2020); a Bayesian latent spatial model for mapping biomarkers of the progression of Alzheimer's disease (Dai *et al.*, 2021); the Bayesian multilevel modeling to improve statistical inferences in fMRI analysis (Chen, Bürkner, *et al.*, 2019; Chen, Xiao, *et al.*, 2019; Chen *et al.*, 2021) and a hierarchical Bayesian model to investigate mechanisms of reinforcement learning and decision-making (Ahn, Haines and Zhang, 2017).

7.4.5 Limitations and perspectives

While the Bayesian approach is known to improve the uncertainty of statistical inferences when dealing with small samples data set, as illustrated by our results, there is no doubt that this study would benefit from a larger sampling size. Conventional frequentist power analyses (Bhalerao and Kadam, 2010) could estimate the minimum number of samples required to obtain a significant effect for a statistical power such as 80%. When considering the standard deviation of MEP amplitudes and fMRI BOLD signals reported in PAS (López-Alonso *et al.*, 2014) and in fMRI literature (Krivánková *et al.*, 2013), we estimated that when assuming random sampling, at least

50 subjects would be required for MEP analysis and more than 100 subjects would be required for hemodynamic analysis using fMRI BOLD. Despite the inherent limitation of power analysis which may underestimate the sample size (Gelman and Carlin, 2014), in practice, it is challenging to conduct acquisitions with this amount of subjects especially considering all three different interventions.

We only involved one model for each investigation in this study. It is indeed recommended to construct multiple models based on different hypotheses of the same question and then quantitatively compare these models using techniques such as cross-validation to choose the most reliable one, providing a trade-off between overfitting and underfitting (Gelman *et al.*, 2020). For instance, we proposed a linear relationship between cortical excitability and hemodynamic responses evoked by a finger-tapping task. However, such association might reach a plateau when excitability changes are either too low or too high, suggesting some non-linear models. Moreover, the neurovascular system includes different aspects like excitatory and inhibitory neurons, glial cells, the vasculature components like pericytes (Populations, 2017). The interaction between inhibitory and excitatory neurons, the glial cell mediated signalling pathways, and their role in neurovascular coupling have been simplified in this linear model. A more detailed metabolism model involving blood flow dynamics (Buxton, 2021) may improve our inferences by comparing it with the model proposed in this study. Considering such advanced model comparisons, applied within a Bayesian framework, could be of great interest but was out of the scope of this study. Moreover, we conducted TMS following the recommendations of the International Federation of Clinical Neurophysiology (Rossi *et al.*, 2009), which means our data set should not explore extreme conditions between excitability and hemodynamic response, which are more likely to exhibit eventual nonlinear relationships.

Another limitation of our study was that the M1 excitability was not assessed at the same time as the finger-tapping task, but sequentially, hence we did not propose a fusion model to pool the relationship between cortical excitability and hemodynamic responses at the single-trial level. We indeed considered the mean and variance of MEP amplitudes and HbO/HbR time courses within the whole Session as the input for the correlation analysis. This might reduce the resulted correlation values considering additional fluctuations of the baseline excitability and hemodynamic responses. However, since it has been shown that PAS modulated excitability changes could last for more than 30 minutes (Stefan, 2000; Lee *et al.*, 2017), we are confident that

our investigation of cortical excitability using MEP after spTMS and hemodynamic response elicited by finger tapping was indeed still within this PAS effective duration window.

As perspectives for this study, it would be of great interest to investigate the relationship between spTMS evoked HbO/HbR and the corresponding MEP amplitude, when occurring exactly at the same time, therefore, preventing confounds introduced by fluctuations of excitability and hemodynamic responses along the time. Such an investigation may help us in understanding the integrity of neurovascular coupling during the transit cortical excitability change induced by spTMS. Furthermore, the effect of stable cortical excitability changes (induced by PAS) on this integrity can be explored by comparing the spTMS evoked hemodynamic responses before and after PAS interventions. Additionally, since fNIRS data were recorded during the whole experiments (i.e., also during spTMS and PAS intervention), our data would allow assessing dynamically the evolution of MEP and hemodynamic responses during PAS. However, such analysis would require modeling fNIRS response using advanced deconvolution techniques to handle the overlapping of TMS pulses induced hemodynamic responses (Machado *et al.*, 2021), and will be considered in our future investigations.

7.5 Conclusion

In this study, we proposed for the first time hierarchical Bayesian modeling to investigate the relationship between motor task-related hemodynamic responses and M1 excitability. When compared with sham control condition, a substantial M1 excitability increase was found after PAS25 and a subtle reduction of M1 excitability was found after PAS10. PAS effects on motor task-related hemodynamic responses were observed mainly around the peak of HbO/HbR time courses. We showed a large probability of positive correlations between PAS effects on MEP amplitudes and hemodynamic responses. Such correlations were also mainly exhibited around the peak of HbO/HbR time courses. Diagnostics of sampling MCMC chains showed no pathological behaviour, ensuring the reliability of our results. Finally, this study also demonstrated the power of the Bayesian data analysis when dealing with relatively high variability and small sample size data while providing informative inferences.

7.6 Supplementary material

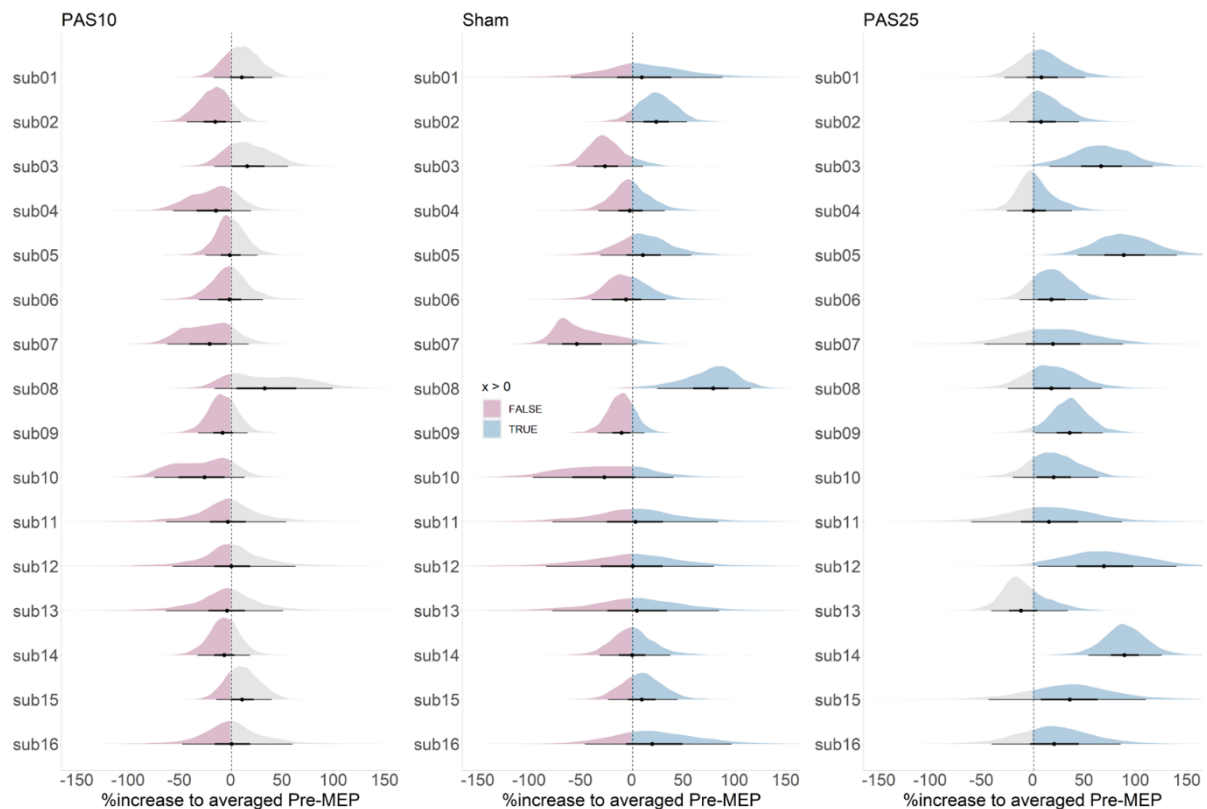


Fig.7.S1 PAS effects on M1 excitability at the individual level. Each column presents the individual level posterior distribution of the intervention effect from PAS10, sham and PAS25, respectively. Posterior predictive simulations of post-PAS MEP amplitudes were conducted by assuming the same pre-PAS MEP amplitude for all subjects, i.e., the averaged pre-PAS MEP amplitude obtained for all subjects over all 40 Sessions. The blue area represents the probability of obtaining a relative increase (in%) for the post-PAS MEP amplitude when compared to the pre-PAS MEP amplitude, whereas the pink area represents the probability of obtaining a relative decrease (in %). The black dot represents the median of each posterior distribution, and the surrounding bars show the corresponding 50% and 90% credibility intervals. Overall, large between-subject variability can be observed for both interventions. Note that missing Sessions were also included using posterior predictive simulations within the model, based on prior distributions and partial pooled information from other Sessions.

Chapter 8

General Discussion

8.1 Summary of main contributions and limitations

The main objective of this thesis was to develop and evaluate a “*personalized Near Infra-Red Optical Tomography (NIROT) workflow*” and to apply it to investigate the cortical hemodynamic activity associated with cortical excitability modulated by Paired Associative Stimulation (PAS). This thesis involves both methodological developments and their applications. The following sections will discuss the contributions and limitations of each study reported in this thesis.

8.1.1 Development and evaluation of MEM framework for NIROT

In Chapter 4, the Maximum Entropy on the Mean (MEM) framework, previously proposed in the context of EEG/MEG source localization (Amblard, Lapalme and Lina, 2004; Grova, Daunizeau, *et al.*, 2006; Chowdhury *et al.*, 2013), was *adapted and improved for conducting NIROT* (Cai *et al.*, 2021, submitted). We also applied a generalized implementation of depth weighting from EEG/MEG field to NIROT. For the first time, we successfully integrated depth-weighting into the MEM framework and showed the ability of this new MEM approach to reconstruct hemodynamic generators with different depths of the underlying generators. Moreover, we comprehensively investigated the role of depth weighting in NIROT using different parameter values for both MEM and the widely used reconstruction method - Minimum Norm Estimate (MNE). We pointed out that depth weighting could indeed control the effective field of view of NIROT. Regarding temporal accuracy, we showed that even if MEM is a nonlinear method not optimized for accurate estimation of the time courses of the generators, our proposed new MEM initialization in Chapter 4, provided similar temporal accuracy when compared to MNE linear method. This result was very important, especially in our subsequent studies investigating the time delay between HbO and HbR finger tapping responses, and even more when investigating changes in hemodynamic time courses elicited by excitability modulation using TMS. Regarding robustness and reliability of MEM reconstruction, we emphasized the importance of evaluating the method with realistic simulations, especially when in the context of source reconstruction techniques, ground truth is lacking. We

conducted 4,000 simulations with different depths and sizes. Based on our simulation results, we are confident that our proposed MEM method for NIROT is exhibiting better source reconstruction performance, when compared to widely used MNE, especially when dealing with low signal to noise ratio (SNR) signals. However, we would like to disclose several limitations in this first study. **First**, even when considering realistic simulations, simulations can only represent a simplified version of the underlying problem. Therefore, simulation studies are necessary, but could not be sufficient to evaluate our methodology for real fNIRS data applications. Hence a follow-up study was to further validate our proposed method on real data acquired under a well-controlled paradigm. This overall strategic approach of validating a reconstruction method using simulated data first, followed by applying it to real data is recommended for the evaluation of source imaging in similar fields (Kavuri *et al.*, 2012; Shimokawa *et al.*, 2012, 2013a; Chowdhury *et al.*, 2013, 2016; Tremblay *et al.*, 2018; Pellegrino *et al.*, 2020). **Second**, several fNIRS reconstruction studies (Yamashita *et al.*, 2016b; Wheelock, Culver and Eggebrecht, 2019) also considered mixed linear models to disentangle brain fNIRS responses from extra-cerebral superficial layers signals (skin and muscle layers). Such an approach is promising to integrate denoising processes with the reconstruction procedure which may further improve its accuracy. In this first study, we only considered short channel regression to remove the superficial layer's noise, whereas more advanced approaches could be considered in our future studies. **Finally**, as reviewed in Chapter 1, there are many other reconstruction methods proposed for NIROT in the literature, including several linear methods using different regularization approaches such as the ℓ_1 – norm (Matsuura and Okabe, 1995; Lu, Lighter and Styles, 2018) and the ℓ_0 – norm (Mohimani, Babaie-Zadeh and Jutten, 2009; Prakash *et al.*, 2014) extensions of MNE, as well as non-linear methods such as a hierarchical Bayesian approach (Shimokawa *et al.*, 2013a; Yamashita *et al.*, 2016b). It would be of great interest to compare MEM with these methods, but this was out of the scope of our proposed study.

8.1.2 Evaluation and application of the personalized NIROT workflow using MEM

For the second evaluation step, when assessing new reconstruction methodology by applying it to real data, it is recommended to consider relatively well-controlled tasks for which we have some good knowledge on underlying brain activity, such as finger tapping (Yamashita *et al.*, 2016b), visual tasks (Zeff *et al.*, 2007; Eggebrecht *et al.*, 2012) and median nerve stimulations (Huppert *et*

al., 2017). The rationale is that the underlying cortical activations associated with these well-controlled tasks are well known, and a ‘ground truth’ can then be obtained by applying the same task with other neuroimaging techniques, for instance using fMRI investigations. In Chapter 5, *we extended our previous work on MEM NIROT reconstruction to further evaluate our method using well-controlled finger tapping data acquired using fNIRS*. For the first time, we also integrated several methodologies developed in the lab to propose a workflow entitled *personalized NIROT using MEM, combining personalized fNIRS sensor layout to maximize light sensitivity to targeted brain regions and accurate local NIROT using MEM*. In this second study, considering fMRI Z-maps as our reference for evaluation, reconstruction performances were quantitatively evaluated using well-defined validation metrics proposed in our previous studies (Chowdhury *et al.*, 2013; Hedrich *et al.*, 2017). Doing so, we introduced a carefully designed approach to extract true positive and true negative regions from fMRI activation maps, considering the known within-subject variability of the main fMRI activation cluster (Zandbelt *et al.*, 2008; Quiton *et al.*, 2014), exploiting fMRI inference at the group level to more accurately defined the true positive region at the individual level. Furthermore, to compare reconstruction performances between MEM and MNE, we adapted to this approach, the Area Under the Receiver Operating Characteristic Curve (AUC) calculation, previously introduced for EEG/MEG source imaging (Grova, Daunizeau, *et al.*, 2006; Chowdhury *et al.*, 2013). These adaptations in our way to define fMRI reference at the individual level were not considered in previous literature (Yamashita *et al.*, 2016b), in which only significant regions from individual-level fMRI maps were used as the ground truth. Our results showed that MEM provided more accurate reconstructed spatial maps than MNE, when compared to fMRI reference. Improved spatial accuracy of MEM when compared to MNE was then further confirmed, considering the whole HbO/HbR reconstructed time courses, rather than assessing hemodynamic responses only at the peak of corresponding time courses. Furthermore, we revealed that even when reconstructed maps were additionally spatially thresholded to force them to be focal, MEM still outperformed MNE. Regarding temporal accuracy of reconstructed time courses, MEM provided a similar temporal accuracy to MNE.

Importantly, we demonstrated the ability of both MEM and MNE to recover the peak time delay between the reconstrued time courses of HbO and HbR, in agreement with the literature (Jasdzewski *et al.*, 2003; Steinbrink *et al.*, 2006). Additionally, we further demonstrated that MEM

provided reliable reconstructions quantitatively assessed with validation metrics (e.g., AUC, SD and Dmin), whereas discriminability of those metrics over bootstrap resampled task-evoked hemodynamic responses was considered to assess the reliability (M. Yu *et al.*, 2018; Wang *et al.*, 2020). The reliability evaluation result is important to support our initial hypothesis that this personalized NIROT workflow was indeed designed to improve the reliability of fNIRS technique when measuring the human brain hemodynamics, from acquisition planning to local 3D reconstruction. **Firstly**, subject-specific anatomical MRI (e.g., 1mm isotropic T1- and T2-weighted images) was used to promote accurate head modeling. To further improve the reliability of head modeling, we considered both T1- and T2-weighted images to ensure accurate tissue segmentation, whereas most published studies in either EEG/MEG or fNIRS source imaging typically consider only T1-weighted MRI for this task. **Secondly**, Novi *et al.*, (2020) suggested that taking into account spatial information of fNIRS montage improves fNIRS reproducibility. We used a neuronavigation system to guide the installation and digitization of fNIRS sensors and also to add around 150 extra head points in order to further improve the accuracy of the co-registration procedure. It is worth noting that most fNIRS studies use standard head caps which are not specific to each subject's head anatomy, and fNIRS detection sensitivity is not optimized based on the underlying anatomy of each individual. The installation of caps is usually based on few head fiducials, and the locations of optodes are also rarely digitized. Hence, errors associated with cap installation and co-registration will result in less reliability of fNIRS measurements and localization results. **Thirdly**, we applied a long jittering between task events as suggested by Aarabi, Osharina and Wallois, 2017, in order to minimize the systemic blood circulation introduced “physiological noise”, which shares a similar frequency range with the expected hemodynamic fluctuations. Although we thoroughly investigated the reliability using within-subject variability estimated from a resampling technique, we also acknowledge that it would be preferable to conduct this evaluation with a well-designed test-retest reliability study. Additionally, since fMRI and fNIRS acquisitions were not performed simultaneously, between-scan task performance variability including the influence of processes like attention or arousal (Novi *et al.*, 2020), might also cause some potential differences between NIROT and fMRI images.

8.1.3 Application of personalized NIROT workflow on a simultaneous PAS/fNIRS study

In Chapter 6, we applied the personalized NIROT using MEM workflow to investigate hemodynamic correlates of fluctuations in neuronal excitability. ***This work pushed the challenge on our workflow to a new level, since the goal was to find the hemodynamic activity changes before and after the brain stimulation modulated cortical excitability, rather than only simply quantifying the response to the task.*** Therefore, our objective requires the whole workflow to be highly sensitive to small fluctuations of hemodynamic signals that are related to neuronal excitability changes, and in the meantime to be substantially accurate and reliable to report less false-positive localizations. The contributions of this work can then be discussed from two perspectives. Firstly, ***from a scientific perspective***, our study was, to the best of our knowledge, the first one investigating the relationship between cortical excitability and hemodynamic activity using simultaneous PAS-fNIRS in humans. We achieved two main results: 1) fluctuations of cortical excitability were positively correlated with fluctuations of hemodynamic responses to the finger-tapping task when pooling results from all interventions; 2) there was also a linear relationship between the effects of PAS on excitability and hemodynamic activity when considering sessions exhibiting concordant PAS effects on MEP, HbO and HbR. This study further confirms the feasibility of simultaneous fNIRS and PAS to investigate the relationship between cortical excitability and hemodynamic processes. Moreover, the fact that we demonstrated PAS effects were impacting hemodynamic activity within the same region, is relevant for the application of non-invasive brain stimulation techniques for the treatment of neuropsychiatric disorders. This means that PAS may be applied to therapeutic approaches in which modulation of hemodynamic response is required. Finally, the tight link between excitability and hemodynamic activity may suggest that the effect on hemodynamics might also be monitored via the standard spTMS technique. Secondly, ***from a methodological perspective***, the findings reported in this study are illustrating the ability of our workflow in detecting small hemodynamic fluctuations after excitability modulations. Although it is difficult to compare our findings with a similar study conducted using fMRI (Kriváneková *et al.*, 2013), we actually showed the expected trend of hemodynamic activity after the intervention, whereas in their fMRI study, Kriváneková *et al.*, (2013) showed unpredictable BOLD fluctuations following PAS interventions. It is also worth noting that we proposed here for the first time a resampling technique allowing us to extract reliable and robust HbO/HbR estimations from fNIRS reconstructions. Especially, this strategy was suitable to consider the variability of these underlying hemodynamic responses, instead of

using only one averaged response among all trials. Our proposed methodology using bootstrap resampling can be further applied to other general fNIRS applications to improve the reliability of fNIRS results. However, some limitations remained for this study. **Firstly**, we only focused on finger tapping responses before/after intervention and not to fNIRS responses elicited by spTMS. Since the finger tapping was not performed at the same time as spTMS, this may bring some variability into the correlation analysis due to background fluctuations of the excitability and hemodynamic responses themselves. **Secondly**, this study was small sample-sized ($n=16$), and this might have ended up reducing the statistical power. Based on the conventional power analysis (Bhalerao and Kadam, 2010) considering the variances of MEP and fMRI BOLD signal reported in PAS literature (López-Alonso *et al.*, 2014) and fMRI study (Kriváneková *et al.*, 2013), at least 50 subjects would be required to expect significant ($p<.05$, power of 80%) group-level inferences on PAS effect measured by MEP ratios, and at least few hundreds of subjects would be necessary for an expected significant fMRI BOLD changes after the PAS intervention. Despite the validity of power analysis that has been questioned in the statistical field (Gelman and Carlin, 2014), conducting our experiment with the sample size estimated by the above power analysis would have been practically quite challenging, given the complexity of the paradigms. **Thirdly**, MEPs have been commonly used to assess cortical excitability, but it is not a direct measurement as it also involves confounds like spinal cord excitability (Suppa *et al.*, 2017). Although it is still under debate, more direct measurements such as scalp EEG response at the time of spTMS might be a better candidate for assessing TMS-induced cortical activity (Kimiskidis, 2016; Tremblay *et al.*, 2019). **Finally**, although we performed a resampling technique to extract more reliable MEP and HbO/HbR measures, the variance of them was not directly involved in the analysis but only the final arithmetic mean.

8.1.4 Application of probabilistic modeling (Bayesian data analysis) to investigate the correlation between task-related hemodynamic responses and neuronal excitability.

In the previous study, we reported the expected trend of correlation between task-related hemodynamic responses and cortical excitability. However, *we acknowledge that variabilities on both fNIRS measured task response and MEP representing PAS effects were not directly involved in data analysis.* Variability is often discussed in the literature but rarely directly involved in the analysis. Therefore, we revisited data analysis from the previous study, this time considering

the inter-/intra-subject variability on both brain stimulation-induced cortical excitability and task-related hemodynamic responses. We proposed hierarchical Bayesian models to investigate: 1) PAS effects on M1 excitability; 2) PAS effects on the whole-time course of task-related hemodynamic responses, and 3) the correlation between them. The rationale to apply hierarchical models was that the so-called “involvement of variability in the analysis” is all about modeling the heterogeneity of the variables of interest (e.g., MEP, HbO/HbR) exhibited at each stage of analysis and each nest of data. Hierarchical models are known to be good candidates to encode inter-/intra-subject heterogeneity. However, constructing an appropriate model does not guarantee accurate estimations and the implementation of hierarchical models is rather complicated. It is known in the statistics field, but not so well recognized in the neuroimaging field yet, that hierarchical model may intrinsically cause model identifiability issues (term used in frequentist statistics) or degeneracy issues (term used in Bayesian statistics), which require a more sophisticated model solver, otherwise, the final estimation might be biased (Papaspiliopoulos, Roberts and Sköld, 2007). More importantly, the model solver has to provide sufficient diagnostic statistics to validate the reliability of estimation results, especially considering the fact that hierarchical models usually introduce hyperparameters which results in a complex geometry of the parameter space that is difficult to fully explore without special care. Fortunately, the dynamic HMC (Betancourt, 2017) implemented in Stan (Stan Development Team, 2020b) fulfills the above strict but essential requirements. Hence, we applied this technique to solve the models proposed in Chapter 7. Bayesian data analysis has been used in the neuroimaging field, but the methodologies proposed in most of the literature were mainly based on the previous generation Bayesian techniques, therefore suffering from criticisms regarding accuracy, validity, reliability, and computation cost (see Chapter 3). We introduced and applied here, for the first time, the latest developments of Bayesian data analysis workflow in the field of fNIRS. To our best knowledge, even when considering the whole neuroimaging field, only a few recent studies have considered similar techniques (Ahn, Haines and Zhang, 2017; Chen, Bürkner, *et al.*, 2019; Chen, Xiao, *et al.*, 2019; Hashemi *et al.*, 2020; Chen *et al.*, 2021; Dai *et al.*, 2021). Taking advantage of this approach, we found correlations of PAS effects on excitability and hemodynamic activity without requiring to constrain the data for concordance of PAS effects on MEP, HbO, and HbR as was the case in our first analysis proposed in Chapter 6. This last complementary study is therefore supports and extends our findings and interpretations. We also demonstrated PAS effects on the whole

HbO/HbR time-courses of task-related hemodynamic. As expected, PAS effects on task-related HbO/HbR changes before and after interventions mainly occurred around the peak amplitude, which was consistent with the correlation findings showing the relationship between hemodynamic activity and cortical excitability only exhibited around the peak amplitude of HbO/HbR. Finally, we also showed that PAS effects on cortical excitability can be more pronounced when assessing excitability with higher intensity for spTMS, without changing the stimulation intensity of the intervention per se. In terms of limitations, we only involved one model for each investigation in this study. It is usually recommended to conduct multiple models and then quantitatively compare them using techniques such as cross-validation to choose the most reliable model that achieves an appropriate trade-off between overfitting and underfitting (Vehtari, Gelman and Gabry, 2017). Similar to the limitations reported in Chapter 6, we only focused on finger tapping responses in fNIRS, which were not performed at the same time as spTMS. This may bring potential confounds to the correlation analysis, and may explain the reason why the correlation values we found were overall not very high.

8.2 Future directions

8.2.1 Upgrading NIROT workflow using a hybrid montage containing both locally optimized montage and global fNIRS measurements

Literature has shown that fNIRS signal contains not only cortical hemodynamic signals but also components from systemic physiological fluctuations (Scholkmann, Kleiser, *et al.*, 2014; Tachtsidis and Scholkmann, 2016). Although short channel regression could reduce the influence of such physiological noise exhibited on scalp measurements (Zeff *et al.*, 2007; Gregg *et al.*, 2010), the resulting fNIRS signals remain uncleaned. Studies using global averaged fNIRS signal (Haeussinger *et al.*, 2014) or applying a principal component spatial filter algorithm (Zhang, Noah and Hirsch, 2016; Zhang *et al.*, 2017) have shown the ability to further remove remaining physiological noise exhibited in the brain. We hypothesize that combining these two measures (short channel and global averaged fNIRS signal) will provide more accurate cortical hemodynamic response estimations. Therefore, inspired by our pilot work on simultaneous high-density EEG/fNIRS, in which we installed a 256-channel high-density EEG cap on top of an optimal montage (see Fig8.1a and b), *we propose a new approach that would combine standard fNIRS cap/patch on top of a glued personalized optimal montage (see Fig8.1c and d)*. This

hybrid montage should take advantage of personalized optimal montage to prioritize the fNIRS sensitivity to the targeting ROI, as well as sampling sufficient hemodynamic fluctuations from other head regions, providing a more accurate estimate of global systemic fluctuations in the brain and superficial layers. Eventually, this hybrid montage would sample systemic physiological fluctuations using: 1) local short-distance channels from personalized optimal montage; 2) global short distance channels distributed along the standard fNIRS cap; 3) global conventional distance (3cm) channels distributed along the standard fNIRS cap. Whereas a whole head fNIRS cap would also measure the above three components, this hybrid montage should preserve the advantage of optimal montage to maximize the probing ability for specific ROIs. In practice, additional extra acquisition preparation time would just take about 10 to 20 minutes for additional standard cap/patch installation. Additionally, the noise components estimated from this hybrid montage can be used as nuisance regressors within a GLM framework (von Lühmann, Li, *et al.*, 2020; von Lühmann, Ortega-Martinez, *et al.*, 2020) or treated as instrumental variables to regularize the hidden noise model in a more advanced Bayesian framework (see the next subsection). Finally, it is also of great interest to apply personalized NIROT workflow using currently available wearable high-density fNIRS devices (Zhao *et al.*, 2021), such as the LUMO fNIRS neuroimaging ecosystem (<https://www.gowerlabs.co.uk/lumo>) in which fNIRS layout can be customized to the individual subject and a high-density montage can improve the fNIRS reconstruction accuracy (White, 2010).

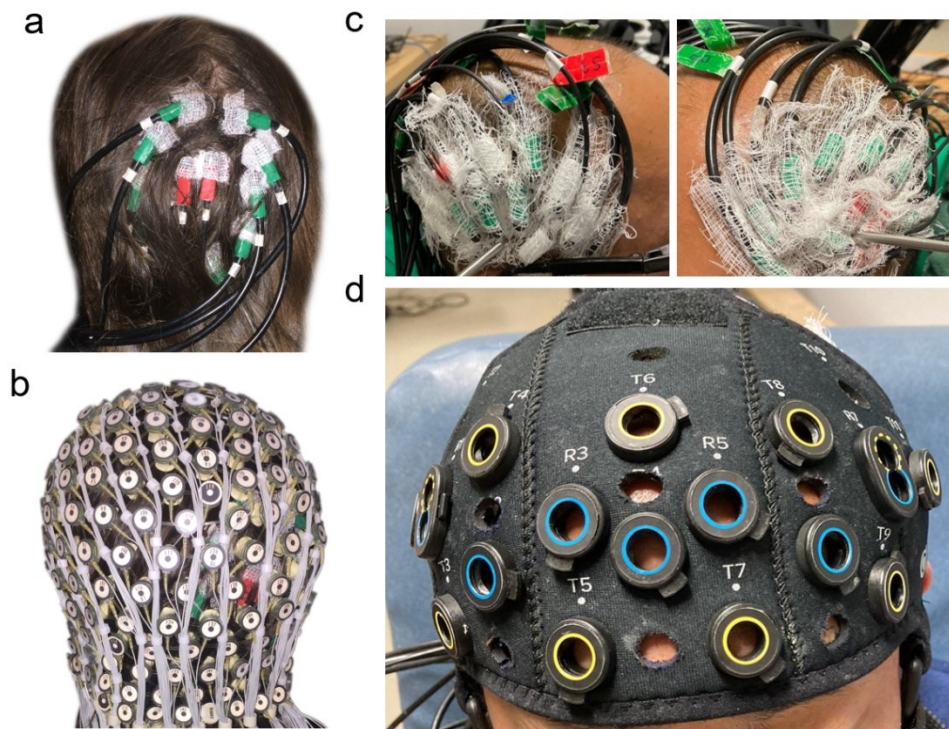


Fig.8.1 Demonstration of a possible hybrid montage. a) personalized optimal fNIRS montage targeting the right visual cortex. b) a 256 channels high-density EEG cap covered on top of fNIRS montage for a pilot concurrent EEG/fNIRS study. c) the personalized optimal fNIRS montage targeting the left and the right auditory cortex, combining local short-distance channels for sampling the physiological noise exhibited in the scalp and optimized channels probing the ROI, d) example of a standard fNIRS cap/patch applied on top of a personalized optimal montage to measure the global physiological noise exhibited in both scalp and cortex.

8.2.2 Assessment of the integrity of neurovascular coupling at the time of transient discharges evoked by TMS under the stable cortical excitability changes modulated by PAS

This perspective will extend the work presented in Chapter 6 and Chapter 7 by further investigating the correlation between MEP and spTMS induced fNIRS fluctuations, instead of finger tapping response. This investigation will benefit from the fact that the spTMS and hemodynamic measurement are time-locked, so that the variability of baseline excitability fluctuation on the correlation analysis would then be experimentally controlled. However, this approach will bring other methodological challenges, since the spTMS session should be considered as an event-related design with temporally overlapped hemodynamic responses. This requires a deconvolution method (Machado *et al.*, 2021) to estimate the Hemodynamic Response Function (HRF) from the

fNIRS data acquired during spTMS. Considering the goal is to investigate not only the HRF of spTMS but also the integrity of neurovascular coupling during each single TMS pulse, the analyzing methodology should also be able to “decode” the amplitude of each neuronal stimuli during the stimulation event from the fNIRS signal alone. Such analysis would give us a unique opportunity to investigate how changes in cortical excitability are learned during PAS intervention per se. Eventually, the decoded stimulus amplitudes from the fNIRS signal alone (representing the neuronal activity estimated from fNIRS alone by assuming the convolution model) will be compared with the MEP amplitudes (representing the transient neuronal response to each spTMS). If these two sequences of amplitude are correlated, it will indicate the integrity of the neurovascular coupling at the time of transient discharges evoked by spTMS. Such a promising investigation would shed light on underlying mechanisms linking TMS and hemodynamic responses associated either to neuronal activity or to local changes in HbO/HbR concentrations elicited by contracting vessels at the time of TMS pulses. One concurrent fMRI/TMS study showed expected BOLD signal fluctuations varying along with different stimulation intensities (Navarro de Lara *et al.*, 2017), but a recent similar study claimed no BOLD signal changes during TMS (Rafiei *et al.*, 2021). A well-designed fNIRS/TMS study argued that the TMS “evoked” hemodynamic responses reported previously in fNIRS studies may be largely biased by the contribution of vessel contractions, when considering that similar TMS induced fNIRS responses were found on the shoulder and on the head (Näsi *et al.*, 2011). Our proposed methodology could provide a unique way to investigate this challenging problem. If the two sequences of amplitude are correlated, we could prove that TMS indeed evokes a hemodynamic response. This considers the fact that the intensity of spTMS used in our experimental protocol is constant (same “dose” for each spTMS), but the neuronal response (indirectly represented by MEP) to spTMS is varying due to the background fluctuations of cortical plasticity. If TMS only changes HbO/HbR concentrations by vessel contraction, the decoded stimuli amplitude from fNIRS data alone should be consistent, assuming no plasticity associated with TMS-induced vessel contraction per se.

This model can also be applied to the fNIRS/PAS data to further investigate two questions. **First**, studying fNIRS fluctuations during spTMS before and after PAS is actually investigating the hemodynamic responses evoked by transit excitability changes (by spTMS) on top of stable excitability changes (by PAS). This study reproduces a “healthy model of an epileptic condition”.

Patients with focal epilepsy show transit excitability increases, in the form of transient epileptiform discharges and seizures (Badawy *et al.*, 2010), occurring on top of stable augmented excitability (Badawy *et al.*, 2007; Tombini *et al.*, 2013). Such excitability impairment may have a hemodynamic correlate, hence allowing us to tune and investigate stable and phasic changes of brain excitability and associated hemodynamic responses. **Second**, we can investigate the development of plasticity and the corresponding hemodynamic responses during PAS intervention per se. This study would bring insights into understanding the mechanism of PAS especially considering its effects on hemodynamic activity.

In practice, we would propose a new HRF deconvolution model, in which physiological noise can be estimated from short distance channels using the temporally embedded canonical correlation analysis (von Lühmann, Li, *et al.*, 2020; von Lühmann, Ortega-Martinez, *et al.*, 2020) and then applied it as an instrumental variable to regularize the hidden noise model. The HRF can be modeled by the Gaussian process (Neal, 1998) which can conveniently encode the assumption on the smoothness of HRF and will estimate the whole covariance matrix of the HRF itself. The amplitude of each event stimuli can be modeled as parameters instead of constant values as assumed in the conventional GLM analysis. As conducted in Chapter 7, to provide reliable estimations, the model could be solved by dynamic HMC (Betancourt, 2017) in Stan (Stan Development Team, 2020b). Preliminary results of this proposed method are presented in Fig.8.2. Using realistic simulations, we are able to first accurately estimate the HRF and then decode the stimuli amplitudes, providing a correlation of 0.8 between the estimated stimuli amplitude to the ground truth based on simulations. Finally, this technique can be further applied to our fNIRS related studies. For instance, we could use it for the application of simultaneous EEG/fNIRS in the assessment of the epileptic focus during awake and sleep conditions. This could help us to assess the pathological condition, especially on hemodynamic activity, at the time of transient EEG discharges in epilepsy. We could also use it to investigate the impact of external auditory stimulations on sleep, using a personalized simultaneous EEG with fNIRS during whole night recordings. Hemodynamic responses evoked by event-related designed auditory stimulations can be estimated and further compared under different sleep stages.

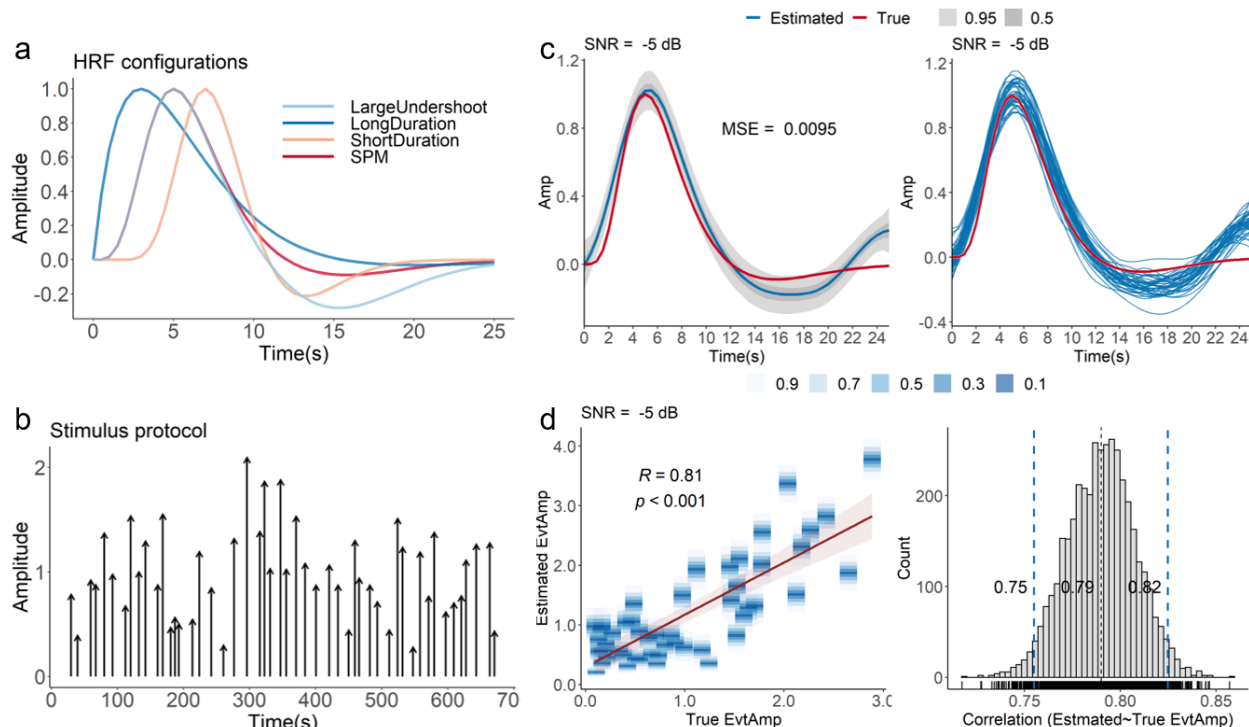


Fig.8.2 Preliminary results of the proposed method for deconvolution of HRF and estimation of stimuli amplitudes. a) four HRF configurations used for realistic simulations, b) realistic stimulus protocol that is randomly sampled from TMS/fNIRS data during spTMS, both times and amplitudes of 50 events are extracted from a randomly selected slice among 75 MEPs during a randomly selected spTMS run among the whole data set. c) estimated HRFs (blue) when compared with the ground truth (red), each blue line in the right figure shows a possible HRF that supports the model and data, estimated by Bayesian framework, d) the linear regression between estimated stimuli amplitudes and the ground truth stimuli amplitudes, the histogram of the corresponding correlation value is shown on the right side.

8.3 Conclusion

In the first part of this thesis, we developed a new fNIRS reconstruction method using the MEM framework and integrated it with personalized optimal montage, therefore proposing a new personalized NIROT workflow. The MEM reconstruction method was carefully validated using realistic simulations considering different hemodynamic generator locations, sizes, and depths. The personalized NIROT workflow was evaluated using a well-controlled motor task and compared with the fMRI activation map as the reference. Our results showed that the proposed methodology provided more accurate spatial reconstruction maps and similar temporal accuracy when compared to the widely used approach – MNE. More importantly, we demonstrated the

reliability of our MEM performance results, as well as its robustness when dealing with low SNR fNIRS signals. Following these methodological developments and evaluations, we applied the proposed workflow to the investigation of the relationship between hemodynamic activity and cortical excitability using the simultaneous fNIRS and PAS technique. We found a considerable positive association between the fluctuations of cortical excitability and the fluctuations of hemodynamic responses to the finger tapping task. A positive linear relationship between PAS effects on cortical excitability and hemodynamic activity was also illustrated by our advanced analysis method using the Bayesian data analysis. These studies validated the feasibility of simultaneous fNIRS and PAS technique, and demonstrated that PAS effects on hemodynamic activity are relevant for the application of non-invasive brain stimulation techniques for the treatment of neuropsychiatric disorders. Our findings may contribute to further expanding the field of non-invasive brain stimulation application for treating brain disorders by targeting those areas for which a modulation of hemodynamic activity is desired. Overall, this thesis involved both methodological developments and the corresponding applications. It contributed to the relevant field in both scientific and methodological perspectives.

Bibliography

- Aarabi, A., Osharina, V. and Wallois, F. (2017) ‘Effect of confounding variables on hemodynamic response function estimation using averaging and deconvolution analysis: An event-related NIRS study’, *NeuroImage*, 155(February), pp. 25–49. doi: 10.1016/j.neuroimage.2017.04.048.
- Aasted, C. M. *et al.* (2015) ‘Anatomical guidance for functional near-infrared spectroscopy: AtlasViewer tutorial’, *Neurophotonics*, 2(2), p. 020801. doi: 10.1117/1.NPh.2.2.020801.
- Abdelnour, F., Genovese, C. and Huppert, T. (2010) ‘Hierarchical Bayesian regularization of reconstructions for diffuse optical tomography using multiple priors.’, *Biomedical optics express*, 1(4), pp. 1084–1103. doi: 10.1364/BOE.1.001084.
- Abrahamyan, A. *et al.* (2011) ‘Improving visual sensitivity with subthreshold transcranial magnetic stimulation’, *Journal of Neuroscience*, 31(9), pp. 3290–3294. doi: 10.1523/JNEUROSCI.6256-10.2011.
- Ah Sen, C. B. *et al.* (2017) ‘Active and resting motor threshold are efficiently obtained with adaptive threshold hunting’, *PLoS ONE*, 12(10). doi: 10.1371/journal.pone.0186007.
- Ahmed, M. H., Ghatge, M. S. and Safo, M. K. (2020) ‘Hemoglobin: Structure, Function and Allostery’, in *Physiology & behavior*, pp. 345–382. doi: 10.1007/978-3-030-41769-7_14.
- Ahn, W.-Y., Haines, N. and Zhang, L. (2017) ‘Revealing Neurocomputational Mechanisms of Reinforcement Learning and Decision-Making With the hBayesDM Package’, *Computational Psychiatry*, 1(0), p. 24. doi: 10.1162/cpsy_a_00002.
- Allen, E. A. *et al.* (2007) ‘Transcranial magnetic stimulation elicits coupled neural and hemodynamic consequences’, *Science*, 317(5846), pp. 1918–1921. doi: 10.1126/science.1146426.
- Allison, T. *et al.* (1991) ‘Potentials evoked in human and monkey cerebral cortex by stimulation of the median nerve: A review of scalp and intracranial recordings’, *Brain*, 114(6), pp. 2465–2503. doi: 10.1093/brain/114.6.2465.
- Amblard, C., Lapalme, E. and Lina, J. M. (2004) ‘Biomagnetic Source Detection by Maximum Entropy and Graphical Models’, *IEEE Transactions on Biomedical Engineering*, 51(3), pp. 427–442. doi: 10.1109/TBME.2003.820999.
- Aoyama, Y. *et al.* (2009) ‘Stimulus intensity dependence of cerebral blood volume changes in left frontal lobe by low-frequency rTMS to right frontal lobe: A near-infrared spectroscopy study’, *Neuroscience Research*, 63(1), pp. 47–51. doi: 10.1016/j.neures.2008.10.003.
- Arai, N. *et al.* (2007) ‘Differences in after-effect between monophasic and biphasic high-frequency rTMS of the human motor cortex’, *Clinical Neurophysiology*, 118(10), pp. 2227–2233. doi: 10.1016/j.clinph.2007.07.006.
- Arridge, S. R. *et al.* (1993) ‘A finite element approach for modeling photon transport in tissue’, *Medical Physics*, 20(2), pp. 299–309. doi: 10.1118/1.597069.
- Arridge, S. R. (1999) ‘Optical tomography in medical imaging’, *Inverse Problems*, 15(2), p. R41. doi: 10.1088/0266-5611/15/2/022.
- Arridge, S. R. (2011) ‘Methods in diffuse optical imaging’, *Philosophical Transactions of the*

- Royal Society A: Mathematical, Physical and Engineering Sciences*, 369(1955), pp. 4558–4576. doi: 10.1098/rsta.2011.0311.
- Attias, H. (1999) ‘Inferring Parameters and Structure of Latent Variable Models by Variational Bayes’, in *15th Conference on Uncertainty in Artificial Intelligence*. Morgan-Kaufman, pp. 21–30. Available at: <http://arxiv.org/abs/1301.6676>.
- Avigdor, T. *et al.* (2021) ‘Fast oscillations ≥ 40 Hz localize the epileptogenic zone: An electrical source imaging study using high-density electroencephalography’, *Clinical Neurophysiology*, 132(2), pp. 568–580. doi: 10.1016/j.clinph.2020.11.031.
- Awiszus, F. *et al.* (1999) ‘Characterisation of paired-pulse transcranial magnetic stimulation conditions yielding intracortical inhibition or I-wave facilitation using a threshold-hunting paradigm’, *Experimental Brain Research*, 129(2), pp. 317–324. doi: 10.1007/s002210050901.
- Aydin, Ü. *et al.* (2020) ‘Magnetoencephalography resting state connectivity patterns as indicatives of surgical outcome in epilepsy patients’, *Journal of Neural Engineering*, 17(3), p. 35007. doi: 10.1088/1741-2552/ab8113.
- Badawy, R. A. B. *et al.* (2007) ‘Changes in cortical excitability differentiate generalized and focal epilepsies’, *Annals of Neurology*, 61(4), pp. 324–331. doi: 10.1002/ana.21087.
- Badawy, R. A. B. *et al.* (2010) ‘Predicting seizure control: Cortical excitability and antiepileptic medication’, *Annals of Neurology*, 67(1), pp. 64–73. doi: 10.1002/ana.21806.
- Bale, G., Elwell, C. E. and Tachtsidis, I. (2016) ‘From Jöbsis to the present day: a review of clinical near-infrared spectroscopy measurements of cerebral cytochrome-c-oxidase’, *Journal of Biomedical Optics*, 21(9), p. 091307. doi: 10.1117/1.JBO.21.9.091307.
- Bandettini, P. A. *et al.* (1992) ‘Time course EPI of human brain function during task activation’, *Magnetic Resonance in Medicine*, 25(2), pp. 390–397. doi: 10.1002/mrm.1910250220.
- Barker, A. T., Jalinous, R. and Freeston, I. L. (1985) ‘Non-Invasive Magnetic Stimulation of Human Motor Cortex’, *The Lancet*, 325(8437), pp. 1106–1107. doi: 10.1016/S0140-6736(85)92413-4.
- Bauernfeind, G. *et al.* (2014) ‘Separating heart and brain: On the reduction of physiological noise from multichannel functional near-infrared spectroscopy (fNIRS) signals’, *Journal of Neural Engineering*, 11(5). doi: 10.1088/1741-2560/11/5/056010.
- Beer (1852) ‘Bestimmung der Absorption des rothen Lichts in farbigen Flüssigkeiten’, *Annalen der Physik und Chemie*, 162(5), pp. 78–88. doi: 10.1002/andp.18521620505.
- Bert, P. (1878) *La pression barométrique: recherches de physiologie expérimentale*. G. Masson.
- Betancourt, M. (2016) ‘Diagnosing Suboptimal Cotangent Disintegrations in Hamiltonian Monte Carlo’, *arXiv 1604.00695*. Available at: <http://arxiv.org/abs/1604.00695>.
- Betancourt, M. (2017) ‘A Conceptual Introduction to Hamiltonian Monte Carlo’, *eprint arXiv:1701.02434*, p. 60. doi: <https://arxiv.org/abs/1701.02434>.
- Betancourt, M. *et al.* (2017) ‘The geometric foundations of Hamiltonian Monte Carlo’, *Bernoulli*, 23(4A), pp. 2257–2298. doi: 10.3150/16-BEJ810.
- Betancourt, M. (2019) ‘The Convergence of Markov Chain Monte Carlo Methods: From the

- Metropolis Method to Hamiltonian Monte Carlo', *Annalen der Physik*, 531(3), pp. 1–6. doi: 10.1002/andp.201700214.
- Betancourt, M. and Girolami, M. (2015) 'Hamiltonian Monte Carlo for Hierarchical Models', *Current Trends in Bayesian Methodology with Applications*, pp. 79–101. doi: 10.1201/b18502-5.
- Betancourt, M. J. and Girolami, M. (2013) 'Hamiltonian Monte Carlo for Hierarchical Models', *arXiv 1312.0906*. <http://arxiv.org/abs/1312.0906>.
- Bhalerao, S. and Kadam, P. (2010) 'Sample size calculation', *International Journal of Ayurveda Research*, 1(1), p. 55. doi: 10.4103/0974-7788.59946.
- Bienenstock, E. L., Cooper, L. N. and Munro, P. W. (1982) 'Theory for the development of neuron selectivity: Orientation specificity and binocular interaction in visual cortex', *Journal of Neuroscience*, 2(1), pp. 32–48. doi: 10.1523/jneurosci.02-01-00032.1982.
- Blackmore, J. *et al.* (2019) 'Ultrasound Neuromodulation: A Review of Results, Mechanisms and Safety', *Ultrasound in Medicine and Biology*, 45(7), pp. 1509–1536. doi: 10.1016/j.ultrasmedbio.2018.12.015.
- Bliss, T. V. P. and Lomo, T. (1973) 'Long-lasting potentiation of synaptic transmission in the dentate area of the anaesthetized rabbit following stimulation of the perforant path', *The Journal of Physiology*, 232(2), pp. 331–356. doi: 10.1113/jphysiol.1973.sp010273.
- Bliss, T. V. and Lomo, T. (1970) 'Plasticity in a monosynaptic cortical pathway.', *The Journal of physiology*, 207(2), p. 61P. Available at: <http://www.ncbi.nlm.nih.gov/pubmed/5511138> (Accessed: 31 January 2021).
- Bloch, F. (1946) 'Nuclear induction', *Physical review*, 70(7–8), p. 460.
- Boas, D. A., Brooks, D. H., *et al.* (2001) 'Imaging the body with diffuse optical tomography', *IEEE Signal Processing Magazine*, 18(6), pp. 57–75. doi: 10.1109/79.962278.
- Boas, D. A., Gaudette, T., *et al.* (2001) 'The accuracy of near infrared spectroscopy and imaging during focal changes in cerebral hemodynamics', *NeuroImage*, 13(1), pp. 76–90. doi: 10.1006/nimg.2000.0674.
- Boas, D. A. *et al.* (2002a) 'Three dimensional Monte Carlo code for photon migration through complex heterogeneous media including the adult human head', *Optics Express*, 10(3), p. 159. doi: 10.1364/OE.10.000159.
- Boas, D. A. *et al.* (2002b) 'Three dimensional Monte Carlo code for photon migration through complex heterogeneous media including the adult human head', *Optics Express*, 10(3), p. 159. doi: 10.1364/OE.10.000159.
- Boas, D. A. *et al.* (2004a) 'Improving the diffuse optical imaging spatial resolution of the cerebral hemodynamic response to brain activation in humans', *Optics Letters*, 29(13), p. 1506. doi: 10.1364/ol.29.001506.
- Boas, D. A. *et al.* (2004b) 'Improving the diffuse optical imaging spatial resolution of the cerebral hemodynamic response to brain activation in humans', *Optics Letters*, 29(13), p. 1506. doi: 10.1364/OL.29.001506.
- Boas, D. A. and Dale, A. M. (2005) 'Simulation study of magnetic resonance imaging–guided

- cortically constrained diffuse optical tomography of human brain function', *Applied Optics*, 44(10), p. 1957. doi: 10.1364/AO.44.001957.
- Boas, D. A., Dale, A. M. and Franceschini, M. A. (2004) 'Diffuse optical imaging of brain activation: Approaches to optimizing image sensitivity, resolution, and accuracy', in *NeuroImage*. Academic Press, pp. S275–S288. doi: 10.1016/j.neuroimage.2004.07.011.
- Boden, S. *et al.* (2007) 'The oxygenation response to functional stimulation: Is there a physiological meaning to the lag between parameters?', *NeuroImage*, 36(1), pp. 100–107. doi: 10.1016/j.neuroimage.2007.01.045.
- Boor, C. de (2001) *A Practical Guide to Splines - Revised Edition*, Springer-Verlag, New York.
- Botvinik-Nezer, R. *et al.* (2020) 'Variability in the analysis of a single neuroimaging dataset by many teams', *Nature*, 582(7810), pp. 84–88. doi: 10.1038/s41586-020-2314-9.
- Bouguer, P. (1729) 'Essai d'optique, sur la gradation de la lumiere', *Paris, France: Claude Jombert*, pp. 16–22. doi: 10.1259/jrs.1922.0026.
- Braack, E. M. ter, Koopman, A.-W. E. and Putten, M. J. A. M. van (2016) 'Early TMS evoked potentials in epilepsy: A pilot study', *Clinical Neurophysiology*, 127(9), pp. 3025–3032. doi: 10.1016/j.clinph.2016.06.003.
- Bridgeford, E. *et al.* (2018) 'Multiscale Graph Correlation'. doi: 10.5281/ZENODO.1246967.
- Brigadoi, S. *et al.* (2014) 'Motion artifacts in functional near-infrared spectroscopy: A comparison of motion correction techniques applied to real cognitive data', *NeuroImage*, 85, pp. 181–191. doi: 10.1016/j.neuroimage.2013.04.082.
- Brigadoi, S. *et al.* (2018) 'Array Designer: automated optimized array design for functional near-infrared spectroscopy', *Neurophotonics*, 5(03), p. 1. doi: 10.1117/1.nph.5.3.035010.
- Brooks, S. *et al.* (2011) *Handbook of markov chain monte carlo*. CRC press.
- Brooks, S. P. and Gelman, A. (1998) 'General methods for monitoring convergence of iterative simulations', *Journal of Computational and Graphical Statistics*, 7(4), pp. 434–455. doi: 10.1080/10618600.1998.10474787.
- Buxton, R. B. *et al.* (2004) 'Modeling the hemodynamic response to brain activation', *NeuroImage*, 23(SUPPL. 1), pp. 220–233. doi: 10.1016/j.neuroimage.2004.07.013.
- Buxton, R. B. (2012) 'Dynamic models of BOLD contrast', *NeuroImage*, 62(2), pp. 953–961. doi: 10.1016/j.neuroimage.2012.01.012.
- Buxton, R. B. (2021) 'The thermodynamics of thinking: Connections between neural activity, energy metabolism and blood flow: Thermodynamics of thinking', *Philosophical Transactions of the Royal Society B: Biological Sciences*, 376(1815). doi: 10.1098/rstb.2019.0624rstb20190624.
- Cabrerizo, M. *et al.* (2014) 'Induced effects of transcranial magnetic stimulation on the autonomic nervous system and the cardiac rhythm', *Scientific World Journal*, 2014. doi: 10.1155/2014/349718.
- Cai, Z. *et al.* (2021) 'Diffuse optical reconstructions of NIRS data using Maximum Entropy on the Mean', *bioRxiv*, p. 2021.02.22.432263. doi: 10.1101/2021.02.22.432263.

- Cao, N., Nehorai, A. and Jacobs, M. (2007) ‘Image reconstruction for diffuse optical tomography using sparsity regularization and expectation-maximization algorithm’, *Opt Express*, 15(21), pp. 13695–13708. doi: 142886 [pii].
- Cao, T. T. *et al.* (2013) ‘A near infra-red study of blood oxygenation changes resulting from high and low frequency repetitive transcranial magnetic stimulation’, *Brain Stimulation*, 6(6), pp. 922–924. doi: 10.1016/j.brs.2013.04.006.
- Carp, J. (2012) ‘The secret lives of experiments: Methods reporting in the fMRI literature’, *NeuroImage*, 63(1), pp. 289–300. doi: 10.1016/j.neuroimage.2012.07.004.
- Carson, R. G. and Kennedy, N. C. (2013) ‘Modulation of human corticospinal excitability by paired associative stimulation’, *Frontiers in Human Neuroscience*, 7(December), pp. 1–28. doi: 10.3389/fnhum.2013.00823.
- Casula, E. P. *et al.* (2016) ‘Spike-timing-dependent plasticity in the human dorso-lateral prefrontal cortex’, *NeuroImage*, 143, pp. 204–213. doi: 10.1016/j.neuroimage.2016.08.060.
- Chandler, K. E. *et al.* (2003) ‘Plasticity of GABAB Receptor-Mediated Heterosynaptic Interactions at Mossy Fibers after Status Epilepticus’, *Journal of Neuroscience*, 23(36), pp. 11382–11391. doi: 10.1523/jneurosci.23-36-11382.2003.
- Chen, G., Bürkner, P. C., *et al.* (2019) ‘An integrative Bayesian approach to matrix-based analysis in neuroimaging’, *Human Brain Mapping*, 40(14), pp. 4072–4090. doi: 10.1002/hbm.24686.
- Chen, G., Xiao, Y., *et al.* (2019) ‘Handling Multiplicity in Neuroimaging Through Bayesian Lenses with Multilevel Modeling’, *Neuroinformatics*, 17(4), pp. 515–545. doi: 10.1007/s12021-018-9409-6.
- Chen, G. *et al.* (2021) ‘To pool or not to pool: Can we ignore cross-trial variability in FMRI?’, *NeuroImage*, 225(September 2020), p. 117496. doi: 10.1016/j.neuroimage.2020.117496.
- Chen, J. and Intes, X. (2011) ‘Comparison of Monte Carlo methods for fluorescence molecular tomography-computational efficiency’, *Medical Physics*, 38(10), pp. 5788–5798. doi: 10.1118/1.3641827.
- Chen, R. and Seitz, R. J. (2001) ‘Changing cortical excitability with low-frequency magnetic stimulation’, *Neurology*, 57(3), pp. 379–380. doi: 10.1212/WNL.57.3.379.
- Chen, W. L. *et al.* (2020) ‘Functional Near-Infrared Spectroscopy and Its Clinical Application in the Field of Neuroscience: Advances and Future Directions’, *Frontiers in Neuroscience*, 14(July), pp. 1–15. doi: 10.3389/fnins.2020.00724.
- Chiang, T. C. *et al.* (2007) ‘Elevated haemoglobin levels in the motor cortex following 1 Hz transcranial magnetic stimulation: A preliminary study’, *Experimental Brain Research*, 181(4), pp. 555–560. doi: 10.1007/s00221-007-0952-x.
- Chowdhury, R. A. *et al.* (2013) ‘MEG Source Localization of Spatially Extended Generators of Epileptic Activity: Comparing Entropic and Hierarchical Bayesian Approaches’, *PLoS ONE*. Edited by G. R. Barnes, 8(2), p. e55969. doi: 10.1371/journal.pone.0055969.
- Chowdhury, R. A. *et al.* (2015) ‘MEG–EEG Information Fusion and Electromagnetic Source Imaging: From Theory to Clinical Application in Epilepsy’, *Brain Topography*, 28(6), pp. 785–812. doi: 10.1007/s10548-015-0437-3.

- Chowdhury, R. A. *et al.* (2016) ‘Complex patterns of spatially extended generators of epileptic activity: Comparison of source localization methods cMEM and 4-ExSo-MUSIC on high resolution EEG and MEG data’, *NeuroImage*, 143, pp. 175–195. doi: 10.1016/j.neuroimage.2016.08.044.
- Chowdhury, R. A. (2016) ‘Localization of generators of epileptic activity in the brain using multimodal data fusion of EEG and MEG data’.
- Chowdhury, R. A. *et al.* (2018) ‘Reproducibility of EEG-MEG fusion source analysis of interictal spikes: Relevance in presurgical evaluation of epilepsy’, *Human Brain Mapping*, 39(2), pp. 880–901. doi: 10.1002/hbm.23889.
- Clarke, D. D. and Sokoloff, L. (1999) ‘Regulation of Cerebral Metabolic Rate. In: Siegel GJ, Agranoff BW, Albers RW, et al., editors. Basic Neurochemistry: Molecular, Cellular and Medical Aspects. 6th edition.’, in. Philadelphia: Lippincott-Raven; Available at: <https://www.ncbi.nlm.nih.gov/books/NBK28194/> (Accessed: 6 February 2021).
- Cooper, R. J. *et al.* (2012) ‘A systematic comparison of motion artifact correction techniques for functional near-infrared spectroscopy’, *Frontiers in Neuroscience*, 6(OCT), pp. 1–10. doi: 10.3389/fnins.2012.00147.
- Craig M. Bennett *et al.* (2010) ‘Neural Correlates of Interspecies Perspective Taking in the Post-Mortem Atlantic Salmon: An Argument For Proper Multiple Comparisons Correction’, *Journal of Serendipitous and Unexpected Results*, (1), pp. 1:1-5. doi: 10.1088/1751-8113/44/8/085201.
- Crane, N. J. *et al.* (2003) ‘Evidence of a heterogeneous tissue oxygenation: renal ischemia / reperfusion injury in a large animal’, *Journal of Biomedical Optics*, 18(3), pp. 035001–7. doi: 10.1117/1.
- Cui, X. *et al.* (2011) ‘A quantitative comparison of NIRS and fMRI across multiple cognitive tasks’, *NeuroImage*, 54(4), pp. 2808–2821. doi: 10.1016/j.neuroimage.2010.10.069.
- Cui, X., Bray, S. and Reiss, A. L. (2010) ‘Functional near infrared spectroscopy (NIRS) signal improvement based on negative correlation between oxygenated and deoxygenated hemoglobin dynamics’, *NeuroImage*, 49(4), pp. 3039–3046. doi: 10.1016/j.neuroimage.2009.11.050.
- Culver, J. P. *et al.* (2003) ‘Diffuse optical tomography of cerebral blood flow, oxygenation, and metabolism in rat during focal ischemia’, *Journal of Cerebral Blood Flow and Metabolism*, 23(8), pp. 911–924. doi: 10.1097/01.WCB.0000076703.71231.BB.
- Curtin, A. *et al.* (2017) ‘Evaluation of evoked responses to pulse-matched high frequency and intermittent theta burst transcranial magnetic stimulation using simultaneous functional near-infrared spectroscopy’, *Neurophotonics*, 4(04), p. 1. doi: 10.1117/1.NPh.4.4.041405.
- Curtin, A., Tong, S., *et al.* (2019) ‘A systematic review of integrated functional near-infrared spectroscopy (fNIRS) and transcranial magnetic stimulation (TMS) studies’, *Frontiers in Neuroscience*, 13(FEB). doi: 10.3389/fnins.2019.00084.
- Curtin, A., Ayaz, H., *et al.* (2019) ‘Enhancing neural efficiency of cognitive processing speed via training and neurostimulation: An fNIRS and TMS study’, *NeuroImage*, 198(May), pp. 73–82. doi: 10.1016/j.neuroimage.2019.05.020.
- Dai, N. *et al.* (2021) ‘A Bayesian latent spatial model for mapping the cortical signature of

- progression to Alzheimer's disease', *Canadian Journal of Statistics*, 49(1), pp. 46–62. doi: 10.1002/cjs.11588.
- Dale, A. M. *et al.* (2000) 'Dynamic statistical parametric mapping: Combining fMRI and MEG for high-resolution imaging of cortical activity', *Neuron*, 26(1), pp. 55–67. doi: 10.1016/S0896-6273(00)81138-1.
- Dale, A. M. and Sereno, M. I. (1993) 'Improved Localization of Cortical Activity by Combining EEG and MEG with MRI Cortical Surface Reconstruction: A Linear Approach', *Journal of Cognitive Neuroscience*, 5(2), pp. 162–176. doi: 10.1162/jocn.1993.5.2.162.
- Das, T., Dileep, B. P. V. and Dutta, P. K. (2018) 'Generalized curved beam back-projection method for near-infrared imaging using banana function', *Applied Optics*, 57(8), p. 1838. doi: 10.1364/ao.57.001838.
- Daunizeau, J. *et al.* (2007) 'Symmetrical event-related EEG/fMRI information fusion in a variational Bayesian framework', *NeuroImage*, 36(1), pp. 69–87. doi: 10.1016/j.neuroimage.2007.01.044.
- Davila-Pérez, P. *et al.* (2018) 'The Effects of Waveform and Current Direction on the Efficacy and Test–Retest Reliability of Transcranial Magnetic Stimulation', *Neuroscience*, 393, pp. 97–109. doi: 10.1016/j.neuroscience.2018.09.044.
- Day, B. L. *et al.* (1989) 'Electric and magnetic stimulation of human motor cortex: surface EMG and single motor unit responses.', *The Journal of Physiology*, 412(1), pp. 449–473. doi: 10.1113/jphysiol.1989.sp017626.
- Dehghani, H., White, B. R., *et al.* (2009) 'Depth sensitivity and image reconstruction analysis of dense imaging arrays for mapping brain function with diffuse optical tomography', *Applied Optics*, 48(10), p. D137. doi: 10.1364/AO.48.00D137.
- Dehghani, H., Eames, M. E., *et al.* (2009) 'Near infrared optical tomography using NIRFAST: Algorithm for numerical model and image reconstruction', *Communications in Numerical Methods in Engineering*, 25(6), pp. 711–732. doi: 10.1002/cnm.1162.
- Delpy, D. T. *et al.* (1988) 'Estimation of optical pathlength through tissue from direct time of flight measurement', *Physics in Medicine and Biology*, 33(12), pp. 1433–1442. doi: 10.1088/0031-9155/33/12/008.
- Delpy, D. T. and Cope, M. (1997) 'Quantification in tissue near-infrared spectroscopy', *Philosophical Transactions of the Royal Society B: Biological Sciences*, 352(1354), pp. 649–659. doi: 10.1098/rstb.1997.0046.
- Dienel, G. A. and Hertz, L. (2001) 'Glucose and lactate metabolism during brain activation', *Journal of Neuroscience Research*, 66(5), pp. 824–838. doi: 10.1002/jnr.10079.
- Ding, L. (2009) 'Reconstructing cortical current density by exploring sparseness in the transform domain', *Physics in Medicine and Biology*, 54(9), pp. 2683–2697. doi: 10.1088/0031-9155/54/9/006.
- Duane, S. *et al.* (1987) 'Hybrid Monte Carlo', *Physics Letters B*, 195(2), pp. 216–222. doi: 10.1016/0370-2693(87)91197-X.
- Duncan, A. *et al.* (1995) 'Optical pathlength measurements on adult head, calf and forearm and

- the head of the newborn infant using phase resolved optical spectroscopy’, *Physics in Medicine and Biology*, 40(2), pp. 295–304. doi: 10.1088/0031-9155/40/2/007.
- Eggebrecht, A. T. *et al.* (2012) ‘A quantitative spatial comparison of high-density diffuse optical tomography and fMRI cortical mapping’, *NeuroImage*, 61(4), pp. 1120–1128. doi: 10.1016/j.neuroimage.2012.01.124.
- Eggebrecht, A. T. *et al.* (2014) ‘Mapping distributed brain function and networks with diffuse optical tomography’, *Nature Photonics*, 8(6), pp. 448–454. doi: 10.1038/nphoton.2014.107.
- Eggebrecht, A. T., Muccigrosso, D. and Culver, J. P. (2019) ‘NeuroDOT: an extensible Matlab toolbox for streamlined optical brain mapping (Conference Presentation)’, in Fantini, S. *et al.* (eds) *Optical Tomography and Spectroscopy of Tissue XIII*. SPIE, p. 51. doi: 10.1117/12.2510526.
- Eilers, P. H. C. and Marx, B. D. (2010) ‘Splines, knots, and penalties’, *Wiley Interdisciplinary Reviews: Computational Statistics*, 2(6), pp. 637–653. doi: 10.1002/wics.125.
- Eklund, A., Nichols, T. E. and Knutsson, H. (2016) ‘Cluster failure: Why fMRI inferences for spatial extent have inflated false-positive rates’, *Proceedings of the National Academy of Sciences of the United States of America*, 113(28), pp. 7900–7905. doi: 10.1073/pnas.1602413113.
- von Ellenrieder, N. *et al.* (2016) ‘Detection and Magnetic Source Imaging of Fast Oscillations (40–160 Hz) Recorded with Magnetoencephalography in Focal Epilepsy Patients’, *Brain Topography*, 29(2), pp. 218–231. doi: 10.1007/s10548-016-0471-9.
- Erdoğan, S. B., Yücel, M. A. and Akin, A. (2014) ‘Analysis of task-evoked systemic interference in fNIRS measurements: Insights from fMRI’, *NeuroImage*, 87, pp. 490–504. doi: 10.1016/j.neuroimage.2013.10.024.
- Eschweiler, G. W. *et al.* (2000) ‘Left prefrontal activation predicts therapeutic effects of repetitive transcranial magnetic stimulation (rTMS) in major depression’, *Psychiatry Research - Neuroimaging*, 99(3), pp. 161–172. doi: 10.1016/S0925-4927(00)00062-7.
- Fang, Q. *et al.* (2004) ‘Microwave image reconstruction from 3-D fields coupled to 2-D parameter estimation’, *IEEE Transactions on Medical Imaging*, 23(4), pp. 475–484. doi: 10.1109/TMI.2004.824152.
- Fang, Q. (2010) ‘Mesh-based Monte Carlo method using fast ray-tracing in Plücker coordinates’, *Biomedical Optics Express*, 1(1), p. 165. doi: 10.1364/BOE.1.000165.
- Fang, Q. and Boas, D. A. (2009) ‘Monte Carlo Simulation of Photon Migration in 3D Turbid Media Accelerated by Graphics Processing Units’, *Optics Express*, 17(22), p. 20178. doi: 10.1364/oe.17.020178.
- Fantini, S. and Franceschini, M. A. (2002) ‘Frequency-domain techniques for tissue spectroscopy and imaging’, in *Handbook of optical biomedical diagnostics*, pp. 405–453. Available at: <http://dx.doi.org/10.1016/B978-0-444-53075-2.00004-6>.
- Farzan, F. *et al.* (2016) ‘Characterizing and modulating brain circuitry through transcranial magnetic stimulation combined with electroencephalography’, *Frontiers in Neural Circuits*, 10(SEP). doi: 10.3389/fncir.2016.00073.
- Feldman, D. E. (2000) ‘Timing-based LTP and LTD at vertical inputs to layer II/III pyramidal cells in rat barrel cortex’, *Neuron*, 27(1), pp. 45–56. doi: 10.1016/S0896-6273(00)00008-8.

- Feldman, D. E. (2009) 'Synaptic Mechanisms for Plasticity in Neocortex', *Annual Review of Neuroscience*, 32(1), pp. 33–55. doi: 10.1146/annurev.neuro.051508.135516.
- Feldman, D. E. (2012) 'The Spike-Timing Dependence of Plasticity', *Neuron*, 75(4), pp. 556–571. doi: 10.1016/j.neuron.2012.08.001.
- Ferradal, S. L. *et al.* (2016) 'Functional Imaging of the Developing Brain at the Bedside Using Diffuse Optical Tomography', *Cerebral Cortex*, 26(4), pp. 1558–1568. doi: 10.1093/cercor/bhu320.
- Ferrari, M., Mottola, L. and Quaresima, V. (2004) 'Principles, techniques, and limitations of near infrared spectroscopy', *Canadian Journal of Applied Physiology*, 29(4), pp. 463–487. doi: 10.1139/h04-031.
- Ferrari, M. and Quaresima, V. (2012) 'A brief review on the history of human functional near-infrared spectroscopy (fNIRS) development and fields of application', *NeuroImage*, 63(2), pp. 921–935. doi: 10.1016/j.neuroimage.2012.03.049.
- Fischl, B. *et al.* (2002) 'Whole brain segmentation: Automated labeling of neuroanatomical structures in the human brain', *Neuron*, 33(3), pp. 341–355. doi: 10.1016/S0896-6273(02)00569-X.
- Fischl, B. and Dale, A. M. (2000) 'Measuring the thickness of the human cerebral cortex from magnetic resonance images', *Proceedings of the National Academy of Sciences of the United States of America*, 97(20), pp. 11050–11055. doi: 10.1073/pnas.200033797.
- Fishell, A. K. *et al.* (2019) 'Mapping brain function during naturalistic viewing using high-density diffuse optical tomography', *Scientific reports*, 9(1), p. 11115. doi: 10.1038/s41598-019-45555-8.
- Fisher, R. (1955) 'Statistical Methods and Scientific Induction', *Journal of the Royal Statistical Society: Series B (Methodological)*, 17(1), pp. 69–78. doi: 10.1111/j.2517-6161.1955.tb00180.x.
- Fisher, R. A. (1925) *Statistical methods for research workers, Statistical methods for research workers, 11th ed. rev.* Oliver and Boyd: Edinburgh.
- Fitzgerald, P. B., Fountain, S. and Daskalakis, Z. J. (2006) 'A comprehensive review of the effects of rTMS on motor cortical excitability and inhibition', *Clinical Neurophysiology*, 117(12), pp. 2584–2596. doi: 10.1016/j.clinph.2006.06.712.
- Fonov, V. *et al.* (2009) 'Unbiased nonlinear average age-appropriate brain templates from birth to adulthood', *NeuroImage*, 47, p. S102. doi: 10.1016/s1053-8119(09)70884-5.
- Fonov, V. *et al.* (2011) 'Unbiased average age-appropriate atlases for pediatric studies', *NeuroImage*, 54(1), pp. 313–327. doi: 10.1016/j.neuroimage.2010.07.033.
- Fox, P. T. *et al.* (2006) 'Intensity modulation of TMS-induced cortical excitation: Primary motor cortex', *Human Brain Mapping*, 27(6), pp. 478–487. doi: 10.1002/hbm.20192.
- Fox, P. T. (2012) 'The coupling controversy', *NeuroImage*, 62(2), pp. 594–601. doi: 10.1016/j.neuroimage.2012.01.103.
- Fox, P. T. and Raichle, M. E. (1986) 'Focal physiological uncoupling of cerebral blood flow and oxidative metabolism during somatosensory stimulation in human subjects.', *Proceedings of the National Academy of Sciences*, 83(4), pp. 1140–1144. doi: 10.1073/pnas.83.4.1140.

- Fragoso, T. M., Bertoli, W. and Louzada, F. (2018) ‘Bayesian Model Averaging: A Systematic Review and Conceptual Classification’, *International Statistical Review*, 86(1), pp. 1–28. doi: 10.1111/insr.12243.
- Fratello, F. *et al.* (2006) ‘Modulation of corticospinal excitability by paired associative stimulation: Reproducibility of effects and intraindividual reliability’, *Clinical Neurophysiology*, 117(12), pp. 2667–2674. doi: 10.1016/j.clinph.2006.07.315.
- Freche, D. *et al.* (2018) ‘A quantitative physical model of the TMS-induced discharge artifacts in EEG’, *PLOS Computational Biology*. Edited by D. Marinazzo, 14(7), p. e1006177. doi: 10.1371/journal.pcbi.1006177.
- Friston, K. *et al.* (2008) ‘Multiple sparse priors for the M/EEG inverse problem’, *NeuroImage*, 39(3), pp. 1104–1120. doi: 10.1016/j.neuroimage.2007.09.048.
- Fröhlich, F. (2016) ‘Synaptic Plasticity’, in *Network Neuroscience*. Elsevier, pp. 47–58. doi: 10.1016/b978-0-12-801560-5.00004-5.
- Fuchs, M. *et al.* (1999) ‘Linear and nonlinear current density reconstructions’, *Journal of Clinical Neurophysiology*, 16(3), pp. 267–295. doi: 10.1097/00004691-199905000-00006.
- Fukui, Y., Ajichi, Y. and Okada, E. (2003) ‘Monte Carlo prediction of near-infrared light propagation in realistic adult and neonatal head models’, *Applied Optics*, 42(16), p. 2881. doi: 10.1364/ao.42.002881.
- Furubayashi, T. *et al.* (2013) ‘Cortical hemoglobin concentration changes underneath the coil after single-pulse transcranial magnetic stimulation: A near-infrared spectroscopy study’, *Journal of Neurophysiology*, 109(6), pp. 1626–1637. doi: 10.1152/jn.00980.2011.
- Furutsu, K. and Yamada, Y. (1994) ‘Diffusion approximation for a dissipative random medium and the applications’, *Physical Review E*, 50(5), pp. 3634–3640. doi: 10.1103/PhysRevE.50.3634.
- Gabry, J. *et al.* (2019) ‘Visualization in Bayesian workflow’, *Journal of the Royal Statistical Society. Series A: Statistics in Society*, 182(2), pp. 389–402. doi: 10.1111/rssa.12378.
- Gabry, J. and Mahr, T. (2020) ‘bayesplot: Plotting for Bayesian Models’. Available at: <https://mc-stan.org/bayesplot>.
- Gauthier, C. J. and Hoge, R. D. (2012) ‘Magnetic resonance imaging of resting OEF and CMRO₂ using a generalized calibration model for hypercapnia and hyperoxia’, *NeuroImage*, 60(2), pp. 1212–1225. doi: 10.1016/j.neuroimage.2011.12.056.
- Gauthier, C. J. and Hoge, R. D. (2013) ‘A generalized procedure for calibrated MRI incorporating hyperoxia and hypercapnia’, *Human Brain Mapping*, 34(5), pp. 1053–1069. doi: 10.1002/hbm.21495.
- Gelfand, A. E. and Smith, A. F. M. (1990) ‘Sampling-based approaches to calculating marginal densities’, *Journal of the American Statistical Association*, 85(410), pp. 398–409. doi: 10.1080/01621459.1990.10476213.
- Gelman, A. *et al.* (2008) ‘A weakly informative default prior distribution for logistic and other regression models’, *Annals of Applied Statistics*, 2(4), pp. 1360–1383. doi: 10.1214/08-AOAS191.
- Gelman, A. *et al.* (2013a) *Bayesian data analysis*. 3rd edn. CRC press. Available at:

<http://www.stat.columbia.edu/~gelman/book/>.

Gelman, A. *et al.* (2013b) *Bayesian Data Analysis Third edition*. 3rd edn. CRC press. Available at: <http://www.stat.columbia.edu/~gelman/book/>.

Gelman, A. *et al.* (2020) ‘Bayesian workflow’, *arXiv*.

Gelman, A. and Carlin, J. (2014) ‘Beyond Power Calculations: Assessing Type S (Sign) and Type M (Magnitude) Errors’, *Perspectives on Psychological Science*, 9(6), pp. 641–651. doi: 10.1177/1745691614551642.

Gelman, A., Hill, J. and Vehtari, A. (2020) *Regression and other stories*. Cambridge University Press.

Gelman, A. and Rubin, D. B. (1992) ‘Inference from iterative simulation using multiple sequences’, *Statistical Science*, 7(4), pp. 457–472. doi: 10.1214/ss/1177011136.

Gelman, A., Simpson, D. and Betancourt, M. (2017) ‘The prior can often only be understood in the context of the likelihood’, *Entropy*, 19(10), pp. 1–13. doi: 10.3390/e19100555.

Gelman, A. and Stern, H. (2006) ‘The difference between “significant” and “not significant” is not itself statistically significant’, *American Statistician*, 60(4), pp. 328–331. doi: 10.1198/000313006X152649.

Geman, S. and Geman, D. (1984) ‘Stochastic Relaxation, Gibbs Distributions, and the Bayesian Restoration of Images’, *IEEE Transactions on Pattern Analysis and Machine Intelligence*, PAMI-6(6), pp. 721–741. doi: 10.1109/TPAMI.1984.4767596.

Giambattistelli, F. *et al.* (2014) ‘The spontaneous fluctuation of the excitability of a single node modulates the internodes connectivity: A TMS-EEG study’, *Human Brain Mapping*, 35(4), pp. 1740–1749. doi: 10.1002/hbm.22288.

Gilks, W. R., Thomas, A. and Spiegelhalter, D. J. (1994) ‘A Language and Program for Complex Bayesian Modelling’, *The Statistician*, 43(1), p. 169. doi: 10.2307/2348941.

Glover, G. H. (2011) ‘Overview of functional magnetic resonance imaging’, *Neurosurgery Clinics of North America*. NIH Public Access, pp. 133–139. doi: 10.1016/j.nec.2010.11.001.

Gomez, L. J., Goetz, S. M. and Peterchev, A. V (2018) ‘Design of transcranial magnetic stimulation coils with optimal trade-off between depth, focality, and energy’, *Journal of Neural Engineering*, 15(4), p. 046033. doi: 10.1088/1741-2552/aac967.

Gonçalves, S. I. *et al.* (2006) ‘Correlating the alpha rhythm to BOLD using simultaneous EEG/fMRI: Inter-subject variability’, *NeuroImage*, 30(1), pp. 203–213. doi: 10.1016/j.neuroimage.2005.09.062.

Gow, D. *et al.* (2004) ‘Induction of long-term plasticity in human swallowing motor cortex following repetitive cortical stimulation’, *Clinical Neurophysiology*, 115(5), pp. 1044–1051. doi: 10.1016/j.clinph.2003.12.001.

Gramigna, V. *et al.* (2017) ‘Near-Infrared Spectroscopy in Gait Disorders: Is It Time to Begin?’, *Neurorehabilitation and Neural Repair*, pp. 402–412. doi: 10.1177/1545968317693304.

Gregg, N. M. *et al.* (2010) ‘Brain specificity of diffuse optical imaging: improvements from superficial signal regression and tomography.’, *Frontiers in neuroenergetics*, 2. doi:

10.3389/fnene.2010.00014.

Groiss, S. J. *et al.* (2013) ‘Quadri-pulse stimulation induces stimulation frequency dependent cortical hemoglobin concentration changes within the ipsilateral motor cortical network’, *Brain Stimulation*, 6(1), pp. 40–48. doi: 10.1016/j.brs.2011.12.004.

Grova, C., Makni, S., *et al.* (2006) ‘Anatomically informed interpolation of fMRI data on the cortical surface’, *NeuroImage*, 31(4), pp. 1475–1486. doi: 10.1016/j.neuroimage.2006.02.049.

Grova, C., Daunizeau, J., *et al.* (2006) ‘Evaluation of EEG localization methods using realistic simulations of interictal spikes’, *NeuroImage*, 29(3), pp. 734–753. doi: 10.1016/j.neuroimage.2005.08.053.

Grova, C. *et al.* (2008) ‘Concordance between distributed EEG source localization and simultaneous EEG-fMRI studies of epileptic spikes’, *NeuroImage*, 39(2), pp. 755–774. doi: 10.1016/j.neuroimage.2007.08.020.

Grova, C. *et al.* (2016) ‘Intracranial EEG potentials estimated from MEG sources: A new approach to correlate MEG and iEEG data in epilepsy’, *Human Brain Mapping*, 37(5), pp. 1661–1683. doi: 10.1002/hbm.23127.

Grover, V. P. B. *et al.* (2015) ‘Magnetic Resonance Imaging: Principles and Techniques: Lessons for Clinicians’, *Journal of Clinical and Experimental Hepatology*. Elsevier, pp. 246–255. doi: 10.1016/j.jceh.2015.08.001.

Habermehl, C. *et al.* (2014) ‘Optimizing the regularization for image reconstruction of cerebral diffuse optical tomography’, *Journal of Biomedical Optics*, 19(9), p. 096006. doi: 10.1117/1.jbo.19.9.096006.

Hada, Y. *et al.* (2006) ‘Detection of cerebral blood flow changes during repetitive transcranial magnetic stimulation by recording hemoglobin in the brain cortex, just beneath the stimulation coil, with near-infrared spectroscopy’, *NeuroImage*, 32(3), pp. 1226–1230. doi: 10.1016/j.neuroimage.2006.04.200.

Haeussinger, F. B. *et al.* (2014) ‘Reconstructing functional near-infrared spectroscopy (fNIRS) signals impaired by extra-cranial confounds: An easy-to-use filter method’, *NeuroImage*, 95, pp. 69–79. doi: 10.1016/j.neuroimage.2014.02.035.

Hallett, M. (2000) ‘Transcranial magnetic stimulation and the human brain’, *Nature*, 406(6792), pp. 147–150. doi: 10.1038/35018000.

Hallett, M. (2007) ‘Transcranial Magnetic Stimulation: A Primer’, *Neuron*, 55(2), pp. 187–199. doi: 10.1016/j.neuron.2007.06.026.

Hallett, M. *et al.* (2017) ‘Contribution of transcranial magnetic stimulation to assessment of brain connectivity and networks’, *Clinical Neurophysiology*, 128(11), pp. 2125–2139. doi: 10.1016/j.clinph.2017.08.007.

Hämäläinen, M. S. and Ilmoniemi, R. J. (1994) ‘Interpreting magnetic fields of the brain: minimum norm estimates’, *Medical & Biological Engineering & Computing*, 32(1), pp. 35–42. doi: 10.1007/BF02512476.

Hanaoka, N. *et al.* (2007) ‘Deactivation and activation of left frontal lobe during and after low-frequency repetitive transcranial magnetic stimulation over right prefrontal cortex: A near-infrared

- spectroscopy study', *Neuroscience Letters*, 414(2), pp. 99–104. doi: 10.1016/j.neulet.2006.10.002.
- Hansen, P. C. (1999) 'The L-curve and its use in the numerical treatment of inverse problems'.
- Hansen, P. C. (2000) 'The L-Curve and its Use in the Numerical Treatment of Inverse Problems', in *Computational Inverse Problems in Electrocardiology*, ed. P. Johnston, *Advances in Computational Bioengineering*, 4, pp. 119–142. doi: 10.1.1.33.6040.
- Harrison, L. M. *et al.* (2007) 'Diffusion-based spatial priors for imaging', *NeuroImage*, 38(4), pp. 677–695. doi: 10.1016/j.neuroimage.2007.07.032.
- Harrison, R. L. (2009) 'Introduction to Monte Carlo simulation', *AIP Conference Proceedings*, 1204, pp. 17–21. doi: 10.1063/1.3295638.
- Hashemi, M. *et al.* (2020) 'The Bayesian Virtual Epileptic Patient: A probabilistic framework designed to infer the spatial map of epileptogenicity in a personalized large-scale brain model of epilepsy spread', *NeuroImage*, 217, p. 116839. doi: 10.1016/j.neuroimage.2020.116839.
- Haskell, R. C. *et al.* (1994) 'Boundary conditions for the diffusion equation in radiative transfer', *Journal of the Optical Society of America A*, 11(10), p. 2727. doi: 10.1364/josaa.11.002727.
- Hassanpour, M. S. *et al.* (2017) 'Mapping effective connectivity within cortical networks with diffuse optical tomography', *Neurophotonics*, 4(4), p. 041402. doi: 10.1117/1.nph.4.4.041402.
- Hastie, T. J. (2017) 'Generalized additive models', in *Statistical Models in S*. doi: 10.1201/9780203738535.
- Hattemer, K. *et al.* (2007) 'Excitability of the motor cortex during ovulatory and anovulatory cycles: A transcranial magnetic stimulation study', *Clinical Endocrinology*, 66(3), pp. 387–393. doi: 10.1111/j.1365-2265.2007.02744.x.
- Haufe, S. *et al.* (2008) 'Combining sparsity and rotational invariance in EEG/MEG source reconstruction', *NeuroImage*, 42(2), pp. 726–738. doi: 10.1016/j.neuroimage.2008.04.246.
- Hauk, O., Wakeman, D. G. and Henson, R. (2011) 'Comparison of noise-normalized minimum norm estimates for MEG analysis using multiple resolution metrics', *NeuroImage*, 54(3), pp. 1966–1974. doi: 10.1016/j.neuroimage.2010.09.053.
- Hayakawa, C. K. *et al.* (2001) 'Perturbation Monte Carlo methods to solve inverse photon migration problems in heterogeneous tissues', *Optics Letters*, 26(17), p. 1335. doi: 10.1364/OL.26.001335.
- Hebb, D. O. (1949) 'The Organization of Behavior: A Neuropsychological Theory (Wiley, New York)'.
- Hedrich, T. *et al.* (2017) 'Comparison of the spatial resolution of source imaging techniques in high-density EEG and MEG', *NeuroImage*, 157(December 2016), pp. 531–544. doi: 10.1016/j.neuroimage.2017.06.022.
- Hedrich, T. (2020) 'Combining high-density electrical source imaging and hemodynamic responses to epileptic discharges', (January).
- Heers, M. *et al.* (2016) 'Localization Accuracy of Distributed Inverse Solutions for Electric and Magnetic Source Imaging of Interictal Epileptic Discharges in Patients with Focal Epilepsy', *Brain Topography*, 29(1), pp. 162–181. doi: 10.1007/s10548-014-0423-1.

- Herold, F. *et al.* (2020) ‘New directions in exercise prescription: Is there a role for brain-derived parameters obtained by functional near-infrared spectroscopy?’, *Brain Sciences*, 10(6), pp. 14–23. doi: 10.3390/brainsci10060342.
- Hiraoka, M. *et al.* (1993) ‘A Monte Carlo investigation of optical pathlength in inhomogeneous tissue and its application to near-infrared spectroscopy’, *Physics in Medicine and Biology*, 38(12), pp. 1859–1876. doi: 10.1088/0031-9155/38/12/011.
- Hirose, M. *et al.* (2011) ‘On-line effects of quadripulse transcranial magnetic stimulation (QPS) on the contralateral hemisphere studied with somatosensory evoked potentials and near infrared spectroscopy’, *Experimental Brain Research*, 214(4), pp. 577–586. doi: 10.1007/s00221-011-2855-0.
- Hoffman, M. D. and Gelman, A. (2014) *The no-U-turn sampler: Adaptively setting path lengths in Hamiltonian Monte Carlo*, *Journal of Machine Learning Research*. Available at: <http://mcmc-jags.sourceforge.net> (Accessed: 31 December 2020).
- Hoge, R. D. *et al.* (1999) ‘Investigation of BOLD signal dependence on cerebral blood flow and oxygen consumption: The deoxyhemoglobin dilution model’, *Magnetic Resonance in Medicine*, 42(5), pp. 849–863. doi: 10.1002/(SICI)1522-2594(199911)42:5<849::AID-MRM4>3.0.CO;2-Z.
- Huang, Y. Z. *et al.* (2005) ‘Theta burst stimulation of the human motor cortex’, *Neuron*, 45(2), pp. 201–206. doi: 10.1016/j.neuron.2004.12.033.
- Huneau, C., Benali, H. and Chabriat, H. (2015) ‘Investigating human neurovascular coupling using functional neuroimaging: A critical review of dynamic models’, *Frontiers in Neuroscience*, 9(DEC), pp. 1–12. doi: 10.3389/fnins.2015.00467.
- Huppert, T. *et al.* (2017) ‘Comparison of group-level, source localized activity for simultaneous functional near-infrared spectroscopy-magnetoencephalography and simultaneous fNIRS-fMRI during parametric median nerve stimulation’, *NeuroPhotonics*, 4(1), p. 015001. doi: 10.1117/1.NPh.4.1.015001.
- Huppert, T. J. *et al.* (2006) ‘A temporal comparison of BOLD, ASL, and NIRS hemodynamic responses to motor stimuli in adult humans’, *NeuroImage*, 29(2), pp. 368–382. doi: 10.1016/j.neuroimage.2005.08.065.
- Ioannides, A. A., Bolton, J. P. R. and Clarke, C. J. S. (1990) ‘Continuous probabilistic solutions to the biomagnetic inverse problem’, *Inverse Problems*, 6(4), pp. 523–542. doi: 10.1088/0266-5611/6/4/005.
- Ioannidis, J. P. A. (2005) ‘Why most published research findings are false’, *PLoS Medicine*, 2(8), pp. 2–8. doi: 10.1371/journal.pmed.0020124.
- Ishimaru, A. (1978) ‘Diffusion approximation’, in *Wave Propagation and Scattering in Random Media*. Elsevier, pp. 175–190. doi: 10.1016/b978-0-12-374701-3.x5001-7.
- Izzetoglu, M. *et al.* (2010) ‘Motion artifact cancellation in NIR spectroscopy using discrete Kalman filtering’, *BioMedical Engineering Online*, 9, pp. 1–10. doi: 10.1186/1475-925X-9-16.
- Jacques, S. L. (2013) ‘Erratum: Optical properties of biological tissues: A review (Physics in Medicine and Biology (2013) 58)’, *Physics in Medicine and Biology*, 58(14), pp. 5007–5008. doi: 10.1088/0031-9155/58/14/5007.

- Jahani, S. *et al.* (2018) ‘Motion artifact detection and correction in functional near-infrared spectroscopy: a new hybrid method based on spline interpolation method and Savitzky–Golay filtering’, *NeuroPhotonics*, 5(01), p. 1. doi: 10.1117/1.nph.5.1.015003.
- James, W. (1890) *The principles of psychology*. New York: Henry Holt & Co. Henry holt and company.
- Jaszewski, G. *et al.* (2003) ‘Differences in the hemodynamic response to event-related motor and visual paradigms as measured by near-infrared spectroscopy’, *NeuroImage*, 20(1), pp. 479–488. doi: 10.1016/S1053-8119(03)00311-2.
- Jenkinson, M. *et al.* (2012) ‘FSL.’, *NeuroImage*, 62(2), pp. 782–90. doi: 10.1016/j.neuroimage.2011.09.015.
- Jirsa, V. K. *et al.* (2017) ‘The Virtual Epileptic Patient: Individualized whole-brain models of epilepsy spread’, *NeuroImage*, 145, pp. 377–388. doi: 10.1016/j.neuroimage.2016.04.049.
- Jöbsis, F. F. (1977) ‘Noninvasive, infrared monitoring of cerebral and myocardial oxygen sufficiency and circulatory parameters’, *Science*, 198(4323), pp. 1264–1266. doi: 10.1126/science.929199.
- Joseph, D. K. *et al.* (2006a) ‘Diffuse optical tomography system to image brain activation with improved spatial resolution and validation with functional magnetic resonance imaging’, *Applied Optics*, 45(31), p. 8142. doi: 10.1364/AO.45.008142.
- Joseph, D. K. *et al.* (2006b) ‘Diffuse optical tomography system to image brain activation with improved spatial resolution and validation with functional magnetic resonance imaging’, *Applied Optics*, 45(31), p. 8142. doi: 10.1364/AO.45.008142.
- Jung, P. and Ziemann, U. (2009) ‘Homeostatic and nonhomeostatic modulation of learning in human motor cortex’, *Journal of Neuroscience*, 29(17), pp. 5597–5604. doi: 10.1523/JNEUROSCI.0222-09.2009.
- Kammer, T. *et al.* (2001) ‘Motor threshold in humans: a transcranial magnetic stimulation study comparing different pulse waveforms, current directions aKammer, T., Beck, S., Thielscher, A., Laubis-Hermann, U., & Topka, H. (2001). Motor threshold in humans: a transcranial magnetic ’, *Clinical Neurophysiology*, 112, pp. 250–8.
- Kashou, N. H. *et al.* (2016) ‘Hand-grasping and finger tapping induced similar functional near-infrared spectroscopy cortical responses’, *NeuroPhotonics*, 3(2), p. 025006. doi: 10.1117/1.nph.3.2.025006.
- Kavuri, V. C. *et al.* (2012) ‘Sparsity enhanced spatial resolution and depth localization in diffuse optical tomography’, *Biomedical Optics Express*, 3(5), p. 943. doi: 10.1364/boe.3.000943.
- Kawaguchi, H. *et al.* (2008) ‘Theoretical analysis of crosstalk between oxygenated and deoxygenated haemoglobin in focal brain-activation measurements by near-infrared topography’, *Opto-electronics Review*, 16(4), pp. 404–412. doi: 10.2478/s11772-008-0032-1.
- Kawaguchi, H., Koyama, T. and Okada, E. (2007) ‘Effect of probe arrangement on reproducibility of images by near-infrared topography evaluated by a virtual head phantom’, *Applied Optics*, 46(10), p. 1658. doi: 10.1364/AO.46.001658.
- Kay, M. (2020) ‘tidybayes: Tidy Data and Geoms for Bayesian Models. R package version 2.3.0.’,

<https://mjskay.github.io/tidybayes/>. DOI: 10.5281/zenodo.1308151. doi: 10.5281/zenodo.1308151.

Kimbrell, T. A. *et al.* (2002) 'Left prefrontal-repetitive transcranial magnetic stimulation (rTMS) and regional cerebral glucose metabolism in normal volunteers', *Psychiatry Research - Neuroimaging*, 115(3), pp. 101–113. doi: 10.1016/S0925-4927(02)00041-0.

Kimiskidis, V. K. (2016) 'Transcranial magnetic stimulation (TMS) coupled with electroencephalography (EEG): Biomarker of the future', *Revue Neurologique*. Elsevier Masson SAS, pp. 123–126. doi: 10.1016/j.neuro.2015.11.004.

Kirilina, E. *et al.* (2012) 'The physiological origin of task-evoked systemic artefacts in functional near infrared spectroscopy', *NeuroImage*, 61(1), pp. 70–81. doi: 10.1016/j.neuroimage.2012.02.074.

Kirilina, E. *et al.* (2013) 'Identifying and quantifying main components of physiological noise in functional near infrared spectroscopy on the prefrontal cortex', *Frontiers in Human Neuroscience*, 7(DEC), pp. 1–17. doi: 10.3389/fnhum.2013.00864.

Klomjai, W., Katz, R. and Lackmy-Vallée, A. (2015) 'Basic principles of transcranial magnetic stimulation (TMS) and repetitive TMS (rTMS)', *Annals of Physical and Rehabilitation Medicine*. Elsevier Masson SAS, pp. 208–213. doi: 10.1016/j.rehab.2015.05.005.

Koch, S. P. (2010) 'High-resolution optical functional mapping of the human somatosensory cortex', *Frontiers in Neuroenergetics*, 2(June), pp. 1–8. doi: 10.3389/fnene.2010.00012.

Koeneke, S. *et al.* (2006) 'Extensive training of elementary finger tapping movements changes the pattern of motor cortex excitability', *Experimental Brain Research*, 174(2), pp. 199–209. doi: 10.1007/s00221-006-0440-8.

Komssi, S. and Kähkönen, S. (2006) 'The novelty value of the combined use of electroencephalography and transcranial magnetic stimulation for neuroscience research', *Brain Research Reviews*, 52(1), pp. 183–192. doi: 10.1016/j.brainresrev.2006.01.008.

Kozel, F. A. *et al.* (2009) 'Using simultaneous repetitive Transcranial Magnetic Stimulation/functional Near Infrared Spectroscopy (rTMS/fNIRS) to measure brain activation and connectivity', *NeuroImage*, 47(4), pp. 1177–1184. doi: 10.1016/j.neuroimage.2009.05.016.

Kriváneková, L. *et al.* (2013) 'Relation of brain stimulation induced changes in MEP amplitude and BOLD signal', *Brain Stimulation*, 6(3), pp. 330–339. doi: 10.1016/j.brs.2012.06.004.

Kwong, K. K. *et al.* (1992) 'Dynamic magnetic resonance imaging of human brain activity during primary sensory stimulation', *Proceedings of the National Academy of Sciences of the United States of America*, 89(12), pp. 5675–5679. doi: 10.1073/pnas.89.12.5675.

Lahr, J. *et al.* (2016) 'No difference in paired associative stimulation induced cortical neuroplasticity between patients with mild cognitive impairment and elderly controls', *Clinical Neurophysiology*, 127(2), pp. 1254–1260. doi: 10.1016/j.clinph.2015.08.010.

Lambert, J. H. (1760) *Photometria sive de mensura et gradibus luminis, colorum et umbrae*. sumptibus vidvae E. Klett, typis CP Detleffsen.

Lapalme, E., Lina, J. M. and Mattout, J. (2006) 'Data-driven parceling and entropic inference in MEG', *NeuroImage*, 30(1), pp. 160–171. doi: 10.1016/j.neuroimage.2005.08.067.

- Laplace, P.-S. (1810) ‘Mémoire sur les approximations des formules qui sont fonctions de très grands nombres et sur leur applications aux probabilités’, *Memoires de l’Academie des Sciences de Paris*.
- Di Lazzaro, V. *et al.* (1998) ‘Comparison of descending volleys evoked by transcranial magnetic and electric stimulation in conscious humans’, *Electroencephalography and Clinical Neurophysiology - Electromyography and Motor Control*, 109(5), pp. 397–401. doi: 10.1016/S0924-980X(98)00038-1.
- Di Lazzaro, V. *et al.* (2004) ‘The physiological basis of transcranial motor cortex stimulation in conscious humans’, *Clinical Neurophysiology*, 115(2), pp. 255–266. doi: 10.1016/j.clinph.2003.10.009.
- Di Lazzaro, V. *et al.* (2014) ‘Immediate and late modulation of interhemispheric imbalance with bilateral transcranial direct current stimulation in acute stroke’, *Brain Stimulation*, 7(6), pp. 841–848. doi: 10.1016/j.brs.2014.10.001.
- Di Lazzaro, V., Rothwell, J. and Capogna, M. (2018) ‘Noninvasive Stimulation of the Human Brain: Activation of Multiple Cortical Circuits’, *Neuroscientist*, 24(3), pp. 246–260. doi: 10.1177/1073858417717660.
- Lee, J. C. *et al.* (2017) ‘Paired-Associative Stimulation-Induced Long-term Potentiation-Like Motor Cortex Plasticity in Healthy Adolescents’, *Frontiers in Psychiatry*, 8(May), pp. 1–8. doi: 10.3389/fpsy.2017.00095.
- Legon, W. *et al.* (2014) ‘Transcranial focused ultrasound modulates the activity of primary somatosensory cortex in humans’, *Nature Neuroscience*, 17(2), pp. 322–329. doi: 10.1038/nn.3620.
- Levy, W. B. and Steward, O. (1983) ‘Temporal contiguity requirements for long-term associative potentiation/depression in the hippocampus’, *Neuroscience*, 8(4), pp. 791–797. doi: 10.1016/0306-4522(83)90010-6.
- Lewandowski, D., Kurowicka, D. and Joe, H. (2009) ‘Generating random correlation matrices based on vines and extended onion method’, *Journal of Multivariate Analysis*, 100(9), pp. 1989–2001. doi: 10.1016/j.jmva.2009.04.008.
- Li, T., Gong, H. and Luo, Q. (2011) ‘Visualization of light propagation in visible Chinese human head for functional near-infrared spectroscopy’, *Journal of Biomedical Optics*, 16(4), p. 045001. doi: 10.1117/1.3567085.
- Lin, F. H. *et al.* (2006) ‘Assessing and improving the spatial accuracy in MEG source localization by depth-weighted minimum-norm estimates’, *NeuroImage*, 31(1), pp. 160–171. doi: 10.1016/j.neuroimage.2005.11.054.
- Liu, A. K., Dale, A. M. and Belliveau, J. W. (2002) ‘Monte Carlo Simulation Studies of EEG and MEG Localization Accuracy’, *Human Brain Mapping*, 62, pp. 47–62. doi: 10.1002/hbm.10024.
- Loo, C. K. *et al.* (2000) ‘Transcranial magnetic stimulation (TMS) in controlled treatment studies: Are some “sham” forms active?’, *Biological Psychiatry*, 47(4), pp. 325–331. doi: 10.1016/S0006-3223(99)00285-1.
- López-Alonso, V. *et al.* (2014) ‘Inter-individual variability in response to non-invasive brain

- stimulation paradigms', *Brain Stimulation*, 7(3), pp. 372–380. doi: 10.1016/j.brs.2014.02.004.
- Lu, W., Lighter, D. and Styles, I. B. (2018) 'L 1 -norm based nonlinear reconstruction improves quantitative accuracy of spectral diffuse optical tomography', *Biomedical Optics Express*, 9(4), p. 1423. doi: 10.1364/boe.9.001423.
- von Lühmann, A., Li, X., *et al.* (2020) 'Improved physiological noise regression in fNIRS: A multimodal extension of the General Linear Model using temporally embedded Canonical Correlation Analysis', *NeuroImage*, 208(September 2019), p. 116472. doi: 10.1016/j.neuroimage.2019.116472.
- von Lühmann, A., Ortega-Martinez, A., *et al.* (2020) 'Using the General Linear Model to Improve Performance in fNIRS Single Trial Analysis and Classification: A Perspective', *Frontiers in Human Neuroscience*, 14(February), pp. 1–17. doi: 10.3389/fnhum.2020.00030.
- Lunn, D. *et al.* (2009) 'The BUGS project: Evolution, critique and future directions', *Statistics in Medicine*, 28(25), pp. 3049–3067. doi: 10.1002/sim.3680.
- Machado, A. *et al.* (2014a) 'Optimal optode montage on electroencephalography/functional near-infrared spectroscopy caps dedicated to study epileptic discharges.', *Journal of biomedical optics*, 19(2), p. 026010. doi: 10.1117/1.JBO.19.2.026010.
- Machado, A. *et al.* (2014b) 'Optimal optode montage on electroencephalography/functional near-infrared spectroscopy caps dedicated to study epileptic discharges', *Journal of Biomedical Optics*, 19(2), p. 026010. doi: 10.1117/1.JBO.19.2.026010.
- Machado, A. *et al.* (2018) 'Optimal positioning of optodes on the scalp for personalized functional near-infrared spectroscopy investigations', *Journal of Neuroscience Methods*, 309(November 2017), pp. 91–108. doi: 10.1016/J.JNEUMETH.2018.08.006.
- Machado, A. *et al.* (2021) 'Deconvolution of hemodynamic responses along the cortical surface using personalized functional near infrared spectroscopy', *Scientific Reports*, pp. 1–19. doi: 10.1038/s41598-021-85386-0.
- MacKay, D. J. C. (1992) 'Bayesian interpolation', *Neural computation*, 4(3), pp. 415–447.
- Maier, M. J. *et al.* (2018) 'Forgiveness and cognitive control – Provoking revenge via theta-burst-stimulation of the DLPFC', *NeuroImage*, 183(August), pp. 769–775. doi: 10.1016/j.neuroimage.2018.08.065.
- Mairbäurl, H. and Weber, R. E. (2012) 'Oxygen transport by hemoglobin', *Comprehensive Physiology*, 2(2), pp. 1463–1489. doi: 10.1002/cphy.c080113.
- Mäki, H. and Ilmoniemi, R. J. (2011) 'Projecting out muscle artifacts from TMS-evoked EEG', *NeuroImage*, 54(4), pp. 2706–2710. doi: 10.1016/j.neuroimage.2010.11.041.
- Marengo-Rowe, A. J. (2006) 'Structure-Function Relations of Human Hemoglobins', *Baylor University Medical Center Proceedings*, 19(3), pp. 239–245. doi: 10.1080/08998280.2006.11928171.
- Mariorenzi, R. *et al.* (1991) 'Non-invasive evaluation of central motor tract excitability changes following peripheral nerve stimulation in healthy humans', *Electroencephalography and Clinical Neurophysiology/ Evoked Potentials*, 81(2), pp. 90–101. doi: 10.1016/0168-5597(91)90002-F.

- Markram, H., Gerstner, W. and Sjöström, P. J. (2011) 'A history of spike-timing-dependent plasticity', *Frontiers in Synaptic Neuroscience*, 3(AUG), pp. 1–24. doi: 10.3389/fnsyn.2011.00004.
- Markram, H., Gerstner, W. and Sjöström, P. J. (2012) 'Spike-timing-dependent plasticity: A comprehensive overview', *Frontiers in Synaptic Neuroscience*, 4(JULY), pp. 2010–2012. doi: 10.3389/fnsyn.2012.00002.
- Martin Wolf, Marco Ferrari and Quaresima, V. (2007) 'Progress of near-infrared spectroscopy and topography for brain and muscle clinical applications', *Journal of Biomedical Optics*, 12(6), p. 062104. doi: 10.1117/1.2804899.
- Matcher, S. J. *et al.* (1995) 'Performance comparison of several published tissue near-infrared spectroscopy algorithms', *Analytical Biochemistry*, 227(1), pp. 54–68. doi: 10.1006/abio.1995.1252.
- Matsuura, K. and Okabe, Y. (1995) 'Selective Minimum-Norm Solution of the Biomagnetic Inverse Problem', *IEEE Transactions on Biomedical Engineering*, 42(6), pp. 608–615. doi: 10.1109/10.387200.
- Mattout, J. *et al.* (2005) 'Multivariate source prelocalization (MSP): Use of functionally informed basis functions for better conditioning the MEG inverse problem', *NeuroImage*, 26(2), pp. 356–373. doi: 10.1016/j.neuroimage.2005.01.026.
- McElreath, R. (2020) *Statistical Rethinking: A Bayesian Course with Examples in R and Stan (2nd ed.)*, CRC Press. CRC Press. Available at: <https://doi.org/10.1201/9780429029608>.
- McNaughton, B. L., Douglas, R. M. and Goddard, G. V. (1978) 'Synaptic enhancement in fascia dentata: Cooperativity among coactive afferents', *Brain Research*, 157(2), pp. 277–293. doi: 10.1016/0006-8993(78)90030-6.
- Merton, P. A. and Morton, H. B. (1980) 'Stimulation of the cerebral cortex in the intact human subject', *Nature*, 285(5762), p. 227. doi: 10.1038/285227a0.
- Mesquita, R. C. *et al.* (2013) 'Blood flow and oxygenation changes due to low-frequency repetitive transcranial magnetic stimulation of the cerebral cortex', *Journal of Biomedical Optics*, 18(6), p. 067006. doi: 10.1117/1.jbo.18.6.067006.
- Metaa, M. R. and Newman, E. A. (2006) 'Glial cells dilate and constrict blood vessels: A mechanism of neurovascular coupling', *Journal of Neuroscience*, 26(11), pp. 2862–2870. doi: 10.1523/JNEUROSCI.4048-05.2006.
- Michou, E. *et al.* (2012) 'Targeting unlesioned pharyngeal motor cortex improves swallowing in healthy individuals and after dysphagic stroke', *Gastroenterology*, 142(1), pp. 29–38. doi: 10.1053/j.gastro.2011.09.040.
- Michou, E. *et al.* (2014a) 'Characterizing the mechanisms of central and peripheral forms of neurostimulation in chronic dysphagic stroke patients', *Brain Stimulation*, 7(1), pp. 66–73. doi: 10.1016/j.brs.2013.09.005.
- Michou, E. *et al.* (2014b) 'Characterizing the mechanisms of central and peripheral forms of neurostimulation in chronic dysphagic stroke patients', *Brain Stimulation*, 7(1), pp. 66–73. doi: 10.1016/j.brs.2013.09.005.

- Minati, L. *et al.* (2011) 'Intra- and extra-cranial effects of transient blood pressure changes on brain near-infrared spectroscopy (NIRS) measurements', *Journal of Neuroscience Methods*, 197(2), pp. 283–288. doi: 10.1016/j.jneumeth.2011.02.029.
- Minkova, L. *et al.* (2019) 'Determinants of inter-individual variability in corticomotor excitability induced by paired associative stimulation', *Frontiers in Neuroscience*, 13(JUL), pp. 1–14. doi: 10.3389/fnins.2019.00841.
- Mochizuki, H. *et al.* (2006) 'Cortical hemoglobin-concentration changes under the coil induced by single-pulse TMS in humans: A simultaneous recording with near-infrared spectroscopy', *Experimental Brain Research*, 169(3), pp. 302–310. doi: 10.1007/s00221-005-0149-0.
- Mochizuki, H. *et al.* (2007) 'Hemoglobin concentration changes in the contralateral hemisphere during and after theta burst stimulation of the human sensorimotor cortices', *Experimental Brain Research*, 180(4), pp. 667–675. doi: 10.1007/s00221-007-0884-5.
- Mohimani, H., Babaie-Zadeh, M. and Jutten, C. (2009) 'A fast approach for overcomplete sparse decomposition based on smoothed ℓ_0 norm', *IEEE Transactions on Signal Processing*, 57(1), pp. 289–301. doi: 10.1109/TSP.2008.2007606.
- Molavi, B. and Dumont, G. A. (2010) 'Wavelet based motion artifact removal for Functional Near Infrared Spectroscopy', *2010 Annual International Conference of the IEEE Engineering in Medicine and Biology Society, EMBC'10*, pp. 5–8. doi: 10.1109/IEMBS.2010.5626589.
- Molins, A. *et al.* (2008) 'Quantification of the benefit from integrating MEG and EEG data in minimum ℓ_2 -norm estimation', *NeuroImage*, 42(3), pp. 1069–1077. doi: 10.1016/j.neuroimage.2008.05.064.
- Müller-Dahlhaus, F., Ziemann, U. and Classen, J. (2010) 'Plasticity resembling spike-timing dependent synaptic plasticity: The evidence in human cortex', *Frontiers in Synaptic Neuroscience*, 2(JUL), pp. 1–11. doi: 10.3389/fnsyn.2010.00034.
- N, H. and SK, S. (2018) 'Stress assessment by means of heart rate derived from functional near-infrared spectroscopy', *Journal of Biomedical Optics*, 23(11), p. 1. doi: 10.1117/1.jbo.23.11.115001.
- Nakamura, K. *et al.* (2016) 'Estimation of partial optical path length in the brain in subject-specific head models for near-infrared spectroscopy', *Optical Review*, 23(2), pp. 316–322. doi: 10.1007/s10043-016-0179-9.
- Näsi, T. *et al.* (2011) 'Magnetic-stimulation-related physiological artifacts in hemodynamic near-infrared spectroscopy signals', *PLoS ONE*, 6(8). doi: 10.1371/journal.pone.0024002.
- Navarro de Lara, L. I. *et al.* (2017) 'High-sensitivity TMS/fMRI of the Human Motor Cortex Using a Dedicated Multichannel MR Coil', *NeuroImage*, 150(June 2016), pp. 262–269. doi: 10.1016/j.neuroimage.2017.02.062.
- Navarro De Lara, L. I. *et al.* (2015) 'A novel coil array for combined TMS/fMRI experiments at 3 T', *Magnetic Resonance in Medicine*, 74(5), pp. 1492–1501. doi: 10.1002/mrm.25535.
- Neal, R. (1996) 'Bayesian Learning for Neural Networks', *LECTURE NOTES IN STATISTICS - NEW YORK- SPRINGER VERLAG-*.
- Neal, R. M. (1993) *Probabilistic inference using Markov chain Monte Carlo methods*. Department

- of Computer Science, University of Toronto Toronto, Ontario, Canada. Available at: <http://library1.nida.ac.th/termpaper6/sd/2554/19755.pdf>.
- Neal, R. M. (1998) ‘Regression and Classification Using Gaussian Process Priors’, *Bayesian Statistics*, 6, pp. 475–501.
- Neal, R. M. (2003) ‘Slice sampling’, *Annals of Statistics*, 31(3), pp. 705–767. doi: 10.2307/3448415.
- Neal, R. M. (2010) ‘MCMC Using Hamiltonian Dynamics’, *Handbook of Markov Chain Monte Carlo*, 54, pp. 113–162.
- Nissilä, I. *et al.* (2002) ‘Optical measurement of hemodynamic changes in the contralateral motor cortex induced by transcranial magnetic stimulation’, *Proceedings of the 13th International Conference on Biomagnetism (BIOMAG 2002)*, (August), pp. 851–854.
- Noguchi, Y., Watanabe, E. and Sakai, K. L. (2003) ‘An event-related optical topography study of cortical activation induced by single-pulse transcranial magnetic stimulation’, *NeuroImage*, 19(1), pp. 156–162. doi: 10.1016/S1053-8119(03)00054-5.
- Novi, S. L. *et al.* (2020) ‘Integration of Spatial Information Increases Reproducibility in Functional Near-Infrared Spectroscopy’, *Frontiers in Neuroscience*, 14(July), pp. 1–12. doi: 10.3389/fnins.2020.00746.
- Nummenmaa, A. *et al.* (2007) ‘Automatic relevance determination based hierarchical Bayesian MEG inversion in practice’, *NeuroImage*, 37(3), pp. 876–889. doi: 10.1016/j.neuroimage.2007.04.021.
- O’Leary, M. A. *et al.* (1995) ‘Experimental images of heterogeneous turbid media by frequency-domain diffusing-photon tomography’, *Optics Letters*, 20(5), p. 426. doi: 10.1364/ol.20.000426.
- O’Shea, J., Taylor, P. C. J. and Rushworth, M. F. S. (2008) ‘Imaging causal interactions during sensorimotor processing’, *Cortex*, 44(5), pp. 598–608. doi: 10.1016/j.cortex.2007.08.012.
- Ogawa, S. *et al.* (1990) ‘Brain magnetic resonance imaging with contrast dependent on blood oxygenation’, *Proceedings of the National Academy of Sciences of the United States of America*, 87(24), pp. 9868–9872. doi: 10.1073/pnas.87.24.9868.
- Okada, E. *et al.* (1996) ‘Experimental validation of Monte Carlo and finite-element methods for the estimation of the optical path length in inhomogeneous tissue’, *Applied Optics*, 35(19), p. 3362. doi: 10.1364/ao.35.003362.
- Okawa, S., Hoshi, Y. and Yamada, Y. (2011) ‘Improvement of image quality of time-domain diffuse optical tomography with lp sparsity regularization’, *Biomedical Optics Express*, 2(12), p. 3334. doi: 10.1364/boe.2.003334.
- Okui, N. and Okada, E. (2005) ‘Wavelength dependence of crosstalk in dual-wavelength measurement of oxy- and deoxy-hemoglobin’, *Journal of Biomedical Optics*, 10(1), p. 011015. doi: 10.1117/1.1846076.
- Oliviero, A. *et al.* (1999) ‘Cerebral blood flow and metabolic changes produced by repetitive magnetic brain stimulation’, *Journal of Neurology*, 246(12), pp. 1164–1168. doi: 10.1007/s004150050536.

- Papaspiliopoulos, O., Roberts, G. O. and Sköld, M. (2007) 'A general framework for the parametrization of hierarchical models', *Statistical Science*. Institute of Mathematical Statistics, pp. 59–73. doi: 10.1214/088342307000000014.
- Park, E. *et al.* (2017) 'Real-time measurement of cerebral blood flow during and after repetitive transcranial magnetic stimulation: A near-infrared spectroscopy study', *Neuroscience Letters*, 653, pp. 78–83. doi: 10.1016/j.neulet.2017.05.039.
- Parks, N. A. (2013) 'Concurrent application of TMS and near-infrared optical imaging: methodological considerations and potential artifacts', *Frontiers in Human Neuroscience*, 7, p. 592. doi: 10.3389/fnhum.2013.00592.
- Pascual-Leone, A., Gates, J. R. and Dhuna, A. (1991) 'Induction of speech arrest and counting errors with rapid-rate transcranial magnetic stimulation', *Neurology*, 41(5), pp. 697–702. doi: 10.1212/WNL.41.5.697.
- Pascual-Marqui, R. D. (2002) 'Standardized low-resolution brain electromagnetic tomography (sLORETA): technical details', *Methods Find Exp Clin Pharmacol*, 24(Suppl D), pp. 5–12.
- Pascual-Marqui, R. D., Michel, C. M. and Lehmann, D. (1994) 'Low resolution electromagnetic tomography: a new method for localizing electrical activity in the brain', *International Journal of Psychophysiology*, 18(1), pp. 49–65. doi: 10.1016/0167-8760(84)90014-X.
- Paulsen, K. D. and Jiang, H. (1995) 'Spatially varying optical property reconstruction using a finite element diffusion equation approximation', *Medical Physics*, 22(6), pp. 691–701. doi: 10.1118/1.597488.
- Paus, T. *et al.* (1997) 'Transcranial magnetic stimulation during positron emission tomography: A new method for studying connectivity of the human cerebral cortex', *Journal of Neuroscience*, 17(9), pp. 3178–3184. doi: 10.1523/jneurosci.17-09-03178.1997.
- Paus, T. *et al.* (1998) 'Dose-Dependent Reduction of Cerebral Blood Flow During Rapid-Rate Transcranial Magnetic Stimulation of the Human Sensorimotor Cortex', *Journal of Neurophysiology*, 79(2), pp. 1102–1107. doi: 10.1152/jn.1998.79.2.1102.
- Paus, T. and Wolforth, M. (1998) 'Transcranial magnetic stimulation during PET: Reaching and verifying the target site', in *Human Brain Mapping*. Wiley-Blackwell, pp. 399–402. doi: 10.1002/(SICI)1097-0193(1998)6:5/6<399::AID-HBM13>3.0.CO;2-H.
- Pawar, A. A. *et al.* (2008) 'Transcranial magnetic stimulation: A new therapeutic tool in psychiatry', *Medical Journal Armed Forces India*, 64(2), pp. 158–160. doi: 10.1016/S0377-1237(08)80064-0.
- Pellegrino, G., Machado, A., *et al.* (2016) 'Hemodynamic response to interictal epileptiform discharges addressed by personalized EEG-fNIRS recordings', *Frontiers in Neuroscience*, 10(MAR), p. 102. doi: 10.3389/fnins.2016.00102.
- Pellegrino, G., Hedrich, T., *et al.* (2016) 'Source localization of the seizure onset zone from ictal EEG/MEG data', *Human Brain Mapping*, 37(7), pp. 2528–2546. doi: 10.1002/hbm.23191.
- Pellegrino, G. *et al.* (2018) 'Bilateral Transcranial Direct Current Stimulation Reshapes Resting-State Brain Networks: A Magnetoencephalography Assessment', *Neural Plasticity*, 2018. doi: 10.1155/2018/2782804.

- Pellegrino, G. *et al.* (2019) 'Transcranial direct current stimulation over the sensory-motor regions inhibits gamma synchrony', *Human Brain Mapping*, 40(9), pp. 2736–2746. doi: 10.1002/hbm.24556.
- Pellegrino, G. *et al.* (2020) 'Accuracy and spatial properties of distributed magnetic source imaging techniques in the investigation of focal epilepsy patients', *Human Brain Mapping*, 41(11), pp. 3019–3033. doi: 10.1002/hbm.24994.
- Penny, W. D. *et al.* (2011) *Statistical parametric mapping: the analysis of functional brain images*, Elsevier.
- Penrose, R. (1955) 'A generalized inverse for matrices', *Mathematical Proceedings of the Cambridge Philosophical Society*, 51(3), pp. 406–413. doi: 10.1017/S0305004100030401.
- Perutz, M. F. *et al.* (1998) 'The stereochemical mechanism of the cooperative effects in hemoglobin revisited', *Annual Review of Biophysics and Biomolecular Structure*. Annu Rev Biophys Biomol Struct, pp. 1–34. doi: 10.1146/annurev.biophys.27.1.1.
- Pfeifer, M. D., Scholkmann, F. and Labruyère, R. (2018) 'Signal processing in functional near-infrared spectroscopy (fNIRS): Methodological differences lead to different statistical results', *Frontiers in Human Neuroscience*, 11, p. 641. doi: 10.3389/fnhum.2017.00641.
- Phillips, A. A. *et al.* (2015) 'Neurovascular coupling in humans: Physiology, methodological advances and clinical implications', *Journal of Cerebral Blood Flow and Metabolism*, 36(4), pp. 647–664. doi: 10.1177/0271678X15617954.
- Di Pino, G. *et al.* (2014) 'Modulation of brain plasticity in stroke: A novel model for neurorehabilitation', *Nature Reviews Neurology*, 10(10), pp. 597–608. doi: 10.1038/nrneurol.2014.162.
- Piper, S. K. *et al.* (2014) 'A wearable multi-channel fNIRS system for brain imaging in freely moving subjects', *NeuroImage*, 85(0 1), pp. 64–71. doi: 10.1016/j.neuroimage.2013.06.062.
- Player, M. J. *et al.* (2012) 'Paired associative stimulation increases motor cortex excitability more effectively than theta-burst stimulation', *Clinical Neurophysiology*, 123(11), pp. 2220–2226. doi: 10.1016/j.clinph.2012.03.081.
- Pogue, B. W. *et al.* (1995) 'Initial assessment of a simple system for frequency domain diffuse optical tomography', *Physics in Medicine and Biology*, 40(10), pp. 1709–1729. doi: 10.1088/0031-9155/40/10/011.
- Populations, T. variation and factors influencing vertical migration behavior in D. (2017) 'The neurovascular unit coming of age: a journey through neurovascular coupling in health and disease Costantino 96(1): 17–42. doi:10.1016/j.neuron.2017.07.030. The neurovascular unit coming of age: a journe', *Physiology & behavior*, 176(1), pp. 139–148. doi: 10.1016/j.neuron.2017.07.030.The.
- Prahl, S. A. (1989) 'A Monte Carlo model of light propagation in tissue', *Dosimetry of Laser Radiation in Medicine and Biology*, 10305(June), p. 1030509. doi: 10.1117/12.2283590.
- Prakash, J. *et al.* (2014) 'Sparse recovery methods hold promise for diffuse optical tomographic image reconstruction', *IEEE Journal on Selected Topics in Quantum Electronics*, 20(2). doi: 10.1109/JSTQE.2013.2278218.

- Purcell, E. M., Torrey, H. C. and Pound, R. V (1946) 'Resonance absorption by nuclear magnetic moments in a solid', *Physical review*, 69(1–2), p. 37.
- Quiton, R. L. *et al.* (2014) 'Intersession reliability of fMRI activation for heat pain and motor tasks', *NeuroImage: Clinical*, 5, pp. 309–321. doi: 10.1016/j.nicl.2014.07.005.
- R Core Team (2020) 'R: A Language and Environment for Statistical Computing'. Vienna, Austria. Available at: <http://www.r-project.org/>.
- Raffin, E. *et al.* (2015a) 'Bringing transcranial mapping into shape: Sulcus-aligned mapping captures motor somatotopy in human primary motor hand area', *NeuroImage*, 120, pp. 164–175. doi: 10.1016/j.neuroimage.2015.07.024.
- Raffin, E. *et al.* (2015b) 'Bringing transcranial mapping into shape: Sulcus-aligned mapping captures motor somatotopy in human primary motor hand area', *NeuroImage*, 120, pp. 164–175. doi: 10.1016/j.neuroimage.2015.07.024.
- Rafiei, F. *et al.* (2021) 'Transcranial magnetic stimulation alters multivoxel patterns in the absence of overall activity changes', *Human Brain Mapping*, (April), pp. 1–17. doi: 10.1002/hbm.25466.
- Reed, T. and Cohen Kadosh, R. (2018) 'Transcranial electrical stimulation (tES) mechanisms and its effects on cortical excitability and connectivity', *Journal of Inherited Metabolic Disease*, 41(6), pp. 1123–1130. doi: 10.1007/s10545-018-0181-4.
- Ridding, M. C. and Rothwell, J. C. (2007) 'Is there a future for therapeutic use of transcranial magnetic stimulation?', *Nature Reviews Neuroscience*. Nature Publishing Group, pp. 559–567. doi: 10.1038/nrn2169.
- Robert, C. P. and Casella, G. (1999) *Monte Carlo Statistical Methods*. New York, NY: Springer New York (Springer Texts in Statistics). doi: 10.1007/978-1-4757-3071-5.
- Roberts, G. O. and Rosenthal, J. S. (2004) 'General state space Markov chains and MCMC algorithms', *Probability Surveys*, 1(none), pp. 20–71. doi: 10.1214/1549578041000000024.
- Romei, V. *et al.* (2008) 'Spontaneous fluctuations in posterior α -band EEG activity reflect variability in excitability of human visual areas', *Cerebral Cortex*, 18(9), pp. 2010–2018. doi: 10.1093/cercor/bhm229.
- Rossi, S. *et al.* (2009) 'Safety, ethical considerations, and application guidelines for the use of transcranial magnetic stimulation in clinical practice and research', *Clinical Neurophysiology*. Elsevier, pp. 2008–2039. doi: 10.1016/j.clinph.2009.08.016.
- Rossini, P. M. *et al.* (1994) 'Non-invasive electrical and magnetic stimulation of the brain, spinal cord and roots: basic principles and procedures for routine clinical application. Report of an IFCN committee', *Electroencephalography and Clinical Neurophysiology*, 91(2), pp. 79–92. doi: 10.1016/0013-4694(94)90029-9.
- Rossini, P. M. *et al.* (2015a) 'Non-invasive electrical and magnetic stimulation of the brain, spinal cord, roots and peripheral nerves: Basic principles and procedures for routine clinical and research application: An updated report from an I.F.C.N. Committee', *Clinical Neurophysiology*, 126(6), pp. 1071–1107. doi: 10.1016/j.clinph.2015.02.001.
- Rossini, P. M. *et al.* (2015b) 'Non-invasive electrical and magnetic stimulation of the brain, spinal cord, roots and peripheral nerves: Basic principles and procedures for routine clinical and research

- application: An updated report from an I.F.C.N. Committee', *Clinical Neurophysiology*, 126(6), pp. 1071–1107. doi: 10.1016/j.clinph.2015.02.001.
- Rossini, P. M. and Caramia, M. D. (1992) 'Central conduction studies and magnetic stimulation.', *Current opinion in neurology and neurosurgery*, 5(5), pp. 697–703.
- Roy, C. S. and Sherrington, C. S. (1890) 'On the Regulation of the Blood-supply of the Brain', *The Journal of Physiology*, 11(1–2), pp. 85–158. doi: 10.1113/jphysiol.1890.sp000321.
- Rubin, D. B. (2004) *Multiple imputation for nonresponse in surveys*. John Wiley & Sons.
- Safo, M. K. *et al.* (2011) 'Hemoglobin-ligand binding: Understanding Hb function and allostery on atomic level', *Biochimica et Biophysica Acta - Proteins and Proteomics*. Biochim Biophys Acta, pp. 797–809. doi: 10.1016/j.bbapap.2011.02.013.
- Safo, M. K. and Bruno, S. (2011) 'Allosteric effectors of hemoglobin: past, present and future', *Chemistry and biochemistry of oxygen therapeutics: from transfusion to artificial blood*, pp. 285–300.
- Sakakibara, E. *et al.* (2016) 'Detection of resting state functional connectivity using partial correlation analysis: A study using multi-distance and whole-head probe near-infrared spectroscopy', *NeuroImage*, 142, pp. 590–601. doi: 10.1016/j.neuroimage.2016.08.011.
- Salo, K. S. T. *et al.* (2020) 'EEG Artifact Removal in TMS Studies of Cortical Speech Areas', *Brain Topography*, 33(1), pp. 1–9. doi: 10.1007/s10548-019-00724-w.
- Santosa, H. *et al.* (2017) 'Characterization and correction of the false-discovery rates in resting state connectivity using functional near-infrared spectroscopy', *Journal of Biomedical Optics*, 22(5), p. 055002. doi: 10.1117/1.JBO.22.5.055002.
- Sarasso, S. *et al.* (2014) 'Quantifying cortical EEG responses to TMS in (Un)consciousness', *Clinical EEG and Neuroscience*, 45(1), pp. 40–49. doi: 10.1177/1550059413513723.
- Sasai, S. *et al.* (2011) 'Frequency-specific functional connectivity in the brain during resting state revealed by NIRS', *NeuroImage*, 56(1), pp. 252–257. doi: 10.1016/j.neuroimage.2010.12.075.
- Sato, H. *et al.* (2004) 'Practicality of wavelength selection to improve signal-to-noise ratio in near-infrared spectroscopy', *NeuroImage*, 21(4), pp. 1554–1562. doi: 10.1016/j.neuroimage.2003.12.017.
- Sato, M. A. *et al.* (2004) 'Hierarchical Bayesian estimation for MEG inverse problem', *NeuroImage*, 23(3), pp. 806–826. doi: 10.1016/j.neuroimage.2004.06.037.
- Sato, M. aki (2001) 'Online model selection based on the variational Bayes', *Neural Computation*, 13(7), pp. 1649–1681. doi: 10.1162/089976601750265045.
- Scarapicchia, V. *et al.* (2017) 'Functional magnetic resonance imaging and functional near-infrared spectroscopy: Insights from combined recording studies', *Frontiers in Human Neuroscience*, 11(August), pp. 1–12. doi: 10.3389/fnhum.2017.00419.
- Schmitz, C. H. *et al.* (2005) 'Design and implementation of dynamic near-infrared optical tomographic imaging instrumentation for simultaneous dual-breast measurements', *Applied Optics*, 44(11), p. 2140. doi: 10.1364/AO.44.002140.
- Schneider, P. *et al.* (2011) 'Fast 3D near-infrared breast imaging using indocyanine green for

- detection and characterization of breast lesions', *RoFo Fortschritte auf dem Gebiet der Rontgenstrahlen und der Bildgebenden Verfahren*, 183(10), pp. 956–963. doi: 10.1055/s-0031-1281726.
- Scholkmann, F. *et al.* (2010) 'How to detect and reduce movement artifacts in near-infrared imaging using moving standard deviation and spline interpolation', *Physiological Measurement*, 31(5), pp. 649–662. doi: 10.1088/0967-3334/31/5/004.
- Scholkmann, F. *et al.* (2013) 'End-tidal CO₂: An important parameter for a correct interpretation in functional brain studies using speech tasks', *NeuroImage*, 66, pp. 71–79. doi: 10.1016/j.neuroimage.2012.10.025.
- Scholkmann, F., Kleiser, S., *et al.* (2014) 'A review on continuous wave functional near-infrared spectroscopy and imaging instrumentation and methodology', *NeuroImage*, pp. 6–27. doi: 10.1016/j.neuroimage.2013.05.004.
- Scholkmann, F., Klein, S. D., *et al.* (2014) 'Cerebral hemodynamic and oxygenation changes induced by inner and heard speech: a study combining functional near-infrared spectroscopy and capnography', *Journal of Biomedical Optics*, 19(1), p. 017002. doi: 10.1117/1.jbo.19.1.017002.
- Secomb, T. W. (2016) 'Hemodynamics', in *Comprehensive Physiology*. Hoboken, NJ, USA: John Wiley & Sons, Inc., pp. 975–1003. doi: 10.1002/cphy.c150038.
- Seewoo, B. J. *et al.* (2019) 'Frequency-specific effects of low-intensity rTMS can persist for up to 2 weeks post-stimulation: A longitudinal rs-fMRI/MRS study in rats', *Brain Stimulation*, 12(6), pp. 1526–1536. doi: 10.1016/j.brs.2019.06.028.
- Sejnowski, T. J. (1977) 'Storing covariance with nonlinearly interacting neurons', *Journal of Mathematical Biology*, 4(4), pp. 303–321. doi: 10.1007/BF00275079.
- Selb, J. *et al.* (2005) 'Improved sensitivity to cerebral hemodynamics during brain activation with a time-gated optical system: analytical model and experimental validation', *Journal of Biomedical Optics*, 10(1), p. 011013. doi: 10.1117/1.1852553.
- Shimokawa, T. *et al.* (2012) 'Hierarchical Bayesian estimation improves depth accuracy and spatial resolution of diffuse optical tomography', *Optics Express*, 20(18), p. 20427. doi: 10.1364/OE.20.020427.
- Shimokawa, T. *et al.* (2013a) 'Extended hierarchical Bayesian diffuse optical tomography for removing scalp artifact', *Biomedical Optics Express*, 4(11), p. 2411. doi: 10.1364/boe.4.002411.
- Shimokawa, T. *et al.* (2013b) 'Extended hierarchical Bayesian diffuse optical tomography for removing scalp artifact', *Biomedical Optics Express*, 4(11), p. 2411. doi: 10.1364/BOE.4.002411.
- Shinba, T. *et al.* (2018) 'Increase of frontal cerebral blood volume during transcranial magnetic stimulation in depression is related to treatment effectiveness: A pilot study with near-infrared spectroscopy', *Psychiatry and Clinical Neurosciences*, 72(8), pp. 602–610. doi: 10.1111/pcn.12680.
- Siebner, H. R., Peller, M., *et al.* (2001) 'Activation of frontal premotor areas during suprathreshold transcranial magnetic stimulation of the left primary sensorimotor cortex: A glucose metabolic PET study', *Human Brain Mapping*, 12(3), pp. 157–167. doi: 10.1002/1097-0193(200103)12:3<157::AID-HBM1012>3.0.CO;2-V.

- Siebner, H. R., Takano, B., *et al.* (2001) ‘Continuous transcranial magnetic stimulation during positron emission tomography: A suitable tool for imaging regional excitability of the human cortex’, *NeuroImage*, 14(4), pp. 883–890. doi: 10.1006/nimg.2001.0889.
- Siebner, H. R. *et al.* (2009) ‘Consensus paper: Combining transcranial stimulation with neuroimaging’, *Brain Stimulation*, 2(2), pp. 58–80. doi: 10.1016/j.brs.2008.11.002.
- Silvanto, J., Muggleton, N. and Walsh, V. (2008) ‘State-dependency in brain stimulation studies of perception and cognition’, *Trends in Cognitive Sciences*, 12(12), pp. 447–454. doi: 10.1016/j.tics.2008.09.004.
- Silvanto, J. and Pascual-Leone, A. (2008) ‘State-dependency of transcranial magnetic stimulation’, *Brain Topography*. *Brain Topogr*, pp. 1–10. doi: 10.1007/s10548-008-0067-0.
- Singh, A. *et al.* (2019) ‘Personalized repetitive transcranial magnetic stimulation temporarily alters default mode network in healthy subjects’, *Scientific Reports*, 9(1), pp. 1–12. doi: 10.1038/s41598-019-42067-3.
- van der Sluis, A. (1969) ‘Condition numbers and equilibration of matrices’, *Numerische Mathematik*, 14(1), pp. 14–23. doi: 10.1007/BF02165096.
- Smith, S. M. *et al.* (2004) ‘Advances in functional and structural MR image analysis and implementation as FSL’, in *NeuroImage*. Academic Press, pp. S208–S219. doi: 10.1016/j.neuroimage.2004.07.051.
- Smitha, K. A. *et al.* (2017) ‘Resting state fMRI: A review on methods in resting state connectivity analysis and resting state networks’, *Neuroradiology Journal*. SAGE Publications Inc., pp. 305–317. doi: 10.1177/1971400917697342.
- Sohrabpour, A. and He, B. (2021) ‘Exploring the Extent of Source Imaging: Recent Advances in Noninvasive Electromagnetic Brain Imaging’, *Current Opinion in Biomedical Engineering*, p. 100277. doi: 10.1016/j.cobme.2021.100277.
- Sommer, M. *et al.* (2006) ‘Half sine, monophasic and biphasic transcranial magnetic stimulation of the human motor cortex’, *Clinical Neurophysiology*, 117(4), pp. 838–844. doi: 10.1016/j.clinph.2005.10.029.
- Sotero, R. C. and Trujillo-Barreto, N. J. (2007) ‘Modelling the role of excitatory and inhibitory neuronal activity in the generation of the BOLD signal’, *NeuroImage*, 35(1), pp. 149–165. doi: 10.1016/j.neuroimage.2006.10.027.
- Stan Development Team (2020a) ‘RStan: the R interface to Stan, 2.21.2’. Available at: <http://mc-stan.org/>.
- Stan Development Team (2020b) ‘Stan Modeling Language Users Guide and Reference Manual, 2.25.0’. Available at: <https://mc-stan.org>.
- Stefan, K. (2000) ‘Induction of plasticity in the human motor cortex by paired associative stimulation’, *Brain*, 123(3), pp. 572–584. doi: 10.1093/brain/123.3.572.
- Stefan, K. *et al.* (2002) ‘Mechanisms of enhancement of human motor cortex excitability induced by interventional paired associative stimulation’, *Journal of Physiology*, 543(2), pp. 699–708. doi: 10.1113/jphysiol.2002.023317.

- Steinbrink, J. *et al.* (2006) ‘Illuminating the BOLD signal: combined fMRI-fNIRS studies’, *Magnetic Resonance Imaging*, 24(4), pp. 495–505. doi: 10.1016/j.mri.2005.12.034.
- Stokes, M. G. *et al.* (2013) ‘Biophysical determinants of transcranial magnetic stimulation: Effects of excitability and depth of targeted area’, *Journal of Neurophysiology*, 109(2), pp. 437–444. doi: 10.1152/jn.00510.2012.
- Strafella, A. P. *et al.* (2003) ‘Striatal dopamine release induced by repetitive transcranial magnetic stimulation of the human motor cortex’, *Brain*, 126(12), pp. 2609–2615. doi: 10.1093/brain/awg268.
- Strangman, G. *et al.* (2002) ‘A Quantitative Comparison of Simultaneous BOLD fMRI and NIRS Recordings during Functional Brain Activation’, *NeuroImage*, 17(2), pp. 719–731. doi: 10.1006/nimg.2002.1227.
- Strangman, G. E., Li, Z. and Zhang, Q. (2013) ‘Depth Sensitivity and Source-Detector Separations for Near Infrared Spectroscopy Based on the Colin27 Brain Template’, *PLoS ONE*, 8(8). doi: 10.1371/journal.pone.0066319.
- Strangman, G., Franceschini, M. A. and Boas, D. A. (2003) ‘Factors affecting the accuracy of near-infrared spectroscopy concentration calculations for focal changes in oxygenation parameters’, *NeuroImage*, 18(4), pp. 865–879. doi: 10.1016/S1053-8119(03)00021-1.
- Strigaro, G. *et al.* (2015) ‘Abnormal motor cortex plasticity in juvenile myoclonic epilepsy’, *Seizure*, 30, pp. 101–105. doi: 10.1016/j.seizure.2015.06.004.
- Suppa, A. *et al.* (2016) ‘Ten Years of Theta Burst Stimulation in Humans: Established Knowledge, Unknowns and Prospects’, *Brain Stimulation*, 9(3), pp. 323–335. doi: 10.1016/j.brs.2016.01.006.
- Suppa, A. *et al.* (2017) ‘The associative brain at work: Evidence from paired associative stimulation studies in humans’, *Clinical Neurophysiology*, 128(11), pp. 2140–2164. doi: 10.1016/j.clinph.2017.08.003.
- Sutoko, S. *et al.* (2019) ‘Denoising of neuronal signal from mixed systemic low-frequency oscillation using peripheral measurement as noise regressor in near-infrared imaging’, *NeuroPhotonics*, 6(01), p. 1. doi: 10.1117/1.NPh.6.1.015001.
- Süzen, M., Giannoula, A. and Durduran, T. (2010) ‘Compressed sensing in diffuse optical tomography’, *Optics Express*, 18(23), p. 23676. doi: 10.1364/oe.18.023676.
- Svaasand, L. O. (1993) ‘Tissue characterization and imaging using photon density waves’, *Optical Engineering*, 32(2), p. 258. doi: 10.1117/12.60749.
- Tachtsidis, I. *et al.* (2009) ‘False Positives In Functional Nearinfrared Topography’, in *Advances in Experimental Medicine and Biology*. Adv Exp Med Biol, pp. 307–314. doi: 10.1007/978-0-387-85998-9_46.
- Tachtsidis, I. and Scholkmann, F. (2016) ‘False positives and false negatives in functional near-infrared spectroscopy: issues, challenges, and the way forward’, *NeuroPhotonics*. doi: 10.1117/1.NPh.3.3.031405.
- Tadel, F. *et al.* (2011) ‘Brainstorm: A user-friendly application for MEG/EEG analysis’, *Computational Intelligence and Neuroscience*, 2011, p. 879716. doi: 10.1155/2011/879716.

- Talelli, P., Greenwood, R. J. and Rothwell, J. C. (2007) 'Exploring Theta Burst Stimulation as an intervention to improve motor recovery in chronic stroke', *Clinical Neurophysiology*, 118(2), pp. 333–342. doi: 10.1016/j.clinph.2006.10.014.
- Taylor, J. L. and Loo, C. K. (2007) 'Stimulus waveform influences the efficacy of repetitive transcranial magnetic stimulation', *Journal of Affective Disorders*, 97(1–3), pp. 271–276. doi: 10.1016/j.jad.2006.06.027.
- Thomas, B. and Laplace, P.-S. (1763) 'LII. An essay towards solving a problem in the doctrine of chances. By the late Rev. Mr. Bayes, F. R. S. communicated by Mr. Price, in a letter to John Canton, A. M. F. R. S', *Philosophical Transactions of the Royal Society of London*, 53, pp. 370–418. doi: 10.1098/rstl.1763.0053.
- Thomson, R. H. *et al.* (2011) 'Blood oxygenation changes resulting from suprathreshold transcranial magnetic stimulation', *Brain Stimulation*, 4(3), pp. 165–168. doi: 10.1016/j.brs.2010.10.003.
- Thomson, R. H. *et al.* (2012) 'Intensity dependent repetitive transcranial magnetic stimulation modulation of blood oxygenation', *Journal of Affective Disorders*, 136(3), pp. 1243–1246. doi: 10.1016/j.jad.2011.08.005.
- Thomson, R. H. *et al.* (2013) 'Blood oxygenation changes modulated by coil orientation during prefrontal transcranial magnetic stimulation', *Brain Stimulation*, 6(4), pp. 576–581. doi: 10.1016/j.brs.2012.12.001.
- Thomson, R. H., Daskalakis, Z. J. and Fitzgerald, P. B. (2011) 'A near infra-red spectroscopy study of the effects of pre-frontal single and paired pulse transcranial magnetic stimulation', *Clinical Neurophysiology*, 122(2), pp. 378–382. doi: 10.1016/j.clinph.2010.08.003.
- Tian, F. *et al.* (2012) 'Test-retest assessment of cortical activation induced by repetitive transcranial magnetic stimulation with brain atlas-guided optical topography', *Journal of Biomedical Optics*, 17(11), p. 116020. doi: 10.1117/1.jbo.17.11.116020.
- Tik, M. *et al.* (2017) 'Towards understanding rTMS mechanism of action: Stimulation of the DLPFC causes network-specific increase in functional connectivity', *NeuroImage*, 162(September), pp. 289–296. doi: 10.1016/j.neuroimage.2017.09.022.
- Tombini, M. *et al.* (2013) 'Mobile phone emissions modulate brain excitability in patients with focal epilepsy', *Brain Stimulation*, 6(3), pp. 448–454. doi: 10.1016/j.brs.2012.07.006.
- Tong, Y. *et al.* (2012) 'Low-frequency oscillations measured in the periphery with near-infrared spectroscopy are strongly correlated with blood oxygen level-dependent functional magnetic resonance imaging signals.', *Journal of biomedical optics*, 17(10), p. 106004. doi: 10.1117/1.JBO.17.10.106004.
- Tong, Y. *et al.* (2013) 'Evaluating the effects of systemic low frequency oscillations measured in the periphery on the independent component analysis results of resting state networks', *NeuroImage*, 76, pp. 202–215. doi: 10.1016/J.NEUROIMAGE.2013.03.019.
- Tong, Y., Lindsey, K. P. and Frederick, B. D. (2011) 'Partitioning of physiological noise signals in the brain with concurrent near-infrared spectroscopy and fMRI', *Journal of Cerebral Blood Flow and Metabolism*, 31(12), pp. 2352–2362. doi: 10.1038/jcbfm.2011.100.

- Tremblay, J. *et al.* (2018) ‘Comparison of source localization techniques in diffuse optical tomography for fNIRS application using a realistic head model’, *Biomedical Optics Express*, 9(7), p. 2994. doi: 10.1364/boe.9.002994.
- Tremblay, S. *et al.* (2019) ‘Clinical utility and prospective of TMS–EEG’, *Clinical Neurophysiology*. Elsevier Ireland Ltd, pp. 802–844. doi: 10.1016/j.clinph.2019.01.001.
- Tremblay, S. *et al.* (2020) ‘The study of noninvasive brain stimulation using molecular brain imaging: A systematic review’, *NeuroImage*, 219(June), p. 117023. doi: 10.1016/j.neuroimage.2020.117023.
- Tromberg, B. J. *et al.* (1993) ‘Properties of photon density waves in multiple-scattering media’, *Applied Optics*, 32(4), p. 607. doi: 10.1364/ao.32.000607.
- Trujillo-Barreto, N. J., Aubert-Vázquez, E. and Valdés-Sosa, P. A. (2004a) ‘Bayesian model averaging in EEG/MEG imaging’, *NeuroImage*, 21(4), pp. 1300–1319. doi: 10.1016/j.neuroimage.2003.11.008.
- Trujillo-Barreto, N. J., Aubert-Vázquez, E. and Valdés-Sosa, P. A. (2004b) ‘Bayesian model averaging in EEG/MEG imaging’, *NeuroImage*, 21(4), pp. 1300–1319. doi: 10.1016/j.neuroimage.2003.11.008.
- Tsang, P., Bailey, A. Z. and Nelson, A. J. (2015) ‘Rapid-rate paired associative stimulation over the primary somatosensory cortex’, *PLoS ONE*, 10(3), p. e0120731. doi: 10.1371/journal.pone.0120731.
- Tupak, S. V. *et al.* (2013) ‘Inhibitory transcranial magnetic theta burst stimulation attenuates prefrontal cortex oxygenation’, *Human Brain Mapping*, 34(1), pp. 150–157. doi: 10.1002/hbm.21421.
- Valentin Amrhein, Sander Greenland, B. M. *et al.* (2019) ‘Retire statistical significance Valentin Amrhein, Sander Greenland, Blake McShane and more than 800 signatories’, *Nature*, 567, pp. 305–307.
- Vasta, R. *et al.* (2017) ‘The movement time analyser task investigated with functional near infrared spectroscopy: an ecologic approach for measuring hemodynamic response in the motor system’, *Aging Clinical and Experimental Research*, 29(2), pp. 311–318. doi: 10.1007/s40520-016-0566-x.
- Vehtari, A. *et al.* (2020) ‘Rank-normalization, folding, and localization: An improved R for assessing convergence of MCMC’, *Bayesian Analysis*. doi: 10.1214/20-ba1221.
- Vehtari, A., Gelman, A. and Gabry, J. (2017) ‘Practical Bayesian model evaluation using leave-one-out cross-validation and WAIC’, *Statistics and Computing*, 27(5), pp. 1413–1432. doi: 10.1007/s11222-016-9696-4.
- Ventrucci, M. and Rue, H. (2016) ‘Penalized complexity priors for degrees of freedom in Bayesian P-splines’, *Statistical Modelling*, 16(6), pp. 429–453. doi: 10.1177/1471082X16659154.
- Vogelstein, J. T. *et al.* (2019) ‘Discovering and deciphering relationships across disparate data modalities’, *eLife*, 8, pp. 1–32. doi: 10.7554/eLife.41690.
- Voigt, J., Carpenter, L. and Leuchter, A. (2019) ‘A systematic literature review of the clinical efficacy of repetitive transcranial magnetic stimulation (rTMS) in non-treatment resistant patients

- with major depressive disorder 11 Medical and Health Sciences 1103 Clinical Sciences', *BMC Psychiatry*, 19(1). doi: 10.1186/s12888-018-1989-z.
- Walker, S. A., Fantini, S. and Gratton, E. (1997) 'Image reconstruction by backprojection from frequency-domain optical measurements in highly scattering media', *Applied Optics*, 36(1), p. 170. doi: 10.1364/ao.36.000170.
- Wang, L., Jacques, S. L. and Zheng, L. (1995) 'MCML-Monte Carlo modeling of light transport in multi-layered tissues', *Computer Methods and Programs in Biomedicine*, 47(2), pp. 131–146. doi: 10.1016/0169-2607(95)01640-F.
- Wang, W. T., Xu, B. and Butman, J. A. (2017) 'Improved SNR for combined TMS-fMRI: A support device for commercially available body array coil', *Journal of Neuroscience Methods*, 289, pp. 1–7. doi: 10.1016/j.jneumeth.2017.06.020.
- Wang, Z. *et al.* (2020) 'Statistical analysis of data repeatability measures', *arXiv*, pp. 1–26.
- Wasserstein, R. L. and Lazar, N. A. (2016) 'The ASA's Statement on p-Values: Context, Process, and Purpose', *American Statistician*. American Statistical Association, pp. 129–133. doi: 10.1080/00031305.2016.1154108.
- Wasserstein, R. L., Schirm, A. L. and Lazar, N. A. (2019) 'Moving to a World Beyond "p < 0.05"', *American Statistician*. American Statistical Association, pp. 1–19. doi: 10.1080/00031305.2019.1583913.
- Watanabe, T. *et al.* (2014) 'Bidirectional effects on interhemispheric resting-state functional connectivity induced by excitatory and inhibitory repetitive transcranial magnetic stimulation', *Human Brain Mapping*, 35(5), pp. 1896–1905. doi: 10.1002/hbm.22300.
- Wheelock, M. D., Culver, J. P. and Eggebrecht, A. T. (2019) 'High-density diffuse optical tomography for imaging human brain function', *Review of Scientific Instruments*, 90(5). doi: 10.1063/1.5086809.
- White, B. R. *et al.* (2009) 'Resting-state functional connectivity in the human brain revealed with diffuse optical tomography', *NeuroImage*, 47(1), pp. 148–156. doi: 10.1016/j.neuroimage.2009.03.058.
- White, B. R. (2010) 'Quantitative evaluation of high-density diffuse optical tomography: *in vivo* resolution and mapping performance', *Journal of Biomedical Optics*, 15(2), p. 026006. doi: 10.1117/1.3368999.
- White, B. R. and Culver, J. P. (2010) 'Quantitative evaluation of high-density diffuse optical tomography: *in vivo* resolution and mapping performance.', *Journal of biomedical optics*, 15(2), p. 026006. doi: 10.1117/1.3368999.
- Whiteman, A. C. *et al.* (2017) 'Investigation of the sensitivity of functional near-infrared spectroscopy brain imaging to anatomical variations in 5- to 11-year-old children near-infrared spectroscopy brain imaging to', 5(1). doi: 10.1117/1.NPh.5.1.011009.Downloaded.
- Wickham, H. *et al.* (2019) 'Welcome to the tidyverse', *Journal of Open Source Software*, 4(43), p. 1686. doi: 10.21105/joss.01686.
- Wijeakumar, S. *et al.* (2017) 'Validating an image-based fNIRS approach with fMRI and a working memory task', *NeuroImage*, 147(December 2015), pp. 204–218. doi:

- 10.1016/j.neuroimage.2016.12.007.
- Witt, S. T., Laird, A. R. and Meyerand, M. E. (2008) 'Functional neuroimaging correlates of finger-tapping task variations: An ALE meta-analysis', *NeuroImage*, 42(1), pp. 343–356. doi: 10.1016/j.neuroimage.2008.04.025.
- Wolters, A. *et al.* (2003) 'A temporally asymmetric Hebbian rule governing plasticity in the human motor cortex', *Journal of Neurophysiology*, 89(5), pp. 2339–2345. doi: 10.1152/jn.00900.2002.
- Wolters, A. *et al.* (2005a) 'Timing-dependent plasticity in human primary somatosensory cortex', *Journal of Physiology*, 565(3), pp. 1039–1052. doi: 10.1113/jphysiol.2005.084954.
- Wolters, A. *et al.* (2005b) 'Timing-dependent plasticity in human primary somatosensory cortex', *Journal of Physiology*, 565(3), pp. 1039–1052. doi: 10.1113/jphysiol.2005.084954.
- Woolrich, M. W. *et al.* (2001) 'Temporal autocorrelation in univariate linear modeling of FMRI data', *NeuroImage*, 14(6), pp. 1370–1386. doi: 10.1006/nimg.2001.0931.
- Woolrich, M. W. *et al.* (2004) 'Multilevel linear modelling for FMRI group analysis using Bayesian inference', *NeuroImage*, 21(4), pp. 1732–1747. doi: 10.1016/j.neuroimage.2003.12.023.
- Worsley, K. J. (2001) 'Statistical analysis of activation images. Ch 14, in Functional MRI: an introduction to methods, Jezzard P, Matthews PM, Smith SM, editors.' New York: Oxford University Press.
- Yamamoto, T. *et al.* (2002) 'Arranging optical fibres for the spatial resolution improvement of topographical images', *Physics in Medicine and Biology*, 47(18), pp. 3429–3440. doi: 10.1088/0031-9155/47/18/311.
- Yamanaka, K. *et al.* (2010) 'Transcranial magnetic stimulation of the parietal cortex facilitates spatial working memory: Near-infrared spectroscopy study', *Cerebral Cortex*, 20(5), pp. 1037–1045. doi: 10.1093/cercor/bhp163.
- Yamashita, O. *et al.* (2016a) 'Multi-subject and multi-task experimental validation of the hierarchical Bayesian diffuse optical tomography algorithm', *NeuroImage*, 135, pp. 287–299. doi: 10.1016/j.neuroimage.2016.04.068.
- Yamashita, O. *et al.* (2016b) 'Multi-subject and multi-task experimental validation of the hierarchical Bayesian diffuse optical tomography algorithm', *NeuroImage*, 135, pp. 287–299. doi: 10.1016/j.neuroimage.2016.04.068.
- Yamashita, Y., Maki, A. and Koizumi, H. (2001) 'Wavelength dependence of the precision of noninvasive optical measurement of oxy-, deoxy-, and total-hemoglobin concentration', *Medical Physics*, 28(6), pp. 1108–1114. doi: 10.1118/1.1373401.
- Yao, R., Intes, X. and Fang, Q. (2017) 'A Rapid Approach to Build Jacobians for Optical Tomography via Monte Carlo Method and Photon "Replay"', *Bio-Optics: Design and Application*, 3(2), pp. 8–10. doi: 10.1364/BODA.2017.BoW3A.3.
- Yao, R., Intes, X. and Fang, Q. (2018) 'Direct approach to compute Jacobians for diffuse optical tomography using perturbation Monte Carlo-based photon "replay"', *Biomedical Optics Express*, 9(10), p. 4588. doi: 10.1364/boe.9.004588.
- Yaroslavsky, A. N. *et al.* (2002) 'Optical properties of selected native and coagulated human brain

- tissues in vitro in the visible and near infrared spectral range', *Physics in Medicine and Biology*, 47(12), pp. 2059–2073. doi: 10.1088/0031-9155/47/12/305.
- Ye, J. C. *et al.* (2009) 'NIRS-SPM: Statistical parametric mapping for near-infrared spectroscopy', *NeuroImage*, 44(2), pp. 428–447. doi: 10.1016/j.neuroimage.2008.08.036.
- Yoshida, Y. *et al.* (2011) 'Phantom experiments for quantitative evaluation of topographic image by mapping algorithm', in Hielscher, A. H. and Taroni, P. (eds) *Optics InfoBase Conference Papers*. International Society for Optics and Photonics, p. 80881D. doi: 10.1117/12.889808.
- Yu, L. *et al.* (2018) 'Scalable and massively parallel Monte Carlo photon transport simulations for heterogeneous computing platforms', *Journal of Biomedical Optics*, 23(01), p. 1. doi: 10.1117/1.jbo.23.1.010504.
- Yu, M. *et al.* (2018) 'Statistical harmonization corrects site effects in functional connectivity measurements from multi-site fMRI data', *Human Brain Mapping*, 39(11), pp. 4213–4227. doi: 10.1002/hbm.24241.
- Yücel, M. A. *et al.* (2014) 'Reducing motion artifacts for long-term clinical NIRS monitoring using collodion-fixed prism-based optical fibers', *NeuroImage*, 85, pp. 192–201. doi: 10.1016/j.neuroimage.2013.06.054.
- Yücel, M. A. *et al.* (2016) 'Mayer waves reduce the accuracy of estimated hemodynamic response functions in functional near-infrared spectroscopy', *Biomedical Optics Express*, 7(8), p. 3078. doi: 10.1364/boe.7.003078.
- Yücel, M. A. *et al.* (2020) 'Best Practices for fNIRS publications', *Neurophotonics*, (in revisi.
- Yücel, M. A. *et al.* (2021) 'Best practices for fNIRS publications', *Neurophotonics*, 8(01), pp. 1–34. doi: 10.1117/1.nph.8.1.012101.
- Zandbelt, B. B. *et al.* (2008) 'Within-subject variation in BOLD-fMRI signal changes across repeated measurements: Quantification and implications for sample size', *NeuroImage*, 42(1), pp. 196–206. doi: 10.1016/j.neuroimage.2008.04.183.
- Zangrandi, A. *et al.* (2019) 'Conditioning transcranial magnetic stimulation of ventral premotor cortex shortens simple reaction time', *Cortex*, 121, pp. 322–331. doi: 10.1016/j.cortex.2019.09.006.
- Zeff, B. W. *et al.* (2007) 'Retinotopic mapping of adult human visual cortex with high-density diffuse optical tomography', *Proceedings of the National Academy of Sciences*, 104(29), pp. 12169–12174. doi: 10.1073/pnas.0611266104.
- Zhai, Y. and Cummer, S. A. (2009) 'Fast tomographic reconstruction strategy for diffuse optical tomography', *Optics Express*, 17(7), p. 5285. doi: 10.1364/oe.17.005285.
- Zhan, Y. *et al.* (2012a) 'Image Quality Analysis of High-Density Diffuse Optical Tomography Incorporating a Subject-Specific Head Model', *Frontiers in Neuroenergetics*, 4(MAY), p. 6. doi: 10.3389/fnene.2012.00006.
- Zhan, Y. *et al.* (2012b) 'Singular value decomposition based regularization prior to spectral mixing improves crosstalk in dynamic imaging using spectral diffuse optical tomography', *Biomedical Optics Express*, 3(9), p. 2036. doi: 10.1364/boe.3.002036.

- Zhang, X. *et al.* (2017) ‘Signal processing of functional NIRS data acquired during overt speaking’, *Neurophotonics*, 4(04), p. 1. doi: 10.1117/1.nph.4.4.041409.
- Zhang, X., Noah, J. A. and Hirsch, J. (2016) ‘Separation of the global and local components in functional near-infrared spectroscopy signals using principal component spatial filtering’, *Neurophotonics*, 3(1), p. 015004. doi: 10.1117/1.nph.3.1.015004.
- Zhang, Y. *et al.* (2005) ‘Eigenvector-based spatial filtering for reduction of physiological interference in diffuse optical imaging’, *Journal of Biomedical Optics*, 10(1), p. 011014. doi: 10.1117/1.1852552.
- Zhao, H. *et al.* (2002) ‘Maps of optical differential pathlength factor of human adult forehead, somatosensory motor and occipital regions at multi-wavelengths in NIR’, *Physics in Medicine and Biology*, 47(12), pp. 2075–2093. doi: 10.1088/0031-9155/47/12/306.
- Zhao, H. *et al.* (2021) ‘Design and validation of a mechanically flexible and ultra-lightweight high-density diffuse optical tomography system for functional neuroimaging of newborns’, *Neurophotonics*, 8(01), pp. 1–18. doi: 10.1117/1.nph.8.1.015011.
- Zhao, Q., Ji, L. and Jiang, T. (2006) ‘Improving performance of reflectance diffuse optical imaging using a multicentered mode’, *Journal of Biomedical Optics*, 11(6), p. 064019. doi: 10.1117/1.2400703.
- Zhu, C. and Liu, Q. (2013) ‘Review of Monte Carlo modeling of light transport in tissues’, *Journal of Biomedical Optics*, 18(5), p. 050902. doi: 10.1117/1.jbo.18.5.050902.
- Ziemann, U. and Siebner, H. R. (2015) ‘Inter-subject and intersession variability of plasticity induction by non-invasive brain stimulation: Boon or bane?’, *Brain Stimulation*. Elsevier Inc., pp. 662–663. doi: 10.1016/j.brs.2015.01.409.
- Zijlstra, W. G., Buursma, A. and van Assendelft, O. W. (2000) *Visible and near infrared absorption spectra of human and animal haemoglobin: determination and application*. VSP.
- Zimmer, L. and Luxen, A. (2012) ‘PET radiotracers for molecular imaging in the brain: Past, present and future’, *NeuroImage*, 61(2), pp. 363–370. doi: 10.1016/j.neuroimage.2011.12.037.
- Zonta, M. *et al.* (2003) ‘Neuron-to-astrocyte signaling is central to the dynamic control of brain microcirculation’, *Nature Neuroscience*, 6(1), pp. 43–50. doi: 10.1038/nn980.
- Zuo, X.-N., Xu, T. and Milham, M. P. (2019) ‘Harnessing reliability for neuroscience research’, *Nature Human Behaviour*, 3(8), pp. 768–771. doi: 10.1038/s41562-019-0655-x.